Study on Controlled CVD Growth of Monolayer MoS_2 and its Heterostructures for Optoelectronic Applications

A Thesis Submitted to
Indian Institute of Technology Guwahati
For the Degree of

Doctor of Philosophy

By

Larionette P. L. Mawlong

Centre for Nanotechnology
Indian Institute of Technology Guwahati
Guwahati-781039, India

June 2020

Dedicated

To my family who have always believed in me.

Centre for Nanotechnology
Indian Institute of Technology Guwahati
Guwahati-781039, India

STATEMENT

The work contained in the thesis entitled "**Study on Controlled CVD Growth of Monolayer MoS_2 and its Heterostructures for Optoelectronic Applications**" has been carried out by me at Indian Institute of Technology Guwahati under the supervision of **Prof. P. K. Giri**, Professor, Department of Physics and Centre for Nanotechnology, Indian Institute of Technology Guwahati. This work has not been submitted elsewhere for the award of any degree.

Larionette P. L. Mawlong

Roll No. - **136153008**

Senior Research Fellow
Centre for Nanotechnology
Indian Institute of Technology Guwahati
Guwahati-781039, India

Prof. P. K. Giri
Professor
Department of Physics
and Centre for Nanotechnology
Indian Institute of Technology Guwahati
Guwahati-781039, India
Phone: ***+91 361 2582703****, Fax:* ***+91 361 2690762***
Email: ***giri@iitg.ac.in***

CERTIFICATE

This is to certify that the work contained in the thesis entitled "***Study on Controlled CVD Growth of Monolayer MoS_2 and its Heterostructures for Optoelectronic Applications***" has been carried out by **Ms. Larionette P. L. Mawlong** at Indian Institute of Technology Guwahati under my supervision. This work has not been submitted elsewhere for the award of any degree.

Prof. P. K. Giri
Thesis supervisor

ACKNOWLEDGEMENT

It is my pleasure to acknowledge everyone who contributed to the journey towards the successful completion of my Ph.D. Thesis.

First and foremost, I would like to express my deepest appreciation to my Supervisor, Prof. P. K. Giri, who has given me the opportunity to work under his guidance. His vast knowledge and immense passion for Science has greatly inspired me and shaped my perception of scientific research. Not to mention, his strong technical expertise and practical skills about semiconductor material synthesis and device fabrication have helped me throughout the time of my research. I am extremely grateful to him for providing the essential arrangements, laboratory facilities and giving me the complete freedom in my work throughout my research days to accomplish my goal.

Throughout the process of my research, I would also like to thank the Doctoral Committee members, Prof. H. B. Nemade, Dr. Subhash Thota, and Dr. U. N. Maiti for their constant encouragement, critical input and insightful comments. I am extending my heartfelt thanks to our Head of the Centre for Nanotechnology, other faculty members of the Centre, members and staff of the Central Instruments Facilities (CIF) and Centre for Nanotechnology, especially Indrajit Talukdar, Kaustubh Acharya, Pranjoli Das, Chandan Borgohain, Madhurjya Borah and Sujit Deb for their constant help and support towards the completion of my Ph.D. research work.

A special thanks to my department and CIF for providing me with a good research environment with state-of-the-art research facilities. I am also extremely grateful to Indian Institute of Technology Guwahati for providing financial assistance, a safe and enjoyable working environment and good accommodation, as well as, the Central Workshop, Department of Mechanical Engineering for the fabrication of essential components used in my experimental setup. My appreciation also extends to my collaborators, Prof. T. N. Narayanan from Tata Institute of Fundamental Research, India, Dr. H. Sugimoto from Kobe University, Japan, Dr. Wolfgang Theis from the University of Birmingham, UK, for providing the opportunity to use a number of their laboratory facilities.

The completion of this work would have not been possible without the aid of my seniors and fellow labmates, Dr. Ramesh Ghosh, Dr. Ravi K. Biroju, Dr. Sk. Md. Obaidullah, Dr. Rajender Gone, Dr. Jitendra Kumar, Dr. Kamal Kumar Paul, Dr. Sumana, Somorjit, Joydip, Ruma, Sumaiya, Abhilasha, Neda, Tarik, Ravinder, Koushik, Tadasha and Abdul, who made

this research work fun and exciting. A heartfelt and sincere thanks to them and my close friends Banri, Kamal, Abhilasha, and Dangka for the support and love through my ups and downs during my Ph.D. journey.

Finally, I am extremely grateful and indebted to my family, who I value the most. I am thankful to my parents for teaching me to be persistent and strong and for their patience and constant encouragement, my sisters Lily, Nanz, Gwen and Suz who were always there for me in good times and in bad. Last but not the least, a special thanks to my grandmother Annie Mawlong who has always been a bundle of joy and brightens up my life. My journey would have not been possible without the endless love and support from my entire family.

Larionette P. L. Mawlong

IIT Guwahati

Contents

Synopsis

Atomically thin two-dimensional (2D) transition metal dichalcogenides (TMDs) are progressively attracting interest due to their exceptional structural, optical and electronic properties, promising for the wide range of applications. Among 2D TMDs, MoS_2 has attracted significant attention due to its abundance in nature, tunable optical band gap, high chemical stability, remarkable mechanical properties and efficient carrier generation. In bulk this semiconducting material has an indirect band gap of 1.2 eV whereas monolayer MoS_2 (1L-MoS_2) has a direct bandgap of 1.9 eV. The vast difference in the electronic structure of the bulk in comparison with the 1L-MoS_2 offers a great opportunity for diverse applications e.g., in photodetectors, light-emitting devices, phototransistors, sensors etc. However, these versatile applications demand growth of large-scale, layer-controlled, high quality 1L-MoS_2. Usually, 1L-MoS_2 is obtained through a top-down approach such as mechanical exfoliation or liquid exfoliation. However, these approaches are difficult to use in the fabrication of large-scale devices because they produce randomly distributed flakes and provide limited control of the number of layers in the MoS_2 film. A more promising technique for the growth of large area 1L-MoS_2 is by one-step chemical vapour deposition (CVD) method using MoO_3 and sulphur as precursors. Additionally, this method have demonstrated to produce high quality 1L-MoS_2 film with high crystallinity favorable for the fabrication of high quality devices and circuits based on MoS_2.

Monolayer MoS_2 normally has weak photoluminescence (PL) because of the poor light absorption due to the atomic thickness. It is still a challenge to obtain high and stable PL emission from 1L-MoS_2, mainly because of the intrinsic defects leading to n-type doping. Thus, this has been one of the major limitation of 1L-MoS_2 and is still at the core of research interest. To tune the optical properties of 1L-MoS_2, controlling the carrier density is one of the most effective methods. Methods such as electrical doping, chemical doping, and by forming vertical heterostructures (HSs) with other materials have been adopted in the literature. By interfacing 1L-MoS_2 with other materials (plasmonic, TMDs, etc.), the PL intensity can be improved and other optoelectronic properties can be modulated effectively. Our study focuses on the large area chemical vapor deposition growth of 1L-MoS2 on variety of substrates and in-situ growth of 1L-MoS_2@ TiO_2 HS, forming type II heterojunction, which shows complete conversion of trions to neutral excitons and thus giving rise to the ultra-high PL emission. Additionally, to further improve the PL enhancement in 1L-MoS_2, plasmonic (Ag/Au) nanoparticles (NPs)

were introduced in between the HS. The combined effect of the restrained trion emissions and conversion to neutral exciton emissions and the localized surface plasmon in Ag/Au NPs underneath the 1L-MoS_2 film which initiates exciton-plasmon coupling between excitons of the 1L-MoS_2 and surface plasmons of the Ag /Au NPs at the MoS_2/Ag or MoS_2/Au interface leads to the giant enhancement of the PL.

Another effective way to understand the effect of charge transfer in the tuning of the optical properties of MoS_2 is to study the charge transfer mechanism. However, in these studies, the role of defects in PL quenching of the 1L-MoS_2 has not been addressed. To our knowledge, there is no report on the charge transfer from WS_2 QDs to 1L-MoS_2 and the resulting doping and PL quenching effect. It is interesting to study the role of defects in the charge transfer dynamics in the 1L-MoS_2 layers through PL spectroscopy and its implications for future applications. In the literature, the studies on heterostructures have been usually performed on chemically grown 2D layers, which are often multilayered and crystalline quality of layer is inferior to that grown by chemical vapor deposition (CVD) techniques.

Next, 1L-MoS_2, being a direct band gap material, is favorable for the light emission and broadband efficient photodetection. However, the performances of the 2D 1L-MoS_2 based photodetectors are limited by the low light absorbance of monolayer MoS_2. Thus the integration of MoS2 with other low-dimensional high light harvesting materials such as WS_2 quantum dots (QDs) leads to substantial enhancement in the light absorption resulting in high photoresponsivity along with fast response due to high carrier mobility in the 1L-MoS_2. Under reverse bias, the 1L-MoS_2/WS_2 QD heterojunction photodetector shows high, broadband and ultra-fast photoresponse. Our results contain key step for the development of practical commercial devices for light emission and broadband photodetection.

This thesis presents a systematic study on the controlled growth of 1L-MoS_2 film and its various plasmonic and type-II HSs with tunable optical properties for applications in light emission and broadband photodetection. We believe that these studies are very significant to address the current challenges of energy and multifunctional optoelectronic applications of 2D materials. The complete thesis work has been organized into seven chapters as detailed below:

Chapter 1 presents a brief introduction on the important properties, growth techniques of monolayer MoS_2 and their potential applications, such as field-effect transistors (FETs), memory devices, photodetectors, solar cells, electrocatalysts for HER, and lithium ion batteries. Furthermore, the major challenges related to growth mechanism i.e., large-scale

synthesis technique, to achieve high quality MoS_2 films is discussed. Recent progress on the fabrication of 2D MoS_2 based hybrids with plasmonic metal nanoparticles/suitable semiconductors (0D, 1D and 2D) semiconductor for light emitting and broadband photodetection applications are presented. A brief account of the experimental techniques used is also presented. The chapter ends with a motivation for the present work. A brief discussion on the important features of 1L-MoS_2 HSs and their potential technological applications in the above field are addressed in this chapter. The problems and challenges of utilizing 1L-MoS_2 as well as its HSs in the device applications and the key parameters to improve the devices performances are discussed and the motivation of the present work is presented at the end of the chapter.

Chapter 2 presents a systematic study for the understanding of the nucleation and growth mechanism of chemical vapour deposition (CVD) grown MoS_2. Our results demonstrates two types of MoS_2 flakes. One with uniform planar thickness (monolayer and bilayer) and the other with multilayer flakes. By tuning the growth temperature and carrier gas flow, the formation of these two types of flakes can be controlled. The growth process essentially depends on the concentration of the vapour precursor (MoS_2 and S). A higher concentration of the reactants promotes self-seeding nucleation, which further leads to few to multi-layer MoS_2, while a lower concentration of the reactants facilitates the 2D planar nucleation that leads to monolayer/bilayer MoS_2 growth. Furthermore, using the optimized condition for monolayer growth, we have synthesized a continuous film of monolayer MoS_2 covering an area as large as a few mm^2 on a variety of different substrates. In this process, the growth is allowed to take place in the naturally formed gap between masked with circular openings and the substrate, when the latter is placed on top of the former inside a CVD system. This work provides valuable insights on the controlled growth of large area monolayer MoS_2 that is crucial for exploring its novel applications.

In **Chapter 3, w**e demonstrate a simple technique to enhance the PL emission by controlling the population of trions and excitons by forming a core-shell heterostructure (HS) of MoS_2 on TiO_2. TiO_2 nanorods (NRs) with diameter ~200 nm and length ~1µm are coated with a 1L-MoS_2 shell by CVD method and the 1L-MoS_2@TiO_2 HS shows strong enhancement of PL intensity by about two orders of magnitude over the pristine 1L-MoS_2 at room temperature. The enhancement of PL in the HS is attributed to: firstly, the p-doping in the MoS_2 lattice through charge transfer from MoS_2 to TiO_2 and secondly, the radiative recombination of excitons, which dominates over the non-radiative ones in the HS, as confirmed by the low

temperature PL analysis. This work provides a novel route to grow a core-shell HS of 1L-MoS_2 and TiO_2 NRs for strong enhancement of PL promising future practical applications.

Chapter 4 presents a simple and powerful strategy to achieve a dramatically high PL enhancement of 1L-MoS_2 using plasmonic Au/Ag NPs grown on TiO_2 nanostructures (NSs) as a substrate. An array of Au NPs were coated on the hydrothermally grown hierarchical TiO_2 NSs followed by a direct CVD growth of monolayer MoS_2 shell, forming a TiO_2/Au/MoS_2 ternary core-shell HS. This architecture allows a strong interaction between the incident light and 1L-MoS_2 leading to a ~463-fold enhancement in PL intensity compared to the pristine 1L-MoS_2 at room temperature. The Raman and HRTEM analyses reveal the formation of TiO_2/Au/MoS_2 core-shell HS. Our study reveals two major mechanisms for the enhancement of PL intensity in 1L-MoS_2. Firstly, the excess electrons responsible for trion emission are transferred from the MoS_2 to TiO_2 at the interface of MoS_2/TiO_2, leading to the heavy p-doping effect in MoS_2 lattice, which enhances the neutral exciton emissions and restrains the trion emissions. Secondly, the exciton-plasmon coupling between excitons of the 1L-MoS_2 and surface plasmons of the Au NPs at the MoS_2/Au interface is believed to enhance PL emission enormously. The present study have demonstrated that MoS_2 based HS offers a promising way to improve future nanophotonic and optoelectronic devices, such as photodetectors, plasmonic field-effect transistors etc.

Chapter 5 presents an investigation of the tunability of the photoluminescence (PL) of the monolayer MoS_2 (1L-MoS_2) by decorating it with WS_2 quantum dots (WS_2 QD). The direct bandgap 1L-MoS_2 and WS_2 QDs are grown by chemical vapor deposition and liquid exfoliation methods, respectively. The room temperature PL spectrum of bare 1L-MoS_2 is systematically quenched with its decoration with WS_2 QDs at different concentrations. This quenching of the PL is traced to the charge transfer from the WS_2 QD to 1L-MoS_2 resulting in the conversion of the neutral exciton to trion, thus making the 1L-MoS_2 n-type doped. Additionally, the presence of defects may be another dominant factor that alters the PL emission. The doped electron density up to $\Delta n_e \sim 1.5 \times 10^{13}$ cm^{-2} indicates high n-type doping in the 1L-MoS_2. We show that by solving the four-energy level model involving coupled carrier dynamics based on the coupled rate equations, we can have a better understanding of the contribution of the defects in the recombination dynamics of the hybrid structure. Our results suggest an effective way to manipulate the electron density through doping technique, which is advantageous to tune the optical and electrical properties of monolayer TMDs for optoelectronic applications.

Chapter 6 presents CVD growth of 1L-MoS_2 decorated with WS_2 QDs for optoelectronic applications. In this work, we incorporate WS_2 QDs with direct CVD grown monolayer MoS_2 on Si/SiO_2 substrate and fabricate a vertical heterojunction photodetector (PD). The 1L-MoS_2/WS_2 QD heterojunction PD can operate at a very low bias (0.1 V) and with fast photo-response speed exhibiting photocurrent growth and decay times of 18.5µs and 95.4µs, respectively. The enhanced performance of the heterojunction PD is attributed to the fast transfer of photogenerated electrons from WS_2 QDs to monolayer MoS_2 and n-doping in MoS_2. We evaluate various device parameters to realize the superiority of the p-n heterojunction photodetector operated under a low bias. This work offers a detailed insights to understand and fabricate the next generation multifunctional optoelectronic devices based on the 1L-MoS_2 and WS_2 heterojunction.

Chapter 7 presents the summary and highlights of the contributions of the present thesis. Future scope of work on monolayer MoS_2, and its HSs with other materials for different optoelectronic applications are presented at the end.

List of Publications:

A. In Peer-Reviewed Journals:

1. Larionette P L Mawlong, Kamal Kumar Paul, P. K. Giri, "Direct CVD Growth of Monolayer MoS_2 on TiO_2 Nanorods and Evidence for Doping Induced Strong Photoluminescence Enhancement" *J. Phys. Chem. C.*, 122 (26), 15017 (2018).
2. Larionette P. L. Mawlong, Abhilasha Bora and P. K. Giri, "Couple Charge Transfer Dynamics and Photoluminescence Quenching in Monolayer MoS_2 Decorated with WS_2 Quantum Dots" *Sci. Rep.*, 9, 19414 (2019).
3. Biroju, Ravi; D. Das, R. Sharma, S. Pal, Larionette. P. L. Mawlong, K. Bhorkar, P. K. Giri, A. Singh, T. N. Narayanan, "On the Hydrogen Evolution Reaction Activity of Graphene-MoS_2 van der Waals Heterostructures", *ACS Energy Letter 2*, 6, 1355 (2017)
4. Kamal Kumar Paul, Larionette P. L. Mawlong and P. K. Giri, "Trion Inhibited Strong Excitonic Emission and Efficient Broadband Photodetection by In-situ CVD Grown Monolayer MoS_2 on TiO_2 Nanostructure". *ACS Appl. Mater. Interface* 10 (49), 42812 (2018)
5. Abhilasha Bora, Larionette P. L. Mawlong, Ruma Das, and P. K. Giri, Understanding the excitation wavelength dependent spectral shift and large exciton binding energy of WS_2 quantum dots and its interaction with single-walled carbon nanotubes, *J. Colloids & Interf. Sci.* 561, 519 (2020)
6. Joydip Ghosh, Larionette P. L. Mawlong, G. B. Manasa, Alexander J Pattison, Wolfgang Theis, Sudip Chakraborty and P. K. Giri, Solid-state synthesis of stable and color tunable cesium lead halide perovskite nanocrystals and mechanism of high-erformance photodetection in monolayer $MoS_2/CsPbBr_3$ vertical heterojunction, *J. Mater. Chem. C.* 8, 8917 (2020)

B. Additional Publications:

7. Ramesh Ghosh, Joydip Ghosh, Ruma Das, Larionette P. L. Mawlong, Kamal Kumar Paul and P. K. Giri, Multifunctional Ag Nanoparticle Decorated Si Nanowires for sensing, photocatalysis and light Emission Applications, *J. Colloids & Interface Sci.* 532, 464 (2018)

C. Manuscript Submitted:

1. Larionette P. L. Mawlong, Kamal K. Paul and P. K. Giri, "Exciton-Plasmon Coupling and Giant Photoluminescence Enhancement in Hierarchical designed TiO_2/Au/MoS_2 Ternary Core-Shell Heterostructure"
2. Larionette P. L. Mawlong, Kamal K. Paul and P. K. Giri, "A High-Performance Hybrid 2D/0D Photodetector based on 1L-MoS_2/WS_2 Quantum Dot Heterostructure"

D. Conference Papers Presented:

1. Larionette P. L. Mawlong, Ravi K. Biroju and P. K. Giri, "*Tunable Visible Photoluminescence from Two Dimensional MoS_2 nanodots*" International Conference on Advanced Nanomaterial and Nanotechnology **(ICANN 2015)**, IIT Guwahati, 8th-11th December 2015.
2. Larionette P. L. Mawlong, Ravi K. Biroju and P. K. Giri, "The Effect of Rapid Thermal Annealing on the Two Dimensional MoS_2 Layers Grown By Chemical Vapour Deposition" National

Conference on Recent Advances in Nanoscience and Nanotechnology **(NCRANNT-2016),** *NEHU, Shillong, 8-9 September, 2016.* ***(Best Poster Award).***

3. Larionette P. L. Mawlong, Ravi K. Biroju and P. K. Giri, "Low temperature Raman and Photoluminescence studies of monolayer and few layer MoS_2", International Conference on Emerging Trends in Nanomaterials Science & Technology **(ICETNMST-2017),** NIT Nagaland, Dimapur, 4-6 January, 2017.
4. Larionette P. L. Mawlong, Kamal Kumar Paul and P. K. Giri "Enhancement in the Photoluminescence Intensity of CVD Grown Monolayer MoS_2 Film on TiO_2 nanorods Array Template", International Conference on Advanced Nanomaterial and Nanotechnology **(ICANN-2017),** 18-21 December, 2017 ***(Best Poster Award)***
5. Larionette P. L. Mawlong, Kamal Kumar Paul and P. K. Giri "*Solar Light Driven Enhanced Photocatalysis by CVD Grown Monolayer MoS_2 Film on TiO_2 Nanorods Array*" Conference on Advances in Catalysis for Energy and Environment **(CACEE-2018)**, TIFR Mumbai, 10-12 January, 2018.
6. Larionette P. L. Mawlong, Kamal Kumar Paul and P. K. Giri "*Simultaneous Photoluminescence Enhancement in CVD Grown Single Layer MoS_2 and TiO_2 NRs in the MoS_2@TiO_2 Heterojunction"* International Conference on Optoelectronic and Nano Materials for Advanced Technology **(icONMAT-2019),** CUSAT Kochi, 3-5 January, 2019.
7. Larionette P. L. Mawlong, Abhilasha Bora and P. K. Giri "*Tunability of the Photoluminescence and Coupled Charge Transfer Dynamics in Monolayer MoS_2 Decorated with WS_2 Quantum Dots*" Graphene2020 virtual international conference and expo, 19-23 October, 2020. ***(Best Poster Award)***

E. Workshops Attended:

1. *INUP Familiarization workshop on 'Nanofabrication Technologies', IISc Bangalore, March, 2014.*
2. *'National workshop on MEMS/NEMS and Theranostic devices (NWNTD-2015)', IIT Guwahati, 16-17 March, 2015.*
3. *'National Workshop on Advanced Probing Techniques in TEM', IIT Guwahati, 15-16 February, 2016.*
4. *'2nd National Workshop on MEMS/NEMS and Theranostic devices (NWNTD-2016', IIT Guwahati 21-22 March, 2016.*
5. *'3rd National Workshop on MEMS/NEMS and Theranostic devices (NWNTD-2017', IIT Guwahati 21-23 March, 2017.*
6. *'4th National Workshop on MEMS/NEMS and Theranostic devices (NWNTD-2017', IIT Guwahati 26-28 February, 2018.*

List of Abbreviations

Abbreviation	***Description***
0D	Zero dimensional
1D	One dimensional
2D	Two dimensional
3D	Three dimensional
1L	Single Layer
CVD	Chemical Vapor Deposition
DRS	Diffuse Reflectance Spectroscopy
EDS	Energy Dispersive X-ray Spectroscopy
FESEM	Field Emission Scanning Electron Microscopy
FETEM	Field Emission Transmission Electron Microscopy
FWHM	Full Width at Half Maxima
HER	Hydrogen Evolution Reaction
HRTEM	High Resolution Transmission Electron Microscopy
HS	Heterostructure
NC	Nanocrystal
NS	Nanostructure
NIR	Near Infrared
NP	Nanoparticle
NR	Nanorod
NT	Nanotube
NW	Nanowire
O_V	Oxygen vacancy
PL	Photoluminescence
QC	Quantum Confinement
QD	Quantum Dot
RTA	Rapid Thermal Annealing
SAED	Selected Area Electron Diffraction
SPR	Surface Plasmon Resonance
STEM	Scanning Transmission Electron Microscopy

TEM	Transmission Electron Microscopy
TRPL	Time Resolved Photoluminescence
UV-Vis	Ultraviolet Visible
XPS	X-ray Photoelectron Spectroscopy
XRD	X-ray Diffraction

Chapter 1

Introduction

Ground breaking research on graphene and its fundamental physics have led to the discovery of graphene-like two dimensional (2D) layered nanomaterials aiming to overcome the shortcomings of graphene and expanding its range of applications. Among these 2D materials, the family of transition metal dichalcogenides (TMDs), such as MoS_2, WS_2, $MoSe_2$, WSe_2, etc., are 2D layered semiconductors that have attracted much attention worldwide in the recent years due to their remarkable properties, and these are utilized for the exploration of two-dimensional physics and device applications. Among the TMDs, molybdenum disulfide (MoS_2) has been one of the most studied TMDs due to its unique optical and electrical properties during the transition from indirect bandgap to direct bandgap when scaled down from bulk to monolayer form. This tunability of its nature of bandgap makes it a promising candidate for various optoelectronic applications, such as solar cells,[1-2] photodetectors,[3-4] light-emitting diodes[5-6] and phototransistor.[7-9] The Mo and S atoms in MoS_2 have strong ionic bonding, and different layers of MoS_2 are held together by a weak van der Waals (vdW) force. Owing to weak forces, the atomically thin layers are weakly bonded; they can be easily isolated and stacked with other materials forming a huge variety of heterostructures (HSs) without the limitations of lattice matching.[10] With the formation of the HS through the introduction of additional structural complexities, the distinctive properties such as electrical, optical, and structural can be tuned selectively, thus, leading to a material with unique and much superior properties. By manipulating such novel properties, we can have a detailed understanding of the MoS_2 based HSs, which are potential candidates for future optoelectronic applications. In this chapter, we briefly review the important attributes of MoS_2, the recent strategies for the growth of MoS_2 with different nanostructures, and the emerging applications such as sensors, photodetectors, electrocatalysts for HER, and solar cells. Finally, a perspective on major challenges, the focus of the present thesis, along with its main contributions are described at the end of the chapter.

1.1. Properties of MoS_2

1.1.1 Crystal Structure of MoS_2

MoS_2 is a layered material, represented by a generalized formula MX_2, (M= transition metal (Mo) and X=chalcogen (S)), where the Mo atoms in a hexagonal plane is sandwiched between two planes of S atoms.[11] This layered structure are covalently bonded in a sequence of S-Mo-S, and the sandwich layers are held together by weak van der Waals forces, as shown in **Fig 1.1(a).**

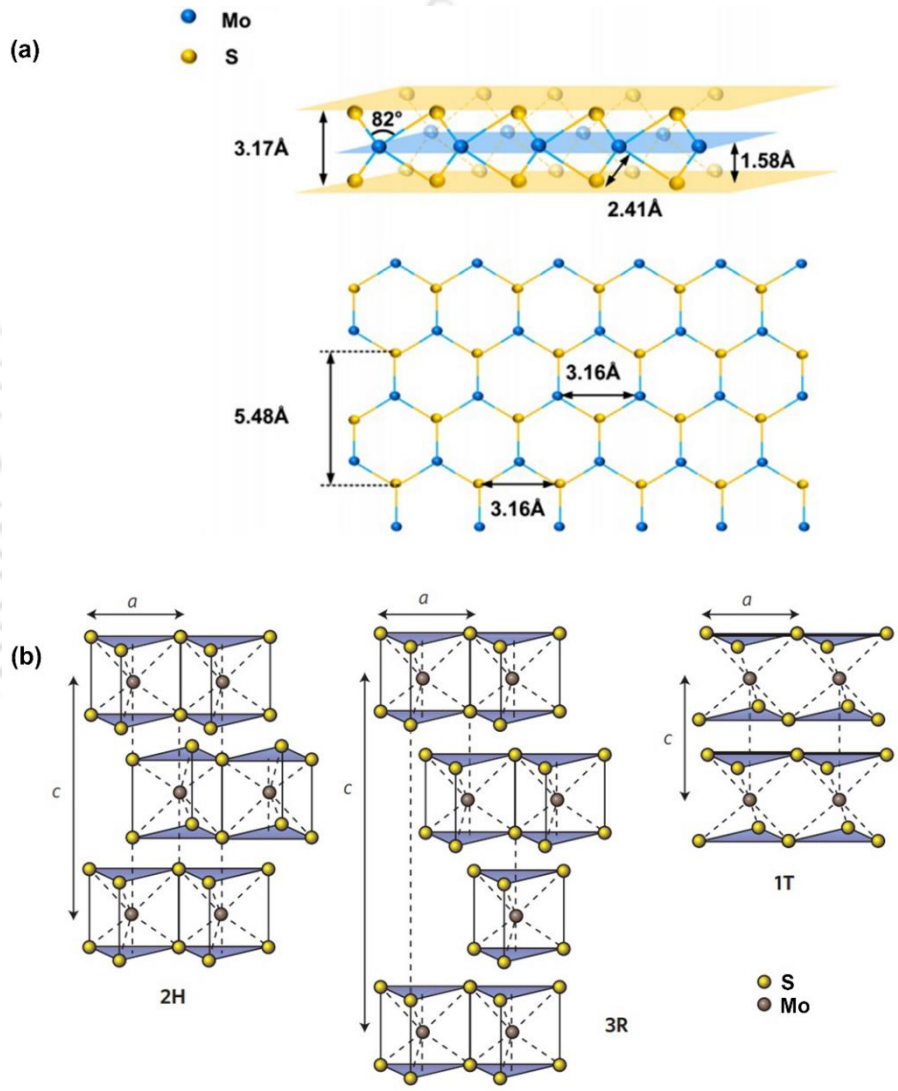

Fig. 1.1. (a) Schematic representation of MoS_2 crystal structure showing lateral view (top) and top view (bottom). Adapted from Ref. [11] (b) Side view of the schematics of the structural polytypes of MoS_2: 2H (hexagonal symmetry, two layers per repeat unit, trigonal prismatic coordination), 3R (rhombohedral symmetry, three layers per repeat unit, trigonal prismatic coordination) and 1T (tetragonal symmetry, one layer per repeat unit, octahedral coordination). Adapted from Ref. [12]

Depending on the order of layer stacking and the metal atom coordination, MoS_2 has three stacking polytypes: 1T, 2H, and 3R, as shown in **Fig. 1.1(b)**. The 2H phase has trigonal prismatic

coordination with hexagonal symmetry, which is more stable and dominant in nature as compared to 3R and 1T phases. The 1T phase is a metastable metallic phase composed of octahedral Mo coordination with tetragonal symmetry, whereas 3R phase is trigonal prismatic having three layers per cell in rhombohedral symmetry and is unstable and upon heating can easily transform to 2H phase.[12]

1.1.2. Electronic Band Structure of MoS_2

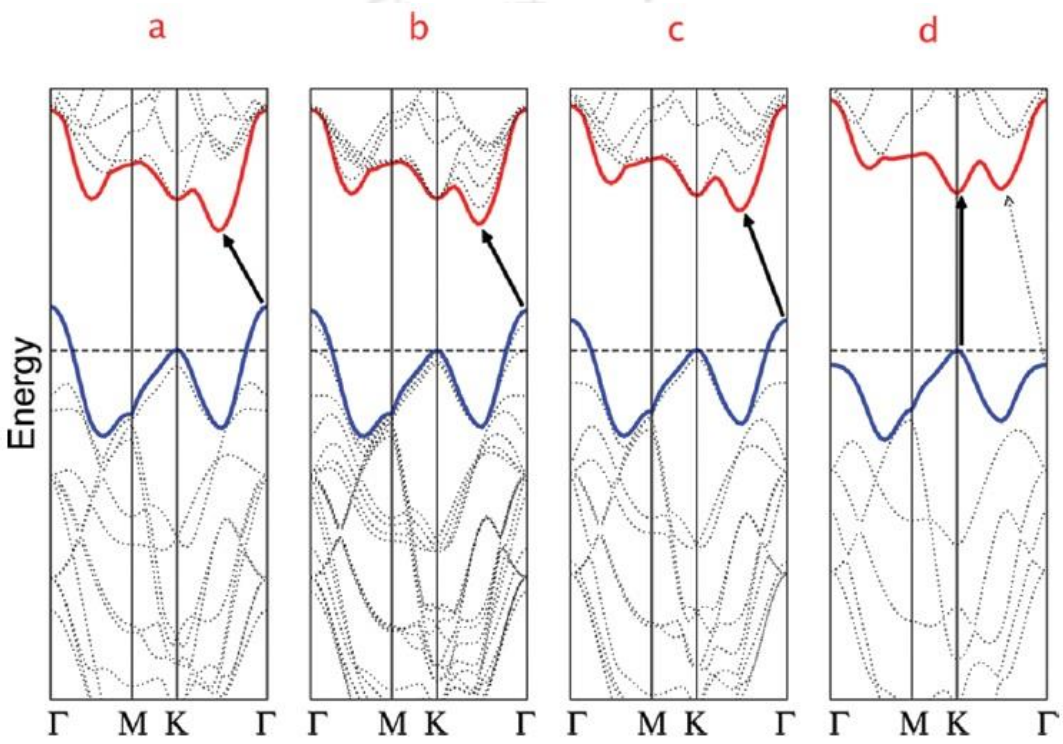

Fig. 1.2. Band structure of MoS_2 calculated by first-principle density function theory (DFT) from bulk to monolayer MoS_2 (a→d). The horizontal dashed lines denote the Fermi levels. The black arrows show the fundamental bandgaps (direct or indirect) for each system. The top of the valence bands and bottom of the conduction band is highlighted by blue and red solid lines, respectively. Adopted from Ref. [13]

The electronic band structure of MoS_2 has been calculated from the first principles density functional theory[13] when its thickness is reduced from bulk to monolayer, as shown in **Fig. 1.2**. Bulk MoS_2 is an indirect bandgap semiconductor having a bandgap of 1.2 eV, with the valence band maximum (VBM) located at the Γ point in the Brillouin zone, while the conduction band minimum (CBM) is located midpoint along the Γ-K symmetry. With the decrease in the number of layers, the band structure is strongly affected due to interlayer interaction, quantum confinement, and long-rang Coulomb effects.[14-16] At the K point of the Brillouin zone, the conduction band states are mainly contributed by the d-orbitals of the Mo atoms and are rather

unaffected by interlayer interactions. On the other hand, near the Γ point, the conduction band states are due to hybridization between the d-orbitals of Mo atoms and the p_z-orbitals of S atoms and are liable to be influenced by interlayer interactions. Therefore, at the Γ point, the bands are more affected by the reduction in the number of layers in MoS_2.[13] Finally, monolayer MoS_2 is a direct bandgap semiconductor where the VBM and CBM are coinciding at the K-point with minimum band edge separation of about 1.9 eV.

1.1.3. Optical properties of MoS_2

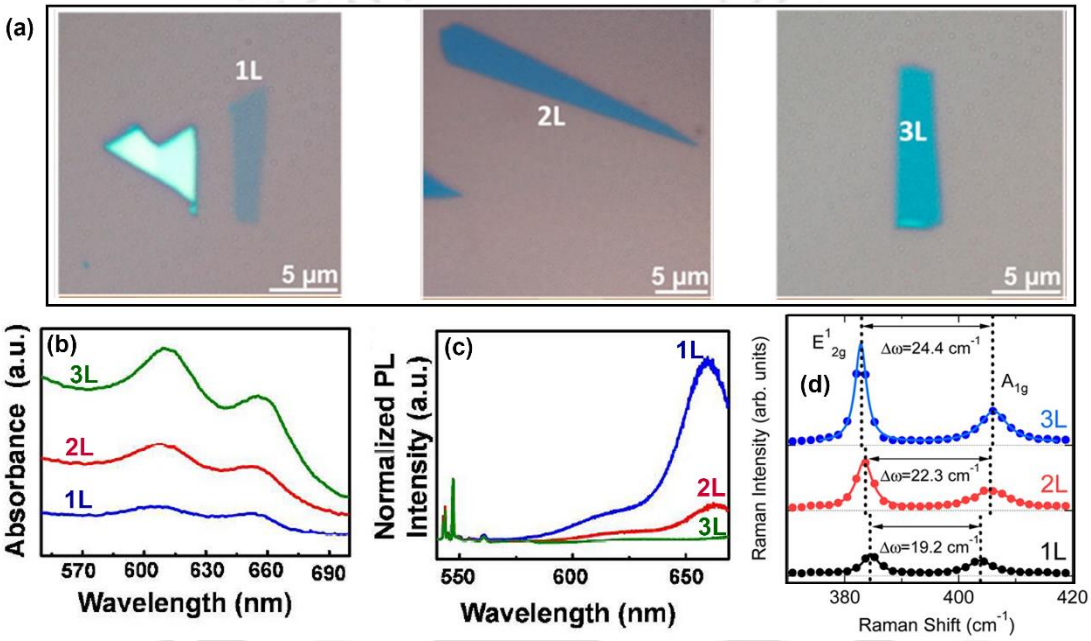

Fig. 1.3. (a) Optical microscope images of mechanically exfoliated 1L, 2L, and 3L MoS_2 on SiO_2/Si substrates. (b) UV-vis absorbance spectra of 1L, 2L, and 3L MoS_2; (c) Photoluminescence spectra of 1L, 2L, and 3L MoS_2 and (d) Raman spectra of 1L, 2L, and 3L MoS_2. Adopted from Ref. [17-19]

The understanding of the optical properties of MoS_2 is highly desirable for various applications in optoelectronics. The optical properties are usually studied using different techniques, such as ultraviolet-visible (UV-vis) spectroscopy, photoluminescence (PL), and Raman spectroscopy. The direct optical band gap in monolayer MoS_2 has unfolded an entirely new prospect in optical properties and optoelectronics. **Fig. 1.3(a)** shows the optical microscope image of the ultrasonically exfoliated monolayer (1L), bilayer (2L), and trilayer (3L) MoS_2. The absorption spectra display two pronounced peaks at 655 nm (1.89 eV) and 610 nm (2.03 eV), which correspond to the direct excitonic transitions at the K point in the Brillouin zone, which is known as the A and B transitions[13, 20] as shown in **Fig. 1.3(b).** Usually, the bulk MoS_2 does not show any

photoluminescence (PL) due to its indirect bandgap (1.2 eV). A huge change in the PL intensity is observed while comparing 3L, 2L to 1L MoS_2, as shown in **Fig. 1.3(c)**. A noticeable strong PL intensity was detected for the 1L MoS_2 at ~ 665 nm, which also correlates with the lower absorption resonance in the peak position and can be attributed to the direct excitonic transition.[13] Thus, the transition from an indirect bandgap to a direct bandgap material is responsible for the PL enhancement in the 1L MoS_2. One unique feature in MoS_2 PL emission is the contribution of negatively charged excitons, called trions (A^-) consisting of a neutral exciton bound with an electron by Coulomb interactions. The A^- emission energy is much lower than the neutral exciton and their difference in energy corresponds to the trion binding energy. In order to achieve high luminescence efficiency, it is highly desirable to minimize the population of trions. The PL intensity is inversely proportional to the number of layers in MoS_2. MoS_2 has two characteristic Raman modes, the E_{2g}, and A_{1g} modes. The E_{2g} is an in-plane vibrational mode resulting from the opposite vibration of two S atoms with respect to the Mo, while the A_{1g} mode is ascribed to the out-of-plane vibration of only S atoms in opposite directions. The frequency difference between these two modes determines the layer number. As we thin down MoS_2 to monolayer, the E_{2g} mode undergoes a blue shift while the A_{1g} mode undergoes a redshift, as shown in **Fig. 1.3(d).** With the increase in the layer number, the vibration of the atoms is suppressed by the interlayer Van der Waals force, leading to higher force constants. Thus, it is expected that both E_{2g} and A_{1g} modes will stiffen with increasing number of layers. The redshift of the E_{2g} peak suggests that the long-range Coulombic interlayer interactions in multilayer MoS_2 may dominate the change of atomic vibration and hence overcome increased interlayer Van der Waals force.[21]

A lot of attention is drawn towards other properties of electrons (the spin and quantum state) for the information storage and/or processing in MoS_2. The study of the spin and valley quantum states of the material for data and signal transfer is called the spintronics and valleytronics. The strong spin–orbit interaction along with the lack of inversion in monolayer MoS_2, leads to a break in spin degeneracy along the Γ-K line of the conduction and the valence bands, resulting in the splitting of the valence band by 148 meV.[22] The electronic band structure of monolayer MoS_2 exhibits two separate valleys, the valence band maxima and the conduction band minima at both the K+ (or K) and K_ (or –K or K') points of the Brillouin zone, as shown in **Fig. 1.4(a).**[23] For the optical transitions to occur in these valleys, change in the angular momentum of +1 for the K+ point and -1 for the K_ point is necessary. The broken inversion symmetry in monolayer MoS_2 causes the

valley Hall effect, where on the application of an in-plane electric field, excitons may dissociate. These electrons and holes in opposing valleys will then deflect in the opposite direction under the action of the electric field. This effect opens up new possibilities for using these additional degrees of freedom as an information career in the future and next-generation electronics.

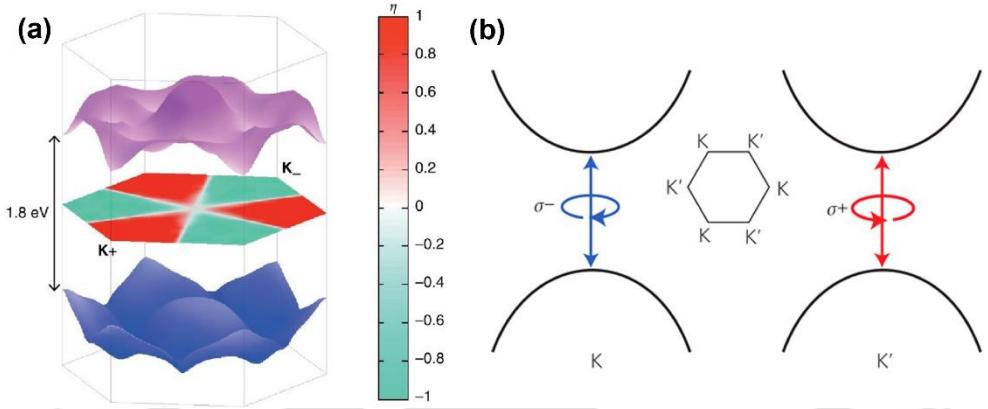

Fig. 1.4. (a) Illustration of the band structure in the first Brillouin zone with top valence band (blue) and bottom conduction band (purple). The centre hexagon is the Brillouin zone demonstrating the K (or K+, shown in red) and the K' (or K_ or –K, shown in teal) valleys, η(k) is the k-resolved degree of optical polarization between the top of the valence bands and the bottom of the conduction bands. Adopted from Ref.[23] (b) Schematics of the valley-dependent optical selection rules at K (or K+) and the K' (or K_ or –K) valleys in k-space with left-circular (blue) and right-circular(red) spin-polarization. Adopted from Ref. [24]

The control of the excitons spin and confinement within a particular valley with circularly polarized light is possible when a specific valley would agree to certain optical selection rules whereby the excitons in the K valley are excited with the right-handed (σ+) polarised light, and the excitons in the K' valley are excited with the left-handed (σ-) polarised light as shown in **Fig. 1.4(b)**.[24] On the other hand, the recombination of the excitons in the K valley will emit light that is σ+ polarised, and in the K' valley it will be σ- polarised. Additionally, the spin-orbit valence band splitting at the K and K' points has opposite signs of spin for each of the valleys. Thus, there is a coupling of spin and valley states in MoS_2, which result in valley dependent optical polarization selection for specific valleys.[22] The valley lifetime of electrons in MoS_2 is of the order of nanoseconds and holes' valley lifetime is relatively longer. However, the valley lifetime of excitons in MoS_2 is of a few picoseconds. The relatively short exciton valley lifetime hinders the progress in the valleytronic quantum device. Therefore, prolonging the valley lifetime is crucial for the future practical application of valleytronics.

1.2. Synthesis of 2D MoS_2

There have been considerable efforts to synthesize controllable, large scale, high-quality monolayer to few-layer MoS_2 by using various top-down and the bottom-up approaches, which include mechanical exfoliation, chemical exfoliation, hydrothermal method, physical vapor deposition, chemical vapor deposition (CVD), etc.

1.2.1. Mechanical exfoliation

The mechanical exfoliation method offers MoS_2 of the highest quality, crystallinity, and facilitates to study the pristine properties and eventually, the device performances. In this process, a small amount of high-quality natural bulk MoS_2 crystal is adhered to a stretch of adhesive tape, followed by repeatedly mechanically peeling off with sticky tape and then pressed into the substrate. Upon repeating the process, MoS_2 flakes with different shapes, sizes, and layer numbers are present on the substrate. This process is quick and cost-effective, however, this tape-assisted micromechanical exfoliation method offers very low yield, and it has a disadvantage, as it is not possible to produce large uniform sheet size.

1.2.2. Chemical exfoliation

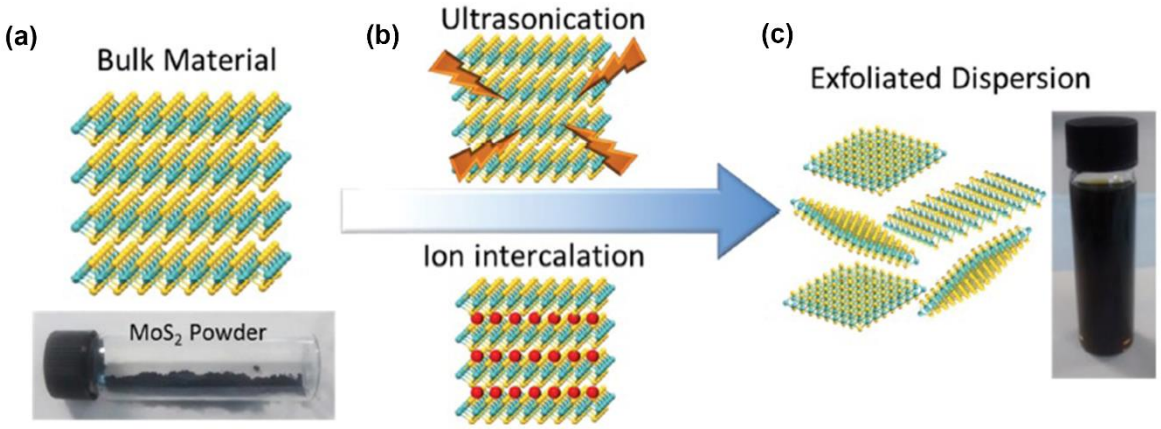

Fig. 1.5. (a) Crystal structure of bulk layered MoS_2 along with an image of bulk MoS_2 powder. (b) Schematic diagram of two conventional liquid exfoliation methods: direct ultrasonication of bulk MoS_2 powder in solvent and ion intercalation (c) Crystal structure of exfoliated MoS_2 along with an image of ultrasonicated MoS_2 dispersion prepared in NMP. Adopted from Ref.[25]

Another class of exfoliation technique is through chemical approaches, such as liquid phase ultrasonication and electrochemical intercalation. These methods are very simple, cost-effective, and enable the production of large volumes of dispersed monolayer and few-layer MoS_2 flakes. In

the liquid phase ultrasonication method, bulk MoS_2 powder is dispersed into organic solvents, like N-methylpyrrolidone (NMP) and isopropyl alcohol (IPA) (**See Fig. 1.5(a,b)**). The solution is then sonicated followed by centrifugation, and the resultant product is monolayer and few-layer MoS_2 flakes in the solution[26], as shown schematically in **Fig. 1.5(c)**. On the other hand, the ion intercalation method uses the concept of insertion of metal ions (Li, Na, K, etc.) in the lamellar space between the MoS_2 layers, leading to an increase in the interlayer spacing, as shown in **Fig. 1.5(a-c)**. One of the most common methods is the electrochemical lithiation discharge process. The most general solution for the Li-ion source is the n-butyl lithium in hexane. Fan et al. developed a simple and efficient process to exfoliate MoS_2 nanosheets using sonication assisted Li intercalation, and the effect is observed within 1.5 hours.[27] These chemical exfoliation techniques could largely increase the production of nanosheets as compared to the mechanical exfoliation process, which is best suited for energy generation and storage applications. However, there are some major drawbacks to these techniques, such as the loss of semiconducting properties in the case of electrochemical intercalation. In contrast, in the ultrasonication process, defects are created in the 2D MoS_2 lattice and reduction of flake size, limiting MoS_2 in large scale integrated circuits and optoelectronic applications.

1.2.3. Physical and chemical vapor deposition

Several attempts have been made to obtain high-quality MoS_2 films with thickness controllability and wafer-scale uniformity by various physical vapor deposition (PVD) methods, such as sputtering,[28] pulsed laser deposition (PLD)[29] and molecular beam epitaxy (MBE).[30] These growth processes were successful in producing large area growth of monolayer to few-layer MoS_2 films. However, there are some disadvantages to these fabrication methods. The films have a high concentration of defects (sulfur deficiency), uneven film thickness, non-stoichiometric polycrystalline films, high film resistivity, and targets are often expensive. Therefore, this limits their practicality in device applications. In recent years, the chemical vapor deposition (CVD) method has attracted much attention because it is one of the most effective methods to synthesize high-quality large-area growth of atomically thin MoS_2, which shows great potential towards device applications. This method has shown to be more feasible over other growth techniques because it could achieve large-area growth and its ease to form layered HS directly, which would mostly prevent interfacial contamination during the transfer process. Additionally, this method

does not require ultra-high vacuum chambers, and therefore the process is cheaper and is relatively more practical to implement in the existing industrial processes.

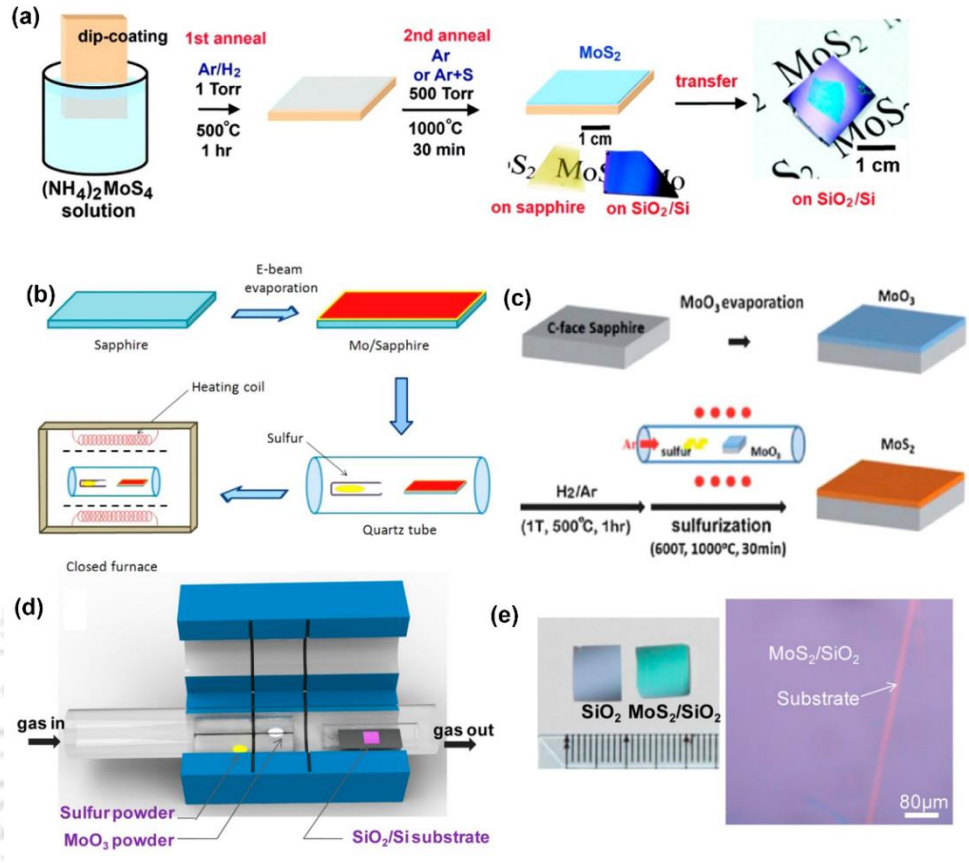

Fig. 1.6. CVD growth of MoS_2 using (a) ammonium thiomolybdate, Adopted from Ref.[31] (b) elemental molybdenum, Adopted from Ref.[32] (c) molybdenum trioxide, Adopted from Ref.[33] and (d) molybdenum trioxide and sulfur as the precursors. (e) Optical photo image contrast between the bare SiO_2/Si substrate and one with CVD grown MoS_2 on it (left). Optical microscope image of as-grown continuous MoS_2 film (right). Adopted from Ref.[34]

Studies have reported that atomically thin MoS_2 films could be primarily grown from precursors, such as ammonium thiomolybdate [$(NH4)_2MoS_4$] solution,[31, 35] a thin deposition of elemental molybdenum [Mo],[32, 36] molybdenum trioxide [MoO_3] powder.[33-34, 37-38] or molybdenum chloride [$MoCl_5$].[39] Liu et al.[31] dip-coated the substrates in $(NH4)_2MoS_4$ solution, and gradually pulled the substrate vertically to obtain a uniform thin film, followed by annealing in gas flow. Through the annealing processes, the $(NH4)_2MoS_4$ film decomposed into various gases (MoS_2, S, H_2S, and NH_3). After the substrate was annealed, the MoS_2 film was deposited onto the substrate, as shown in **Fig. 1.6(a)**. The as-grown samples are mostly a few-layer MoS_2. However, the films are not uniform throughout. In the second method, Mo film is pre-deposited, followed by sulphurization

to obtain MoS_2 film. Laskar et al.[32] deposited the Mo thin films through the e-beam evaporation on a crystalline sapphire substrate followed by a sulphurization process, as shown in **Fig 1.6(b)**. The sulphurization process was conducted at a temperature of ~900 °C. Few layer MoS_2 film was found to cover the entire surface of the substrate. The devices fabricated from this MoS_2 film demonstrated n-type behavior with good mobilities of 10-14 cm^2/Vs. MoO_3 is also one of the most common choices as a precursor. Lin et al.[33] selected MoO_3 as the precursor, and it was predeposited on the c-plane sapphire, followed by a two-step thermal process. The first one was performed at 500 °C in an inert environment of mixed argon and hydrogen (Ar/H_2) under a pressure of 1 Torr. The second step was carried out at 1000°C in the sulfur environment under inert conditions for 30 mins under a pressure of 600 Torr (see **Fig. 1.6(c)**). The films obtained are polycrystalline, few-layered, and large area uniform MoS_2 films grown throughout the entire substrates. Note that the thickness of the film was found to depend on the amount of pre-deposited MoO_3. The MoS_2 device demonstrated that the electron mobility of the device is about 0.8 cm^2/Vs and an on/off current ratio of about 10^5. To further improve the uniformity of the large area growth along with control over layer thickness, a one-step vapor-phase reaction, where the precursors placed in an inert gas environment, are evaporated and transported to the reaction zone, where the gaseous MoO_3 and S react to form MoS_2 on the substrate. Zhang et al.[34] used a three-temperature zone furnace, and the precursors are separately loaded in a 1-inch quartz tube to avoid cross-contamination during the growth. Then the precursors, along with the SiO_2/Si substrates, were sequentially placed in each temperature zone (see **Fig. 1.6(d)**). The typical temperatures for S, MoO_3, and substrates were 120-130°C, 450-600°C and 750-800°C, respectively, and the growth was carried out at low pressure of 0.67 Torr. The as-grown film is a continuous, centimeter-scale, polycrystalline monolayer MoS_2 film (see **Fig. 1.6(e)**). The MoS_2 films are of high quality and comparable to that of exfoliated MoS_2. Growth of bilayer or multilayer MoS_2 was rarely seen, signifying a self-terminated growth mechanism under such conditions. The FET fabricated based on the as-grown MoS_2 shows typical n-type behavior with mobility of ~ 7 cm^2/Vs and an on/off ratio of ~ 10^6. This direct CVD growth of large-area continuous monolayer MoS_2 is ideal for a wide range of electronic and optoelectronic device applications.

1.3. MoS_2 Based Heterostructures

In recent years, MoS_2 based HSs with different materials have been extensively studied to exploit the multifunctional properties of the HS. Several techniques have been developed for synthesizing of high-quality HS of atomically thin 2D MoS_2 with other materials. One of the most impressive properties of MoS_2 is its ease to form HS with different materials. The combined properties of the different materials in the MoS_2 based HSs can create a new product with new and unique properties that can hugely increase the potential of MoS_2 for various applications in novel electronic and optoelectronic devices. The properties of MoS_2 can be engineered by the following ways: (a) plasmonic HSs, (b) 2D van der Waals HSs (c) core-shell HSs, and (d) MoS_2-organic HSs. These modifications of MoS_2 by forming the HSs have shown to be promising in many practical applications. Several reports have been published on the fabrication of MoS_2 HSs with inorganic materials, such as Si,[40-41] ZnO,[42] TiO_2,[43-45] CdS,[46-47] PbS,[4] CdSe,[48] ZnS,[49-50] InP,[51-52] GaN,[53-54] 2D TMDs,[10, 55-57] etc. and organic materials, such as Rubrene,[58-59] P3HT,[60] PTCDA,[61] PEDOT:PSS,[62] different form of carbon (graphene,[35, 63-64] reduced graphene oxide (RGO),[65-67] carbon nanotube (CNT)[68] etc.), noble metal nanoparticles such as Au,[69-70] Ag,[71-72] Pd,[73] etc. For the fabrication of these MoS_2 based HSs, different methods were used, such as PLD, ALD, CVD, solution synthesis, and sputtering, etc.

MoS_2 based HSs pave the way for a broad range of applications due to the improvement in the intrinsic properties of pristine MoS_2. The coupling of MoS_2 with other materials is a promising approach to improve the photocatalytic activity because the HS can cause a rapid charge separation and reduced recombination rate of photoinduced electron-hole pairs. The weak interlayer interaction between the MoS_2 layers makes it feasible to isolate single layers by exfoliation and without restrictions allow the stacking of different materials irrespective of their crystal lattice mismatch. This creates an ease of fabricating any kind of vertical heterostructures by mechanically stacking up the different layers in any preferred order. This flexibility to form HS of MoS_2 is considered highly beneficial for a wide range of applications.

1.4. Application of MoS_2 and its Heterostructures

The most distinct feature of MoS_2 is the widening of the bandgap with the decrease in the number of layers, and its transition from an indirect bandgap in bulk form to a direct bandgap in monolayer. Because of the unique properties, such as finite bandgap, good carrier mobility, thickness,

transparency, dimensionality, and flexibility, MoS_2 has attracted considerable attention for a wide range of applications. To further enhance these properties, the formation of MoS_2 based HS brings them in perspective for the potential applications in the next generation of atomically thin electronic and optoelectronic devices. In this section, we will discuss the promising applications of MoS_2 and its HS in FETs photocatalytic hydrogen production, sensor, solar cells, light emitting devices and photodetector.

1.4.1 Photocatalytic Hydrogen Production

The major challenge in today's world is the rapid human civilization and industrialization, which has triggered the global energy crisis and global warming. Our overconsumption of fossil fuels has also contributed to the pollution of the environment. To overcome the energy crisis, an alternative energy source has become an urgent necessity and an important research area. Among the renewable energy sources, hydrogen production has been regarded as a clean energy resource that can be easily stored. MoS_2 has gained significant attention as a promising candidate as a novel photocatalyst with efficient H_2 production via water splitting. The metallic 1T phase of MoS2 has attracted the most attention in photocatalytic activity as both the edges and basal planes of the 1T phase have high catalytic activity and efficient charge transport, thus preventing electron-hole recombination.[74] Liu et al.[75] synthesized 1T-MoS_2@CdS HS by a one-step solvothermal method resulting in few-layered 1T-MoS_2 nanosheets loaded on the surface of CdS nanorods (NRs). The effective charge transfer between the photoexcited CdS NRs and 1T-MoS_2 could considerably suppress electron-hole recombination in the CdS NRs and contribute to improving photocatalytic activity. The rate of H_2 evolution on 1T-MoS_2@CdS catalysts with different deposition amounts of 1T-MoS_2 is shown in **Fig. 1.7(a).** The rate of H_2 evolution for bare CdS NRs was very low (440 µmol/gh). On the other hand, 1T-MoS_2@CdS HS with 0.2 wt % 1T-MoS_2 attains the maximum H_2 evolution rate of ~17.479 mmol/gh, which is 39 times that of bare CdS NRs. **Fig 1.7(b)** exhibits a schematic mechanism of the role of the 1T-MoS_2 cocatalyst for the enhanced electron transfer for H_2 generation. The formation of HS opens up additional ways for electron-transfer, thus improving the charge separation and subsequently suppresses electron-hole recombination and, as a result, enhances photocatalytic activity. However, the stability and the catalytic performance of noble metal-free co-catalyst are still considered inferior to that of the conventional Pt/Pd co-catalyst.

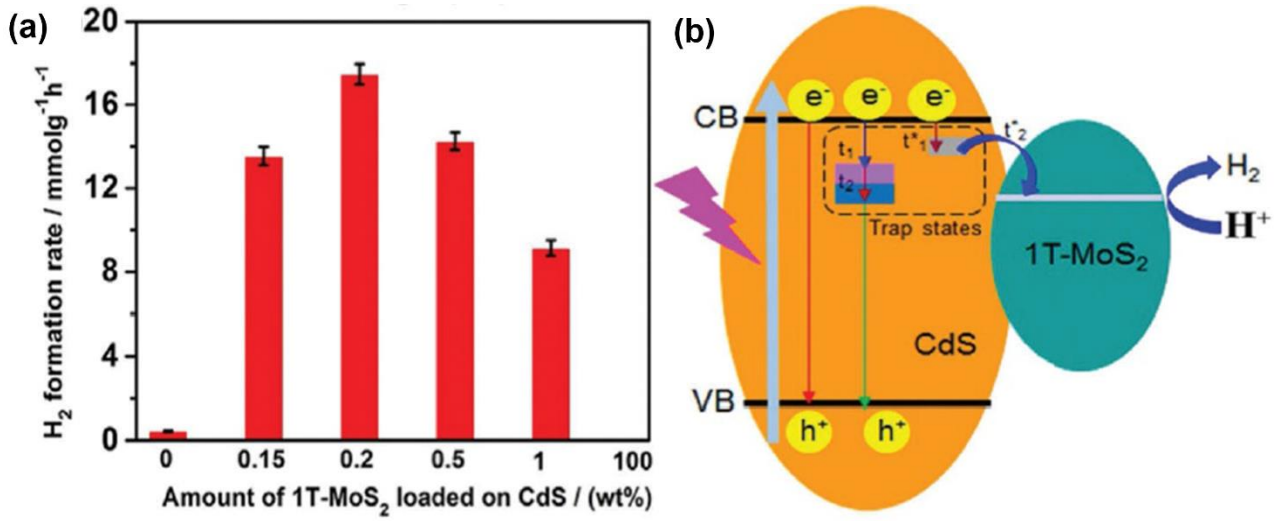

Fig. 1.7. (a) The rate of H_2 evolution on 1T-MoS_2@CdS photocatalysts loaded with different deposition amounts of 1T-MoS_2 under visible-light irradiation. (b) Schematic illustration of the role of the 1T-MoS_2 cocatalyst for the enhanced electron transfer Adopted from Ref[75]

1.4.2. Sensor

Extensive research on new 2D materials for sensing is on high demand due to the tough challenges in meeting the increasing requirement for various kinds of sensors. A 2D atomically thin layered MoS_2 is considered to be a promising candidate due to its excellent features, such as high aspect ratio, high carrier mobility, and low noise level, which makes MoS_2 an outstanding sensing material. Biosensors are essential in today's world in the field of environmental monitoring, agriculture, industrial production, and medical applications. Mao et al.[76] fabricated a biosensor based on MoS_2 nanosheet for the detection of Ag^+. Monolayer MoS_2 was synthesized by the lithium-intercalation technique. The Ag^+ can selectively bind in between two DNA cytosine (C) bases and form stable C– Ag^+–C base pairs. A combined effect of the Ag^+-mediated base pairs "C– Ag^+–C" and the monolayer MoS_2 fluorescent quencher results in the selective detection of Ag^+ ion. The synthesized monolayer MoS_2 exhibits a high fluorescence quenching efficiency within 5 min and a detection limit of 1 nM for Ag^+ ion. Soni et al.[77] synthesized 3D hybrid polyaniline MoS_2 (PANI-MoS_2) nanoflowers via hydrothermal route. The PANI-MoS_2 biosensor was fabricated for the detection of Chronic Myelogenous Leukemia (CML) over a wide range of target DNA concentration (10^{-6}-10^{-17} M). The fabricated PANI-MoS_2 exhibited an enhanced electrochemical performance due to large electroactive surface area, fast electron transfer, and high catalytic activity. The sensor showed high sensitivity and a low limit of detection (3×10^{-18} M) and high stability. Therefore, these studies provide insight into the preparation and functionalization

of MoS_2 for widespread potential in high-performance biomedical devices and other multifunctional applications.

In recent years, MoS_2 has been widely investigated in gas sensing applications for the detection of toxic gases present in the environment. It is important to develop a reliable, selective, inexpensive, and rapid detection gas sensor for determining toxic gases. The gas molecules can be easily adsorbed on the surface of MoS_2. Therefore, MoS_2 is a promising candidate for the fabrication of high-performance gas sensors, such as CO, O_2, NH_3, H_2, NO etc. Yue et al.[78] prepared graphene quantum dots (GQD) and MoS_2 quantum dots (MQD) by a combined process of physical exfoliation and solvothermal treatment followed by mixing both of them in a hot water bath to form a composite of graphene/MoS_2 quantum dots.

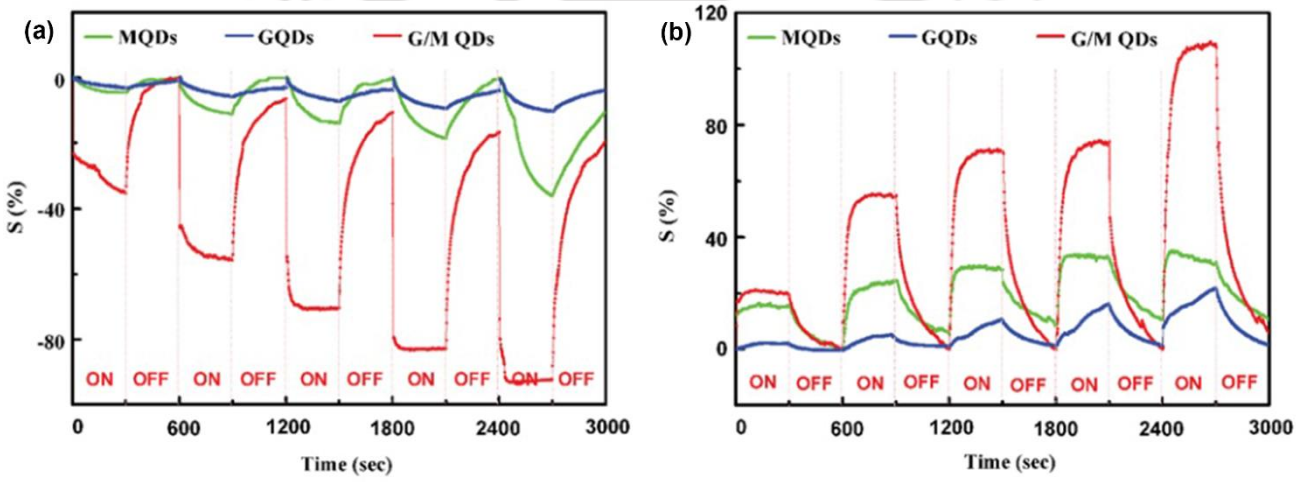

Fig. 1.8. (a and b) The comparative sensing behavior of the MQDs (green), GQDs (blue), and graphene/MoS_2 QDs (red) under increasing (a) NO_2 exposure and (b) NH_3 exposure. Adopted from Ref[78]

The synthesis process for graphene and MoS_2 quantum dots can create some structural defects and vacancies. These sites can serve as adsorption sites for gas molecules. NO_2 acts as charge acceptors, while NH_3 behaves as a charge donor. Therefore, the adsorption of NO_2 will enhance the doping level of the quantum dots and increases their conductance, whereas, for the adsorption of NH_3, it is just the reverse. As compared to bare GQDs and MQDs, the graphene/MoS_2 quantum dots sensor shows high sensitivity towards NO_2 and NH_3 (see **Fig 1.8 (a)** and **(b)**). This is because of the exceptional charge transfer capability of GQD that favors fast charge transfer from MQD to the GQD, thus leading to a very high and fast variation of the resistance. The graphene/MoS_2 quantum dots sensor demonstrated an outstanding gas-sensitive property towards sensing NO_2 and NH_3 gas. The theoretical calculated limits of detections of NO_2 and NH_3 were 41.4 ppb and 35.5

ppb, respectively, and were ascribed to the synergistic effect of graphene and MoS_2 quantum dots. MoS_2 and MoS_2 based HS are potential runners among 2D materials for a huge range of sensing applications.

1.4.3. Photodetector

Photodetectors are devices designed to convert light signals to electric signals, which play an important role in modern society for various practical applications. Due to the superior optical and optoelectronic properties of 2D materials, it can overtake the conventional Si-based photodetectors. Graphene, a well known 2D material has demonstrated to possess remarkable characteristics, such as high carrier mobility, broadband absorption, and fast response time, rendering it as a promising material for various photodetectors over a wide spectral range. However, despite various excellent properties, it's zero bandgap, and low light absorbance in the entire visible region are undesirable for high-performance photodetectors. Among 2D semiconductors, MoS_2 has gained tremendous attention due to their unique properties such as tunability of bandgap, and in monolayer form, its direct bandgap would allow a high absorption coefficient and efficient electron-hole pair generation under photoexcitation. Van der Waals HS made of atomically thin 2D materials have opened up new fields in the fabrication of high-performance photodetectors. X Zhou et al.[79] reported epitaxial growth of $SnSe_2$ nanosheets on monolayer MoS_2 via a two-step CVD growth. **Fig. 1.9(a)** shows a schematic representation of the $SnSe_2/MoS_2$ vertical HS based photodetector under light illumination. The measured I–V characteristic curves of the $SnSe_2/MoS_2$ HS demonstrated high photocurrent with a high responsivity of up to 9.1×10^3 A W^{-1} that was two orders of magnitude higher than that of monolayer MoS_2 devices (see **Fig. 1.9(b)**). The enhanced performance of the $SnSe_2/MoS_2$ photodetector can be attributed to the type-II band alignment of these two materials, which promotes efficient charge transfer from MoS_2 to $SnSe_2$ at the interface. Yang et al.[57] fabricated a vertical p–n heterojunction photodetector based on p-type GaTe and n-type MoS_2. The p-type GaTe was transferred on an n-type MoS_2 wafer by dry stamping. The $GaTe/MoS_2$ device shows better electronics and optoelectronic properties as compared to its counterparts. The p–n $GaTe/MoS_2$ heterojunction exhibits excellent photoresponsivity of 1.36 AW^{-1}, an external quantum efficiency (EQE) of 266% and a high on/off current ratio of ≈ 340 at zero bias voltage. These outstanding properties are attributed to the effective electron–hole separation initiated by

the type II band alignment and the large built-in potential of the p-n heterojunction at the interface. Kang et al.[80] fabricated a vertical hybrid methyl-ammonium lead iodide ($CH_3NH_3PbI_3$) perovskite/MoS_2 photodetector on top of (3-aminopropyl)triethoxysilane (APTES). The APTES causes the n-doping on the MoS_2 region and hence enhances the performance of the hybrid $CH_3NH_3PbI_3$/MoS_2/APTES photodetector. The device demonstrated an enhanced responsivity as high as 1.94×10^6 A W^{-1} and a detectivity of 1.29×10^{12} Jones. This enhancement in the performance is attributed to the long carrier diffusion lengths and high absorption of the $CH_3NH_3PbI_3$) perovskite, thus generating a large number of electrons and holes which are then transferred to the MoS_2 layer. Additionally, the increase in the carrier mobility in MoS_2 induced by electron doping along with the reduced photocarrier recombination leads to the significantly enhanced performance of the photodetector.

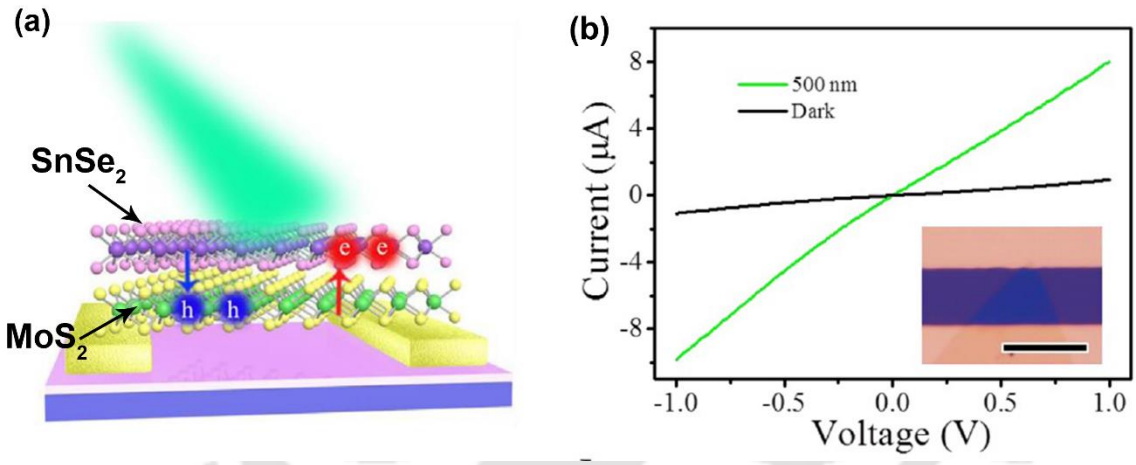

Fig. 1.9. (a) A schematic representation of the charge transfer at the interface of the $SnSe_2$/MoS_2 HS based photodetector under light illumination. (b) I–V curves of the $SnSe_2$/MoS_2 HS under dark and 500 nm light illumination. Inset of (b) shows the optical microscope image of the HS device, scale bar = 5 μm. Adopted from Ref[79]

The performance parameters of MoS_2 and MoS_2 based heterostructure photodetectors are summarized in **Table 1.1.** It is evident from the table that rise time of the device is much slower than commercial photodetectors. The distinct features in the MoS_2-based HSs lay the foundation for further development of other multifunctional optoelectronic applications.

Table 1.1*: Performance parameters of MoS_2 and MoS_2 based heterostructure photodetectors.*

Materials	Spectral Range	Responsivity (A/W)	Detectivity (Jones)	Rise time (s)	Refs
MoS_2	visible	880	-	0.6	[9]
$SnSe_2/MoS_2$	visible	9.1×10^3	9.3×10^{10}	0.2	[79]
ML MoS_2/rubrene	visible	0.326	-	-	[81]
GaTe/MoS_2	visible	1.36	-	< .01	[57]
$CH_3NH_3PbI_3/MoS_2$/APTES	visible	1.94×10^6	1.29×10^{12}	Several seconds	[80]
FL MoS_2/PbS QDs	visible-NIR	6×10^5	5×10^{11}	0.35	[4]
FL MoS_2/PbSe QDs	NIR	1.9×10^{-6}	-	0.25	[3]
1L MoS_2/1L graphene	visible	1.6×10^4	-	0.07	[82]

1.4.4. Solar cells

In recent years, ultrathin MoS_2 has gained serious attention and has been widely explored due to their promising potential in developing high-performance solar cells. For practical application, it is important to develop more cost-effective, high stability solar cell devices. For industrial photovoltaic applications, it is required for the solar cell devices to have stability, high power conversion efficiency (PCE), easy and cost-effective fabrication. These goals can be achieved with the fabrication of MoS_2 based HS with other materials. Tsai et al.[83] fabricated a type-II heterojunction solar cell consisting of CVD grown n-type monolayer MoS_2 on p-type Si substrate. This device demonstrated a high PCE of 5.23%, which is ascribed to the large built-in electric filed introduced by the monolayer MoS_2 near the interface between the MoS_2 and the p-Si. The calculated short circuit current density (J_{sc}) and fill factor (FF) are 22.36 mA/cm^2 and 57.26%, respectively. The high photovoltaic device performance can also be attributed to the broadband absorption and efficient electron−hole pair dissociation. The MoS_2/TMD heterostructures such as MoS_2/WSe_2,[84] MoS_2/graphene/WSe_2,[85] show a huge potential in high-efficiency photovoltaic cell applications. Song et al.[84] fabricated ultrathin MoS_2/WSe_2 van der Waals HS, as shown schematic in **Fig. 1.10(a)**. They demonstrated high external quantum efficiency of over 50% resulting from both high optical absorption and efficient electronic charge carrier collection. Experimental results showed that the absorbance was >90% in the MoS_2/WSe_2 HS, which is in good agreement with the electromagnetic simulations. The MoS_2/WSe_2 HS solar cell exhibited a maximum single-wavelength PCE of 3.4% (**Fig. 1.10(b)**) under light illumination of 633 nm laser excitation with an illumination power of 740 W/cm^2. Atomically thin MoS_2 has been used in solar cells in various

forms such as an electron-transport layer (ETL),[86-87] a hole-transport layer (HTL),[88-89] protective layer,[90] and interfacial layer.[91] Zheng et al.[92] employed liquid-phase exfoliation method followed by a hydrothermal reaction to obtain Graphene-MoS_2 HS. The Graphene-MoS_2 hybrid thin films were used in the in PTB7-Th:PC71BM organic solar cell as an efficient HTL. The device demonstrated a maximum power conversion efficiency of 9.5% and showed good stability over a storage period of 1000 h, while retaining more than 93% of the initial efficiency. Thus, MoS_2 based HS offers great potential as HTL for stable and efficient photovoltaic devices. These reports pave a way of designing and attaining future highly efficient MoS_2 based HS solar cells.

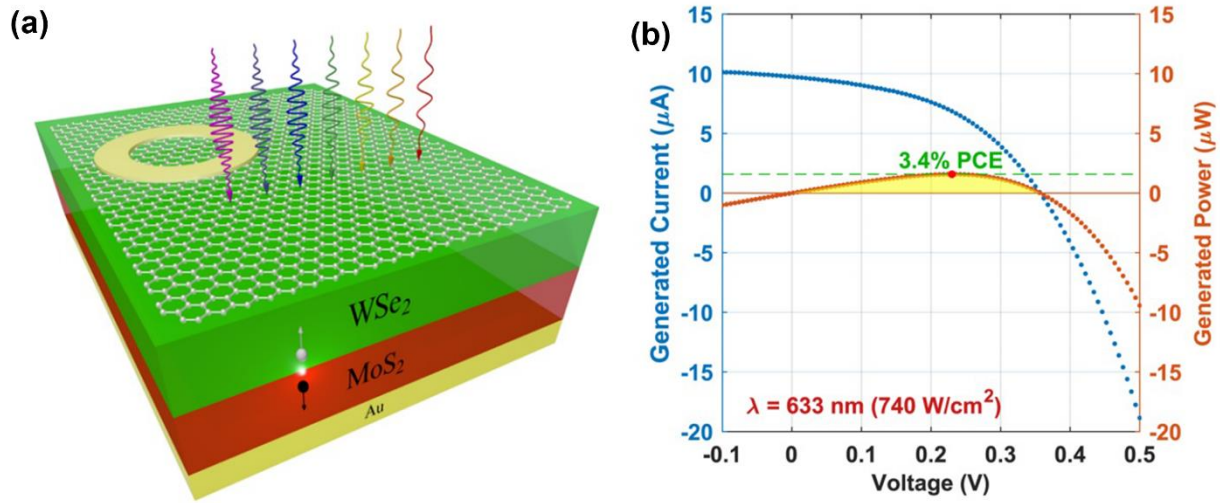

Fig. 1.10. (a) A schematic representation of the MoS_2/WSe_2 van der Waals HS device under illumination. (b) I–V (light blue) and power-voltage (orange) characteristics of the device were excited at λ = 633 nm with an incident power of ~45 μW with a spot size area of ~6 μm^2. The yellow region depicts the generated power from the device with a maximum single-wavelength PCE of 3.4%. Adopted from Ref[84]

1.4.5. Light emitting diode (LED)

In recent years, LEDs have gradually replaced conventional lighting devices because of various advantages, such as low cost, low power consumption, and environment-friendly. LEDs depend on the injection of carriers across a junction, which promotes the recombination of electrons and holes. Among 2D TMDs, monolayer MoS_2 is a potential candidate for light-emitting device due to its direct bandgap nature. However, because of the ultrathin thickness of the monolayer MoS_2, formation of the p-n junction through doping is challenging. Thus, an effective way to construct a p–n junction can be realized by stacking with other semiconductor materials. Nikam et al.[93] fabricated the n-MoS_2/p-MoS_2 HS by a two-step CVD process, followed by transferring the p-

MoS_2/n-MoS_2 HS on top of a p-GaN bilayer to fabricate a tetra-layered (4-L) n-MoS_2/p-MoS_2/p-GaN HS white LED. The electroluminescence (EL) spectra for the n-MoS_2/p-MoS_2/p-GaN HS consists of three emission peaks at 642 nm (n-MoS_2, orange), 525 nm (p-MoS_2, green) and 481 nm (p-GaN, blue). Thus, this device is promising for the fabrication of atomically thin white LED. The n-MoS_2/p-MoS_2/p-GaN white LED device exhibited a luminance of 30,548 Cd/m^2, luminescence efficiency of 29% and the luminous efficacy of 294 lm/W at a bias voltage of 4 V. Thus, this device paves a way towards the fabrication of commercially viable color-tunable, atomically thin and low-cost display LED. Li et al.[94] fabricated 2D/1D HS LED consisting of p-type MoS_2 nano-sheet (NS) transferred by dry transfer method onto n-type CdSe nanowire (NW). The advantage of such a mixed dimension system is that the individual CdSe NW can act as an optical cavity and gain medium, and the atomic thickness of the MoS_2 layer does not strongly absorb the light emitted from the CdSe NW and hence, the MoS_2/CdSe HS provides a new way to achieve high-efficiency LEDs. The mechanism of this light emission of the MoS_2/CdSe heterojunction LED can be understood by the type-II band alignment between the n-CdSe and p-MoS_2. Under forward bias, the built-in potential drops and thus, there will be a flow of electrons from the n-type CdSe NW to p-MoS_2 NS, and simultaneously, there will be the transfer of holes from the p-MoS_2 NS to the n-type CdSe NW. The injected electrons and holes will mostly recombine in the CdSe region, as the CdSe is a direct band-gap semiconductor and it has a higher electron-hole radiative recombination rate. Thus, the EL spectrum is revealed by the band-edge emission of the CdSe NW and shows strong electroluminescence centred at ~709 nm. The MoS_2/CdSe heterojunction LED displays a low turn on voltage of ~1.5 V and a rectification ratio of ~24 at V_{ds} = ±3 V. This mixed dimension LED device, which is superior to both 2D and 1D semiconductors, may find potential application for future high-sensitivity sensors, transparent flexible devices and lasers.

Table 1.2*: Performance parameters of MoS_2 based heterostructure LEDs.*

Device	Emission wavelength (nm)	Voltage (V_{ds})	Maximum EQE (%)	Maximum luminance (Cd/m^2)	Ref.
MoS_2/Si	685	5.5	-	-	[95]
MoS_2/CdSe	709	3	-	-	[94]
n-MoS_2/p-MoS_2/p-GaN	white	4	29	30,548	[93]
p-WSe_2/n-MoS_2	880	3	12	-	[96]
Graphene/Al_2O_3/MoS_2/Al_2O_3/GaN	500-800	-	0.01	-	[97]
hBN/Graphene/hBN/WSe_2/hBN/MoS_2/hBN/Graphene/hBN	750	2.3	5	-	[98]

1.5. Challenges in Fabrication and Application of 2D MoS_2 and its Heterostructures

Over the past decade, 2D MoS_2 has aroused great interest and extensive studies on the fundamental aspects of synthesis, tuning the properties and applications of layered MoS_2 have been explored by numerous researchers. However, some challenges still remain for large scale practical device applications. Firstly, reproducible growth of uniform, large-area, and high-quality monolayer MoS_2 for device applications in the industrial-scale is still challenging. Additionally, the quality of the MoS_2 grown by other techniques has not yet reached that of mechanically exfoliated MoS_2 flakes. In the chemical exfoliation techniques, control over the layer number, flake size, purity, and phases of MoS_2 has proven to still be a major bottleneck. Further advancements in the effective synthesis of stable defect-less MoS_2 and alloying of MoS_2 are still desired. Chemical doping of MoS_2 is a useful technique to enhance the ability of charge transport and other properties. However, to control doping is still a key challenge and requires further studies. Secondly, the integration of MoS_2 with other materials forming hybrid HS allows us to bring out new and unique properties into a single optoelectronic device structure. However, the fabrication of such devices has been successful only at laboratory scale. Thirdly, MoS_2 based HS with other 2D materials has emerged as promising for a wide range of applications. In light-harvesting applications, due to

poor interfacial contact, the MoS_2 based HS often suffer from inadequate light-harvesting, low carrier mobility, and weak contact. A better understanding and optimization of the interfacial contact between the building layers is required. Furthermore, band engineering of MoS_2 based HS can help to achieve hybrid materials of superior electrical performances and tunable band structure, which will enrich the field of HS. Finally, a thorough insight and understanding in the control of charge carrier properties, that is important for many applications is also a significant area that requires further research in both experimental and theoretical study.

1.6. Focus of the Present Thesis

Although MoS_2 has demonstrated considerable potential, some challenges still remain for the fabrication of well-controlled large-area monolayer MoS_2 and its HSs for their wide range of applications in nanotechnology. In the present thesis, we have made an effort for controlled fabrication of large-area monolayer MoS_2 and their HSs with other semiconductors for achieving superior properties from pristine monolayer MoS_2. The main objectives of the present thesis are as follows:

- Fabrication of large-area high-quality monolayer MoS_2 by CVD method.
- Study of the growth mechanism of MoS_2 by tuning the different growth parameters to obtain large-area monolayer MoS_2 growth.
- Fabrication of MoS_2 based HSs with various semiconductors (e.g., TiO_2 and WS_2) and plasmonic NPs (e.g., Ag and Au).
- Fabrication of high-quality core-shell HS between monolayer MoS_2 (shell) and TiO_2 NR (core) by in-situ CVD technique and to study the tunability of the PL of the MoS_2@TiO_2 HS.
- Fabrication of a ternary hybrid system consisting of monolayer MoS_2 (shell) coated over an array of Au NPs on hydrothermally grown TiO_2 nanostructure. Quantitative analysis of the tunable visible PL and the origin of high PL enhancement of monolayer MoS_2 in the ternary heterostructure.
- Quantitative analysis of the tunability in the PL and doping of monolayer MoS_2 decorated with WS_2 QDs. Using the four-energy level model involving coupled charge transfer, a detailed explanation of the behavior of the PL in 1L-MoS_2/WS_2 QD HS.

- Fabrication of high-quality heterojunction between CVD grown monolayer MoS_2 and WS_2 QD for an efficient, high-performance broadband photodetector.

1.7. Organization of the Thesis

The complete thesis work is presented in seven chapters. **Chapter 1** presents a brief overview of the reported research work on the different growth techniques, important properties, and the promising applications of MoS_2 and its heterostructures. **Chapter 2** presents the controlled growth of high-quality large-area monolayer MoS_2 by controlling various growth parameters, such as the carrier gas, growth temperature, precursors, and substrates. **Chapter 3** demonstrates a simple one-step direct synthesis process of the 1L-MoS_2 film by a CVD method over the hydrothermally grown TiO_2 nanorods (NRs) and investigated the strong enhancement of the PL intensity of the 1L-MoS_2 is after the formation of the HS. In **Chapter 4,** we discuss about the dramatically enhanced PL emission and it mechanism from a ternary system consisting of the large area monolayer MoS_2 grown over an array of Au nanoparticles (NPs) coated over hierarchical TiO_2 nanostructure forming a core-shell TiO_2/Au/MoS_2 hybrid structure, where the PL intensity is enhanced by about three orders of magnitude. In **Chapter 5**, we investigated the tunability of the PL and doping of monolayer MoS_2 by decorating it with WS_2 quantum dots (WS_2 QD). A detailed quantitative analysis using the four-energy level model involving coupled charge transfer was employed to explain the quenching of the PL in 1L-MoS_2/WS_2 QD HS. **Chapter 6** demonstrates the fabrication of a vertical heterojunction photodetector (PD) by incorporating WS_2 QDs with direct CVD grown monolayer MoS_2 on Si/SiO_2 substrate. The 1L-MoS_2/WS_2 QD p-n heterojunction acts as an efficient, high-performance broadband photodetector. **Chapter 7** presents a summary of the significant findings and important conclusions of the present thesis and the future scope of work.

References

1. Shanmugam, M.; Durcan, C. A.; Yu, B., Layered Semiconductor Molybdenum Disulfide Nanomembrane Based Schottky-Barrier Solar Cells. *Nanoscale* **2012**, *4*, 7399-7405.
2. Jeon, I.; Kutsuzawa, D.; Hashimoto, Y.; Yanase, T.; Nagahama, T.; Shimada, T.; Matsuo, Y., Multilayered Mos2 Nanoflakes Bound to Carbon Nanotubes as Electron Acceptors in Bulk Heterojunction Inverted Organic Solar Cells. *Organic Electronics* **2015**, *17*, 275-280.
3. Schornbaum, J.; Winter, B.; Schießl, S. P.; Gannott, F.; Katsukis, G.; Guldi, D. M.; Spiecker, E.; Zaumseil, J., Epitaxial Growth of Pbse Quantum Dots on Mos2 Nanosheets and Their near-Infrared Photoresponse. *Advanced Functional Materials* **2014**, *24*, 5798-5806.

4. Kufer, D.; Nikitskiy, I.; Lasanta, T.; Navickaite, G.; Koppens, F. H. L.; Konstantatos, G., Hybrid 2d–0d Mos2–Pbs Quantum Dot Photodetectors. *Advanced Materials* **2015**, *27*, 176-180.
5. Yin, Z., et al., Preparation of Mos2–Moo3 Hybrid Nanomaterials for Light-Emitting Diodes. *Angewandte Chemie International Edition* **2014**, *53*, 12560-12565.
6. Salehzadeh, O.; Tran, N. H.; Liu, X.; Shih, I.; Mi, Z., Exciton Kinetics, Quantum Efficiency, and Efficiency Droop of Monolayer Mos2 Light-Emitting Devices. *Nano Letters* **2014**, *14*, 4125-4130.
7. Choi, W., et al., High-Detectivity Multilayer Mos2 Phototransistors with Spectral Response from Ultraviolet to Infrared. *Advanced Materials* **2012**, *24*, 5832-5836.
8. Radisavljevic, B.; Radenovic, A.; Brivio, J.; Giacometti, V.; Kis, A., Single-Layer Mos2 Transistors. *Nat. Nanotechnol.* **2011**, *6*, 147.
9. Lopez-Sanchez, O.; Lembke, D.; Kayci, M.; Radenovic, A.; Kis, A., Ultrasensitive Photodetectors Based on Monolayer Mos2. *Nature Nanotechnology* **2013**, *8*, 497.
10. Choudhary, N.; Park, J.; Hwang, J. Y.; Chung, H.-S.; Dumas, K. H.; Khondaker, S. I.; Choi, W.; Jung, Y., Centimeter Scale Patterned Growth of Vertically Stacked Few Layer Only 2d Mos2/Ws2 Van Der Waals Heterostructure. *Scientific Reports* **2016**, *6*, 25456.
11. Li, M.; Shi, J.; Liu, L.; Yu, P.; Xi, N.; Wang, Y., Experimental Study and Modeling of Atomic-Scale Friction in Zigzag and Armchair Lattice Orientations of Mos2. *Science and Technology of Advanced Materials* **2016**, *17*, 189-199.
12. Wang, Q. H.; Kalantar-Zadeh, K.; Kis, A.; Coleman, J. N.; Strano, M. S., Electronics and Optoelectronics of Two-Dimensional Transition Metal Dichalcogenides. *Nature Nanotechnology* **2012**, *7*, 699-712.
13. Splendiani, A.; Sun, L.; Zhang, Y.; Li, T.; Kim, J.; Chim, C.-Y.; Galli, G.; Wang, F., Emerging Photoluminescence in Monolayer Mos2. *Nano Lett.* **2010**, *10*, 1271-1275.
14. Ellis, J. K.; Lucero, M. J.; Scuseria, G. E., The Indirect to Direct Band Gap Transition in Multilayered Mos2 as Predicted by Screened Hybrid Density Functional Theory. *Applied Physics Letters* **2011**, *99*, 261908.
15. Kuc, A.; Zibouche, N.; Heine, T., Influence of Quantum Confinement on the Electronic Structure of the Transition Metal Sulfide TS2. *Physical Review B* **2011**, *83*, 245213.
16. Kang, J.; Tongay, S.; Zhou, J.; Li, J.; Wu, J., Band Offsets and Heterostructures of Two-Dimensional Semiconductors. *Applied Physics Letters* **2013**, *102*, 012111.
17. Li, H.; Wu, J.; Yin, Z.; Zhang, H., Preparation and Applications of Mechanically Exfoliated Single-Layer and Multilayer Mos2 and Wse2 Nanosheets. *Accounts of Chemical Research* **2014**, *47*, 1067-1075.
18. Jeon, J.; Jang, S. K.; Jeon, S. M.; Yoo, G.; Jang, Y. H.; Park, J.-H.; Lee, S., Layer-Controlled Cvd Growth of Large-Area Two-Dimensional Mos2 Films. *Nanoscale* **2015**, *7*, 1688-1695.
19. Mouri, S.; Miyauchi, Y.; Matsuda, K., Tunable Photoluminescence of Monolayer Mos2 Via Chemical Doping. *Nano Lett.* **2013**, *13*, 5944-5948.
20. Mak, K. F.; Lee, C.; Hone, J.; Shan, J.; Heinz, T. F., Atomically Thin Mos2: A New Direct-Gap Semiconductor. *Phys. Rev. Lett.* **2010**, *105*, 136805.
21. Lee, C.; Yan, H.; Brus, L. E.; Heinz, T. F.; Hone, J.; Ryu, S., Anomalous Lattice Vibrations of Single- and Few-Layer Mos2. *ACS Nano* **2010**, *4*, 2695-2700.
22. Zhu, Z. Y.; Cheng, Y. C.; Schwingenschlögl, U., Giant Spin-Orbit-Induced Spin Splitting in Two-Dimensional Transition-Metal Dichalcogenide Semiconductors. *Physical Review B* **2011**, *84*, 153402.
23. Cao, T., et al., Valley-Selective Circular Dichroism of Monolayer Molybdenum Disulphide. *Nature Communications* **2012**, *3*, 887.
24. Zeng, H.; Dai, J.; Yao, W.; Xiao, D.; Cui, X., Valley Polarization in Mos2 Monolayers by Optical Pumping. *Nature Nanotechnology* **2012**, *7*, 490-493.
25. Solís-Fernández, P.; Bissett, M.; Ago, H., Synthesis, Structure and Applications of Graphene-Based 2d Heterostructures. *Chemical Society Reviews* **2017**, *46*, 4572-4613.

26. Coleman, J. N., et al., Two-Dimensional Nanosheets Produced by Liquid Exfoliation of Layered Materials. *Science* **2011**, *331*, 568-71.
27. Fan, X.; Xu, P.; Zhou, D.; Sun, Y.; Li, Y. C.; Nguyen, M. A. T.; Terrones, M.; Mallouk, T. E., Fast and Efficient Preparation of Exfoliated 2h Mos2 Nanosheets by Sonication-Assisted Lithium Intercalation and Infrared Laser-Induced 1t to 2h Phase Reversion. *Nano Letters* **2015**, *15*, 5956-5960.
28. Tao, J.; Chai, J.; Lu, X.; Wong, L. M.; Wong, T. I.; Pan, J.; Xiong, Q.; Chi, D.; Wang, S., Growth of Wafer-Scale Mos2 Monolayer by Magnetron Sputtering. *Nanoscale* **2015**, *7*, 2497-2503.
29. Serna, M. I.; Yoo, S. H.; Moreno, S.; Xi, Y.; Oviedo, J. P.; Choi, H.; Alshareef, H. N.; Kim, M. J.; Minary-Jolandan, M.; Quevedo-Lopez, M. A., Large-Area Deposition of Mos2 by Pulsed Laser Deposition with in Situ Thickness Control. *ACS Nano* **2016**, *10*, 6054-6061.
30. Fu, D., et al., Molecular Beam Epitaxy of Highly Crystalline Monolayer Molybdenum Disulfide on Hexagonal Boron Nitride. *Journal of the American Chemical Society* **2017**, *139*, 9392-9400.
31. Liu, K.-K., et al., Growth of Large-Area and Highly Crystalline Mos2 Thin Layers on Insulating Substrates. *Nano Letters* **2012**, *12*, 1538-1544.
32. Laskar, M. R.; Ma, L.; Kannappan, S.; Park, P. S.; Krishnamoorthy, S.; Nath, D. N.; Lu, W.; Wu, Y.; Rajan, S., Large Area Single Crystal (0001) Oriented Mos2. *Applied Physics Letters* **2013**, *102*, 252108.
33. Lin, Y.-C.; Zhang, W.; Huang, J.-K.; Liu, K.-K.; Lee, Y.-H.; Liang, C.-T.; Chu, C.-W.; Li, L.-J., Wafer-Scale Mos2 Thin Layers Prepared by Moo3 Sulfurization. *Nanoscale* **2012**, *4*, 6637-6641.
34. Zhang, J., et al., Scalable Growth of High-Quality Polycrystalline Mos2 Monolayers on Sio2 with Tunable Grain Sizes. *ACS Nano* **2014**, *8*, 6024-6030.
35. Shi, Y., et al., Van Der Waals Epitaxy of Mos2 Layers Using Graphene as Growth Templates. *Nano Letters* **2012**, *12*, 2784-2791.
36. Zhan, Y.; Liu, Z.; Najmaei, S.; Ajayan, P. M.; Lou, J., Large-Area Vapor-Phase Growth and Characterization of Mos(2) Atomic Layers on a Sio(2) Substrate. *Small* **2012**, *8*, 966-71.
37. Ji, Q., et al., Epitaxial Monolayer Mos2 on Mica with Novel Photoluminescence. *Nano Letters* **2013**, *13*, 3870-3877.
38. Lee, Y.-H., et al., Synthesis of Large-Area Mos2 Atomic Layers with Chemical Vapor Deposition. *Advanced Materials* **2012**, *24*, 2320-2325.
39. Yu, Y.; Li, C.; Liu, Y.; Su, L.; Zhang, Y.; Cao, L., Controlled Scalable Synthesis of Uniform, High-Quality Monolayer and Few-Layer Mos2 Films. *Scientific Reports* **2013**, *3*, 1866.
40. Zhang, Y.; Yu, Y.; Mi, L.; Wang, H.; Zhu, Z.; Wu, Q.; Zhang, Y.; Jiang, Y., In Situ Fabrication of Vertical Multilayered Mos2/Si Homotype Heterojunction for High-Speed Visible–near-Infrared Photodetectors. *Small* **2016**, *12*, 1062-1071.
41. Qiao, S.; Cong, R.; Liu, J.; Liang, B.; Fu, G.; Yu, W.; Ren, K.; Wang, S.; Pan, C., A Vertically Layered Mos2/Si Heterojunction for an Ultrahigh and Ultrafast Photoresponse Photodetector. *Journal of Materials Chemistry C* **2018**, *6*, 3233-3239.
42. Kim, M. S.; Roy, S.; Lee, J.; Kim, B. G.; Kim, H.; Park, J.-H.; Yun, S. J.; Han, G. H.; Leem, J.-Y.; Kim, J., Enhanced Light Emission from Monolayer Semiconductors by Forming Heterostructures with Zno Thin Films. *ACS Appl. Mater. Interfaces* **2016**, *8*, 28809-28815.
43. Zhou, W.; Yin, Z.; Du, Y.; Huang, X.; Zeng, Z.; Fan, Z.; Liu, H.; Wang, J.; Zhang, H., Synthesis of Few-Layer Mos2 Nanosheet-Coated Tio2 Nanobelt Heterostructures for Enhanced Photocatalytic Activities. *Small* **2013**, *9*, 140-147.
44. Kaushik, N.; Karmakar, D.; Nipane, A.; Karande, S.; Lodha, S., Interfacial N-Doping Using an Ultrathin Tio2 Layer for Contact Resistance Reduction in Mos2. *ACS Applied Materials & Interfaces* **2016**, *8*, 256-263.
45. Paul, K. K.; Mawlong, L. P. L.; Giri, P. K., Trion-Inhibited Strong Excitonic Emission and Broadband Giant Photoresponsivity from Chemical Vapor-Deposited Monolayer Mos2 Grown in Situ on Tio2 Nanostructure. *ACS Applied Materials & Interfaces* **2018**, *10*, 42812-42825.

46. Liu, Q., et al., In Situ Integration of a Metallic 1t-Mos2/Cds Heterostructure as a Means to Promote Visible-Light-Driven Photocatalytic Hydrogen Evolution. *ChemCatChem* **2016**, *8*, 2614-2619.
47. Liu, Y.; Yu, Y.-X.; Zhang, W.-D., Mos2/Cds Heterojunction with High Photoelectrochemical Activity for H2 Evolution under Visible Light: The Role of Mos2. *The Journal of Physical Chemistry C* **2013**, *117*, 12949-12957.
48. Yuan, Y., et al., Growth of Cdse/Mos2 Vertical Heterostructures for Fast Visible-Wavelength Photodetectors. *Journal of Alloys and Compounds* **2020**, *815*, 152309.
49. Sharma, I.; Mehta, B. R., Enhanced Charge Separation at 2d Mos2/Zns Heterojunction: Kpfm Based Study of Interface Photovoltage. *Applied Physics Letters* **2017**, *110*, 061602.
50. Hu, X.; Deng, F.; Huang, W.; Zeng, G.; Luo, X.; Dionysiou, D. D., The Band Structure Control of Visible-Light-Driven Rgo/Zns-Mos2 for Excellent Photocatalytic Degradation Performance and Long-Term Stability. *Chemical Engineering Journal* **2018**, *350*, 248-256.
51. Lin, S.; Wang, P.; Li, X.; Wu, Z.; Xu, Z.; Zhang, S.; Xu, W., Gate Tunable Monolayer Mos2/Inp Heterostructure Solar Cells. *Applied Physics Letters* **2015**, *107*, 153904.
52. Wang, P., et al., Enhanced Monolayer Mos2/Inp Heterostructure Solar Cells by Graphene Quantum Dots. *Applied Physics Letters* **2016**, *108*, 163901.
53. Zhang, Z.; Qian, Q.; Li, B.; Chen, K. J., Interface Engineering of Monolayer Mos2/Gan Hybrid Heterostructure: Modified Band Alignment for Photocatalytic Water Splitting Application by Nitridation Treatment. *ACS Applied Materials & Interfaces* **2018**, *10*, 17419-17426.
54. Henck, H., et al., Interface Dipole and Band Bending in the Hybrid $P\Ensuremath{-}N$ Heterojunction MoS2 Gan (0001). *Physical Review B* **2017**, *96*, 115312.
55. Xu, S.; Li, D.; Wu, P., One-Pot, Facile, and Versatile Synthesis of Monolayer Mos2/Ws2 Quantum Dots as Bioimaging Probes and Efficient Electrocatalysts for Hydrogen Evolution Reaction. *Advanced Functional Materials* **2015**, *25*, 1127-1136.
56. Kim, M. S.; Seo, C.; Kim, H.; Lee, J.; Luong, D. H.; Park, J.-H.; Han, G. H.; Kim, J., Simultaneous Hosting of Positive and Negative Trions and the Enhanced Direct Band Emission in Mose2/Mos2 Heterostacked Multilayers. *ACS Nano* **2016**, *10*, 6211-6219.
57. Yang, S., et al., Self-Driven Photodetector and Ambipolar Transistor in Atomically Thin Gate-Mos2 P–N Vdw Heterostructure. *ACS Appl. Mater. Interfaces* **2016**, *8*, 2533-2539.
58. He, X.; Chow, W.; Liu, F.; Tay, B.; Liu, Z., Mos2/Rubrene Van Der Waals Heterostructure: Toward Ambipolar Field-Effect Transistors and Inverter Circuits. *Small* **2017**, *13*, 1602558.
59. Park, C.-J.; Park, H. J.; Lee, J. Y.; Kim, J.; Lee, C.-H.; Joo, J., Photovoltaic Field-Effect Transistors Using a Mos2 and Organic Rubrene Van Der Waals Hybrid. *ACS Applied Materials & Interfaces* **2018**, *10*, 29848-29856.
60. Tiwari, S. P.; Verma, R.; Alam, M. B.; Kumari, R.; Sinha, O. P.; Srivastava, R., Charge Transport Study of P3ht Blended Mos2. *Vacuum* **2017**, *146*, 474-477.
61. Wang, S., et al., A Mos2/Ptcda Hybrid Heterojunction Synapse with Efficient Photoelectric Dual Modulation and Versatility. *Advanced Materials* **2019**, *31*, 1806227.
62. Wang, X.; Meng, F.; Jiang, Q.; Zhou, W.; Jiang, F.; Wang, T.; Li, X.; Li, S.; Lin, Y.; Xu, J., Simple Layer-by-Layer Assembly Method for Simultaneously Enhanced Electrical Conductivity and Thermopower of Pedot:Pss/Ce-Mos2 Heterostructure Films. *ACS Applied Energy Materials* **2018**, *1*, 3123-3133.
63. Liu, B., et al., High Performance Photodetector Based on Graphene/Mos2/Graphene Lateral Heterostrurcture with Schottky Junctions. *Journal of Alloys and Compounds* **2019**, *779*, 140-146.
64. Miwa, J. A.; Dendzik, M.; Grønborg, S. S.; Bianchi, M.; Lauritsen, J. V.; Hofmann, P.; Ulstrup, S., Van Der Waals Epitaxy of Two-Dimensional Mos2–Graphene Heterostructures in Ultrahigh Vacuum. *ACS Nano* **2015**, *9*, 6502-6510.
65. Saraf, M.; Natarajan, K.; Mobin, S. M., Emerging Robust Heterostructure of Mos2–Rgo for High-Performance Supercapacitors. *ACS Applied Materials & Interfaces* **2018**, *10*, 16588-16595.

66. Zhang, C.; Chen, G.; Li, C.; Sun, J.; Lv, C.; Fan, S.; Xing, W., In Situ Fabrication of Bi2wo6/Mos2/Rgo Heterojunction with Nanosized Interfacial Contact Via Confined Space Effect toward Enhanced Photocatalytic Properties. *ACS Sustainable Chemistry & Engineering* **2016**, *4*, 5936-5942.
67. Xiao, P.; Mao, J.; Ding, K.; Luo, W.; Hu, W.; Zhang, X.; Zhang, X.; Jie, J., Solution-Processed 3d Rgo–Mos2/Pyramid Si Heterojunction for Ultrahigh Detectivity and Ultra-Broadband Photodetection. *Advanced Materials* **2018**, *30*, 1801729.
68. Jariwala, D.; Sangwan, V. K.; Wu, C.-C.; Prabhumirashi, P. L.; Geier, M. L.; Marks, T. J.; Lauhon, L. J.; Hersam, M. C., Gate-Tunable Carbon Nanotube–Mos2 Heterojunction P-N Diode. *Proceedings of the National Academy of Sciences* **2013**, *110*, 18076-18080.
69. Zheng, X.; Guo, Z.; Zhang, G.; Li, H.; Zhang, J.; Xu, Q., Building a Lateral/Vertical 1t-2h Mos2/Au Heterostructure for Enhanced Photoelectrocatalysis and Surface Enhanced Raman Scattering. *Journal of Materials Chemistry A* **2019**, *7*, 19922-19928.
70. Rahaman, M.; Rodriguez, R. D.; Plechinger, G.; Moras, S.; Schüller, C.; Korn, T.; Zahn, D. R. T., Highly Localized Strain in a Mos2/Au Heterostructure Revealed by Tip-Enhanced Raman Spectroscopy. *Nano Letters* **2017**, *17*, 6027-6033.
71. Chen, J., et al., Ag@Mos2 Core–Shell Heterostructure as Sers Platform to Reveal the Hydrogen Evolution Active Sites of Single-Layer Mos2. *Journal of the American Chemical Society* **2020**, *142*, 7161-7167.
72. Alido, J. P. M.; Sari, F. N. I.; Ting, J.-M., Synthesis of Ag/Hybridized 1t-2h Mos2/Tio2 Heterostructure for Enhanced Visible-Light Photocatalytic Activity. *Ceramics International* **2019**, *45*, 23651-23657.
73. Shang, B.; Cui, X.; Jiao, L.; Qi, K.; Wang, Y.; Fan, J.; Yue, Y.; Wang, H.; Bao, Q.; Fan, X., Lattice-Mismatch-Induced Ultrastable 1t-Phase Mos2–Pd/Au for Plasmon-Enhanced Hydrogen Evolution. *Nano letters* **2019**, *19*, 2758-2764.
74. Yang, D.; Sandoval, S. J.; Divigalpitiya, W. M. R.; Irwin, J. C.; Frindt, R. F., Structure of Single-Molecular-Layer Mos2. *Physical Review B* **1991**, *43*, 12053-12056.
75. Fu, X.; Zhang, L.; Liu, L.; Li, H.; Meng, S.; Ye, X.; Chen, S., In Situ Photodeposition of Mosx on Cds Nanorods as a Highly Efficient Cocatalyst for Photocatalytic Hydrogen Production. *Journal of Materials Chemistry A* **2017**, *5*, 15287-15293.
76. Mao, K.; Wu, Z.; Chen, Y.; Zhou, X.; Shen, A.; Hu, J., A Novel Biosensor Based on Single-Layer Mos2 Nanosheets for Detection of Ag(+). *Talanta* **2015**, *132*, 658-63.
77. Soni, A.; Pandey, C. M.; Pandey, M. K.; Sumana, G., Highly Efficient Polyaniline-Mos2 Hybrid Nanostructures Based Biosensor for Cancer Biomarker Detection. *Analytica Chimica Acta* **2019**, *1055*, 26-35.
78. Yue, N.; Weicheng, J.; Rongguo, W.; Guomin, D.; Yifan, H., Hybrid Nanostructures Combining Graphene–Mos2 Quantum Dots for Gas Sensing. *Journal of Materials Chemistry A* **2016**, *4*, 8198-8203.
79. Zhou, X., et al., Vertical Heterostructures Based on Snse2/Mos2 for High Performance Photodetectors. *2D Materials* **2017**, *4*, 025048.
80. Kang, D.-H.; Pae, S. R.; Shim, J.; Yoo, G.; Jeon, J.; Leem, J. W.; Yu, J. S.; Lee, S.; Shin, B.; Park, J.-H., An Ultrahigh-Performance Photodetector Based on a Perovskite–Transition-Metal-Dichalcogenide Hybrid Structure. *Advanced Materials* **2016**, *28*, 7799-7806.
81. Cho, E. H.; Song, W. G.; Park, C. J.; Kim, J.; Kim, S.; Joo, J., Enhancement of Photoresponsive Electrical Characteristics of Multilayer Mos2 Transistors Using Rubrene Patches. *Nano Research* **2015**, *8*, 790-800.
82. Ma, D., et al., A Universal Etching-Free Transfer of Mos2 Films for Applications in Photodetectors. *Nano Research* **2015**, *8*, 3662-3672.
83. Tsai, M.-L.; Su, S.-H.; Chang, J.-K.; Tsai, D.-S.; Chen, C.-H.; Wu, C.-I.; Li, L.-J.; Chen, L.-J.; He, J.-H., Monolayer Mos2 Heterojunction Solar Cells. *ACS Nano* **2014**, *8*, 8317-8322.

84. Wong, J.; Jariwala, D.; Tagliabue, G.; Tat, K.; Davoyan, A. R.; Sherrott, M. C.; Atwater, H. A., High Photovoltaic Quantum Efficiency in Ultrathin Van Der Waals Heterostructures. *ACS Nano* **2017**, *11*, 7230-7240.
85. Long, M., et al., Broadband Photovoltaic Detectors Based on an Atomically Thin Heterostructure. *Nano Letters* **2016**, *16*, 2254-2259.
86. Barpuzary, D.; Banik, A.; Gogoi, G.; Qureshi, M., Noble Metal-Free Counter Electrodes Utilizing Cu2znsns4 Loaded with Mos2 for Efficient Solar Cells Based on Zno Nanowires Co-Sensitized with Cu in s2–Cdse Quantum Dots. *Journal of Materials Chemistry A* **2015**, *3*, 14378-14388.
87. Yun, J.-M., et al., Efficient Work-Function Engineering of Solution-Processed Mos2 Thin-Films for Novel Hole and Electron Transport Layers Leading to High-Performance Polymer Solar Cells. *Journal of Materials Chemistry C* **2013**, *1*, 3777-3783.
88. Yang, X.; Fu, W.; Liu, W.; Hong, J.; Cai, Y.; Jin, C.; Xu, M.; Wang, H.; Yang, D.; Chen, H., Engineering Crystalline Structures of Two-Dimensional Mos2 Sheets for High-Performance Organic Solar Cells. *Journal of Materials Chemistry A* **2014**, *2*, 7727-7733.
89. Qin, P.; Fang, G.; Ke, W.; Cheng, F.; Zheng, Q.; Wan, J.; Lei, H.; Zhao, X., In Situ Growth of Double-Layer Moo3/Mos2 Film from Mos2 for Hole-Transport Layers in Organic Solar Cell. *Journal of Materials Chemistry A* **2014**, *2*, 2742-2756.
90. Capasso, A.; Matteocci, F.; Najafi, L.; Prato, M.; Buha, J.; Cinà, L.; Pellegrini, V.; Carlo, A. D.; Bonaccorso, F., Few-Layer Mos2 Flakes as Active Buffer Layer for Stable Perovskite Solar Cells. *Advanced Energy Materials* **2016**, *6*, 1600920.
91. Hu, X.; Chen, L.; Tan, L.; Zhang, Y.; Hu, L.; Xie, B.; Chen, Y., Versatile Mos2 Nanosheets in Ito-Free and Semi-Transparent Polymer Power-Generating Glass. *Scientific Reports* **2015**, *5*, 12161.
92. Zheng, X.; Zhang, H.; Yang, Q.; Xiong, C.; Li, W.; Yan, Y.; Gurney, R. S.; Wang, T., Solution-Processed Graphene-Mos2 Heterostructure for Efficient Hole Extraction in Organic Solar Cells. *Carbon* **2019**, *142*, 156-163.
93. Nikam, R. D.; Sonawane, P. A.; Sankar, R.; Chen, Y.-T., Epitaxial Growth of Vertically Stacked P-Mos2/N-Mos2 Heterostructures by Chemical Vapor Deposition for Light Emitting Devices. *Nano Energy* **2017**, *32*, 454-462.
94. Li, P.; Yuan, K.; Lin, D.-Y.; Xu, X.; Wang, Y.; Wan, Y.; Yu, H.; Zhang, K.; Ye, Y.; Dai, L., A Mixed-Dimensional Light-Emitting Diode Based on a P-Mos2 Nanosheet and an N-Cdse Nanowire. *Nanoscale* **2017**, *9*, 18175-18179.
95. Lopez-Sanchez, O.; Alarcon Llado, E.; Koman, V.; Fontcuberta i Morral, A.; Radenovic, A.; Kis, A., Light Generation and Harvesting in a Van Der Waals Heterostructure. *ACS Nano* **2014**, *8*, 3042-3048.
96. Cheng, R.; Li, D.; Zhou, H.; Wang, C.; Yin, A.; Jiang, S.; Liu, Y.; Chen, Y.; Huang, Y.; Duan, X., Electroluminescence and Photocurrent Generation from Atomically Sharp Wse2/Mos2 Heterojunction P–N Diodes. *Nano Letters* **2014**, *14*, 5590-5597.
97. Li, D.; Cheng, R.; Zhou, H.; Wang, C.; Yin, A.; Chen, Y.; Weiss, N. O.; Huang, Y.; Duan, X., Electric-Field-Induced Strong Enhancement of Electroluminescence in Multilayer Molybdenum Disulfide. *Nature Communications* **2015**, *6*, 7509.
98. Withers, F., et al., Light-Emitting Diodes by Band-Structure Engineering in Van Der Waals Heterostructures. *Nature Materials* **2015**, *14*, 301-306.

Chapter 2

Controlled Growth of Monolayer MoS_2 by Chemical Vapour Deposition Method

This chapter introduces three approaches for the growth of monolayer MoS_2. In the first method, an ordered array of two-dimensional MoS_2 nanodots were grown on SiO_2 substrates at a relatively low substrate temperature (500-560 °C) by chemical vapor deposition (CVD) method, which results in the growth of monolayer to few-layer MoS_2. In the CVD technique, the growth parameters such as carrier gas, growth temperature, precursors, and substrates play important roles in the growth of high-quality monolayer MoS_2. In the second process, better control over growth has been achieved that improves the quality, uniformity, and area coverage. By tuning the growth parameters, the growth of purely monolayer MoS_2 was achieved. The understanding of growth mechanisms is based on the nucleation mechanism that depends on the reactant (MoO_3 and S) concentration of the substrate surface. In the last method, large-area continuous monolayer MoS_2 was grown, covering a few mm^2 on various substrates. In this process, a specially designed quartz mask was used, on top of which the substrate was placed. The gap that is formed between the substrate and quartz mask acts as a natural reactor cavity, giving rise to the growth of continuous monolayer MoS_2 film on the substrate in the region covered by the mask. Herein we present a systematic approach for the understanding of nucleation and growth mechanisms of CVD-grown monolayer MoS_2.

2.1. A Low-Temperature Chemical Vapor Deposition Growth of Monolayer and Bilayer MoS_2 dots Array

2.1.1. Introduction

Since the discovery of graphene, the two-dimensional materials have attracted much interest due to their unusual optical, electrical, and mechanical characteristics. Molybdenum disulphide (MoS_2), a transition metal dichalcogenide (TMD), has a layered structure of hexagonally arranged covalently bonded Mo and S atoms. MoS_2 have attracted considerable attention because of its tunability in the band structure ranging from metallic to semiconducting.[1, 2] The vast difference in the electronic structure of the bulk in comparison with the monolayer MoS_2 offers an excellent

opportunity for diverse applications.[3-7] A repeatable and straightforward technique to grow large-area monolayer MoS_2 film is essential for such requests. Over the past few years, considerable efforts have been made to obtaining large-scale atomically thin MoS_2.[8-10] MoS_2 have been fabricated by various methods, such as CVD, hydrothermal synthesis, pulsed laser deposition (PLD), thermal evaporation, magnetron sputtering etc.[11-14] However, the lateral size of MoS_2 domains synthesized by these methods is often restricted to several micrometers, making the synthesis of a large-area MoS_2 thin layer challenging. Among the different methods, CVD has been one of the most promising ways of producing large-area and high-quality MoS_2 thin films. However, there are very few reports on the low temperature CVD growth of monolayer and few layer MoS_2.

2.1.2. Experimental Details

Bilayer and few-layer MoS_2 dots were directly grown on the SiO_2 substrates using an in-house developed CVD system. Commercially procured MoO_3 and S powder were used as precursors for the CVD growth of MoS_2 in a quartz tube-based horizontal muffle furnace. High-purity argon (Ar) gas was used as the carrier gas. At first, the S precursor was kept near the entrance of the quartz tube, away from the central heating zone of the furnace, while the MoO_3 powder was placed at the center of the furnace, and a few pieces of bare SiO_2 substrates were placed near the source power at the rear end side of the quartz tube. Note that both S and MoO_3 precursors were separately loaded in two mini quartz tubes (inner diameter~10 mm) and kept at a distance of 53 cm and 33 cm away from the substrates (see **Fig. 2.1(a)**). This arrangement provides stable evaporation of S and MoO_3 sources at suitable temperatures and avoids any cross-contaminations during the MoS_2 growth. The quartz chamber was pumped down to a base pressure of 1.9×10^{-2} mbar. The central zone temperature was raised to 760°C at the rate of 17°C/min for 45 mins and was allowed to stabilize at this temperature for 15 minutes with Ar as the carrier gas with a flow rate of 100 sccm (standard cubic centimeters per minute) keeping the pressure at 2.2 mbar. Then it was ramped up slowly to 800°C at the rate of 4°C/min, and then maintained at this temperature for 30 mins without changing the gas flow. After the growth process, the system was allowed to cool down naturally to room temperature with an Ar gas flow of 300 sccm. The experimental setup and the complete timeline profile of the CVD growth of MoS_2 dots is shown in **Fig. 2.1(b).** The substrate temperature is controlled by the proper positioning of the substrate inside the furnace. The growth of MoS_2

layer was monitored at four different substrate temperatures. The samples grown at substrate temperatures of 560, 540, 510 and 310°C are named as MS-560, MS-540, MS-510, and MS-310, respectively.

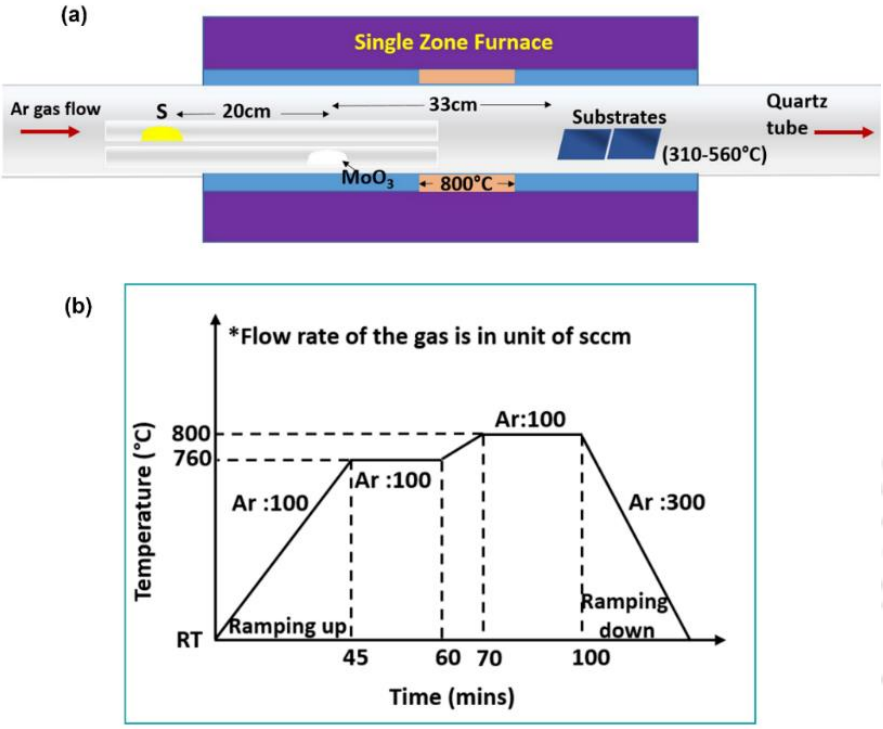

Fig. 2.1. (a) Schematic of the CVD setup for the growth of MoS_2 dots, showing the precise location of S and MoO_3 sources and SiO_2 substrates. (b) Timeline profile and growth parameters of the CVD grown MoS_2 nanodots.

2.1.3. Characterization Techniques

Micro-Raman and photoluminescence (PL) measurements were performed with a high-resolution spectrometer (Horiba 171 LabRam HR), with excitation wavelengths (λ_{ex}) of 488 nm (Ar^+ ion laser). The excitation source was focused with a 100X objective lens, a spot size of 1 μm, and a laser power of 1.5 mW, and the signal was collected by a CCD in a backscattering geometry sent through a multimode fiber grating of 1800 grooves/mm. Surface morphology and microstructure of the as-grown MoS_2 dots were examined by field emission scanning electron microscope (FESEM), FEI-Quanta 400 with an acceleration voltage of 20 kV with spatial resolution: 1.2 nm at 30 kV in SE, 2 nm at 30 kV in BSE (Gold/Carbon), Detectors: SE, BSE. The spectral line shape of the mirco-Raman features was fitted with Lorentzian line shapes. Atomic force microscopy (AFM) (Cypher, Oxford Instruments) images were acquired to confirm the layer thickness of CVD-grown MoS_2.

2.1.4. Results and Discussion

2.1.4.1. Morphology Studies

To understand the morphology of the as-grown samples, FESEM imaging was carried out. A detailed description of the samples and FESEM features is provided in **Table 2.1. Fig. 2.2(a-b)** shows the FESEM images of sample MS-510 at two different magnifications, while **Fig**. **2.2(c-d)** and **Fig. 2.2(e-f)** represent the FESEM images of samples MS-540 and MS-560, respectively. It is evident that in each sample, MoS_2 dots of a variety of sizes are formed. The uniformity of these dots is almost maintained throughout the surface of the sample, over an estimated area of 1 cm×1 cm. We observed that the shape of the MoS_2 dots is mostly circular, and a regular array type structure is formed in all the samples. The observed regular array of MoS_2 dots is likely to be due to the direction of the carrier gas flow. On the other hand, no growth was observed on substrates kept at a temperature below 500 °C.

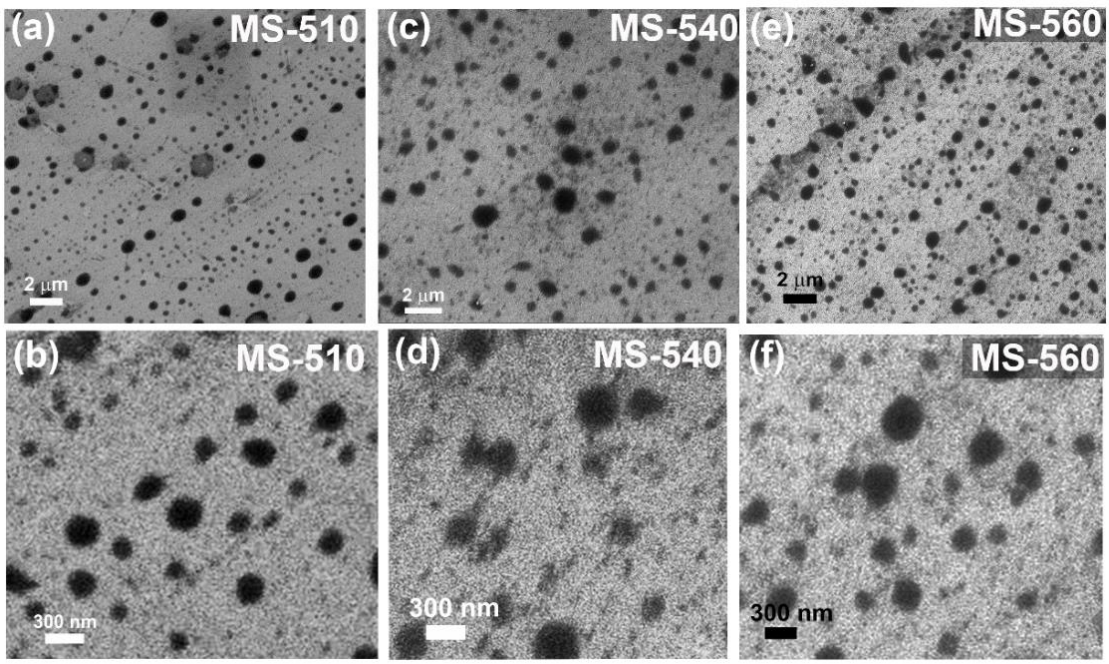

Fig. 2.2. Morphological characteristics of MoS_2 dots grown by a low-temperature CVD method: Low and high-resolution FESEM images of as-grown MoS_2 dots in (a-b) MS-510, (c-d) MS-540 and (e-f) MS-560.

Table 2.1: *Summary of the samples grown at different substrate temperatures by the CVD method. Note that the growth duration and gas flow rate (Ar as carrier gas) were kept identical during the growth of different sample*

Sample Code	Substrate Temperature (°C)	Morphology
MS	-	MoS_2 Flakes
MS-560	560	Circular MoS_2 dots
MS-540	540	Circular MoS_2 dots
MS-510	510	Circular MoS_2 dots
MS-310	310	Absence of MoS_2

2.1.4.2. Raman Analysis

Micro-Raman measurements were performed on the as-grown MoS_2 dot samples, and it was compared with that of the bulk MoS_2 flakes. **Fig. 2.3(a)** represents a comparison of the Raman spectra for different samples, which exhibits two important characteristic Raman modes, which are signatures of the few-layer MoS_2, associated with the phonon modes at 379 and 405 cm^{-1} corresponding to E_{2g} and A_{1g} modes, respectively. In general, the E_{2g} mode arises due to the in-plane vibration of two S atoms with respect to the Mo atoms, while the A_{1g} mode is associated with the out-of-plane vibration of only S atoms in opposite directions with respect to the Mo atoms.[15] These two Raman modes are very sensitive to the local in-plane, edge defects, and impurities present on the atomic layers of MoS_2. In **Fig. 2.3(a),** the growth of MoS_2 for samples MS-560, MS-540 and MS-510 is confirmed by the presence of E_{2g} and A_{1g} Raman bands, which is also consistent with the FESEM images (**Fig. 2.2(a-f)**). On the other hand, in the case of sample MS-310, MoS_2 Raman modes was absent, as evidenced by the absence of the A_{1g} peak in the spectrum. Raman spectrum of MS-310 shows a strong Raman peak at 338 cm^{-1}, which signifies the presence of MoO_3 and negligible presence of S. We also observed a phonon mode stiffening of the characteristic Raman modes, reflected by a blue shift of both the peaks by 3-5 cm^{-1} for all the as-grown samples. The blue-shift is expected to be related to the compressive strain.[16]

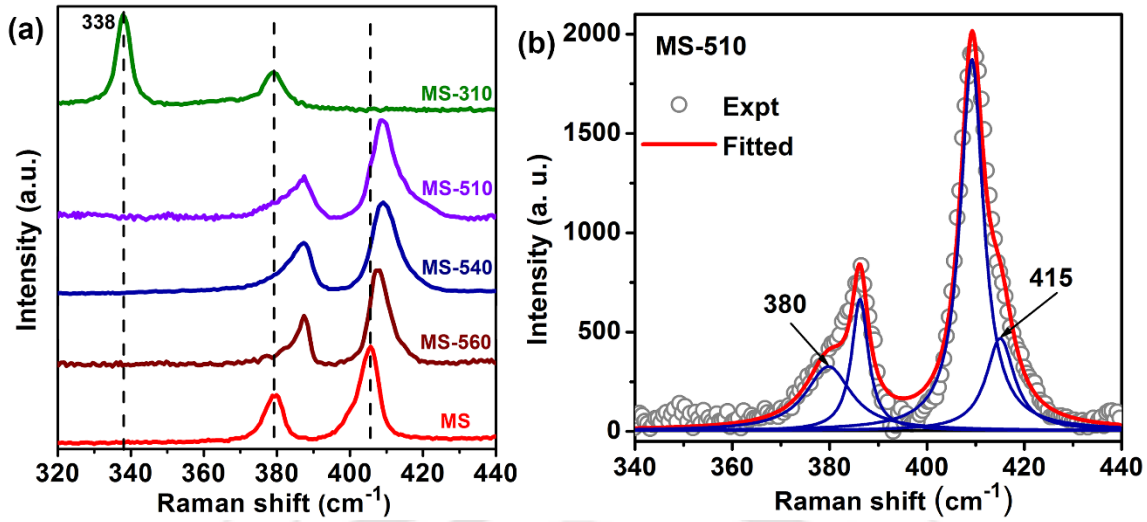

Fig. 2.3: (a) Raman fingerprints of as-grown MoS_2 dots grown at different substrate temperatures. (b) Lorentzian line shape fitting of E_{2g} and A_{1g} modes in MS-510. Note that the peak center of each mode is denoted in cm^{-1} unit.

The line shape parameters of Raman peaks are summarized in **Table 2.2**, which depicts the peak position and frequency difference (Δk) between the A_{1g} and E_{2g} modes. The observed Δk values signify the growth of monolayer and bilayer MoS_2. Lorentzian line shape was fitted for the E_{2g} and A_{1g} bands, as shown in the **Fig. 2.3(b).** There are two new Raman bands fitted at lower and higher frequency sides at 380 and 415 cm^{-1}, respectively. An earlier report suggests that the splitting of the A_{1g} peak into two peaks is due to the appearance of a Raman inactive mode (B_{1u}) at 415 cm^{-1}, which is not prominent in case of bulk MoS_2.[15] However, it becomes significant in case of monolayer MoS_2, which makes the A_{1g} peak (406.9 cm^{-1}) asymmetric towards higher wavenumber. The observed splitting in the E_{2g} Raman mode at 380 cm^{-1} can be attributed to the mechanical strain in the MoS_2 dots.[17] To further investigate the spatial uniformity and layer thickness, position-dependent Raman spectra of as-grown MoS_2 dot array was taken for the as-grown samples. **Fig. 2.4 (a-d)** shows the position-dependent Raman spectra of as-grown MoS_2 dot array in MS-540 and MS-510 and their corresponding optical microscope (OM) image showing scanned area for each spectrum marked with the respective serial number. We observed that the Raman spectra for different locations of a sample are slightly different. In spot 1, for MS-540, we notice that the frequency difference Δk between the Raman bands is ~20.1 cm^{-1}, which indicates the monolayer MoS_2 growth, while in spot 3, Δk ~ 21.5 cm^{-1}, confirming the bilayer growth. Additional Raman bands seen at 347.8 cm^{-1}, 353.4 cm^{-1}, and 366.2 cm^{-1} are assigned to the stretching modes of the doubly coordinated oxygen (Mo−O−Mo) in MoO_2. The observed Raman

bands of MoO_3 and MoO_2 compare well with the reported literature values.[18] Therefore, these results show some inhomogeneity of growth. Analogously, we observed similar growth in MS-510 sample. The extracted peak parameters are shown in **Table 2.3**. Thus, further optimization of the growth parameters is necessary for more uniform growth of the MoS_2 layers at a low temperature.

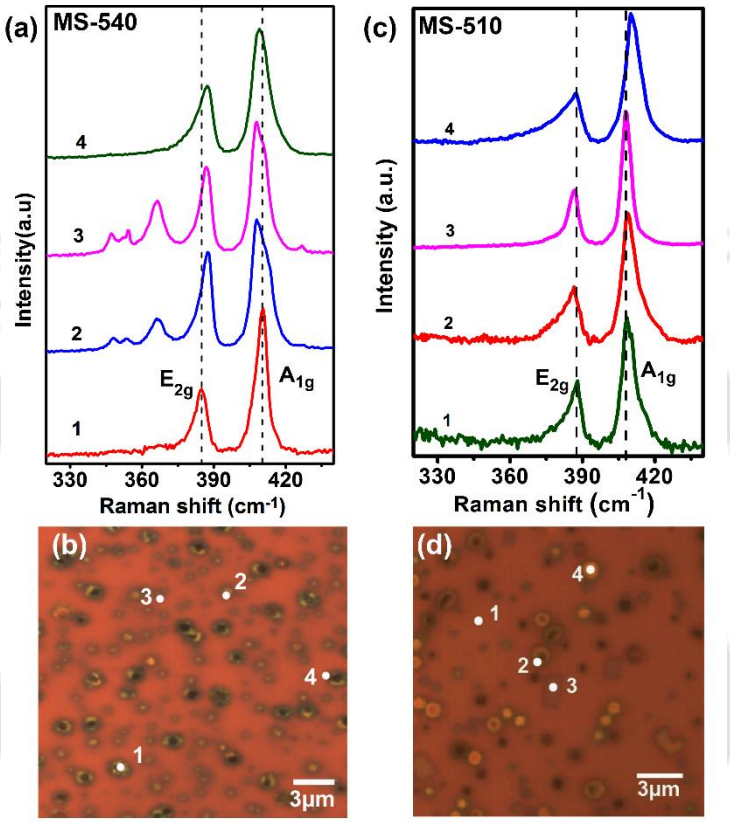

Fig. 2.4: (a,c) Position dependent Raman profile of the MS-540 and MS-510 samples, (b,d) corresponding optical microscope images showing scanned area for each spectrum marked with a serial number.

Table 2.2: *Summary of the E_{2g} and A_{1g} Raman modes and their separation (Δk) for different samples.*

Sample	E_{2g} (cm^{-1})	A_{1g} (cm^{-1})	Δk (cm^{-1})	number of layers in MoS_2
MS	379.3	405.7	26.3	Multi-layers
MS-560	387.7	408.9	21.2	Bilayer
MS-540	387.3	409.0	21.7	Bilayer
MS-510	387.7	408.3	20.6	Monolayer
MS-310	379.4	-	-	-

Table 2.3: *Summary of the E_{2g} and A_{1g} Raman modes for the different locations of MS-540 and MS-510. The peak separation (Δk) signifies the growth of monolayer and bilayer MoS_2 dots.*

Sample	Sample position	E_{2g} (cm^{-1})	A_{1g} (cm^{-1})	Δk (cm^{-1})	Additional bands (cm^{-1})
MS-540	1	388.6	408.7	20.1	-
	2	387.6	408	20.4	347.4, 354.3 and 366.2
	3	386.8	408.3	21.5	347.8, 353.4 and 366.2
	4	387.2	409.1	21.9	-
MS-510	1	388.0	408.3	20.3	-
	2	386.5	408.2	21.7	-
	3	386.9	407.7	20.8	-
	4	387.2	409.9	20.7	-

2.2. CVD growth of monolayer MoS_2

2.2.1. Introduction

From the previous section, a brief understanding of the conditions and critical experimental parameters for the CVD growth of MoS_2 was realized. The next step is to make a few modifications in the CVD technique for the production of high crystal quality monolayer MoS_2. The growth of MoS_2 by the CVD method is usually based on the reaction of the precursors (MoO_3 and S powder) in the vapor phase. Several growth parameters such as the carrier gas, precursors, growth temperature and substrates play a major role in the growth behaviors of MoS_2, since these growth parameters can affect the nucleation of MoS_2.[19-21] Thus, knowing the growth mechanisms in the CVD process is very important to improve the crystal quality of MoS_2. Our study attempts to prove a detailed understanding of the nucleation mechanisms for controlled growth of monolayer MoS_2.

2.2.2. Experimental Details

Monolayer to few-layer MoS_2 was directly grown on Si/SiO_2 substrate using a two-zone furnace-based CVD system. High purity MoO_3 (99.5%, Sigma-Aldrich) and sulfur powder (99.95%, Sigma-Aldrich) were used as precursors for the CVD growth of MoS_2 in a 2-inch diameter quartz tube-based horizontal muffle furnace. High-purity argon (Ar, 99.9999%) gas was used as the

carrier gas. Note that both S (200 mg) and MoO_3 (15 mg) precursors were separately loaded in two quartz boats. The substrate (facing downward) was mounted on top of the boat containing MoO_3 precursor, as shown in **Fig. 2.5.** Another ceramic boat containing sulfur powder was kept at a comparatively lower temperature zone of the furnace. The distance between the sulfur source and MoO_3 source was maintained as 15 cm. The quartz tube placed inside the furnace was purged with Ar gas at 300 sccm for 30 min before the growth to remove the surface adsorbed impurities, followed by a heating up to 150 °C for another 30 min. The temperature of the zone 2 containing the MoO_3 precursor and the substrates was gradually heated to the respective process temperatures (i.e., 650 °C, 700 °C, 750 °C and 800 °C) with a ramping rate of 15 °C/min and was maintained for 5 min, keeping the gas flow rate at 10 sccm. At this stage, the temperature of the sulfur source reached 150 °C. The furnace was then allowed to cool @6.5 °C/min till the temperature went down to room temperature. Furthermore, to examine the effect of carrier gas flux, the gas flux was increased from 5 sccm to 50 sccm, keeping the temperatures of Zone 1 and Zone 2 at 150 °C and 700 °C, respectively.

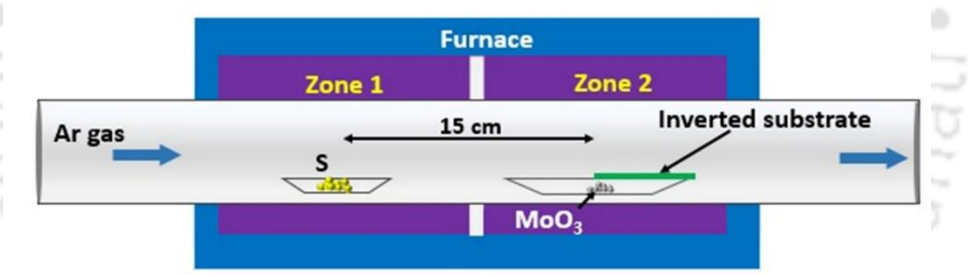

Fig. 2.5. Schematic of the CVD setup for the growth of MoS_2, showing the precise location of S and MoO_3 sources and the substrate.

2.2.3. Results and Discussion

2.2.3.1. Morphology Studies

Fig. 2.6(a-d) shows the OM images of the CVD grown MoS_2 layer in the temperature (substrate) range 650-800 °C. It can be seen that under different growth temperatures, the majority of the MoS_2 flakes have a triangular shape, which arises from the fact that the flake shape is determined by the growth rate of the MoS_2 edges. On the basis of the kinetic Wulff construction (KWC) theory,[22] the edges with the slowest growth rate become the largest, and the fast-growing edges either become small or disappear. For the sample grown at 650 °C, the size of the triangular MoS_2 flakes is ~ 3 µm (see **Fig. 2.6(a)**) and are less in density as compared to those grown at higher

temperatures. At higher growth temperatures (700 °C and 750 °C), the MoS_2 flake size is larger (~ 6 µm) along with an increase in the density of the flakes (**Fig. 2.6(b-c)**). In addition, we observed the formation of island-like nanoparticles at the center of the MoS_2 flakes at **750 °C**. Lastly, at 800 °C, the sizes of the MoS_2 flakes are ~ 1 to 2 µm smaller and have thicker triangular flakes.

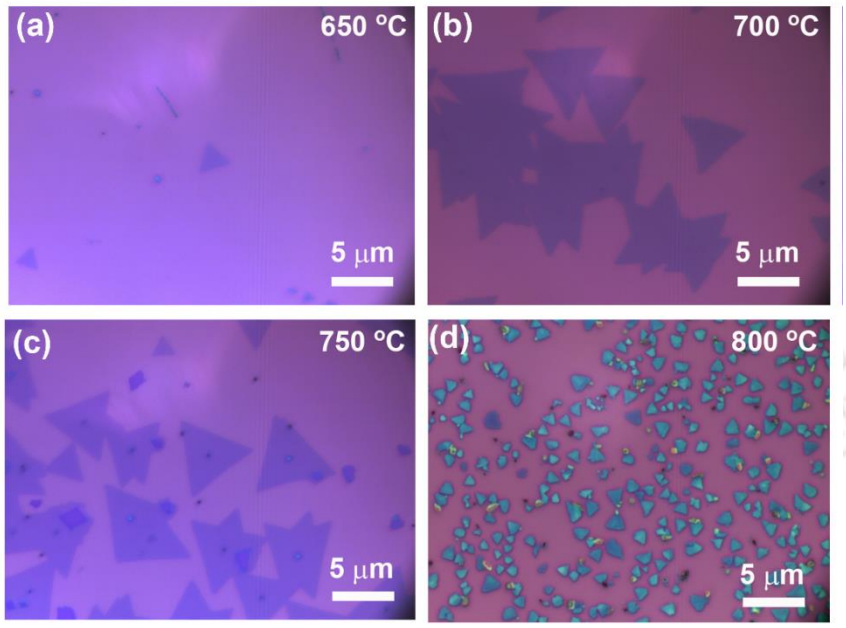

Fig. 2.6. Optical microscope (OM) image of the CVD-grown MoS_2 flakes with the growth temperature at (a) 650 °C, (b) 700 °C, (c) 750 °C, and (d) 800 °C.

To determine the number of MoS_2 layers deposited on the substrate, AFM imaging was carried out. **Fig. 2.7(a-c)** shows the AFM image and height profile of the MoS_2 flake grown at various growth temperatures. For the same growth duration, but at different growth temperatures, we notice distinct differences in the thickness of the MoS_2 flakes. **Fig. 2.7(a)** shows the AFM image of MoS_2 flake grown at 700 °C on the SiO_2 substrate. The flake shows homogenous color contrast, which indicates the uniformity of the MoS_2 flake. The thickness is found to be ~ 0.7 nm from the height profile measurement, which corresponds to monolayer MoS_2. Similarly, at 650 °C, we observed the thickness of the flake to be monolayer. On the other hand, at 750 °C (**Fig. 2.7(b)**), we observe a bright white spot at the center of the MoS_2 flake (as shown earlier in **Fig. 2.6(c)**), and the height profile displays a thickness of ~ 6.5 nm, which corresponds to ~ 9 layers of MoS_2. For another region, the height of the flake was found to be ~ 2.2 nm, which indicates the formation of trilayer MoS_2. In **Fig. 2.7(c),** for the sample grown at 800°C, the MoS_2 flake size is as small as ~ 2 µm, and from the AFM height profile, we can see that MoS_2 flake is multi layered. Thus, we

observe that with an increase in the growth temperature, there is an increase in the thickness of the MoS_2 flakes.

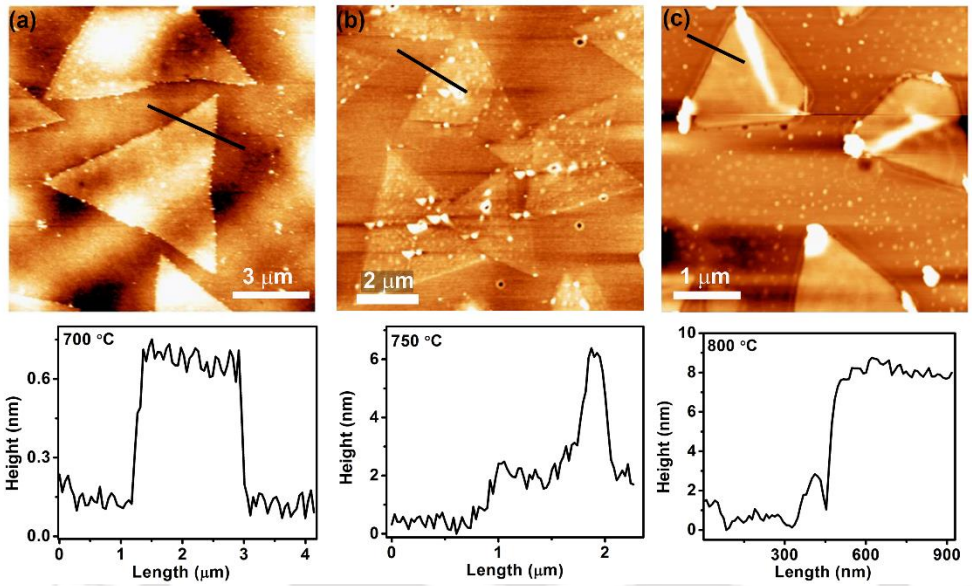

Fig. 2.7. AFM images and height profile of the CVD-grown MoS_2 flakes for the growth temperature at (a) 700 °C, (b) 750 °C, and (c) 800 °C. Note that the height profile is taken across the black line of the corresponding AFM image.

We further investigated the effect of the Ar gas flow rate on the growth of MoS_2. The variation in the carrier gas flux can affect the layer number in the CVD growth of MoS_2. **Fig. 2.8** shows the OM image of the CVD-grown MoS_2 flakes with the Ar gas flux of (a) 5 sccm, (b) 10 sccm, (c) 30 sccm, and (d) 50 sccm. At 5 sccm, no MoS_2 flake was formed on the substrate. This is because of the deficient transport of the gaseous MoO_3 and S precursor to the substrate as low flow rate of carrier gas. As we increase the Ar gas flux to 10 sccm, triangular MoS_2 flakes are formed on the substrate. When the gas flux is at 30 sccm, from the color contrast of the OM image, different layer MoS_2 flakes are present. Finally, at a very high gas flux of 50 sccm, very few small triangular flakes are formed on the substrate, which is due to the fact that the high gas flux can flush out the MoO_3 and S molecules from the substrate. Thus, control of the carrier gas flow rare is important for the growth of monolayer MoS_2 flakes.

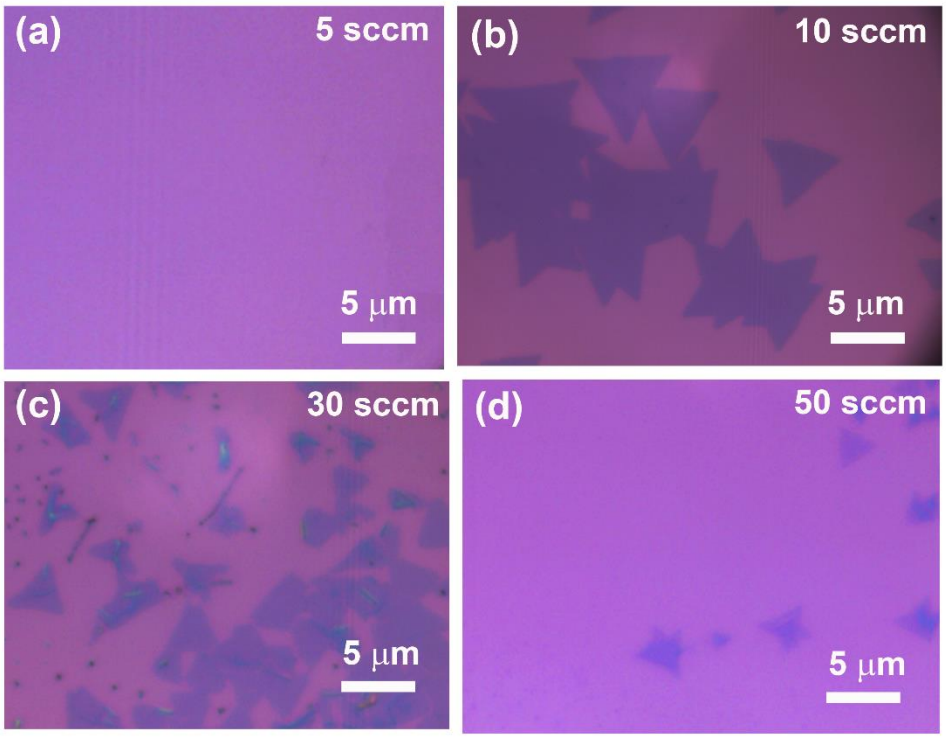

Fig. 2.8. Optical microscope (OM) image of the CVD-grown MoS_2 flakes with the Ar gas flux at (a) 5 sccm, (b) 10 sccm, (c) 30 sccm, and (d) 50 sccm.

2.2.3.2. Raman Analysis

Fig. 2.9 shows the comparative Raman spectra (excited with 488 nm laser) of the CVD grown MoS_2 flakes at different growth temperatures in the range 650-800 ^oC. The Raman spectra show the presence of the two characteristic Raman modes (E_{2g} and A_{1g}) corresponding to the in-plane vibration of Mo and S atoms and out-of-plane vibration of S atoms, respectively, confirming good crystalline quality growth of MoS_2. The separation between the two peaks (Δk) can be used to identify the layer number of MoS_2. At 650 and 700 °C, Δk is found to be ~ 20.3 cm^{-1} and ~ 20.0 $cm^{-1,}$ respectively, which confirms that the thickness of the MoS_2 flake corresponds to monolayer.[15] On the other hand, at 750 and 800 °C, Δk is ~ 22.7 cm^{-1} and ~26.5 cm^{-1}, indicating the formation of trilayer and multilayer MoS_2. These results are consistent with the AFM analyses discussed earlier. The concentration of the MoO_3 and S precursors on the surface of the substrate depends on the evaporation and diffusion rates of the precursors. However, these rates are significantly dependent on temperature. Thus, as a result, with different growth temperatures, there is a difference in the concentration of the precursor on the substrate. At lower growth temperatures (in the range 650 °C to 700°C), a relatively small amount of MoO_{3-x} clusters are transported to the

surface of the substrate. Thus, during the initial growth stage, the MoO_{3-x} clusters are easily transformed into MoS_{2-x} clusters, resulting in the formation of the 2D MoS_2 nucleus on the substrate, which subsequently forms monolayer/bilayer MoS_2 flakes.[23] On the other hand, at higher growth temperatures (750 °C and 800 °C), a larger amount of MoO_{3-x} clusters are deposited on the substrate, followed by sulfurization of the MoO_3 clusters, which quickly fuse into island-like $MoO_{3-x}S_y$ nanoparticles. These nanoparticles act as nucleation sites and favor few-layer growth instead of monolayer growth. As the growth progresses, the nanoparticles are further sulphurized and form island-like multilayer MoS_2 nuclei, while the edge growth of a nucleus forms few-layer MoS_2.[23] These results are consistent with the results of the AFM analysis.

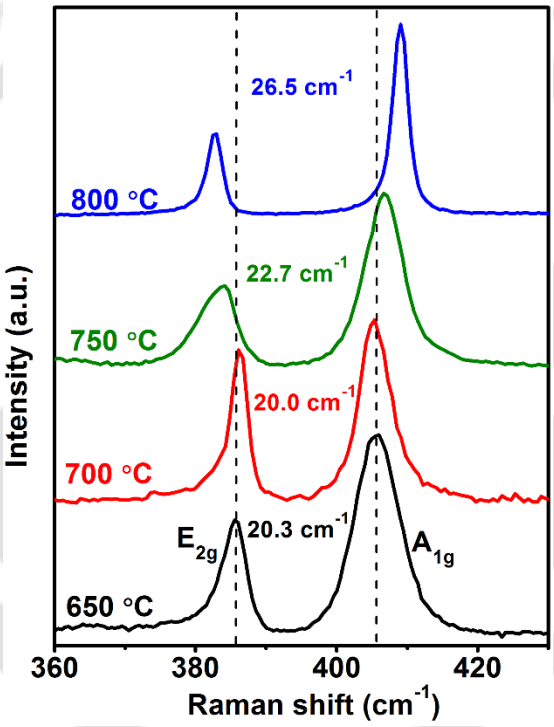

Fig. 2.9. Raman spectra of the CVD-grown MoS_2 flakes at different growth temperatures.

Fig. 2.10. displays the Raman spectra of the CVD-grown MoS_2 flakes with different carrier gas flux. At 10 sccm gas flux, presence of the characteristic Raman modes E_{2g} and A_{1g} confirms MoS_2 growth, while at very low carrier gas flux ≤ 5 sccm, there is an absence of both the Raman peaks as there is no formation of MoS_2. For the 10 sccm case, the frequency difference (Δk) between the Raman modes is ~20.2 cm^{-1}, which corresponds to monolayer MoS_2 growth. Note that monolayer MoS_2 growth was found on the entire substrate. At a higher gas flow rate (30 sccm), the Δk value is ~ 21.4 cm^{-1}, which corresponds to bilayer MoS_2. Note that monolayer MoS2 growth was found

on the entire substrate. At a higher gas flow rate (30 sccm), the Δk value is ~ 21.4 cm^{-1}, which corresponds to bilayer MoS_2. We also observed the presence of both monolayer and bilayer MoS_2 throughout the substrate. The high flow rate can promote the mass transfer process, which is understood by the increase in the layer number. In addition, this condition will create instability, and therefore there is not enough time for the transport of the atoms to the right lattice location to attain minimum surface free energy, and thus this will lead to an increase in the probability of defect formation.[24] At very high Ar gas flux ≥ 50 sccm, Δk value is ~ 21.3 cm^{-1}, which is attributed to bilayer MoS_2. However, we observe a decrease in the number of MoS_2 flakes with an increase in the Ar gas flow rate. This is due to a decrease in the concentration of the vapor precursors (MoO_3 and S) at the substrate owing to the high gas flow rate flushing out the precursors' molecules from the substrate.

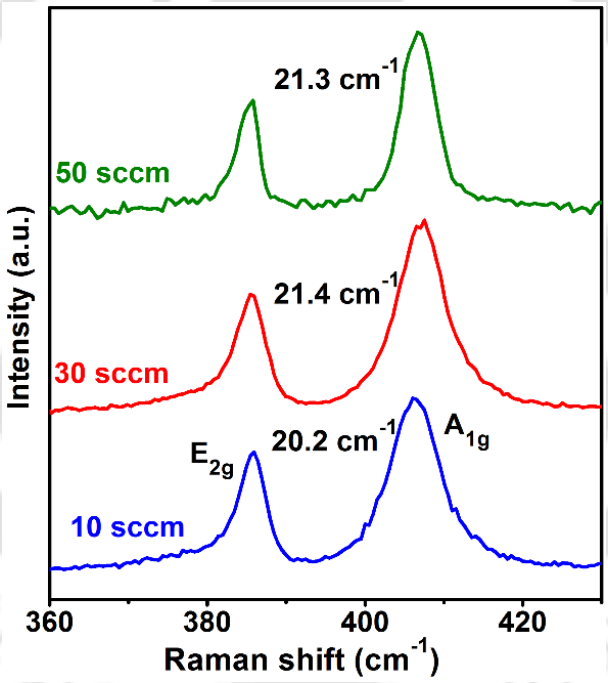

Fig. 2.10. Raman spectra of the CVD-grown MoS_2 flakes with different carrier gas flux.

2.3. Large area CVD growth of monolayer MoS_2

2.3.1. Introduction

Synthesis of large-area monolayer MoS_2 films have attracted significant importance due to their remarkable electrical and optical properties, leading to a wide range of applications. In the previous section, we have successfully grown monolayer MoS_2 domains and have an understanding of the important experimental parameters for the synthesis of high-quality monolayer MoS_2. The next

step is to make modifications in the CVD method for the growth of high quality, large-scale continuous monolayer MoS_2 films. Previous reports have achieved large area MoS_2 growth by sulfurization of ammonium tetrathiomolybdate films[25] or either MoO_3[26, 27] or $MoCl_5$[28]. However, these methods require a substantial level of complexity in the preparation of the precursor, or the growth is carried out at a very high temperature (~ 1000 °C). Thus, a cost-effective and straightforward method of growth is very much desired, but it poses quite a challenge.

In this section, we present the CVD growth of large-area continuous MoS_2 film on different substrates. The film covers an area of a few mm^2. In this method, a specially designed quartz mask with a circular opening is used, on top of which a substrate is placed. Large area continuous monolayer MoS_2 film is formed in the region covered by the mask. The synthesized film show homogeneity of the monolayer MoS_2 film throughout the region covered by the mask.

2.3.2. Experimental Details

Monolayer MoS_2 film was synthesized on different substrates (Si, SiO_2, Quartz and Sapphire) by the CVD method using a two-zone horizontal muffle furnace. Commercially procured high-purity MoO_3 (99.5%, Sigma-Aldrich) and sulfur powder (99.95%, Sigma-Aldrich) were used as precursors for the CVD growth of MoS_2 in a 2-inch quartz tube-based horizontal muffle furnace. High-purity argon (Ar) gas was used as the carrier gas. Note that both S (200 mg) and MoO_3 (15 mg) precursors were separately loaded in two quartz boats and were placed inside the quartz tube at the center of their respective zones for the CVD growth of MoS_2. The substrates were placed face down on top of the quartz mask with a circular opening and then placed on the boat containing MoO_3, as shown in **Fig. 2.11(a).** The distance between the sulfur boat and the MoO_3 boat was maintained at 15 cm. The quartz tube inside the furnace was purged with Ar gas at 300 sccm for 30 min before the growth to remove the surface-adsorbed impurities, followed by heating up to 150 °C for another 30 min. Subsequently, the flow rate was reduced to 10 sccm, and the temperature was ramped at a rate of 15 °C/min up to 700 °C and was maintained for 5 min (see **Fig. 2.11(b)**). At this stage, the temperature at the sulfur boat position reached 150 °C. The furnace was then allowed to cool until the temperature reached to room temperature. Interestingly, monolayer MoS_2 film was observed to be deposited only on the portions of the substrate which were covered by the quartz mask. The unmasked regions of the substrate were found to be

deposited with few-layer and multilayer MoS_2. We observed that in all the substrates, large-area monolayer MoS_2 film was grown.

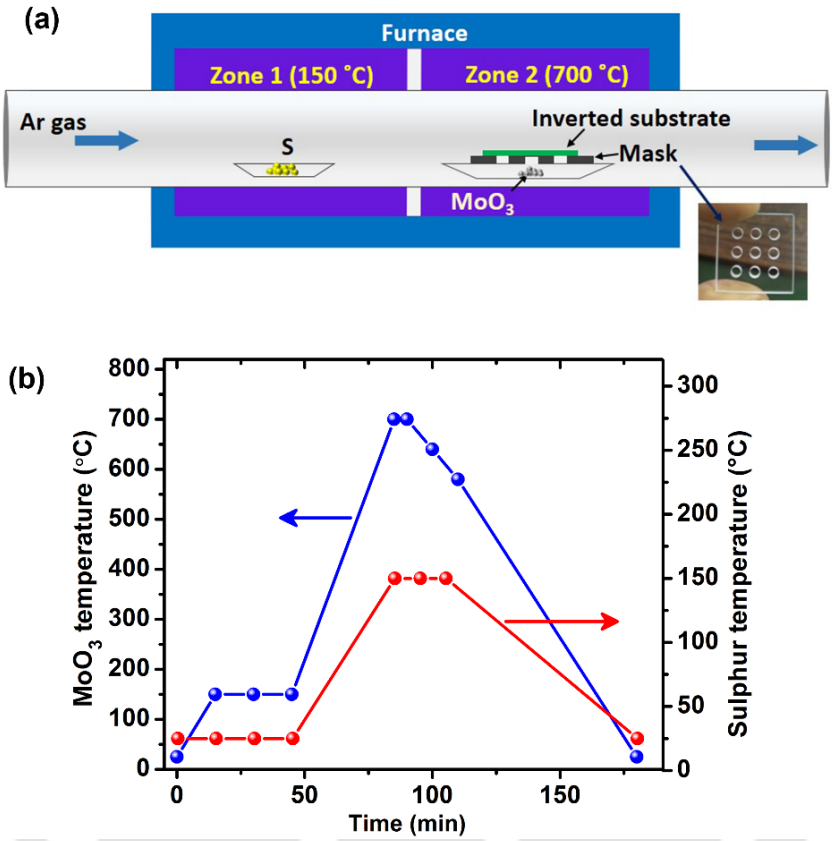

Fig. 2.11. (a) Schematic of the chemical vapor deposition (CVD) setup for the fabrication of monolayer MoS_2 on various substrates. (b) Variation of temperature as a function of time at the MoO_3 boat/substrate and the sulfur boat positions during the CVD process.

2.3.3. Results and Discussion

2.3.3.1. Morphology Studies

Fig. 2.12(a) shows the optical microscope image of monolayer MoS_2 film grown on the sapphire substrate. We observed that the triangular-shaped MoS_2 flakes are formed towards the edge of the substrate and these flakes merge to create a sizeable continuous monolayer film that covers an area of a few mm^2, (See **Fig. 2.12 (a)**). The homogenous color contrast over the entire film indicates layer uniformity.

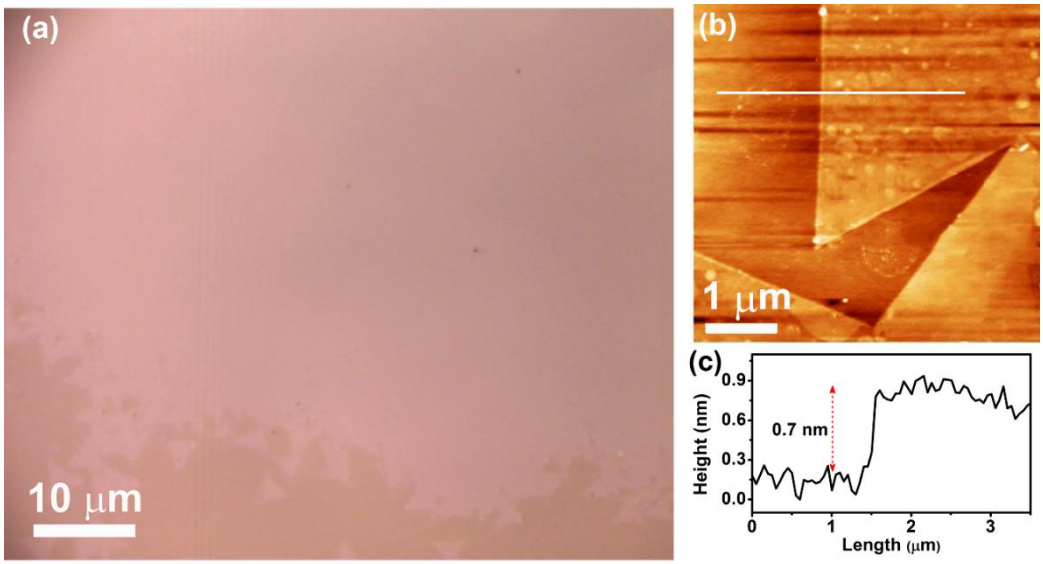

Fig. 2.12. (a) Optical microscope image of large-area monolayer MoS_2 grown on the sapphire substrate. (b) AFM image of triangular-shaped monolayer MoS_2 grown on the sapphire substrate, and (c) AFM height profile is taken along the white line in (b) showing a step height of ~0.7 nm confirming the monolayer MoS_2 growth.

Fig. 2.12 (b) displays the AFM image of the CVD grown triangular-shaped monolayer MoS_2. The triangular-shaped MoS_2 flakes show a tendency to interconnect with each other rather than overlap, and hence they grow to form a continuous film with good uniformity. Furthermore, the AFM height profile taken along the white line in **Fig. 2.12 (b)** reveals a thickness of ~0.7 nm, which confirms the growth of monolayer MoS_2.

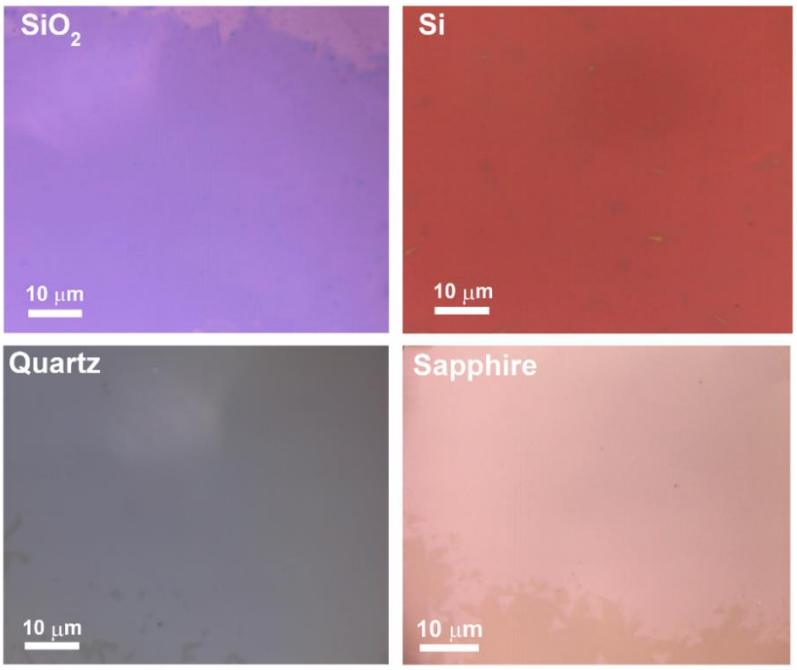

Fig. 2.13. Optical microscope image of large-area MoS_2 film grown on different substrates.

We observed that for all the different substrates (i.e., Si, SiO_2, quartz and sapphire), the MoS_2 film is found to be monolayer, as shown in **Fig. 2.13.**

2.3.3.2. Raman Analysis

To ascertain that the films in **Fig. 2.13** are monolayer MoS_2, we have characterized these samples using micro-Raman spectroscopy. **Fig. 2.14 (a)** shows a digital photograph of the MoS_2 layer grown on a sapphire substrate. The dark circular region is the exposed area of the substrate to the MoO_3 and S source, while the light greenish part corresponds to the masked/ covered regions. **Fig. 2.14(b)** shows an optical microscope image of MoS_2 film at the marked region.

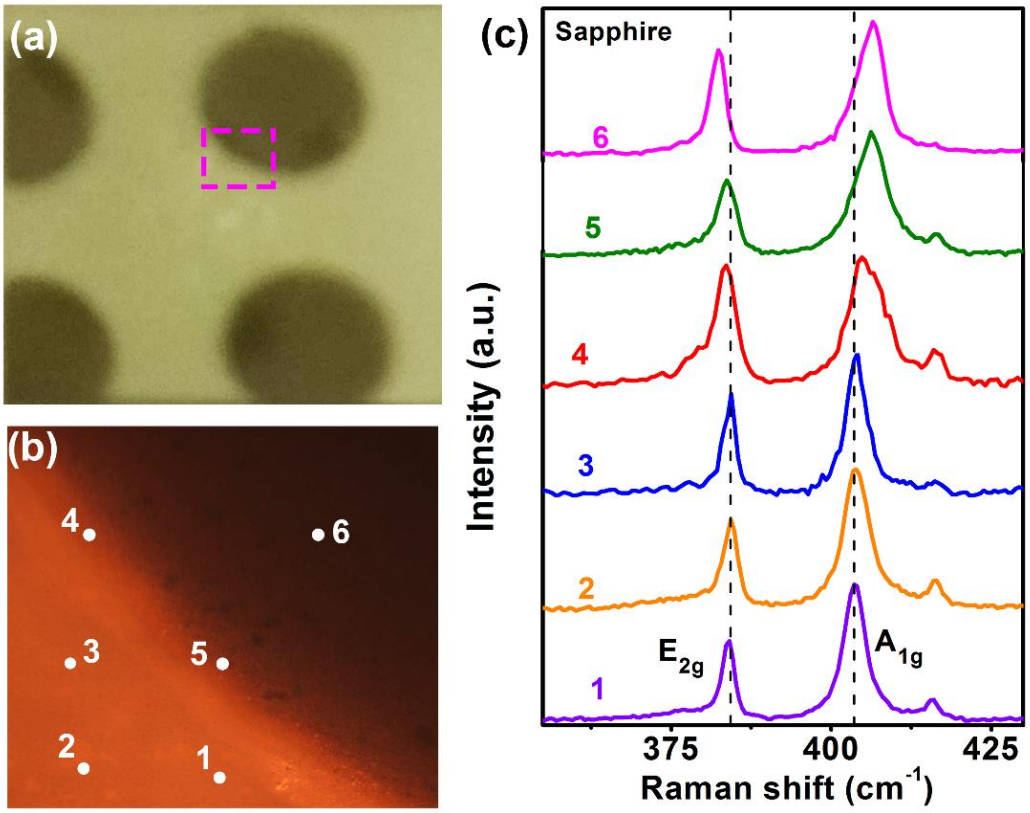

Fig. 2.14. (a) Digital photographs of MoS_2 layer grown on sapphire substrate by the CVD method. (b) The optical microscope images of MoS_2 grown on Sapphire substrate, at the marked region of (a). (c) The Raman spectra of MoS_2 recorded at different positions shown in (b). The vertical dashed line is drawn to indicate the shift of the Raman peaks for various locations.

To quantitatively determine the uniformity of the MoS_2 film, position-dependent Raman studies at different locations on a single continuous film was carried out, as shown in **Fig. 2.14(b).** We observe the presence of both E_{2g} and A_{1g} Raman modes, respectively, which are characteristics of MoS_2. The frequency difference between the Raman modes (Δk) outside the dark circular region

confirms the growth of only monolayer MoS_2, while the dark region appears to be few/multi-layered, (see **Table 2.4).** The full width at half-maxima (FWHM) of the E_{2g} peak is ~ 2.6 cm^{-1}, which is close to that of exfoliated monolayer MoS_2,[28], suggesting good crystalline quality of the CVD grown monolayer MoS_2 film. Therefore, this observation verifies that the MoS_2 film is a continuous monolayer film. Furthermore, we have observed similar results for the films grown on other substrates (See **Fig. 2.15(a)**). The Δk values is found to be 20.0 ± 0.5 cm^{-1} for the MoS_2 film on the different substrates, as tabulated in **Table 2.5**. However, the E_{2g} and A_{1g} peak positions vary from substrate to substrate, as shown in **Fig. 2.15(b).** This might be due to the presence of charged impurities and the built-in strain at the interface between the MoS_2 film and the substrate.[24, 29]

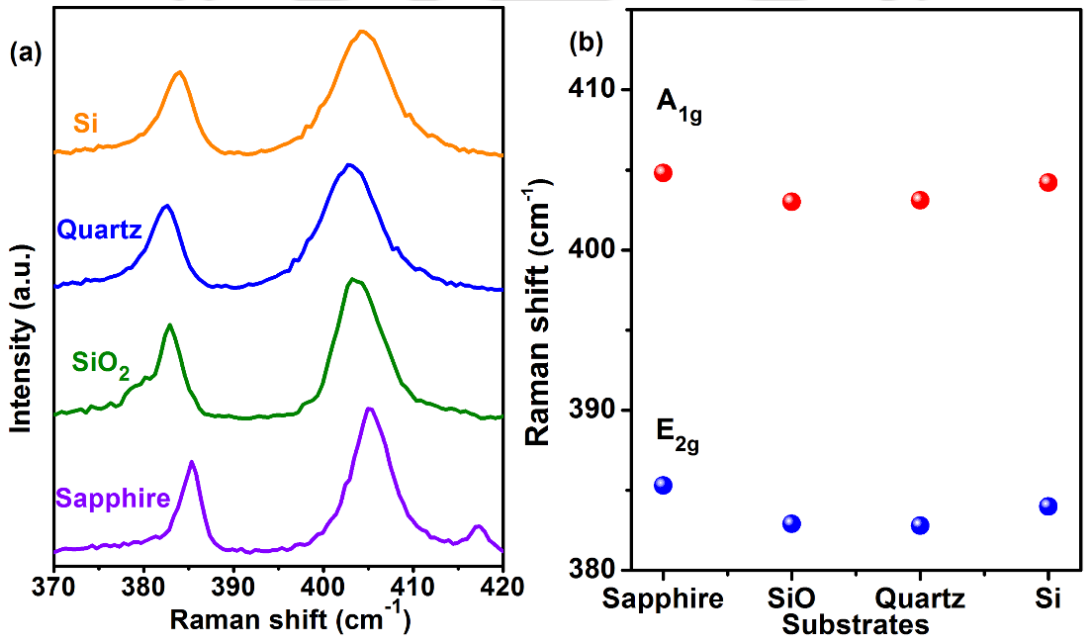

Fig. 2.15. (a) Raman spectra for monolayer MoS_2 grown on various substrates. (b) E_{2g} and A_{1g} Raman peak positions for different substrates.

Table 2.4: *Summary of the Raman peak position, their separation (Δk), and the corresponding layer number for MoS_2 grown on Sapphire substrate at different locations.*

Location in the sample	E_{2g} (cm^{-1})	A_{1g} (cm^{-1})	Δk (cm^{-1})	No. of layers
1	384.1	403.6	19.5	monolayer
2	384.3	403.9	19.6	
3	384.3	404.1	19.8	
4	383.6	404.7	21.1	bilayer
5	383.6	406.2	22.6	trilayer
6	382.1	406.7	24.6	multi-layer

Table 2.5: *Summary of the E_{2g} and A_{1g} Raman modes for the different substrates. The peak separation (Δk ~20 cm^{-1}) signifies the growth of monolayer MoS_2.*

Substrate	E_{2g} (cm^{-1})	A_{1g} (cm^{-1})	Δk (cm^{-1})
Sapphire	384.3	403.8	19.5
SiO_2	385.9	406	20.1
Quartz	383.8	404.1	20.3
Si	384	404.2	20.2

2.3.3.3. Photoluminescence Study

To confirm the large-area growth of monolayer MoS_2 on the sapphire substrate, position-dependent photoluminescence (PL) studies was carried out for the same spot for which the Raman spectra was recorded earlier. **Fig. 2.16(a)** shows a digital photograph of the MoS_2 layer grown on the sapphire substrate and **Fig. 2.16(b)** shows an optical microscope image of MoS_2 at the marked regions**.** The corresponding PL spectra for each locations are shown in **Fig. 2.16(c).** From the Raman analysis, positions 1 to 3 correspond to monolayer MoS_2 growth, while positions 4, 5, and 6 correspond to the bilayer, tri-layer, and multi-layer MoS_2 growth. In **Fig. 2.16(c),** the monolayer PL spectra (positions 1 to 3) exhibit two excitonic peaks at ~623 nm and ~665 nm and can be correlated to the B and the A excitons of MoS_2, respectively.[28] The A exciton peak is derived from the direct bandgap of MoS_2, and B exciton peak arises from the direct gap transition between the

minima of the conduction band and the lower-level valence-band maxima that is created by strong valence-band spin-orbit splitting at the K point[30] For the position 6 (multilayer MoS_2), the PL peak is observed at ~685.7 nm. We also observed a blue shift ~ 20.7 nm in the PL peak position of the monolayer with respect to the multilayer MoS_2. **Fig. 2.16(c)** shows the comparative PL spectra recorded at different positions of the MoS_2 grown on the Sapphire substrate. The PL intensity of the monolayer MoS_2 was observed to be ~ 37.6 times greater than that of multilayer MoS_2. This enhancement in the PL peak intensity and the blue shift in the PL peak position is due to the indirect to direct bandgap transition from bulk to monolayer, consistent with the previous reports.[30] We also observed that, the PL intensity and peak position are almost the same for locations 1 to 3, which is due to the monolayer MoS_2 growth (see inset of **Fig. 2.16(c)**). Thus, the recorded PL spectra at different locations confirm the growth of monolayer MoS_2 outside the dark circular region, while it is multilayer MoS_2 in the dark region.

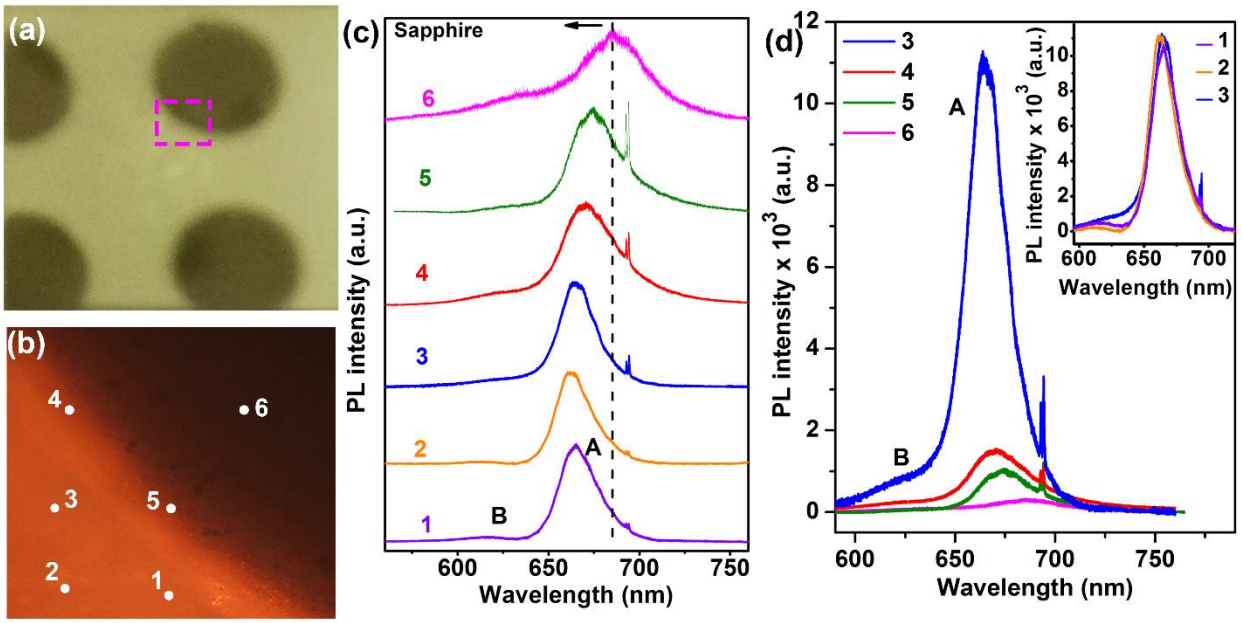

Fig. 2.16. (a) Digital photographs of MoS_2 layer grown on sapphire by the CVD method (b) The optical microscope images of MoS_2 grown on Sapphire substrate, at the marked region of (a). (c) The PL spectra of MoS_2 recorded at different positions shown in (b). The vertical dashed line is drawn to indicate the shift of the Raman peaks for the different locations. (c) Comparative PL spectra of MoS_2 recorded at the different positions of the MoS_2 sample. Inset shows the comparative PL spectra for positions 1 to 3.

Next, we have measured the PL spectra for monolayer MoS_2 on the different substrates. We observe a slight shift in the PL peak positions and the difference in the PL intensity from substrate to substrate, as shown in **Fig. 2.17**. To have a better understanding of the origin of the PL emission, we have deconvoluted each spectrum of the MoS_2 sample grown on different substrates by using

four Gaussian peaks (see **Fig. 2.17(a-d)**). The summary of the peak positions in each sample is listed in **Table 2.6**. Two characteristic PL peaks, B and A^0 centered at ~630 nm and ~660 nm, are ascribed to B exciton and neutral exciton, respectively.[30] The A^0 exciton peak is derived from the direct bandgap of MoS_2, and B exciton peak arises from the direct gap transition between the minima of the conduction band and the lower-level valence-band maxima that is created by strong valence-band spin-orbit splitting at the K point.[30] We also observed the presence of the A^- exciton peak, which is understood to arise from the trions, i.e., negatively charged excitons. The trion emission is caused by light n-type doping of MoS_2 from the substrate or from charged impurities in the CVD grown MoS_2 .[31] In addition, we observed the presence of peak X in all the samples at ~696 nm, and this peak is attributed to the radiative recombination of bound excitons.[31]

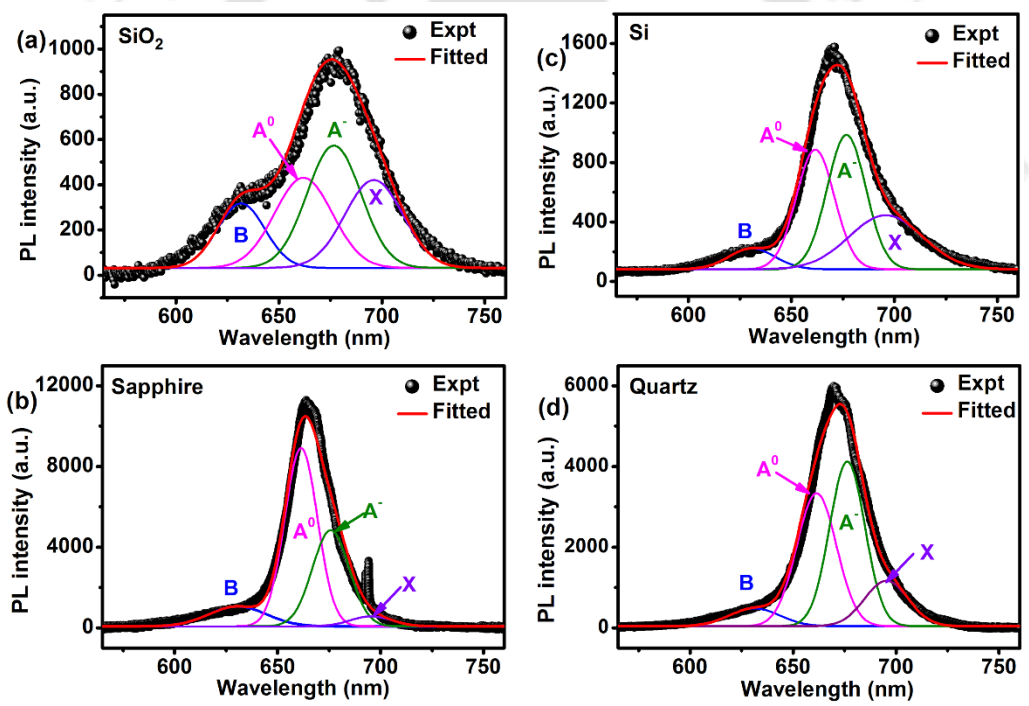

Fig. 2.17: Gaussian deconvolution of the PL spectra for monolayer MoS_2 grown on (a) SiO_2, (b) Si, (c) Sapphire, and (d) Quartz substrates, respectively.

Monolayer MoS_2 grown on SiO_2 substrate shows the lowest PL intensity, while that grown on a sapphire substrate shows the highest intensity. Additionally, there is a blue shift in the PL peak position for Si, Quartz, and Sapphire as compared to SiO_2. Interestingly, the spectral weight of A^0 exciton peak is observed to be the highest (~54.2%) for the Sapphire substrate, while it is the lowest (~26.0 %) in SiO_2 case, and the corresponding spectral weights of the A^- is observed to be ~30.0% and ~ 34%, respectively. The decrease in the population of A^- and an increase in the

population of the neutral excition A^0 on Sapphire leads to the higher PL intensity as well as the blue shift in the PL peak position.[32] We also observed that the spectral weight of the defect peak X is found to be highest in the case of MoS_2 grown on SiO_2 substrate, which is due to the presence of higher defect states in the samples.

Table 2.6: *Summary of the Gaussian deconvoluted PL spectra for monolayer MoS_2 grown on the different substrates.*

	Relative weightage of PL peaks			
Substrate	**B-exciton (B) (%)**	**A-exciton (A) (%)**	**Trion (A^-) (%)**	**Bound exciton (X) (%)**
SiO_2	15.2	26.0	33.2	25.6
Si	6.5	31.2	35.4	26.9
Quartz	6.4	37.8	41.5	14.3
Sapphire	11.2	54.2	30.0	4.6

2.3.3.4. Growth mechanism of monolayer MoS_2 over various substrates

Following the previous report by Mohapatra et al.[33] large-area monolayer MoS_2 film was grown on different substrates (Si, SiO_2, quartz, and Sapphire). Monolayer MoS_2 was grown mainly on the regions covered by a quartz mask. During the early phase of the growth, the vapor pressure of MoO_3 is much higher than that of Sulphur at the position of the substrate as the substrate is placed just above the MoO_3 source and Sulphur is situated at a distance of 15 cm away from the substrate, (see **Fig. 2.18(a, b)**). Therefore, at this stage, MoO_3 molecules are filled in the cavity formed between the substrate and the quartz mask, and these molecules adhere to the surface of the substrate, as shown in **Fig. 2.18(a).** As the temperature increases, the vapor pressure of Sulphur will also increase. At some point, the vapor pressure of Sulphur exceeds that of MoO_3, and as a result, the MoO_3 molecules from the cavity are flushed out. Then, the Sulphur vapor and the MoO_3 molecules react on the surface of the substrate, which further leads to the growth of monolayer MoS_2. When the vapor pressure of Sulphur is much higher compared to that of MoO_3, the reaction stops, and consequently, the remaining MoO_3 molecules from the cavity are flushed out (See **Fig. 2.18(c)**. It is to be noted that, multilayer MoS_2 is grown at the exposed region of the substrate. As the substrate is placed just above the MoO_3 source, the vapor pressure of MoO_3 is very high, and thus at the exposed region, few-layer/multilayer MoS_2 is formed (See **Fig. 2.18(c)**

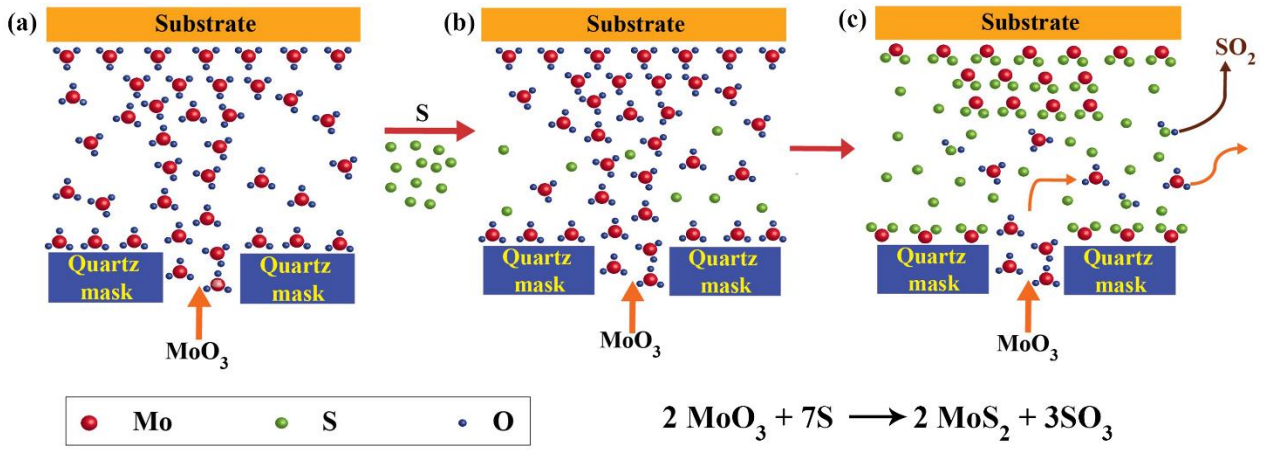

Fig. 2.18. (a-c) Schematic illustration showing the different stages of the growth process of monolayer MoS_2 film by the CVD method.

2.3.4. Conclusion

In summary, this chapter demonstrated firstly, the growth of luminescent monolayer and bilayer MoS_2 dots with controlled size and shape by a low temperature (510-560˚C) CVD technique. The Raman spectra of the samples indicated the growth of the crystalline MoS_2 dots array. Position dependent Raman profiles showed spatial non-uniformity in the layer thickness across the dots. We believe that the low-temperature growth of luminescent MoS_2 dots array will stimulate further studies on its growth on the flexible substrate and its diverse range of applications in optoelectronics, bioimaging, and related areas. Secondly, we have demonstrated the growth of high crystal quality monolayer MoS_2 by making a few modifications in the CVD technique. Several growth parameters such as the carrier gas, precursors and growth temperature were modified in order to understand the growth behaviors of MoS_2. The precursors (MoO_3 and S) were placed at different temperature zone in a two-zoned furnace, which gave independent heating profiles and offered better flexibility in the growth technique. The influence of the change in the growth temperature and the variation of the flow rate of the carrier gas (Ar gas) were also investigated to understand the effect on MoS_2 growth. Thus, our study illustrates a detailed understanding of the nucleation mechanisms for controlled growth of monolayer MoS_2. Finally, we have demonstrated a simple approach to grow high quality, large area continuous monolayer MoS_2 film on different substrates by CVD growth technique. This is achieved by the use of a specially designed quartz mask between the MoO_3 source and the substrate. We have systematically studied the Raman and PL properties of the as-grown MoS_2 on the different substrates. The substrates have a significant

effect on the PL peak intensity and emission wavelength. Our results indicate that the large-area monolayer MoS_2 grown on sapphire substrate contains fewer defects than that of the other substrates. This synthesis method opens up possibility of the large production of high quality continuous MoS_2 films with control of their thicknesses, which can further be applied in the fabrication of optoelectronic devices.

References

1. Butler, S. Z.; Hollen, S. M.; Cao, L.; Cui, Y.; Gupta, J. A.; Gutiérrez, H. R.; Heinz, T. F.; Hong, S. S.; Huang, J.; Ismach, A. F.; Johnston-Halperin, E.; Kuno, M.; Plashnitsa, V. V.; Robinson, R. D.; Ruoff, R. S.; Salahuddin, S.; Shan, J.; Shi, L.; Spencer, M. G.; Terrones, M.; Windl, W.; Goldberger, J. E. *ACS Nano* **2013,** 7, (4), 2898-2926.
2. Wang, Q. H.; Kalantar-Zadeh, K.; Kis, A.; Coleman, J. N.; Strano, M. S. *Nature Nanotechnology* **2012,** 7, (11), 699-712.
3. Radisavljevic, B.; Radenovic, A.; Brivio, J.; Giacometti, V.; Kis, A. *Nat. Nanotechnol.* **2011,** 6, 147.
4. Xu, S.; Li, D.; Wu, P. *Advanced Functional Materials* **2015,** 25, (7), 1127-1136.
5. Paul, K. K.; Mawlong, L. P. L.; Giri, P. K. *ACS Applied Materials & Interfaces* **2018,** 10, (49), 42812-42825.
6. Shi, J.; Ma, D.; Han, G.-F.; Zhang, Y.; Ji, Q.; Gao, T.; Sun, J.; Song, X.; Li, C.; Zhang, Y.; Lang, X.-Y.; Zhang, Y.; Liu, Z. *ACS Nano* **2014,** 8, (10), 10196-10204.
7. Zhao, L.; Chen, K.; Yang, F.; Zheng, M.; Guo, J.; Gu, G.; Zhang, B.; Qin, H.; Cheng, G.; Du, Z. *Nano Energy* **2019,** 62, 38-45.
8. Chen, K.; Wan, X.; Xie, W.; Wen, J.; Kang, Z.; Zeng, X.; Chen, H.; Xu, J. *Advanced Materials* **2015,** 27, (41), 6431-6437.
9. Ghosh, R.; Kim, J.-S.; Roy, A.; Chou, H.; Vu, M.; Banerjee, S. K.; Akinwande, D. *Journal of Materials Research* **2016,** 31, (7), 917-922.
10. Jeon, J.; Jang, S. K.; Jeon, S. M.; Yoo, G.; Jang, Y. H.; Park, J.-H.; Lee, S. *Nanoscale* **2015,** 7, (5), 1688-1695.
11. Rao, C. N. R.; Nag, A. *European Journal of Inorganic Chemistry* **2010,** 2010, (27), 4244-4250.
12. Li, H.; Yin, Z.; He, Q.; Li, H.; Huang, X.; Lu, G.; Fam, D. W. H.; Tok, A. I. Y.; Zhang, Q.; Zhang, H. *Small* **2012,** 8, (1), 63-67.
13. Gong, C.; Huang, C.; Miller, J.; Cheng, L.; Hao, Y.; Cobden, D.; Kim, J.; Ruoff, R. S.; Wallace, R. M.; Cho, K.; Xu, X.; Chabal, Y. J. *ACS Nano* **2013,** 7, (12), 11350-11357.
14. Tao, J.; Chai, J.; Lu, X.; Wong, L. M.; Wong, T. I.; Pan, J.; Xiong, Q.; Chi, D.; Wang, S. *Nanoscale* **2015,** 7, (6), 2497-2503.
15. Li, H.; Zhang, Q.; Yap, C. C. R.; Tay, B. K.; Edwin, T. H. T.; Olivier, A.; Baillargeat, D. *Adv. Funct. Mater.* **2012,** 22, (7), 1385-1390.
16. Hui, Y. Y.; Liu, X.; Jie, W.; Chan, N. Y.; Hao, J.; Hsu, Y.-T.; Li, L.-J.; Guo, W.; Lau, S. P. *ACS Nano* **2013,** 7, (8), 7126-7131.
17. Conley, H. J.; Wang, B.; Ziegler, J. I.; Haglund, R. F.; Pantelides, S. T.; Bolotin, K. I. *Nano Letters* **2013,** 13, (8), 3626-3630.
18. Dieterle, M.; Weinberg, G.; Mestl, G. *Physical Chemistry Chemical Physics* **2002,** 4, (5), 812-821.
19. Kumar, P.; Viswanath, B. *Crystal Growth & Design* **2016,** 16, (12), 7145-7154.
20. Ubaldini, A.; Jacimovic, J.; Ubrig, N.; Giannini, E. *Crystal Growth & Design* **2013,** 13, (10), 4453-4459.

21. Han, G. H.; Kybert, N. J.; Naylor, C. H.; Lee, B. S.; Ping, J.; Park, J. H.; Kang, J.; Lee, S. Y.; Lee, Y. H.; Agarwal, R.; Johnson, A. T. C. *Nature Communications* **2015,** 6, (1), 6128.
22. Shu, H.; Chen, X.; Ding, F. *Chemical Science* **2014,** 5, (12), 4639-4645.
23. Zhou, D.; Shu, H.; Hu, C.; Jiang, L.; Liang, P.; Chen, X. *Crystal Growth & Design* **2018,** 18, (2), 1012-1019.
24. Ghatak, S.; Pal, A. N.; Ghosh, A. *ACS Nano* **2011,** 5, (10), 7707-7712.
25. Liu, K.-K.; Zhang, W.; Lee, Y.-H.; Lin, Y.-C.; Chang, M.-T.; Su, C.-Y.; Chang, C.-S.; Li, H.; Shi, Y.; Zhang, H.; Lai, C.-S.; Li, L.-J. *Nano Letters* **2012,** 12, (3), 1538-1544.
26. Lee, Y.-H.; Zhang, X.-Q.; Zhang, W.; Chang, M.-T.; Lin, C.-T.; Chang, K.-D.; Yu, Y.-C.; Wang, J. T.-W.; Chang, C.-S.; Li, L.-J.; Lin, T.-W. *Advanced Materials* **2012,** 24, (17), 2320-2325.
27. Lin, Y.-C.; Zhang, W.; Huang, J.-K.; Liu, K.-K.; Lee, Y.-H.; Liang, C.-T.; Chu, C.-W.; Li, L.-J. *Nanoscale* **2012,** 4, (20), 6637-6641.
28. Yu, Y.; Li, C.; Liu, Y.; Su, L.; Zhang, Y.; Cao, L. *Scientific Reports* **2013,** 3, (1), 1866.
29. Chakraborty, B.; Bera, A.; Muthu, D. V. S.; Bhowmick, S.; Waghmare, U. V.; Sood, A. K. *Phys. Rev. B* **2012,** 85, (16), 161403.
30. Splendiani, A.; Sun, L.; Zhang, Y.; Li, T.; Kim, J.; Chim, C.-Y.; Galli, G.; Wang, F. *Nano Lett.* **2010,** 10, (4), 1271-1275.
31. Nan, H.; Wang, Z.; Wang, W.; Liang, Z.; Lu, Y.; Chen, Q.; He, D.; Tan, P.; Miao, F.; Wang, X.; Wang, J.; Ni, Z. *ACS Nano* **2014,** 8, (6), 5738-5745.
32. Buscema, M.; Steele, G. A.; van der Zant, H. S. J.; Castellanos-Gomez, A. *Nano Research* **2014,** 7, (4), 561-571.
33. Mohapatra, P. K.; Deb, S.; Singh, B. P.; Vasa, P.; Dhar, S. *Appl. Phys. Lett.* **2016,** 108, (4), 042101.

Chapter 3

Direct CVD Growth of Monolayer MoS_2 on TiO_2 Nanorods and Evidence for Doping Induced Strong Photoluminescence Enhancement

This chapter presents a simple one-step direct synthesis process of 1L-MoS_2 film by a CVD method over hydrothermally prepared TiO_2 nanorods (NRs). The photoluminescence (PL) intensity of the 1L-MoS_2@TiO_2 heterostructure (HS) is dramatically high as compared to that of the bare 1L-MoS_2. This enhancement is understood as a consequence of p-doping and the conversion of trions to neutral excitons. PL and Raman spectra showed the p-doping effect that occurred through the charge transfer between the 1L-MoS_2 and TiO_2 NRs. For further verification about the p-doping in the MoS_2 lattice, a mild oxygen plasma was used to treat the samples, which confirms the doping through the oxygen bonding and charge transfer between MoS_2 and TiO_2 interface. This study offers a novel route to grow a core-shell HS of 1L-MoS_2 and TiO_2 NRs for strong enhancement of PL promising future practical applications.

3.1. Introduction

Among semiconducting transition metal dichalcogenides (TMDs), monolayer molybdenum disulfide (1L-MoS_2) has drawn intense research attention due to its direct bandgap of ~1.90 eV,[1-2] which leads to strong PL emission and strongly enhanced optoelectronic response in its monolayer form. To control the optical properties of 1L-MoS_2, some of the most effective approaches are tuning the carrier density,[3-5] and by forming vertical heterostructures (HSs) with other materials (plasmonic, TMDs, etc.).[6-7] 1L-MoS_2 is usually intrinsically n-type and further n-doping leads to the quenching of PL, while p-doping results in the PL enhancement.[3, 5-6, 8] With the proper utilization of the various intrinsic structural defects, such as vacancies, dislocations, grain boundaries, and edges in both pristine/as-grown MoS_2,[9-10] tuning and improvement of the optical properties of 1L-MoS_2 is highly desirable. Furthermore, the MoS_2 based nano-heterostructures with large bandgap (UV active) semiconductors, e.g. ZnO and TiO_2, are widely reported to form type-II heterojunction at their interfaces, facilitating the charge separation and reduced PL emission. In particular, MoS_2/TiO_2 based nanocomposites show great potential in the areas of both photocatalysis and rechargeable lithium/sodium ion batteries due to their superior

catalytic properties. In addition to the low-cost, abundance, and high chemical stability of both MoS_2 and TiO_2, MoS_2/TiO_2 composites also show complementary advantages. Thus, these type-II HSs exhibit enhanced photocatalysis for energy and environmental applications.[11-13] However, most of these studies have reported on the growth of multilayer MoS_2 on TiO_2, both grown by typical wet chemical methods. In these kinds of HSs, the PL emission is very low because of the indirect bandgap of the multilayer MoS_2. Kim et al.[14] have recently grown ZnO thin-film-based HS with 1L-MoS_2 and demonstrated a PL enhancement up to ~17 times over the pristine 1L-MoS_2. This enhancement was explained based on the conversion of trions to neutral excitons because of the charge exchanges through the interfaces, which induces p-doping in the MoS_2 lattice. They prepared ~50 nm thick ZnO film on the quartz substrate by the sol−gel method and made the heterojunction with the chemical vapor deposition (CVD)-grown 1L-MoS_2 film after transferring it through the typical wet transfer method. However, the transfer method may introduce additional defects and impurities in the 2D material, which is often not desirable. In this chapter, we show a simple one-step direct synthesis process of the 1L-MoS_2 film by a CVD method over the hydrothermally prepared TiO_2 nanorods (NRs). The PL intensity of 1L-MoS_2 is dramatically enhanced after the formation of the HS. This enhancement is explained in terms of p-doping of 1L-MoS_2 layer and the conversion of trions to neutral excitons.

3.2. Experimental Details

3.2.1. Sample Preparation

3.2.1.1. Preparation of vertically aligned TiO_2 NRs on FTO substrate

In a typical synthesis, 25 mL of Milli-Q water was mixed with 25 mL of concentrated hydrochloric acid (HCl) (36.5% to 38% by weight) to reach a total volume of 50 mL in a Teflon-lined stainless steel autoclave (model: BR100, Bergh of Instrument Co.). The mixture was stirred at ambient conditions for 5 min before the addition of 1 mL of titanium butoxide (97%, Sigma-Aldrich). After stirring for another 5 min, one piece of fluorine-doped tin oxide (FTO) substrate (dimension ~1cm×4cm, surface resistivity ~7 Ω/mm^2, Sigma-Aldrich), ultrasonically cleaned for 60 min in a mixed solution of deionized water, acetone, and 2-propanol with volume ratios of 1:1:1, was placed at an angle against the wall of the Teflon-liner with the conducting side facing down. The hydrothermal synthesis was conducted at 150 °C for 17 hrs in an autoclave. Finally, the autoclave was allowed to cool naturally to room temperature, and the FTO substrate was taken out, rinsed

extensively with deionized water, and allowed to dry in ambient air to get a uniformly coated TiO_2 film on the FTO substrate.

3.2.1.2. Growth of monolayer MoS_2 shell over TiO_2 NRs

1L-MoS_2 were directly grown on the TiO_2 NRs by the CVD process using a two zone furnace. High-purity MoO_3 and S powder were used as precursors and placed inside a 2-inch quartz tube-based horizontal muffle furnace at the center of their respective zones. The hydrothermally grown TiO_2 NRs were then placed face down on top of the quartz mask with a circular opening, which were then put on top of the boat containing MoO_3 precursor. The experiment was carried out at 700 °C for 5 min, in a high purity Ar gas environment. Then, the furnace was then allowed to cool down to room temperature, thus, resulting in the growth of monolayer MoS_2 shell over TiO_2 NRs. Further details of the growth is described in **Chapter 2, Section 2.3.2.** To assess the crystal structure of the heterostructure, micro-Raman analysis was performed.

3.2.3. Characterization Techniques

The crystal structure of the as-grown samples has been obtained from X-ray powder diffraction (XRD) pattern (Rigaku RINT 2500 TTRAX-III, Cu k_α radiation). Crystallinity, number of layers, phase, defects etc. in the as-grown MoS_2, as well as the phase composition and crystallinity of as-synthesized TiO_2 NRs, have been studied by high-resolution micro-Raman spectroscopy (LabRam HR800, Jobin Yvon) with excitation wavelength (λ_{ex}) 488 nm (Ar ion laser). The excitation laser beam (1.5 mW) was focused with a 100X objective lens to a spot size 1 μm, which discards the possibility of laser heating induced damage to the sample. The signal was collected by a CCD in a backscattering geometry sent through a multimode fiber grating of 1800 grooves mm^{-1}. Morphology, size, and microstructural properties of the as-synthesized TiO_2 NRs have been studied using a field emission scanning electron microscope (FESEM) (Sigma, Zeiss). The high magnification surface morphology and structures of the pristine MoS_2 and MoS_2@TiO_2 HS have been studied by a field emission transmission electron microscope (FETEM) (JEOL-JEM 2010 operated at 200 kV). Samples for TEM analysis have been prepared on a carbon-coated Cu grid of 300 mesh (Pacific Grid, USA). UV-Vis diffuse reflectance spectroscopy (DRS) measurements of the samples were recorded using a commercial spectrophotometer (PerkinElmer, UV win Lab). Some of the MoS_2@TiO_2 HS samples were exposed to oxygen plasma at a low power (18W) (Harrick plasma, USA).

3.3. Results and Discussion

3.3.1. Morphology Studies

The typical morphology and microstructural properties of the as-grown TiO_2 NRs were first characterized by FESEM. **Fig. 3.1(a)** depicts the top-view FESEM image of pure rutile TiO_2 NRs with diameter ~ 70-240 nm and lengths up to ~1 μm, while the inset shows its enlarged view, which reveals the nearly vertical growth of NRs with a uniform diameter.

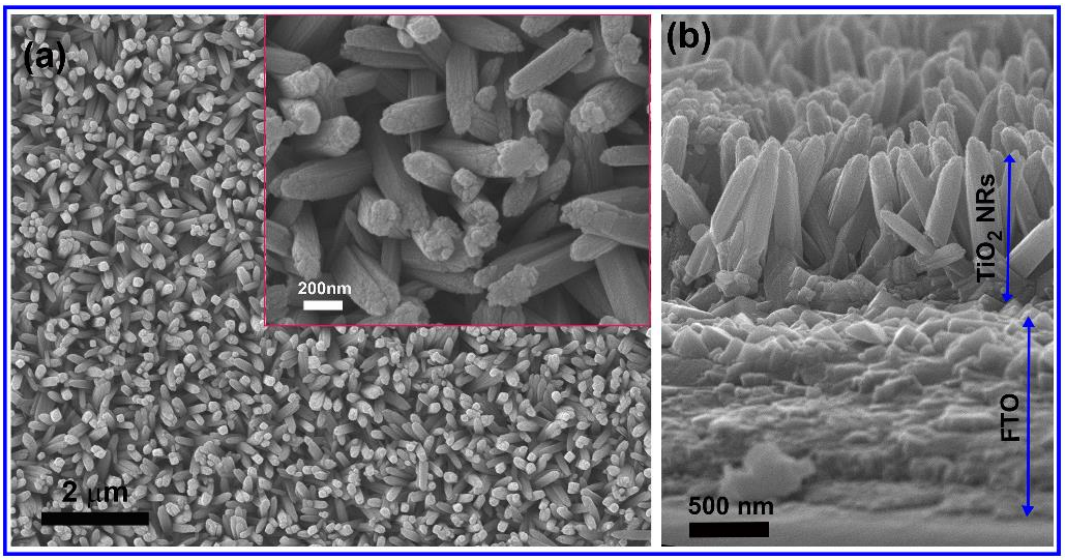

Fig. 3.1: FESEM images of pristine TiO_2 NRs: (a) top view and (b) cross-sectional view. The inset of (a) shows its enlarged view.

Fig. 3.1(b) shows the cross-sectional view of the vertical TiO_2 NRs grown on the FTO substrate. Considering the as-grown TiO_2 NRs as a substrate, large-area monolayer MoS_2 has been grown over TiO_2 NRs via a chemical vapor deposition (CVD) method. The as-grown monolayer MoS_2 shell over the TiO_2 core is atomically thin and thus hard to resolve by the FESEM technique.

FETEM was employed for further characterization of the structures and surface morphologies of the HS. The TiO_2 NRs possess a broad distribution in diameter 90-290 nm. **Fig. 3.2(a)** depicts a typical FETEM image of a TiO_2 NR with diameter of ~200 nm and length ~1μm, which is in good agreement with FESEM analysis. **Fig 3.2(b)** represents the enlarged view of the top portion of the TiO_2 NR. The HRTEM lattice fringe pattern of TiO_2 NR is shown in **Fig. 3.2(c).** The lattice fringe spacing of 0.32 nm corresponds to the lattice constant of (110) planes (see **Fig. 3.2 (c)**).The TEM image in **Fig. 3.2(d,e)** shows a shell of monolayer MoS_2 over the TiO_2 NR core, confirming the core-shell growth of MoS_2@TiO_2 HS. From the HRTEM image of MoS_2@TiO_2 HS, as shown in

Fig. 3.2(f), it is observed that the MoS_2 shell thickness is ~ 0.60 nm, which corresponds to the monolayer MoS_2.

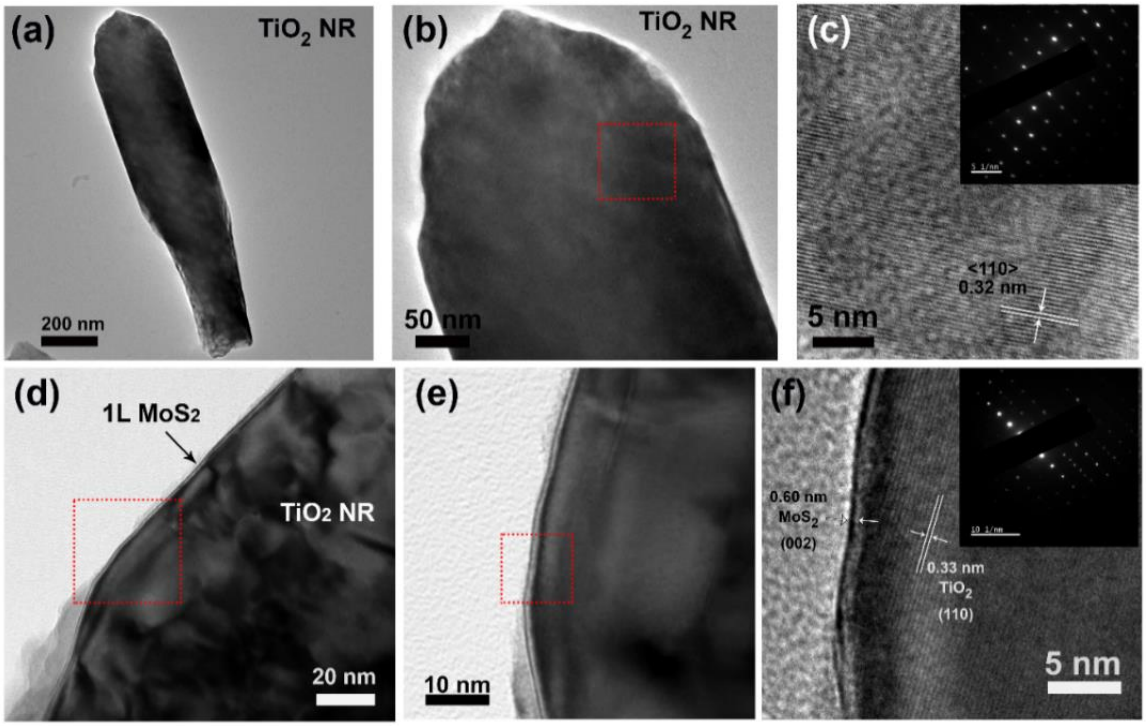

Fig. 3.2: (a) TEM image of a TiO_2 NR, (b) its enlarged view, (c) HRTEM lattice fringe pattern of the selected region for TiO_2 NR shown in (b). The inset in (c) shows the corresponding SAED pattern. (d) TEM image of TiO_2 NR having a monolayer MoS_2 shell over it, (e) Magnified view of the selected region for 1L MoS_2 on TiO_2 NR shown in (d), (f) HRTEM lattice fringe pattern of MoS_2@TiO_2 HSs at the selected region shown in (e). The Inset shows the corresponding SAED pattern

To further confirm the surface covering of monolayer MoS_2 as a shell over the TiO_2 NRs as core, scanning transmission electron microscope (STEM) analysis and energy dispersive X-ray spectrometry (EDS) mapping of the MoS_2@TiO_2 HS were conducted. The EDS pattern of MoS_2@TiO_2 HS shows that the system is composed of Ti, O, Mo, and S, as expected. **Fig. 3.3(a)** shows a STEM image of MoS_2@TiO_2 HS on which elemental mapping analysis was performed. The EDX elemental mapping reveals that the core of the HS is composed of Ti and O elements, as shown in **Fig. 3.3(b,c)**. **Fig. 3.3(d,e)** exhibits the elemental mapping for Mo and S, respectively, which supports our assertion that a continuous MoS_2 film grows over the TiO_2 platform as an outer layer. **Fig. 3.3(f)** shows the corresponding atomic percentage of all the elements, which reveals the S deficiency i.e., the presence of S-vacancy in MoS_2 in the HS sample.

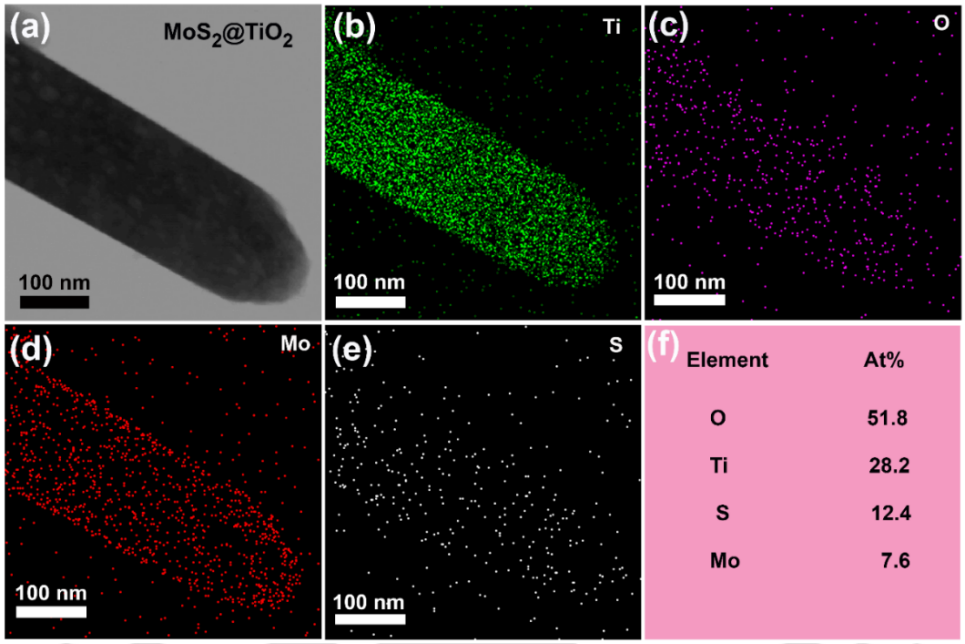

Fig. 3.3: (a) Scanning TEM image and (b-e) energy dispersive X-ray spectroscopy (STEM-EDX) elemental mapping results of core-shell 1L-MoS_2@TiO_2 HS showing the presence of different elements. (f) The atomic percentage of the respective elements in the HS as determined from EDX.

3.3.2. Structural Analysis

3.3.2.1. XRD Analysis

The XRD patterns were recorded to confirm the structure, phase, and crystallinity of MoS_2, TiO_2, and their HSs, as shown in **Fig. 3.4.** No diffraction pattern was detected for atomically thin pristine monolayer MoS2, but for few-layer MoS_2, only one peak (labeled with a "*" mark) was observed at $2\theta \approx 14.3°$, which can be ascribed to the (002) planes of crystalline MoS_2. The hexagonal MoS_2 with a = b = 0.316 nm and c = 1.230 nm is in good agreement with the JCPDS card no. 37-1492. All the XRD peaks for TiO_2 NRs (labeled with "•" mark) match the standard peak value with the rutile phase of TiO_2 (JCPDS card no. 78-1510). Additional peaks detected in the TiO_2 system correspond to the standard FTO related peaks, labeled with "●" mark. It is noteworthy that no diffraction peak is detected in the case of 1L-MoS_2@TiO_2 HS, which may be due to the ultrathin layer of the MoS_2 shell (thickness ~ 0.59 nm) on the TiO_2 NRs, as evidenced from the HRTEM and Raman analyses.

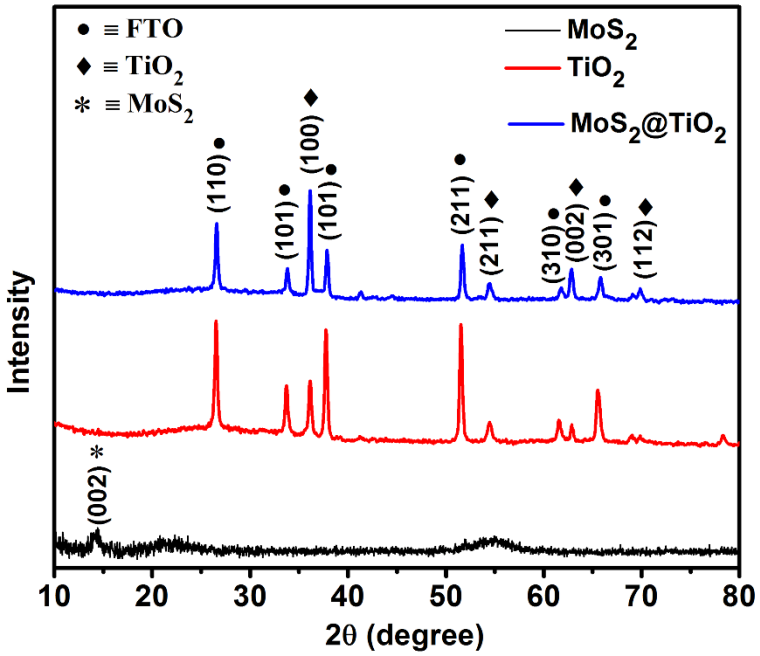

Fig. 3.4. XRD patterns of MoS_2 powder, pristine TiO_2 NRs and 1L-MoS_2@TiO_2 HS. The curves are shifted vertically for clarity of presentation.

3.3.2.2. Raman Analysis

Micro-Raman measurements were performed on the as-synthesized bare 1L-MoS_2, vertical TiO_2 NRs, and 1L-MoS_2@TiO_2 core-shell HS, grown on FTO coated glass substrate. **Fig. 3.5(a)** represents the comparison of Raman spectra for the samples. The growth of monolayer MoS_2 in both the pristine MoS_2 and MoS_2@TiO_2 HS is evidenced from the frequency difference (Δk) of characteristic Raman bands (E_{2g} and A_{1g}), which are estimated to be 19.94 and 20.80 cm^{-1}, respectively (see **Table 3.1**). Both the pristine MoS_2 and its HS exhibit two major characteristic Raman modes of MoS_2: E_{2g} and A_{1g}, associated with the in-plane vibration of two S atoms with respect to the Mo atoms and out-of-plane vibration of only S atoms in opposite directions with respect to the Mo atoms, respectively.[15] For the TiO_2 NRs, there are three Raman active phonon vibrational modes at 237 cm^{-1}, 442 cm^{-1}, and 610 cm^{-1} corresponding to the B_{1g}, E_g, and A_{1g} modes, respectively, corresponding to pure rutile TiO_2. The Raman spectrum of HS is composed of the Raman peaks of both MoS_2 and TiO_2, confirming their co-existence in the HS. Lorentzian line shape was fitted for the E_{2g} and A_{1g} bands of 1L-MoS_2 and E_g band of TiO_2 for both cases, as shown in the **Fig. 3.5(b-d)**.

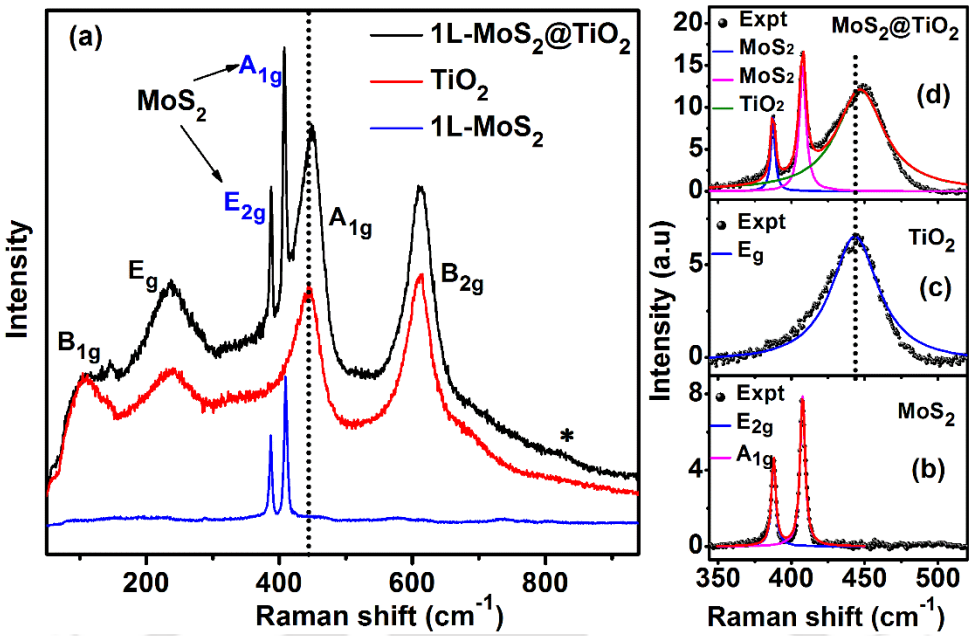

Fig. 3.5. (a) Comparison of the Raman spectra of pristine 1L-MoS_2, TiO_2 NRs and 1L-MoS_2@TiO_2 HS. (b-d) The Lorentzian fittings of the spectra in the range of 340-520 cm^{-1} for pristine 1L-MoS_2, TiO_2 NRs, and 1L-MoS_2@TiO_2, respectively. The symbol '*' indicates the additional peak corresponding to O–Mo–O bonding. The vertical dotted line in each case shows the blue shift in the E_g Raman band of TiO_2.

The E_g mode, a major characteristic Raman mode for TiO_2, shows a blue shift by 2 cm^{-1} in the HS with respect to that of pristine TiO_2 NRs, which may be due to the compressive lattice strain induced by the coated 1L-MoS_2 film over its surface as an outer layer.[12] The doping state of 1L-MoS_2 is also known to be represented by shift of the A_{1g} mode due to strong electron-phonon coupling along the c-axis.[5, 14-15] Here, we observed a relative blue shift of the A_{1g} peak of 1L-MoS_2 in the HS by ~0.8 cm^{-1} with respect to that of the pristine 1L-MoS_2, while a negligible shift was detected in E_{2g} peak. It can be inferred that the blue shift in A_{1g} mode is due to the decrease in the electron density, which may be caused by the electron depletion through the hetero-junction of the HS,[16] causing an effective p-doping effect in the 1L-MoS_2 in the HS. There is an additional peak appearing at 821cm^{-1} in the HS Raman spectrum (see **Fig. 3.5(a)**, marked with '*') that may be attributed to the O–Mo–O bonding.

Table 3.1: *Summary of the Raman modes, their separation (Δ**k**) for 1L-MoS_2 and 1L-MoS_2@TiO_2 HS.*

	Raman modes		
Sample	**E_{2g} (cm^{-1})**	**A_{1g} (cm^{-1})**	**Δk (cm^{-1})**
1L-MoS_2	387.5	407.4	19.9
1L-MoS_2@TiO_2	387.4	408.2	20.8

3.3.3. Optical Analysis

3.3.3.1. UV-Vis Absorption Study

To investigate the optical absorption spectra, the as-prepared samples were analyzed by UV-visible diffuse reflectance spectroscopy (DRS). **Fig. 3.6** shows the Kubelka-Munk (K-M) function F(R) plot of the respective samples corresponding to their reflectance spectra. Inset shows the magnified view of the spectra in the selected region of 560-720 nm, clearly revealing the different absorption modes of MoS_2.

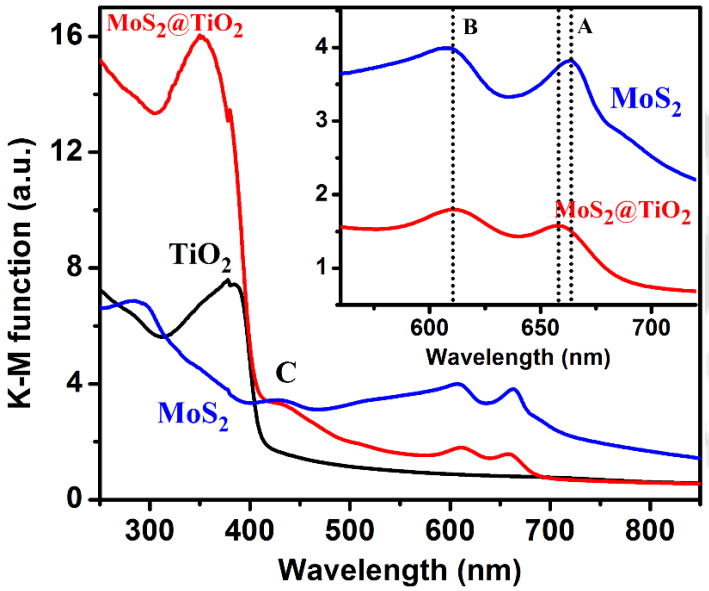

Fig. 3.6. Kubelka–Munk plot of different samples derived from the diffuse reflectance spectra. Inset shows the magnified view. A, B, C, and D represent the characteristic excitonic absorption bands of the 1L-MoS_2.

The spectrum for pristine few-layer MoS_2 shows the intrinsic A and B excitonic absorption bands at 663.5 nm and 609 nm, respectively.[17] In addition, we can clearly observe the C peak at 431.4 nm. The A and B peaks are associated with optical absorption by band-edge excitons, and the C absorption peak is assigned to the direct transition from the deep valence band to the conduction

band.[17] In the MoS_2@TiO_2 HS, besides the strong UV absorption by the TiO_2 core, all the characteristic MoS_2 absorbance peaks are detected with a much lower intensity indicating the uniform growth of atomically thin monolayer MoS_2 over TiO_2. It is noteworthy that peak A is observed to be slightly blue-shifted and detected at 657.1 nm, perhaps due to the quantum confinement effect as the layer number decreases from few layer to monolayer after the formation of HS with TiO_2.

3.3.3.2. Photoluminescence Study

Fig. 3.7(a) shows a comparison of the PL spectra of pristine1L-MoS_2 and 1L-MoS_2@TiO_2 HS, measured at room temperature. The PL peak intensities for the pristine 1L-MoS_2 and 1L-MoS_2@TiO_2 HS are measured to be ~1.5k and ~120k counts, respectively, as shown in **Fig. 3.7(a)**. Thus, the formation of single-layer MoS_2 shell over the TiO_2 NRs provides about 80 fold, i.e., nearly two orders of magnitude enhancement in the PL intensity of 1L-MoS_2 compared to its pristine counterpart. Additionally, the PL spectrum was notably blue shifted by ~12 nm in the case of HS, as compared to that of pristine 1L-MoS_2. To understand the origin of the PL emission, we have deconvoluted the spectra of as-grown 1L-MoS_2 and 1L-MoS_2@TiO_2 HS by fitting them with a few Gaussian peaks: the neutral exciton (A), negative trion (A−), B exciton, and the bound exciton (X) (**Fig. 3.7(b)** and **3.7(c)**). The summary of the spectral weight of each of the individual peaks for both the samples is presented in **Table 3.2**. The A exciton peak is derived from the direct bandgap of MoS_2, while B excitation peak arises from the direct bandgap transition between the minima of the conduction band and the lower-level valence band maxima, formed by the strong valence-band spin-orbit splitting at the K point in the Brillouin Zone[18] . The A^- exciton peak, which is understood as the transition from the trions, is caused by light n-type doping from the substrate or charged impurities in the CVD grown monolayer MoS_2 film,[19] and the X exciton peak is attributed to the radiative recombination of bound excitons.[20] Interestingly, after the formation of the HS, the spectral weight of A exciton peak increased from 41% to 76%, while that of the trion decreased from 23% to nearly 0%, as shown in **Fig. 3.7(b,c)** and **Table 3.2.** The transition due to the defect bound excitons (X) also decreases from ~17% to ~12% after the formation of HS, confirming the lower defect density in the 1L-MoS_2 grown on TiO_2.

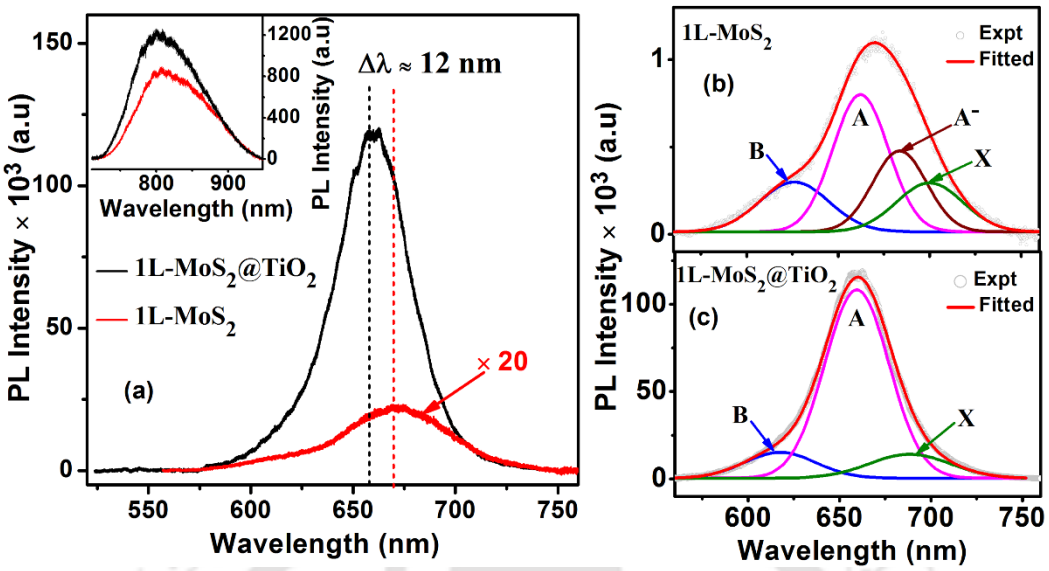

Fig. 3.7: (a) Comparative PL spectra of pristine 1L-MoS_2 and 1L-MoS_2@TiO_2 at room temperature (RT). Inset shows the Comparative PL spectra of pristine 1L-MoS_2 and 1L-MoS_2@TiO_2 in the range 720-950 nm (b, c) Gaussian deconvolution of RT PL spectra of pristine MoS_2 and MoS_2@TiO_2 HS, respectively.

When the heterojunction is formed between the MoS_2 and TiO_2, the excess electrons present in the intrinsically n-type 1L-MoS_2 transfer to the TiO_2 side through the interface due to their particular band alignment.[14] Therefore, this depletion of excess electrons introduces an effective p-type doping in the 1L-MoS_2, as evidenced from the blue shift of Raman and PL spectra, which switches the PL process from trion recombination to exciton recombination, leading to an enormous PL enhancement by the 1L-MoS_2 shell. Note that the pristine TiO_2 NRs show a weak near-infra-red (NIR) PL emission at ~810 nm, which is attributed to the Ti-interstitial defects.[21] The PL spectrum corresponding to the rutile TiO_2 NRs is observed to be increased marginally after the formation of MoS_2@TiO_2 HS, as shown in the inset of **Fig. 3.7(a).** This may be due to the recombination of excess electrons from the Ti-interstitial defect states of TiO_2. After migrating from the MoS_2 side, the excess electrons may reach the Ti-interstitial state through thermal relaxation.

The heterojunction between MoS_2 and TiO_2 usually forms a type-II HS, which facilitates efficient transfer of the photoexcited electrons from MoS_2 side to TiO_2 side, usually resulting in PL quenching.[22] On the contrary, in our case, the charge transfer at the interface most likely occurs through the trions, i.e., the excess electrons in intrinsically n-type 1L-MoS_2, while the neutral excitons are not parted. This can be realized from the much higher binding energy of neutral exciton, 0.5-0.9 eV than that of the trion ~30 meV, generated in the 1L-MoS_2 by the

photoexcitation. Thus, analogous to the typical chemical p-doping process, which converts light-inefficient trions to light-efficient excitons, it may be argued that the controlled interfacial charge transfer induces a p-doping effect, resulting in the giant enhancement of PL.[14] Additionally, CVD growth process generally induces various structural defects in the monolayer MoS_2. Thus, such structural defects in the 1L-MoS_2 shell grown by a CVD method over the TiO_2 core is expected, which is consistent with the STEM elemental composition showing a lower concentration of S, indicating S vacancies. Therefore, oxygen and water molecules adsorbed from the atmosphere can occupy the S vacancy sites and/or oxygen in the TiO_2 lattice may form O-Mo-O or Mo=O bonding, which eventually introduces p-type doping in the MoS_2 film, as compared to pristine 1L-MoS_2. Thus, we believe that the p-doping in1L-MoS_2@TiO_2 HS leads to the conversion from negative trion to neutral exciton,[19] which enhances the PL intensity enormously.

Table 3.2: *Summary of the Gaussian deconvoluted PL spectra showing various species for 1L-MoS_2 and 1L-MoS_2@TiO_2 HS.*

	PL peaks			
Sample	**B-exciton (B) (%)**	**A-exciton (A) (%)**	**trion (A^-) (%)**	**bound exciton (X) (%)**
1L-MoS_2	18.5	40.8	23.3	17.4
1L-MoS_2@TiO_2	11.6	76.3	0	12.1

To understand the relative contribution of non-radiative and radiative processes, low-temperature PL measurements were carried out for both 1L-MoS_2 and 1L-MoS_2@TiO_2 and the results are shown in **Fig. 3.8(a,b).** It is clear that the PL intensity is considerably enhanced at low temperatures for the pristine 1L-MoS_2 sample. A 50X objective lens was used to focus the laser beam and to collect the PL signal at temperatures from 83 K to 287 K in a low-temperature Linkam stage. The temperature dependence of PL intensity I_{PL} (T) can be expressed by the equation:[19, 23]

$$I_{PL}(T) = \frac{I_{LT} \times K_{rad}(T)}{K_{rad}(T) + K_{nonrad}(T)}$$

where I_{LT} is the PL intensity at very low temperature, $K_{rad}(T)$ and $K_{nonrad}(T)$ are the temperature-dependent radiative and nonradiative recombination rates, respectively. The nonradiative recombination rate is reported to be related to the defect trapping rate and electron relaxation within the conduction and valence band of a semiconductor.[18] Most of the semiconducting materials possess extremely low quantum efficiency of emission at higher temperatures due to the higher rate of nonradiative recombination activated with the thermal energy.

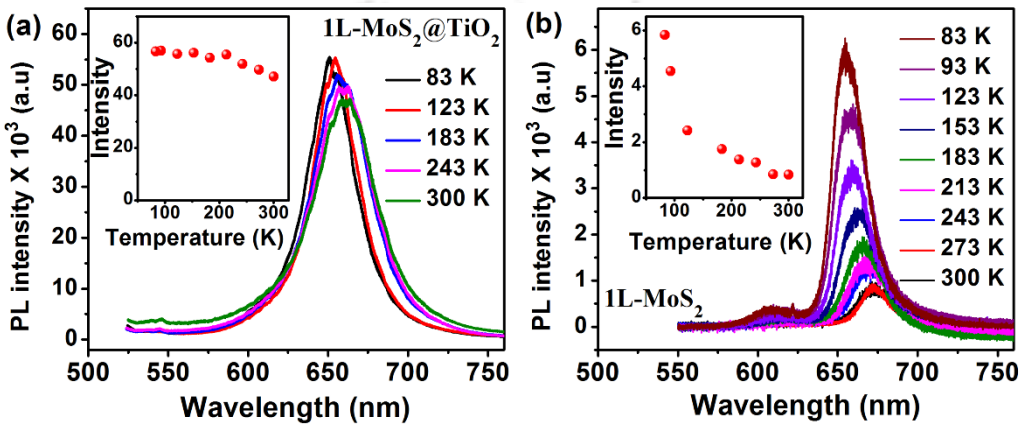

Fig. 3.8. Low-temperature PL spectra for (a) pristine 1L-MoS_2 and (b) 1L-MoS_2@TiO_2 core-shell HS, taken from 83 to 300 K at a regular interval. The inset in each case shows the temperature dependence of the PL intensity.

In the present case, when the temperature increases from 83 K to 300 K, due to the nonradiative recombination, the PL intensity of the pristine 1L-MoS_2 is reduced by ~86%, as shown in **Fig. 3.8(a)** and its inset. Surprisingly, for the same change in temperature, the PL intensity of 1L-MoS_2@TiO_2 HS is observed to be reduced to only by ~17%, as shown in **Fig. 3.8(b)**. Thus, it can be argued from the above equation that the nonradiative recombination rate of the excitons in case of 1L-MoS_2@TiO_2 HS is almost negligible and the PL emission is mostly dominated by radiative recombination.[14, 24] This may also be one of the major reason for enormous PL enhancement at 1L-MoS_2 in MoS_2@TiO_2 HS. Further, it was observed that the nonradiative rate becomes nearly 7 times stronger than the radiative rate at room temperature for the case of pristine 1L-MoS_2, while it is quite small for the HS sample. Thus, no significant quenching of PL is observed with the increase of temperature for the HS sample, which is very significant for its display application.

3.3.4. Effect of Oxygen Plasma Treatment

3.3.4.1. Raman Analysis

To have a more detailed understanding of the mechanism of giant PL enhancement, oxygen plasma treatment was carried out for the pristine 1L-MoS_2 and 1L-MoS_2@TiO_2 HS for various time durations.

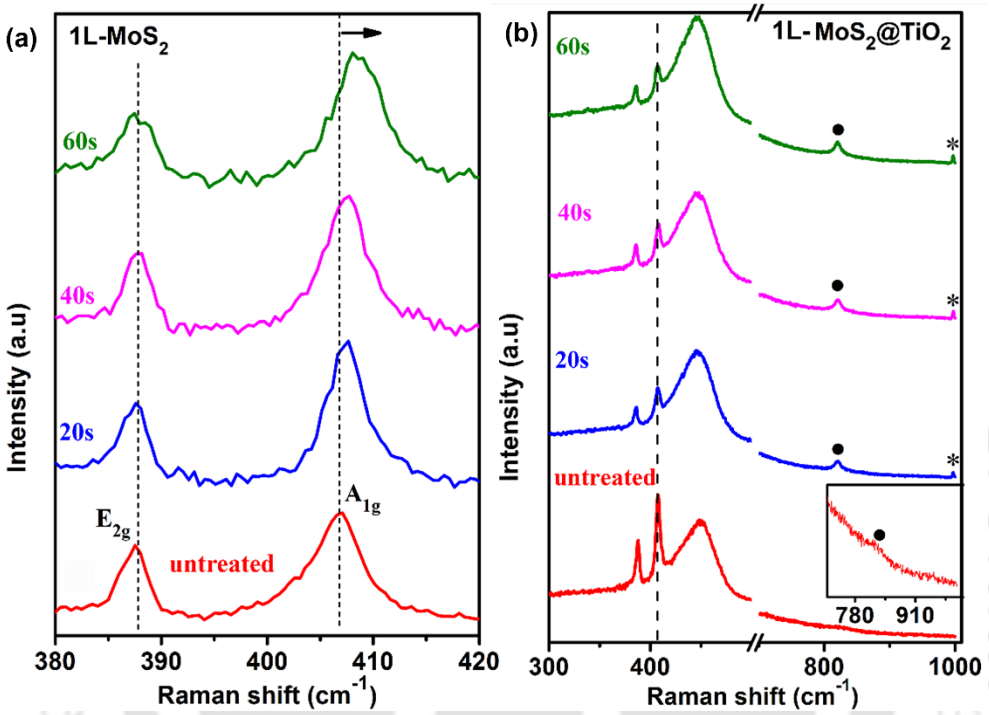

Fig. 3.9. Raman spectra of (a) pristine and oxygen plasma-treated 1L-MoS_2 and (b) pristine and oxygen plasma-treated 1L-MoS_2@TiO_2, for different plasma exposure time: 0-60s. In the case of the untreated sample, the inset shows a magnified view of the spectrum in the range of 740-1010 cm^{-1}. It reveals the evolution of a new peak (marked by symbol '•') after the plasma treatment. The vertical dotted lines indicate the shift in the Raman mode of MoS_2 with the plasma exposure time.

Fig. 3.9(a) shows the Raman spectra of the oxygen plasma-treated 1L-MoS_2 sample irradiated up to 60 sec. It is noteworthy to observe that the E_{2g} mode is not affected much, while the A_{1g} mode ~408 cm^{-1} is blue-shifted monotonically with increasing the oxygen plasma exposure time. This is a clear indication of an effective p-doping in the MoS_2 lattice by oxygen bonding during the plasma treatment.[25] With the more prolonged exposure of 1L-MoS_2 to the oxygen plasma, the position of the A_{1g} peak does not shift further, but the Raman intensity starts decreasing, implying the degradation of the film quality. **Fig. 3.9(b)** shows the Raman spectra of oxygen plasma-treated 1L-MoS_2@TiO_2 HS for different durations of treatment (0-60 s). Note that due to the plasma treatment, the Raman peak intensity is gradually reduced with the plasma exposure time, though

peak positions for E_{2g} and A_{1g} modes are unchanged. The reduced peak intensity signifies the gradual degradation of MoS_2 film quality. Thus, after the growth of 1L-MoS_2 shell over the TiO_2 NRs, the MoS_2 layer becomes optimally p-doped and no further doping is observed even after the oxygen plasma treatment. Interestingly, we observed a systematic increase in the peak intensity for a peak at ~820 cm^{-1} and an additional peak at ~994cm^{-1} is observed to be evolving with increasing the plasma irradiation time, corresponding to the O–Mo–O and Mo=O bonds of molybdenum oxides (see **Fig. 3.9(b)**).[26] These results clearly indicate the p-doping of the underlying MoS_2 layer in the HS sample.

3.3.4.2. Photoluminescence Study

To further investigate the origin behind the strong PL enhancement in the MoS_2@TiO_2 HS, the PL spectra of both the pristine MoS_2 and 1L-MoS_2@TiO_2 HS were recorded after oxygen plasma treatment for various time durations and analyzed.

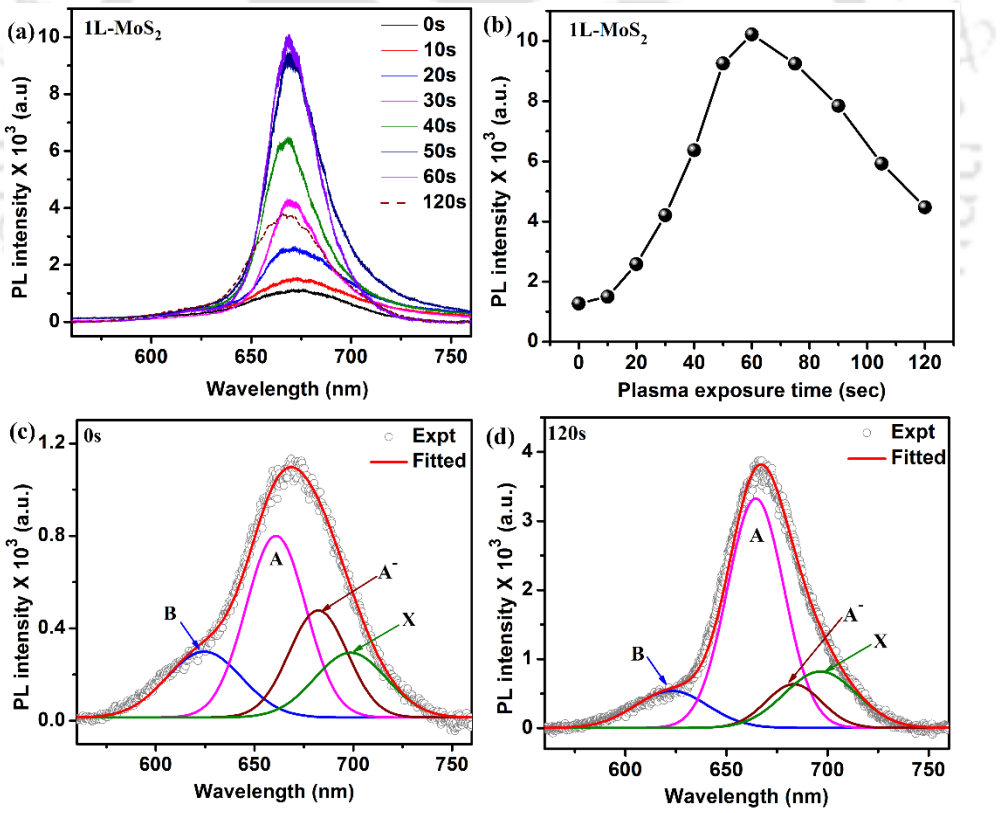

Fig. 3.10. (a) Variation of PL spectra of 1L-MoS_2 as a function of the oxygen plasma exposure time duration. (b) The variation in PL intensity as a function of plasma exposure time. (c,d) Gaussian deconvoluted PL spectra of 1L-MoS_2, after the 60s and 120s oxygen plasma treatment, respectively. The symbols for different fitted peaks are explained in the text.

Fig. 3.10(a) shows a comparison of PL spectra for pristine 1L-MoS_2, before and after O_2 plasma treatment. The PL intensity is observed to be increased with plasma exposure time up to 60sec, and then it decreases gradually, as shown in **Fig. 3.10(b)**. **Fig. 3.10(c,d)** shows the Gaussian deconvolution of the PL spectra of 1L-MoS_2 after oxygen plasma exposure for different time durations: 60 sec and 120 sec, respectively. As the plasma irradiation is reported to introduce S-vacancies in the pristine 1L-MoS_2,[20] the MoS_2 film is p-doped in the course of plasma treatment by the adsorption of oxygen molecules at the vacancy sites, which push away the electrons from the MoS_2. Therefore, the trion contribution is suppressed and hence the neutral exciton emission dominates, which results in the overall increase of PL emission and the blue shift of the A exciton peak. When the irradiation time exceeds 60 sec, we observed a systematic drop in the PL intensity (as shown in **Fig. 3.10(b)**). Thus, at 60 sec plasma irradiation, the doping concentration may reach the optimum value, and beyond which, excessive defects are created by the plasma, which degrades the characteristic properties of MoS_2, consistent with the Raman analysis. After 120 sec of plasma irradiation, the defect induced X peak contribution is maximum in the PL, while A and A^- peaks decrease markedly in weight, as shown in **Table 3.3.**

Fig. 3.11(a) depicts a comparison of PL spectra of 1L-MoS_2@TiO_2 HS before and after oxygen plasma treatment for various time durations. With the increase in plasma treatment time, PL intensity decreased monotonically, as shown **in Fig. 3.11(b).** To understand the change in spectral profile with plasma treatment, each spectrum was deconvoluted. **Fig. 3.11(c,d)** shows the Gaussian deconvolution of the PL spectra for oxygen plasma exposure times: 30 sec and 60 sec, respectively. Due to the negligible contribution of trion A^- in the as-grown MoS_2@TiO_2 HS (see **Table 3.2**), no significant conversion of A^- to A exciton emission is detected after the plasma treatment. However, the contribution of the defect induced X peak increases substantially in the HS with the plasma treatment time, which implies the deterioration of the MoS_2. As a result, the overall intensity goes down with plasma exposure of the HS sample.

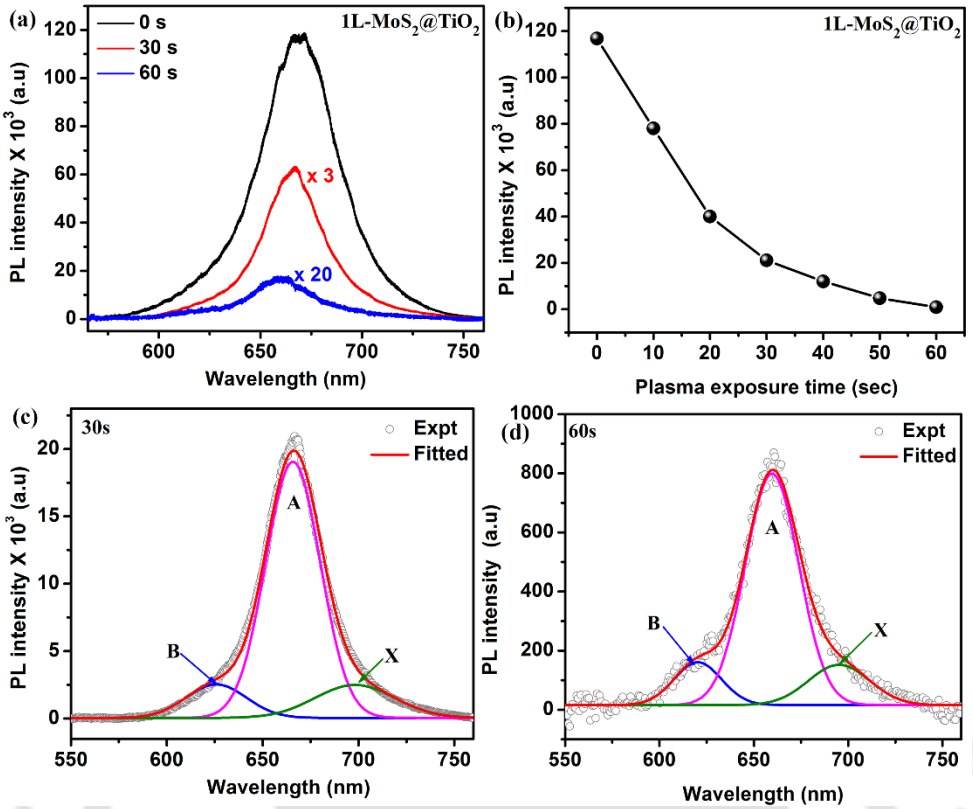

Fig. 3.11. (a) A comparison of PL spectra of 1L-MoS_2@TiO_2, as-grown, and after oxygen plasma treatment with various duration. (b) The change in PL intensity of 1L-MoS_2@TiO_2 with plasma exposure time. (c,d) Gaussian deconvolution of PL spectra of 1L-MoS_2@TiO_2, after the 30s and 60s oxygen plasma treatment, respectively. The symbols for different fitted peaks are explained in the text.

Table 3.3: *Change in different peak contributions in PL with the oxygen plasma treatment for different time durations in pristine 1L-MoS_2 and 1L-MoS_2@TiO_2 HS*

Sample	Plasma exposure time	B-exciton (B) (%)	A-exciton (A) (%)	trion (A^-) (%)	bound exciton (X) (%)
MoS_2	**0s**	18.5	40.8	23.4	17.3
	60s	4.7	73.0	10.2	12.1
	120s	12.0	58.8	10.9	18.3
1L-MoS_2@TiO_2	**0s**	11.6	76.3	0	12.1
	30s	10.8	75.1	0	14.1
	60s	12.0	73.5	0	14.5

3.4. Conclusion

In this chapter, monolayer MoS_2 shell was deposited by a direct CVD process on the hydrothermally grown vertical TiO_2 NRs, forming a MoS_2@TiO_2 core-shell structure. A strong enhancement in PL intensity (by nearly two orders of magnitude) at room temperature in the 1L-MoS_2@TiO_2 NR HS is demonstrated here, for the first time. The formation of 1L-MoS_2@TiO_2 core-shell HS was confirmed by the Raman and HRTEM analyses. The observed strong PL enhancement is explained based on oxygen bonding induced heavy p-doping in MoS_2 lattice, which suppresses the trion emission and increases in neutral exciton emissions. Low-temperature PL measurement on the HS sample indicates the suppression of nonradiative recombination of excitons at the MoS_2, which eventually boosts the PL emission at room temperature. Finally, oxygen plasma irradiation was performed on pristine MoS_2 and MoS_2@TiO_2 HS samples to verify the p-doping through the oxygen bonding at the defect sites in MoS_2, resulting in the enhancement of PL. Our results provide a new and easy way to fabricate MoS_2 based heterostructure and tune the optical properties of MoS_2 to realize its practical applications in optoelectronic or nanophotonic devices.

References

1. Mak, K. F.; Lee, C.; Hone, J.; Shan, J.; Heinz, T. F., Atomically Thin Mos2: A New Direct-Gap Semiconductor. *Phys. Rev. Lett.* **2010**, *105*, 136805.
2. Sarkar, D.; Xie, X.; Liu, W.; Cao, W.; Kang, J.; Gong, Y.; Kraemer, S.; Ajayan, P. M.; Banerjee, K., A Subthermionic Tunnel Field-Effect Transistor with an Atomically Thin Channel. *Nature* **2015**, *526*, 91.
3. Mak, K. F.; He, K.; Lee, C.; Lee, G. H.; Hone, J.; Heinz, T. F.; Shan, J., Tightly Bound Trions in Monolayer Mos2. *Nat. Mater.* **2012**, *12*, 207.
4. Ross, J. S., et al., Electrical Control of Neutral and Charged Excitons in a Monolayer Semiconductor. *Nat. Commun.* **2013**, *4*, 1474.
5. Dhakal, K. P.; Duong, D. L.; Lee, J.; Nam, H.; Kim, M.; Kan, M.; Lee, Y. H.; Kim, J., Confocal Absorption Spectral Imaging of Mos2: Optical Transitions Depending on the Atomic Thickness of Intrinsic and Chemically Doped Mos2. *Nanoscale* **2014**, *6*, 13028-13035.
6. Kim, M. S.; Seo, C.; Kim, H.; Lee, J.; Luong, D. H.; Park, J.-H.; Han, G. H.; Kim, J., Simultaneous Hosting of Positive and Negative Trions and the Enhanced Direct Band Emission in Mose2/Mos2 Heterostacked Multilayers. *ACS Nano* **2016**, *10*, 6211-6219.
7. Park, S.; Kim, M. S.; Kim, H.; Lee, J.; Han, G. H.; Jung, J.; Kim, J., Spectroscopic Visualization of Grain Boundaries of Monolayer Molybdenum Disulfide by Stacking Bilayers. *ACS Nano* **2015**, *9*, 11042-11048.
8. Mouri, S.; Miyauchi, Y.; Matsuda, K., Tunable Photoluminescence of Monolayer Mos2 Via Chemical Doping. *Nano Lett.* **2013**, *13*, 5944-5948.
9. Qiu, H., et al., Hopping Transport through Defect-Induced Localized States in Molybdenum Disulphide. *Nat. Commun.* **2013**, *4*, 2642.

10. van der Zande, A. M.; Huang, P. Y.; Chenet, D. A.; Berkelbach, T. C.; You, Y.; Lee, G.-H.; Heinz, T. F.; Reichman, D. R.; Muller, D. A.; Hone, J. C., Grains and Grain Boundaries in Highly Crystalline Monolayer Molybdenum Disulphide. *Nat. Mater.* **2013**, *12*, 554.
11. Paul, K. K.; Ghosh, R.; Giri, P. K., Mechanism of Strong Visible Light Photocatalysis by Ag 2 O-Nanoparticle-Decorated Monoclinic Tio 2 (B) Porous Nanorods. *Nanotechnology* **2016**, *27*, 315703.
12. Paul, K. K.; Giri, P. K., Role of Surface Plasmons and Hot Electrons on the Multi-Step Photocatalytic Decay by Defect Enriched Ag@Tio2 Nanorods under Visible Light. *J. Phys. Chem. C* **2017**, *121*, 20016-20030.
13. Tan, Y.-H.; Yu, K.; Li, J.-Z.; Fu, H.; Zhu, Z.-Q., Mos2@Zno Nano-Heterojunctions with Enhanced Photocatalysis and Field Emission Properties. *J. Appl. Phys.* **2014**, *116*, 064305.
14. Kim, M. S.; Roy, S.; Lee, J.; Kim, B. G.; Kim, H.; Park, J.-H.; Yun, S. J.; Han, G. H.; Leem, J.-Y.; Kim, J., Enhanced Light Emission from Monolayer Semiconductors by Forming Heterostructures with Zno Thin Films. *ACS Appl. Mater. Interfaces* **2016**, *8*, 28809-28815.
15. Li, H.; Zhang, Q.; Yap, C. C. R.; Tay, B. K.; Edwin, T. H. T.; Olivier, A.; Baillargeat, D., From Bulk to Monolayer Mos2: Evolution of Raman Scattering. *Adv. Funct. Mater.* **2012**, *22*, 1385-1390.
16. Chakraborty, B.; Bera, A.; Muthu, D. V. S.; Bhowmick, S.; Waghmare, U. V.; Sood, A. K., Symmetry-Dependent Phonon Renormalization in Monolayer Mos2 Transistor. *Phys. Rev. B* **2012**, *85*, 161403.
17. Dumcenco, D., et al., Large-Area Epitaxial Monolayer Mos2. *ACS Nano* **2015**, *9*, 4611-4620.
18. Splendiani, A.; Sun, L.; Zhang, Y.; Li, T.; Kim, J.; Chim, C.-Y.; Galli, G.; Wang, F., Emerging Photoluminescence in Monolayer Mos2. *Nano Lett.* **2010**, *10*, 1271-1275.
19. Nan, H., et al., Strong Photoluminescence Enhancement of Mos2 through Defect Engineering and Oxygen Bonding. *ACS Nano* **2014**, *8*, 5738-5745.
20. Tongay, S., et al., Defects Activated Photoluminescence in Two-Dimensional Semiconductors: Interplay between Bound, Charged, and Free Excitons. *Sci. Rep.* **2013**, *3*, 2657.
21. Batakrushna, S.; Giri, P. K.; Kenji, I.; Minoru, F., Microscopic Origin of Lattice Contraction and Expansion in Undoped Rutile Tio 2 Nanostructures. *J. Phys. D: Appl. Phys.* **2014**, *47*, 215302.
22. Zhou, W.; Yin, Z.; Du, Y.; Huang, X.; Zeng, Z.; Fan, Z.; Liu, H.; Wang, J.; Zhang, H., Synthesis of Few-Layer Mos2 Nanosheet-Coated Tio2 Nanobelt Heterostructures for Enhanced Photocatalytic Activities. *Small* **2013**, *9*, 140-147.
23. Gaponenko, M. S.; Lutich, A. A.; Tolstik, N. A.; Onushchenko, A. A.; Malyarevich, A. M.; Petrov, E. P.; Yumashev, K. V., Temperature-Dependent Photoluminescence of Pbs Quantum Dots in Glass: Evidence of Exciton State Splitting and Carrier Trapping. *Phys. Rev. B* **2010**, *82*, 125320.
24. Feldmann, J.; Peter, G.; Göbel, E. O.; Dawson, P.; Moore, K.; Foxon, C.; Elliott, R. J., Linewidth Dependence of Radiative Exciton Lifetimes in Quantum Wells. *Phys. Rev. Lett.* **1987**, *59*, 2337-2340.
25. Wei, X.; Yu, Z.; Hu, F.; Cheng, Y.; Yu, L.; Wang, X.; Xiao, M.; Wang, J.; Wang, X.; Shi, Y., Mo-O Bond Doping and Related-Defect Assisted Enhancement of Photoluminescence in Monolayer Mos2. *AIP Advances* **2014**, *4*, 123004.
26. Pang, Q.; Zhao, Y.; Bian, X.; Ju, Y.; Wang, X.; Wei, Y.; Liu, B.; Du, F.; Wang, C.; Chen, G., Hybrid Graphene@Mos2@Tio2 Microspheres for Use as a High Performance Negative Electrode Material for Lithium Ion Batteries. *J. Mater. Chem. A* **2017**, *5*, 3667-3674.

भारतीय प्रौद्योगिकी संस्थान गुवाहाटी
Indian Institute of Technology Guwahati

Chapter 4

Exciton-Plasmon Coupling and Giant Photoluminescence Enhancement in Hierarchical designed TiO_2/Au/MoS_2 Ternary Core-Shell Heterostructure

In this chapter, we demonstrate a dramatically enhanced photoluminescence (PL) emission from the large-area monolayer MoS_2 grown over an array of plasmonic gold nanoparticles (NPs) coated over hierarchical TiO_2 nanostructures forming a core-shell TiO_2/Au/MoS_2 hybrid structure, where the PL intensity is enhanced by about three orders of magnitude, highest among the reported values. The formation of ternary core-shell heterojunction is evidenced from the high resolution transmission electron microcopy and Raman analyses. Localised surface plasmon resonance induced enhanced adsorption in the system was revealed from the UV-vis absorption spectroscopy. The observed giant PL enhancement in 1L-MoS_2 is resulting from two major aspects: firstly, the heavy p-doping of the MoS_2 lattice caused by the transfer of the excess electrons from the MoS_2 to TiO_2 at the interface, which enhances the neutral exciton emissions and restrained the trion emissions. Secondly, the localized surface plasmon in Au NPs underneath the 1L-MoS_2 film initiates exciton-plasmon coupling between excitons of the 1L-MoS_2 and surface plasmons of the Au NPs at the MoS_2/Au interface. The PL and Raman analyses further confirms the p-doping effect and the enhanced light emission of the heterostructures. This work suggests an easy, novel and rational pathway for the effective improvement in the PL enhancement of 1L-MoS_2, and this attempt may direct to the next generation optoelectronic applications.

4.1. Introduction

Several strategies have been explored in the past few years in order to enhance the characteristic PL emission of 1L-MoS_2 including defect engineering, electrical as well as chemical doping and fabricating a vertical heterojunction of 1L-MoS_2 with other TMDs, semiconductor or metal.[1-3] In the previous chapter, we have demonstrated enhanced PL emission from 1L-MoS_2 shell grown by in-situ CVD technique over TiO_2 nanorods. The PL enhancement was explained on the basis of the conversion of trion to neutral exciton due to the interfacial carrier exchange, leading to a p-doping effect in the MoS_2 lattice. Over the decades, hierarchical core@shell nanoheterostructures have been extensively studied for the remarkable synergistic effects and multifunctional

applications, including enhanced chemical functionalization, encapsulation of the reactive core with a nonreactive shell, leading to the superior and novel optical and catalytic properties.[4-6] In plasmonic excitation, free electrons in metals enable the creation of electric field and its confinement in the vicinity of the metal NPs. Depending on NP's shape, size, contact angle and dielectric constant of the surrounding medium, a localized surface plasmon resonance (LSPR) occurs around the metal NP in order to modulate the optical properties of the system. The core@shell heterojunctions with monolayer MoS_2 shell and metallic NPs (Au/Ag) as functional core have been investigated extensively for their impressive performance in a variety of applications such as photodetectors, light emitting diodes (LEDs), surface enhanced Raman spectroscopy (SERS), and bioimaging.[7] Though, Au/Ag NP based core@shell heterojunction with monolayer TMD as shell has been thoroughly investigated, fabrication of core@shell heterojunction in the vicinity of a 3rd semiconducting material with different dielectric constant has not been reported earlier and may be of great interest in modulating the optical properties of a TMD system. In the present chapter, we report a novel approach to achieve giant enhancement in the PL emission of CVD grown 1L-MoS_2 considering plasmonic NPs coated 3D-TiO_2 nanostructures (NSs) as substrate. Results show that this hybrid structure allows a strong interaction between the incident light and 1L-MoS_2 leading to a giant enhancement in PL intensity compared to pristine 1L-MoS_2 at room temperature. We compare the performance of Ag and Au plasmonic nanoparticles in the enhanced PL emission and elucidate the role of exciton-plasmonic coupling in the strongly enhanced PL emission from 1L-MoS_2 grown on a plasmonic substrate.

4.2. Experimental Details

4.2.1. Sample Preparation

4.2.1.1. Preparation of hierarchical TiO_2 Nanostructures on Titanium Foil

Titanium (Ti) foil was used as-received from Sigma-Aldrich (99.7%) for the growth of hierarchical TiO_2 nanostructures (NSs) considering the Ti foil as source material and substrate. Typically, a clean square piece of Ti foil (thickness ≈ 0.127 mm) after a thorough wash with acetone, 2-propanol and de-ionized (DI) water was heated in ~18% aqueous HCl solution at 90 °C to remove the oxide layer and additional impurities from its surface. The Ti foil was then dried with inert atmosphere and immersed in previously prepared 50 mL of 20 mM aqueous HF solution and transferred to a Teflon-lined stainless steel autoclave (Berghof, BR-100) and treated at 150 °C for

8 h. Then the autoclave was allowed to cool down naturally and the treated Ti foil was gently rinsed with DI water and dried at 80 °C in air to get hierarchical TiO_2 NSs uniformly grown on the Ti substrate.

4.2.1.2. Growth of Au/Ag nanoparticles

An ultra-thin Au/Ag film was deposited on the different substrates, such as TiO_2 NS and Si/SiO_2, by a radio frequency (RF) magnetron sputtering process. A high-purity sputter target (99.999%, diameter 2 inches, custom made) was used for the sputter deposition with a RF power of 8 W under an Ar gas atmosphere. Au/Ag film was deposited in a controlled manner for 10 minutes at the rate of 1 nm min^{-1}. Furthermore, the Au/Ag deposited substrates were then subjected to rapid thermal annealing (RTA) in order to form an array of Au/Ag nanoparticles (NPs). The RTA temperature was maintained at 600 °C for 3 min under a controlled flow of high-purity Ar gas and is found to be the optimum condition for the NP growth. The heating and cooling rates were kept at 20 and 10 °C s^{-1}, respectively.

4.2.1.3. Growth of monolayer MoS_2

1L-MoS_2 was directly grown on the different substrates (Si/SiO_2, TiO_2 NSs, TiO_2/Au, TiO_2/Ag) by the CVD process using a two zone furnace. High-purity MoO_3 and S powder were used as precursors and placed inside a 2-inch quartz tube-based horizontal muffle furnace at the center of their respective zones. The samples were then placed face down on top of the quartz mask with a circular opening, which were then put on top of the boat containing MoO_3 precursor. The temperature of the zone containing the substrates was ramped at a rate of 15 °C/min up to 700 °C and was maintained for 5 min, with an Ar flow rate of 10 sccm. Then, the furnace was allowed to cool down to room temperature. Thus, resulting in the growth of monolayer MoS_2 shell over all the samples. Further details of the growth is described in **Chapter 2, Section 2.3.2.** The morphology, crystal structure and composition of the sample were characterized by FESEM, TEM, XPS and micro-Raman analyses. Details of the samples are given in **Table 4.1**.

Table 4.1: *The details of the samples studied.*

Sample code	Sample description
MoS_2	1L- MoS_2 on SiO_2 substrate
Au/MoS_2	1L-MoS_2 grown over Au NPs on SiO_2 substrate
Ag/MoS_2	1L-MoS_2 grown over Ag NPs on SiO_2 substrate
TiO_2/MoS_2	1L-MoS_2 grown over TiO_2 nanostructure on Ti foil substrate
$TiO_2/Au/MoS_2$	1L-MoS_2 grown over Au NPs decorated on TiO_2 nanostructure
$TiO_2/Ag/MoS_2$	1L-MoS_2 grown over Ag NPs decorated on TiO_2 nanostructure
TiO_2	Hydrothermally grown fluorine doped TiO_2 nanostructure on Ti foil

4.2.2 Characterization Techniques

The details of the FESEM, AFM, PL and Raman were described in **Chapter 2, Section 2.1.3**. X-ray photoelectron spectroscopy (XPS) has been carried out using a PHI X-tool automated photoelectron spectrometer (ULVAC-PHI, Japan) with an Al Kα X-ray beam (1486.6 eV) at a beam current of 20 mA. The C 1s spectrum at 284.8 eV was used as a standard value for the correction of the shift in the binding energy of various elements. The details of the TEM and UV−vis absorption measurements were discussed in **Chapter 3, Section 3.2.3**

4.3. Results and Discussion

4.3.1. Morphology Studies

The morphology and microstructural properties of as-grown TiO_2 NSs and Au or Ag NPs were first studied by FESEM. **Fig. 4.1(a)** depicts the FESEM image of Au NPs over SiO_2 on which the monolayer layer MoS_2 was subsequently grown by in-situ CVD technique. The inset shows a magnified view of FESEM image shown in **Fig. 4.1(a)**, discerning their uniform distribution. **Fig. 4.1(b)** shows the size distribution of Au NPs along with the lognormal fitting, which estimates that the average size of Au NPs are ~ 33.3 nm. **Fig. 4.1(c**) show the FESEM image of Ag NPs showing nearly uniform distribution in their size and density. The inset shows a magnified view of the Ag NPs. **Fig. 4.1(d)** depicts the size distribution of Ag NPs with the lognormal fit showing an average size ~ 39.3 nm. **Fig. 4.1(e)** shows the FESEM image of hierarchical TiO_2 NSs having a lateral dimension ~ 1 µm, grown on a Ti foil substrate. The inset of **Fig. 4.1(e)** shows a magnified view of single TiO_2 NS. **Fig. 4.1(f)** shows the FESEM image of monolayer MoS_2 shell over the TiO_2

NS decorate with Au NPs. Note that the 1L-MoS_2 is not discernable here due to its ultra-low thickness.

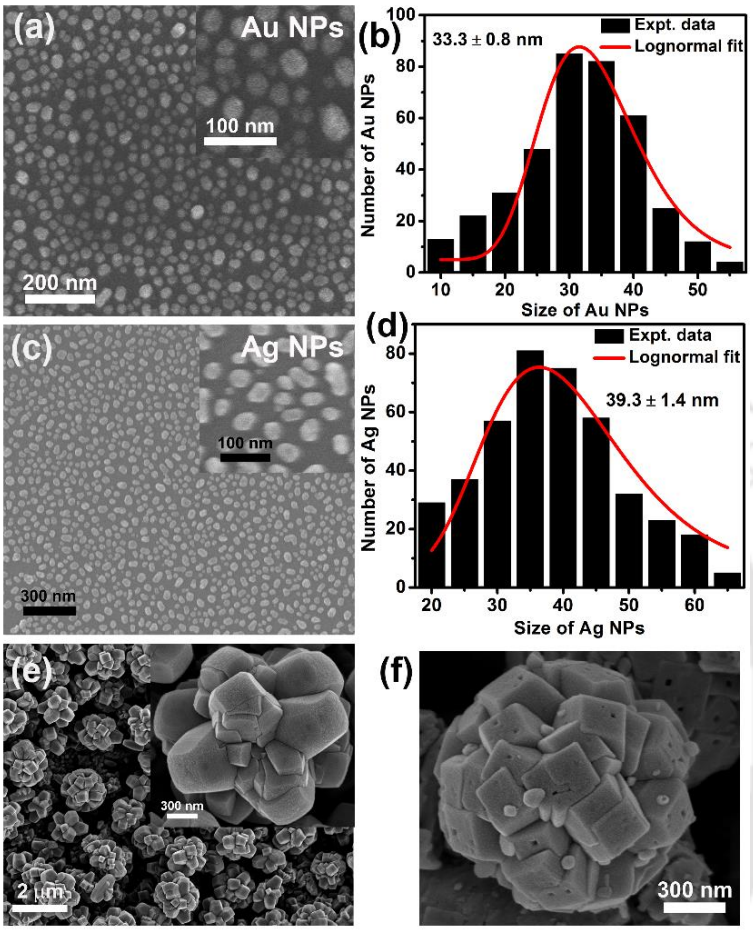

Fig. 4.1. (a) FESEM image of Au NPs, while inset shows its magnified view, and (b) the corresponding size distribution of Au NPs. (c) FESEM images of Ag NPs, the inset shows the magnified view, and (d) the corresponding size distribution. (e) FESEM image of hierarchical TiO_2 NSs grown on Ti foil and the inset shows the magnified view of a single TiO_2 NS. (f) FESEM image of monolayer MoS_2 shell over the TiO_2 NS decorated with Au NPs. Note that the 1L-MoS_2 is not discernable due to its ultra-low thickness.

In order to investigate the surface morphology, microstructural properties and interface of the multijunction systems, the samples were characterized by TEM. **Fig. 4.2(a)** depicts the TEM image of one edge of the hierarchical TiO_2 NSs with a monolayer MoS_2 shell seamlessly covered over the TiO_2 NSs, which confirms the formation of core@shell heterojunction between TiO_2 NSs as core and monolayer MoS_2 as shell. **Fig. 4.2(b)** shows the magnified view of the TiO_2/MoS_2 core@shell structure to clearly discern the monolayer MoS_2 at the interface of TiO_2. The HRTEM lattice fringe pattern of TiO_2/MoS_2 core@shell structure is depicted in **Fig. 4.2(c)** showing monolayer MoS_2 shell with thickness ~ 0.7 nm corresponding to the monolayer MoS_2. STEM

elemental mapping of TiO_2/MoS_2 heterojunction revealing the spatial distribution of the individual components and core@shell structure formation were described in details in our previous work.[8] The TEM image of $TiO_2/Au/MoS_2$ shows the encapsulation of Au/TiO_2 NS with monolayer MoS_2 shell, as shown in **Fig. 4.2(d)**. **Fig. 4.2(e)** depicts the enlarged view of $TiO_2/Au/MoS_2$ shown in **Fig. 4.2(d)**, which confirms the formation of monolayer MoS_2 over Au NP decorated on TiO_2 NS. **Fig. 4.2(e)** displays the HRTEM image of $TiO_2/Au/MoS_2$ showing the interface between different components. It can be noted that the monolayer MoS_2 is grown with overall uniformity over TiO_2/Au NS.

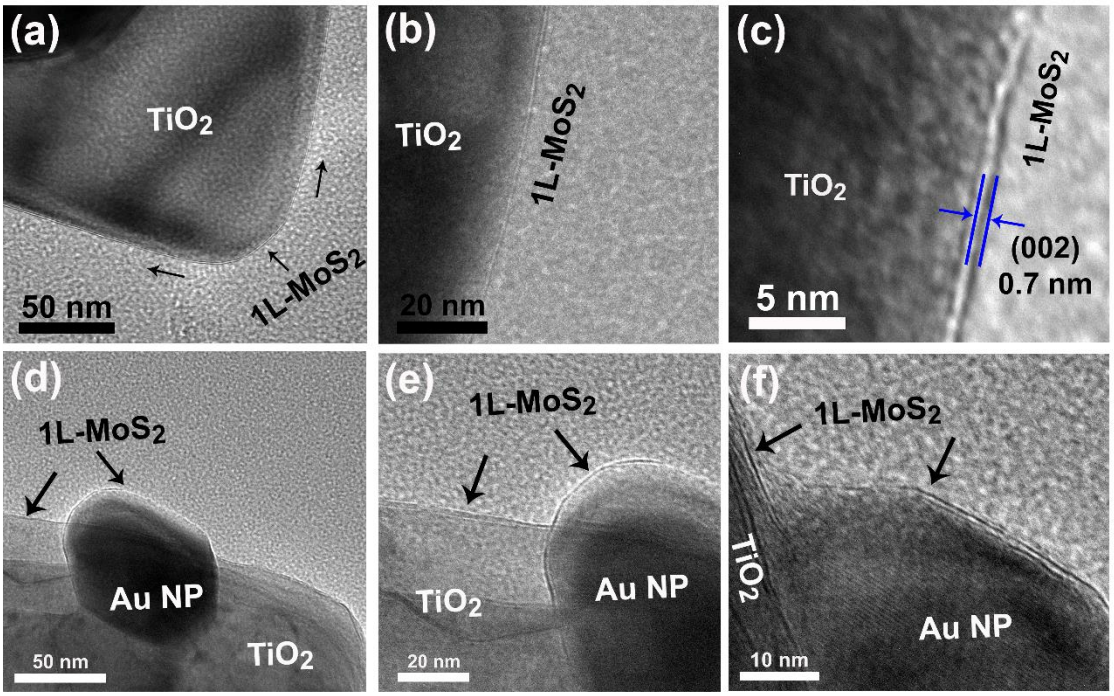

Fig. 4.2. (a) TEM image of TiO_2/MoS_2 sample displaying a seamless monolayer shell over the TiO_2 core, (b) a magnified view of TiO_2/MoS_2 shown in (a). (c) HRTEM lattice fringe pattern of TiO_2/MoS_2 showing the monolayer MoS_2 (thickness ~0.7 nm) covering the surface of TiO_2. (d) TEM image of $TiO_2/Au/MoS_2$ sample showing a uniform monolayer MoS_2 shell over the TiO_2 NS and Au NP, (e) an enlarged view of $TiO_2/Au/MoS_2$ shown in (d). (f) HRTEM lattice fringe pattern of $TiO_2/Au/MoS_2$ showing the interface between two components of the heterojunction system and seamless monolayer MoS_2 shell over the TiO_2 NS decorated with Au NP.

4.3.2. Structural and Compositional Analysis

4.3.2.1. XPS Analysis

The chemical composition, valence state and surface defects associated with the as-grown samples were studied in details by investigating the core level XPS spectra of the samples. **Fig. 4.3(a,b)** exhibit the comparative S 2p and Mo 3d core level XPS spectra, respectively, for the as-grown

MoS_2, TiO_2/MoS_2 and $TiO_2/Au/MoS_2$ samples. In case of pristine MoS_2, there are two distinct peaks of S 2p spectrum detected at 162 eV (S $2p_{3/2}$) and 163.1 eV (S $2p_{1/2}$), while Mo 3d XPS spectrum shows two strong peaks at 228.8 eV (Mo $3d_{5/2}$) and 231.9 eV (Mo $3d_{3/2}$), which are attributable to the 4+ valence state of Mo.[9] Successful growth of MoS_2 is thus confirmed. After the TiO_2/MoS_2 core@shell formation, both the S 2p and Mo 3d spectra are observed to be shifted towards lower binding energy side (~0.5 eV), as shown in **Fig. 4.3(a,b)**, which is due to the reduced charge density in monolayer MoS_2 after the core@shell formation, indicating a charge migration from MoS_2 to TiO_2. After the incorporation of Au or Ag NPs in between the TiO_2/MoS_2 heterojunction, no further shift was observed in the S 2p or Mo 3d binding energies.

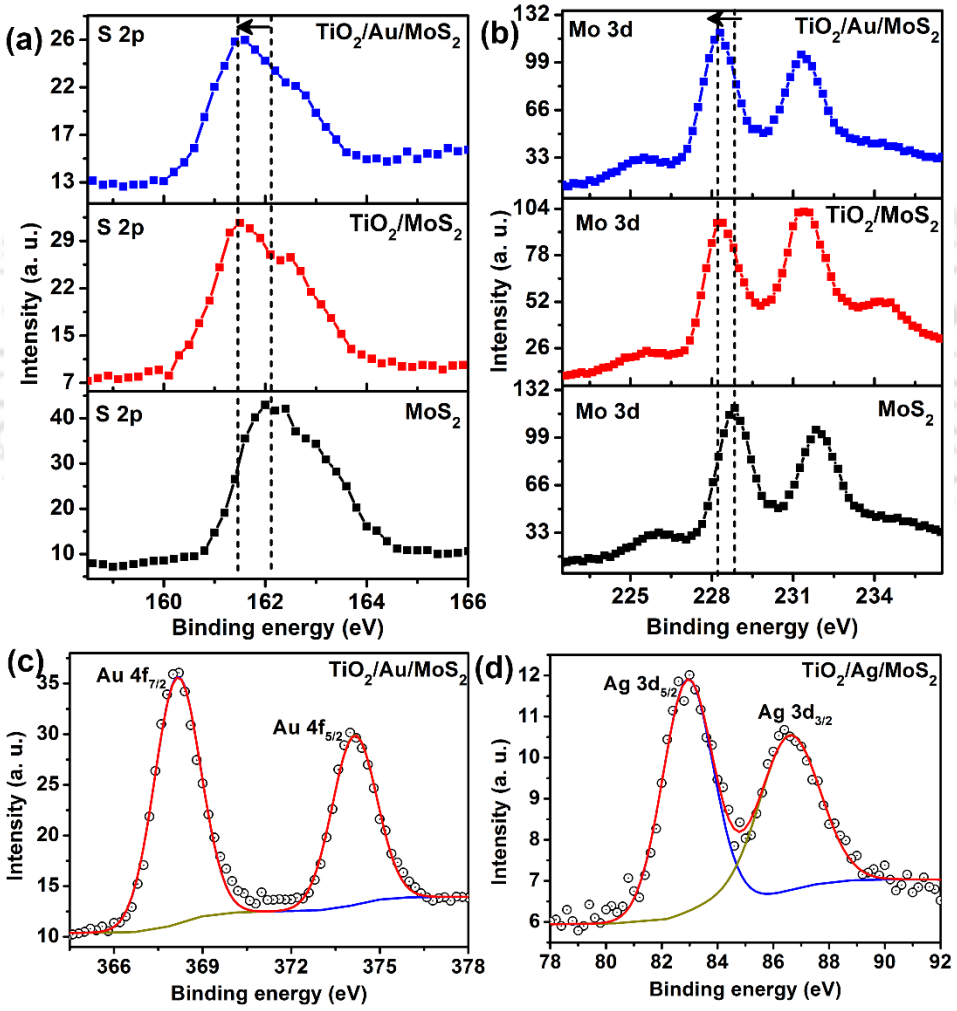

Fig. 4.3. (a) S 2p and (b) Mo 3d core level XPS spectra of MoS_2, TiO_2/MoS_2 and $TiO_2/Au/MoS_2$ samples. The vertical dotted lines show the shift in binding energy in each case. (c) Au 4f and (d) Ag 3d core level XPS spectra of $TiO_2/Au/MoS_2$ and $TiO_2/Ag/MoS_2$, respectively with the Gaussian deconvolution.

Fig. 4.3(c,d) exhibit the Gaussian deconvolution of Au 4f and Ag 3d core level XPS spectra of TiO_2/Au/MoS_2 and TiO_2/Ag/MoS_2, respectively. In each case, the Au or Ag is identified with a characteristic doublet, confirming the presence of metallic Au or Ag NPs, in between the TiO_2/MoS_2 core@shell heterojunction.

In order to investigate the chemical environment of TiO_2 core and its surface defects, Ti 2p and O 1s core level spectra were analyzed. **Fig. 4.4(a,b)** displays the core level Ti 2p XPS spectrum of each heterojunction system, which may be identified with two doublets located at ~458.6 eV (Ti $2p_{3/2}$) and ~464.2 eV (Ti $2p_{1/2}$), respectively with a splitting of 5.6 eV, which confirms the presence of Ti^{4+} valence state and thus the formation of TiO_2.[10] Besides the Ti^{4+} valence state, TiO_2/MoS_2 contains ~9.3% of Ti^{3+} state which increases to 11.8% after the loading of Au NPs on it. Interestingly, the oxygen vacancy (O_V) concentration is found to be increased from 28.2% to 31.5% after the loading of Au NPs into TiO_2/MoS_2 interface as shown in **Fig. 4.4(c,d)**. Thus, it can be concluded that the lattice strain in TiO_2 associated with the nonstoichiometric oxygen vacancy defects increases after the plasmonic NP loading.[11]

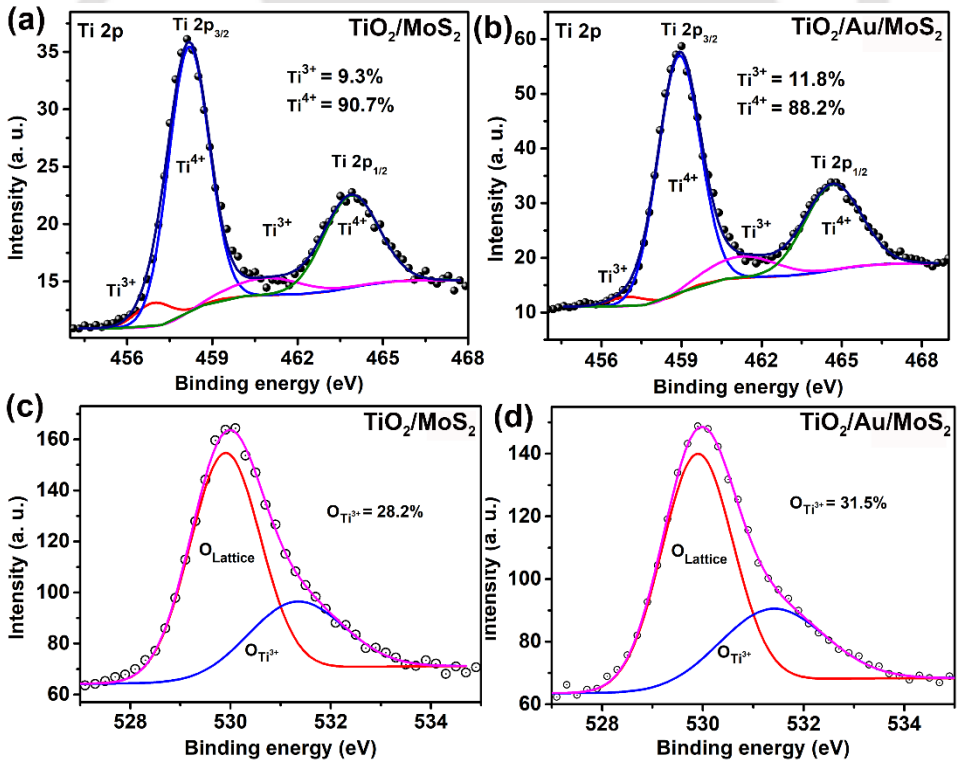

Fig. 4.4: (a,b) Gaussian deconvolution of Ti 2p core level XPS spectra of TiO_2/MoS_2 and TiO_2/Au/MoS_2, respectively. (c,d) Gaussian deconvolution of O 1s XPS spectra for TiO_2/MoS_2 and TiO_2/Au/MoS_2, respectively.

4.3.2.2. Raman Analysis

Micro-Raman measurements were performed on the TiO_2, MoS_2, Au/MoS_2, TiO_2/MoS_2, and TiO_2/Au/MoS_2 in order to investigate the crystallinity, phase, defects and doping in the systems.

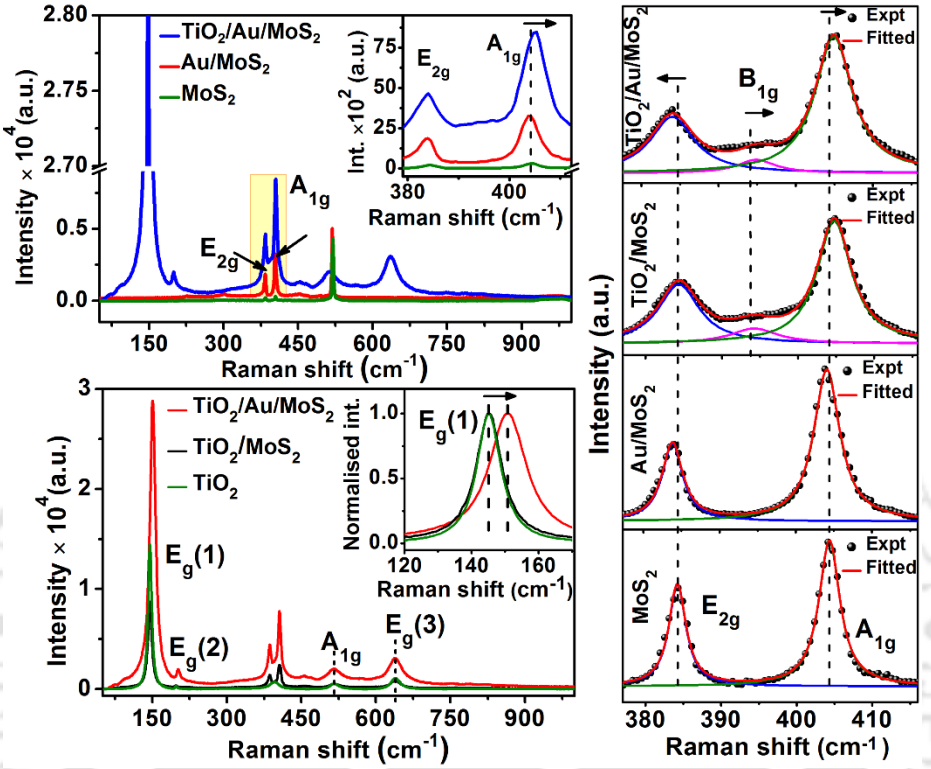

Fig. 4.5: (a) Comparison of the Raman spectra of MoS_2, Au/MoS_2 and TiO_2/Au/MoS_2. Inset shows the peaks in the shaded region corresponding to the characteristic peaks of MoS_2 in bare MoS_2, Au/MoS_2 and TiO_2/Au/MoS_2 in the range of 376-418 cm^{-1}. The vertical dashed lines are used to indicate the shift in Raman modes. (b) Comparison of the Raman spectra of bare TiO_2, TiO_2/MoS_2 and TiO_2/Au/MoS_2. Inset shows the normalized Eg peak of anatase TiO_2 for bare TiO_2, TiO_2/MoS_2 and TiO_2/Au/MoS_2 samples. (c) Lorentzian fitting of Raman modes of MoS_2 (E_{2g} and A_{1g}) for the different samples. The vertical dashed lines are used to indicate the shift in the Raman modes.

A comparative Raman spectra are shown in **Fig. 4.5(a,b)** for the different samples recorded using 514 nm Ar laser. Note that 514 nm excitation was chosen for Raman measurement based on the surface plasmon resonance absorption (shown later) of plasmonic Au NPs used in the heterostructures. MoS_2 exhibits two characteristic Raman modes E_{2g} and A_{1g}, corresponding to the in-plane vibration of two S atoms with respect to the Mo atoms and out-of-plane vibration of only S atoms in opposite directions with respect to the Mo atoms, respectively.[12] The frequency difference (Δk) between the Raman modes E_{2g} and A_{1g} is conventionally used to determine the layer number of the MoS_2 film. For bare MoS_2 and Au/MoS_2 samples, Δk between the two modes are estimated to be ~19.8 and ~20.5 cm^{-1}, respectively, (see **Table 4.2**) confirming the successful

growth of monolayer MoS_2 film, whereas for TiO_2/Au/MoS_2, $\Delta k \sim 21.3$ cm^{-1} as-shown in the inset of **Fig. 4.5(a)**. For bare MoS_2, the E_{2g} and A_{1g} modes appear at ~ 384.4 and ~ 404.2 cm^{-1}, respectively, whereas for Au/MoS_2, the E_{2g} mode red shifts and the A_{1g} mode frequency remains almost unaffected with a notable enhancement in the intensity. The Au NP deposited samples (Au/MoS_2 and TiO_2/Au/MoS_2) show ~11 and ~27 folds enhancement, respectively in the Raman intensity compared to the pristine MoS_2. This enhancement is due to the localized electric field arising from the surface plasmon resonance of the Au NPs, and eventually amplifying the Raman scattering. However, it is to be noted that for TiO_2/Au/MoS_2, the A_{1g} mode is blue shifted as compared to that of MoS_2 and Au/MoS_2. This shift is an indication of p-doping effect of 1L-MoS_2 lattice after the formation of HS with TiO_2, consistent with earlier reports.[8, 13] **Fig. 4.5(b)** shows a comparative Raman spectra of bare TiO_2, TiO_2/MoS_2 and TiO_2/Au/MoS_2. The TiO_2 NS shows the most prominent peaks at 145.1 cm^{-1} (E_g), and a few weak peaks at 198.2 (E_g), 396.8 (B_{1g}), 505 (A_{1g}), and 637.6 cm^{-1} (E_g), corresponding to the Raman active modes of pure anatase phase. The characteristic Raman active modes of other phases (rutile, brookite, TiO_2 (B)) were not observed, which essentially discards the formation of other crystal phases and confirms the growth of pure anatase phase. The Raman spectra of TiO_2/MoS_2 and TiO_2/Au/MoS_2 HS are comprised of the Raman peaks of both MoS_2 and TiO_2, confirming their co-existence in the HS. In TiO_2/MoS_2 HS, no observable shift was detected in the E_g(1) mode of anatase TiO_2 compared to the bare TiO_2 NS. On the other hand, for TiO_2/Au/MoS_2 HS, the characteristic E_g(1) peak is observed to be broadened with a huge blue shift by ~5.6 cm^{-1}, as compared to the bare TiO_2 and TiO_2/MoS_2 (see inset of **Fig. 4.5(b)**). This increase in the FWHM and large blue shift in the E_g(1) peak indicates the increase in the crystalline defects due to oxygen vacancies and strain induced by the oxygen vacancy related Ti relaxation within the anatase TiO_2 after the loading of Au NPs.[11] For a more detailed understanding, Lorentzian line shape was fitted in the range of 377−416 cm^{-1} for the E_{2g} and A_{1g} Raman bands of 1L-MoS_2 and B_{1g} band of TiO_2 for all the samples, as shown in **Fig. 4.5(c)**. For Au/MoS_2, the E_{2g} mode red shifts by ~ 0.7 cm^{-1}, while A_{1g} mode remains almost unaltered with respect to the pristine 1L-MoS_2. This may be due to the uniaxial strain in the 1L-MoS_2 owing to the curvature of the Au NPs.[6] Similarly, for TiO_2/Au/MoS_2 HS, the E_{2g} mode red shifts by ~0.7 cm^{-1} with unaffected A_{1g} mode in comparison with TiO_2/MoS_2 HS. However, the characteristic Raman mode A_{1g} for both the HS samples (TiO_2/Au/MoS_2 and TiO_2/MoS_2) exhibits a relative blue shift by ~0.8 cm^{-1} as compared to the pristine 1L-MoS_2. This blue shift of the A_{1g}

mode indicates an effective p-type doping effect in the MoS_2 layer due to the strong electron–phonon coupling.[14] It can be understood that the shift in A_{1g} mode is due to the transfer of electrons from MoS_2 to TiO_2 at the interface.[15] This further explains the higher Δk value for TiO_2/Au/MoS_2 HS. The characteristic Raman mode B_{1g} for TiO_2 shows a blue shift by ~0.7 cm^{-1} in the TiO_2/Au/MoS_2 HS with respect to that of TiO_2/MoS_2 HS, which may be due to the presence of compressive strain in TiO_2 lattice induced by the loading of Au NPs, and strong interaction between TiO_2 and Au atoms.[16] Similar results were observed with Ag NPs coated heterostructures.

Table 5.1: *Summary of the Raman modes, their separation (Δ**k**) showing various species for 1L-MoS_2 and its HS.*

	Raman modes		
sample	**E_{2g} (cm^{-1})**	**A_{1g} (cm^{-1})**	**Δk (cm^{-1})**
MoS_2	384.41	404.24	19.83
Au/MoS_2	383.71	404.16	20.45
TiO_2/Au/MoS_2	383.72	405.03	21.31
TiO_2/MoS_2	384.40	404.97	20.57

4.3.3. Optical Analysis

4.3.3.1. UV-Vis Absorption Study

UV-visible diffuse reflectance spectroscopy (DRS) was adopted for the detailed investigation of optical absorption properties of the as-prepared samples. **Fig. 4.6** shows the Kubelka-Munk (K-M) plot of each of the samples corresponding to their reflectance spectra against wavelength. Bare TiO_2 NSs exhibit strong excitonic absorption in the UV region but negligibly low absorption in the visible region (above 400 nm). Pristine monolayer MoS_2 displays two distinct absorption peaks at 609 nm and 656 nm, which are attributed to the intrinsic B and A excitonic absorption bands, respectively originating from the band-edge excitons.[8] Another additional peak is detected at 429 nm, which is associated with the direct transition to the conduction band from the deep valence band.[17] In the TiO_2/MoS_2 core@shell heterojunction, apart from the strong UV absorption coming from the TiO_2 core, each characteristic absorption peak of MoS_2 shell has been detected at the identical spectral position. In TiO_2/Ag/MoS_2 and TiO_2/Au/MoS_2 core@shell heterojunction systems, besides the characteristic TiO_2 and MoS_2 absorption bands, two distinct peaks are detected at 435 nm and 539 nm, which are described as the localized surface plasmon resonance

(LSPR) bands of Ag and Au NPs, respectively. As the plasmon resonance frequency directly depends on the dielectric constant of the surrounding medium, this red shift in the SPR bands can be interpreted due to the changed dielectric environment of plasmonic NPs surrounded by the TiO_2 and MoS_2 layers.

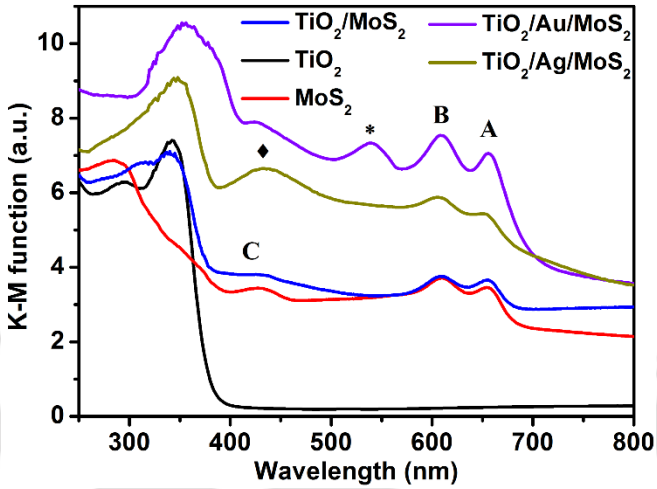

Fig. 4.6: Kubelka–Munk function plot with wavelength for various samples derived from their respective diffuse reflectance spectra. A, B and C are the characteristic excitonic absorption bands of monolayer MoS_2. The symbols '*' and '♦' are the SPR bands of Au and Ag NPs, respectively.

4.3.3.2. Photoluminescence Study

Fig. 4.7(a) displays representative PL spectra of 1L-MoS_2, Au/MoS_2 and TiO_2/Au/MoS_2 HS, measured with 514 nm excitation at room temperature. The peak intensities of these spectra are in an arbitrary unit. The PL peak intensities of TiO_2/Au/MoS_2 and Au/MoS_2 show a substantial enhancement, compared to that of bare 1L-MoS_2 which corresponds to the enhancement factor of ~463 and ~22, respectively. Additionally, the PL spectra of TiO_2/Au/MoS_2 and Au/MoS_2 were observed to be blue shifted with respect to bare 1L-MoS_2. In the Au/MoS_2 heterojunction, the enhancement effect is attributed to; firstly, monolayer MoS_2 was grown over the Au NP forming a core@shell heterojunction. This configuration allows the total incident light to interact with the MoS_2 film rather than partially absorbed or reflected by the Au NPs when Au NPs are on top of MoS_2 layers. Furthermore, the MoS_2 film could re-absorb the light reflected or scattered by Au NPs.[18] Secondly, in plasmonic excitation, a concentrated local electric field is formed at the vicinity of the metal NPs (Au or Ag) creating plasmonic hot spots. These hot spots aid as a source of localized surface plasmon resonance (LSPR). Thus, this field surrounding each Au/Ag NP is coupled with the 1L-MoS_2 by the screening effect and hence leading to the enhanced electromagnetic field at the interface between the Au(Ag) NPs and 1L-MoS_2. In TiO_2/MoS_2 HS,

the giant PL enhancement is attributed to the transfer of excess electrons from MoS_2 to TiO_2, causing heavy p-doping in the 1L-MoS_2.[15] Thus, for $TiO_2/Au/MoS_2$ HS, a combined effect of plasmonic enhancement of Au/MoS_2 HS and charge transfer in TiO_2/MoS_2 HS leads to a dramatic enhancement in the PL intensity. Note that the $TiO_2/Ag/MoS_2$ has a similar configuration to $TiO_2/Au/MoS_2$ HS but shows a much lesser enhancement in the PL intensity (see **Fig. 4.7(b)**).

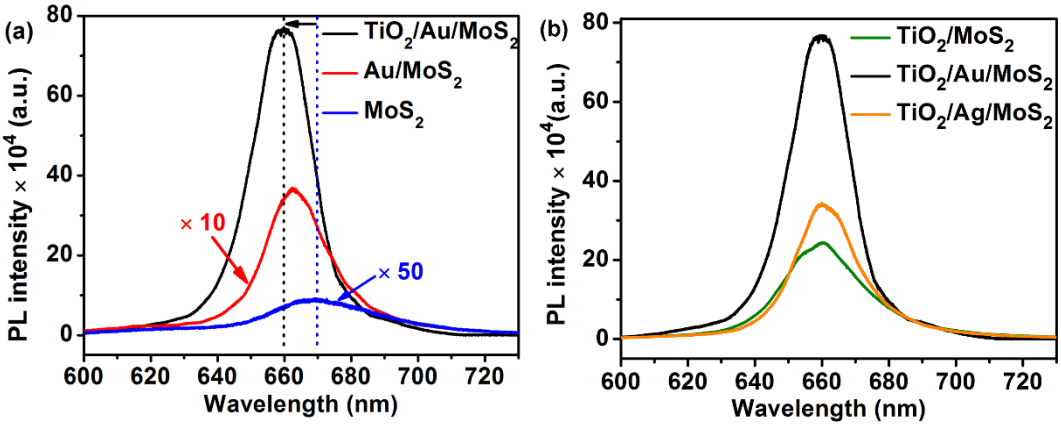

Fig. 4.7: (a) Comparative PL spectra of pristine monolayer MoS_2, Au/MoS_2 and $TiO_2/Au/MoS_2$ at room temperature (RT) (b) Comparative PL spectra of TiO_2/MoS_2, $TiO_2/Ag/MoS_2$ and $TiO_2/Au/MoS_2$ at RT.

For a better understanding of the origin of PL emission and its enhancement, each PL spectrum was deconvoluted with multiple Gaussian peaks. The PL spectra of as-grown samples MoS_2, Au/MoS_2 and $TiO_2/Au/MoS_2$ could be fitted properly with four Gaussian peaks: the neutral exciton (A^0), negative trion (A^-), B exciton, and the bound exciton (X),[19] as depicted in **Fig. 4.8(a-c)**. The spectral weights of the fitted peaks of A^0, A^-, B and X peaks of the as-grown samples are presented in **Table 4.3**. The A^0 and B excitonic peaks originate from the direct band gap transition between valence-band spin-orbit splitting and the minima of the conduction at the K point in the Brillouin Zone.[1] The A^- exciton (trion) peak, is caused by the unintentional substrate doping and charged impurities on the grounds of CVD growth of MoS_2 film,[19] and the radiative recombination of bound excitons from the defect trap states is assigned to the X exciton peak.[19] Interestingly, the spectral weight of A^0 exciton peak is observed to be increased from 38.8 to 66.2%, while that of A^- decreased from 32.7 to 22.4 %, for Au/MoS_2 compared to MoS_2. This increase in the A^0 exciton peak is attributed to the LSPR of Au NPs beneath the monolayer MoS_2. More interestingly, for $TiO_2/Au/MoS_2$ heterojunction, the spectral weight of A^0 exciton peak has increased dramatically from 38.8 to 85.5 %, while that of A^- decreased from 32.7 % to a negligible amount compared to pristine counterpart, as shown in **Figure 4.8(a, b and c)** and **Table 4.3**. This modification in the

spectral weight observed in TiO_2/Au/MoS_2 heterojunction is associated with firstly, the transfer of excess electrons present in 1L-MoS_2 which is intrinsically n-type to the TiO_2 side through the interface due to the appropriate band alignment (type-II) between MoS_2 and TiO_2. Thus, the depletion of electrons from the 1L-MoS_2 by means of charge (electron) transfer would lead to the p-doping effect in the 1L-MoS_2, which leads to the conversion of trions to neutral excitons and thus leads to the PL enhancement of 1L-MoS_2 as mentioned in **Chapter 3, Section 3.3.4.2**. The blue shift of Raman and PL spectra is also consistent with the above scenario.

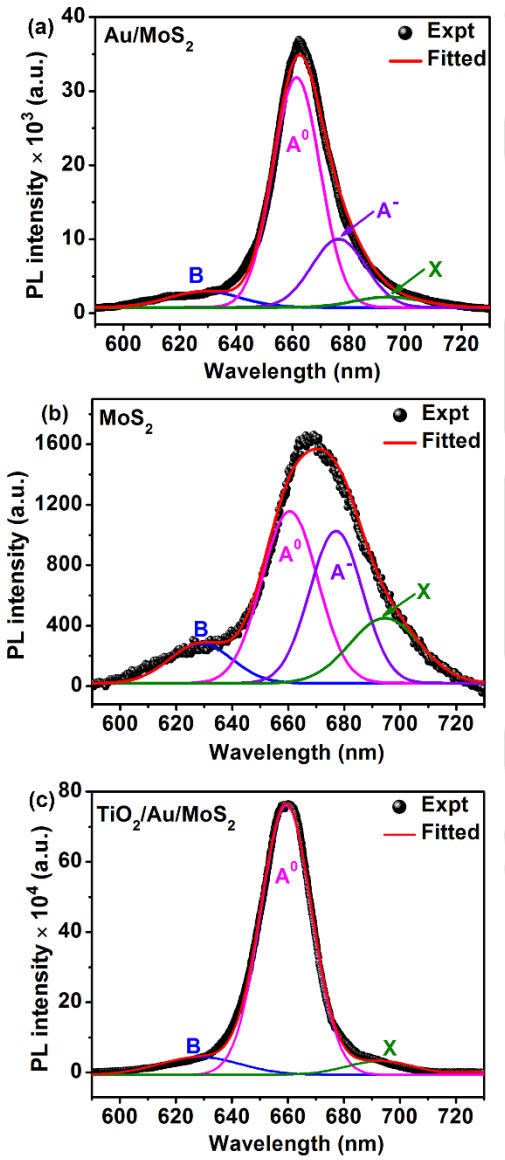

Fig. 4.8: Gaussian deconvolution of RT PL spectra of pristine (a) Au/MoS_2, (b) MoS_2 and (c) TiO_2/Au/MoS_2 HS, respectively.

Secondly, upon illumination with the resonant wavelength of the plasmonic NS, there is a strong collective oscillations of the free electrons in Au/Ag NPs, creating LSPR that couples and interact with the excitons in 1L-MoS_2. Thus, the carrier excitation rate of 1L-MoS_2 through the local field enhancement can be considerably enhanced by the LSPR at the metal/semiconductor interface. The spectral weight of the defect-bound excitons (X) decreases from ~18.4 to~4.4% and to ~ 5.6 % for Au/MoS_2 and TiO_2/Au/MoS_2, respectively, as compared to the pristine MoS_2 due to the lower defect density in 1L-MoS_2 grown on TiO_2 and Au-TiO_2.

Table 4.3: *Summary of the Gaussian deconvoluted PL spectra showing various species for MoS_2, Au/MoS_2 and TiO_2/Au/MoS_2.*

sample	Relative weightage of PL peaks				Overall PL enhancement factor
	B-exciton (B) (%)	A-exciton (A) (%)	Trion (A^-) (%)	Bound exciton	
MoS_2	10.1	38.8	32.7	18.4	1
Au/MoS_2	7.0	66.2	22.4	4.4	22
TiO_2/Au/MoS_2	8.9	85.5	-	5.6	463

4.3.4. Electric Field Enhancement by Au NPs

The intensities of electromagnetic fields around Au NPs can be defined by considering a concentric sphere (Au NPs) of radius a and dielectric constant ε_1 placed in a medium with dielectric constant ε_m in which there exists a uniform static electric field. The field enhancement factor (η) is defined as the intensity ratio of the resultant field ($\overrightarrow{E_2}$) to the incident field ($\overrightarrow{E_0}$),[20] expressed as:

$$\eta = \frac{|\overrightarrow{E_2}|^2}{|\overrightarrow{E_0}|^2} = \left|1 + 2\frac{a^3}{r^3}\frac{\varepsilon_1 - \varepsilon_m}{\varepsilon_1 + \varepsilon_m}\right|^2 = \left|1 + 2\frac{a^3}{r^3}\beta\right|^2 \quad (1)$$

where $\beta = \frac{\varepsilon_1 - \varepsilon_m}{\varepsilon_1 + \varepsilon_m}$ (2)

Now, if we consider a thin outer spherical shell (1L-MoS_2) of radius a_2 with dielectric constant ε_2 over an inner spherical core (Au NPs) of radius a_1 with dielectric constant ε_1 placed in a medium with dielectric constant ε_m as shown in **Fig. 4.9(a)**, the modified field enhancement factor (η) is

$$\eta = \frac{|\vec{E_2}|^2}{|\vec{E_0}|^2} = \left|1 + 2\frac{a_2^3}{r^3}\frac{(\varepsilon_2-\varepsilon_m)(\varepsilon_1+2\varepsilon_2)+f^3(\varepsilon_1-\varepsilon_2)(\varepsilon_m+2\varepsilon_2)}{(\varepsilon_2+2\varepsilon_m)(\varepsilon_1+2\varepsilon_2)+f^3(2\varepsilon_2-2\varepsilon_m)(\varepsilon_1-\varepsilon_2)}\right|^2 = \left|1 + 2\frac{a^3}{r^3}\beta\right|^2 \quad (3)$$

where $\beta = \frac{(\varepsilon_2-\varepsilon_m)(\varepsilon_1+2\varepsilon_2)+f^3(\varepsilon_1-\varepsilon_2)(\varepsilon_m+2\varepsilon_2)}{(\varepsilon_2+2\varepsilon_m)(\varepsilon_1+2\varepsilon_2)+f^3(2\varepsilon_2-2\varepsilon_m)(\varepsilon_1-\varepsilon_2)}$ (4)

and $f = \frac{a_1}{a_2}$ (5)

It is to be noted that, the dielectric constants ε_1, ε_2, and ε_m are complex functions of wavelength and are expressed as $\varepsilon_j = \varepsilon_j' + i\varepsilon_j''$, where j = 1, 2 and m, and both ε_j' and ε_j'' are real. Using the above equations (1), (2) and (3), the calculation of the field enhancement factor η was carried out. The wavelength dependent dielectric constant data for Au and 1L-MoS_2 were attained from previous works.[20-21] **Fig. 4.9(b)** shows the calculated field enhancement factor η around spherical core of Au NP and a thin shell of 1L-MoS_2 in air. Note that, the calculation of η is made at the observing point r = a_2. We observed that the η value shows a peak at ~ 540 nm, for the Au NPs is which is consistent with the absorption spectra shown in **Fig 4.6**. The field enhancement factor is found to be ~ 24, which is also in excellent agreement with the PL enhancement of Au/MoS_2 HS, showing an enhancement of ~ 22 times compared to 1L-MoS_2, as shown in **Fig. 4.7(a).**

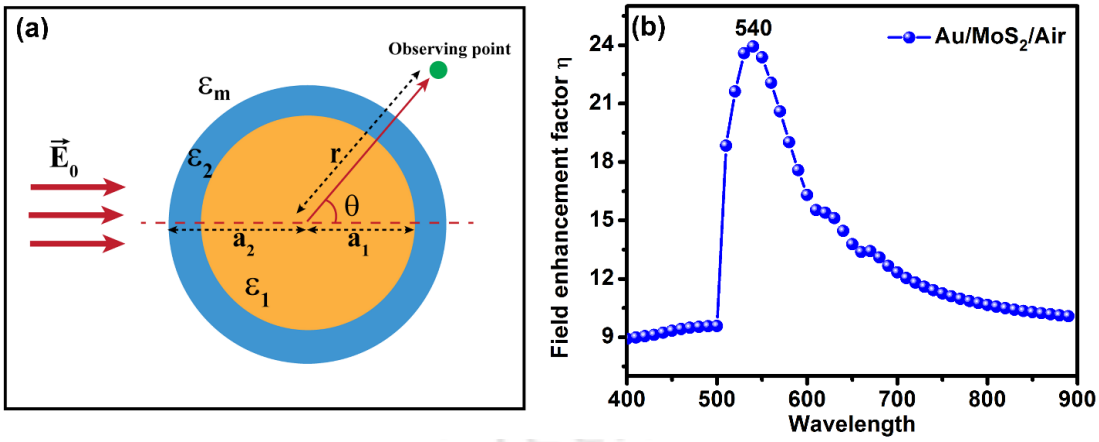

Fig. 4.9: (a) Schematic representation of a concentric spherical core-shell structure consisting of an inner spherical core (Au NPs and an outer spherical shell (1L-MoS_2) in an electric field. (b) Calculated field enhancement factor η of the core shell Au/MoS_2 HS in air.

From our previous work[8] the in situ CVD-grown 1L-MoS_2 shell over the 3D TiO_2 NSs facilitates a PL enhancement factor of 30 as compared to that of 1L-MoS_2 grown on sapphire substrate. On the other hand, the enhancement in the PL intensity of Au/MoS_2 HS is found to be ~ 22 times that of 1L-MoS_2. Thus, for a ternary core-shell TiO_2/Au/MoS_2 hybrid structure, the expected

enhancement of the PL is the combine enhancement of the Au/MoS_2 and the TiO_2/MoS_2 hybrid system, which is ~ (22×30=660) times. However, we observed that the PL enhancement for the TiO_2/Au/MoS_2 HS to be ~ 463 times compared to 1L-MoS_2, which is lesser than the above factor. This lower enhancement factor is primarily due to reduce charge transfer at the TiO_2/MoS_2 interface in the presence of the ultrathin Au NPs. Further, as some of the electron hole pairs generated may be delocalized by the thermal energy and, consequently, nonradiative recombination processes are activated.

4.3.5. Mechanism of giant PL enhancement:

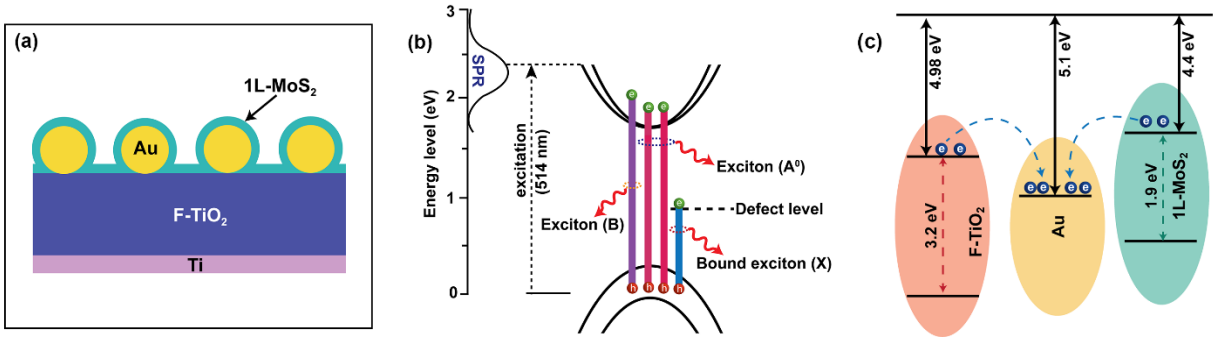

Fig. 4.10: (a) Schematic representation of the TiO_2/Au/MoS_2 HS. (b) The mechanism of plasmon-exciton coupling in MoS_2-Au NP hybrids. (c) Schematic of the band diagram showing the pathways of probable charge transfer from F-TiO_2 to Au and from 1L-MoS_2 to Au, leading to enhanced excitonic PL emissions.

Fig. 4.10(a) shows the schematic representation of the TiO_2/Au/MoS_2 core shell HS, where TiO_2 NS acts as a substrate on which Au NPs are coated and finally a single layer MoS_2 shell is deposited by CVD technique. Upon excitation with 514 nm laser, which is close to the surface plasmon resonance wavelength of the Au NPs, plasmonic hot spot is formed at the vicinity of the Au NP and hence serves as a source of LSPR as shown in **Fig. 4.10(b).** In addition, the 1L-MoS_2 shell over the Au NP creates a coupling between the excitons of MoS_2 and localized surface plasmons of Au NP and thus leading to the enhanced PL intensity. Additionally, from the band alignment of the 1L-MoS_2 and Au NP, there is a possibility of charge transfer from MoS_2 side to the Au NP as shown in **Fig. 4.10(c)**, resulting in reduced trion formation. On the other hand, at the heterojunction between MoS_2 and TiO_2, the excess electrons are transferred from the MoS_2 side to the TiO_2 side resulting in MoS_2 being highly p-doped as can be understood from the type-II band alignment of the 1L-MoS_2 and the TiO_2**.** Furthermore, this leads to the conversion of negative trions to neutral excitons, which enormously enhances the overall PL intensity of 1L-MoS_2.[15] Thus, the 1L-MoS_2 in the ternary HS sample exhibits a dramatic enhancement in the PL emission due to the formation

of special geometry of the heterojunction at the interfaces. Firstly, the MoS_2/TiO_2 interface facilitates the optimum conversion of negative trion to the neutral exciton and secondly, the MoS_2/Au interface enables the electromagnetic field enhancement driven by the LSPR. These two aspects effectively amplify the PL emission intensity. Our theoretical estimate closely matches with the experimental data on plasmonic enhancement factor.

4.4. Conclusion

In summary, this work presents a simple and powerful strategy to achieve a dramatically high PL enhancement in 1L-MoS_2 using plasmonic Au/Ag NPs grown on TiO_2 NSs as a substrate. An array of Au NPs were grown on the hydrothermally grown hierarchical TiO_2 NSs followed by a direct CVD growth of monolayer MoS_2 shell, forming a TiO_2/Au/MoS_2 ternary core-shell HS. This architecture allows a strong interaction between the incident light and 1L-MoS_2 leading to a ~463-fold enhancement in PL intensity compared to the pristine 1L-MoS_2 at room temperature. The Raman and HRTEM analyses reveal the formation of TiO_2/Au/MoS_2 core-shell HS. This work demonstrates two major mechanisms for the enhancement of PL intensity in 1L-MoS_2. Firstly, the excess electrons responsible for trion formation are transferred from the MoS_2 to TiO_2 at the interface of MoS_2/TiO_2, leading to the p-doping effect in MoS_2 lattice, which enhances the neutral exciton emission and inhibit the trion emission. Secondly, the exciton-plasmon coupling between excitons of the 1L-MoS_2 and surface plasmons of the Au NPs at the MoS_2/Au interface is believed to enhance PL emission enormously, as shown from the theoretical estimate of the field enhancement factor. The present study demonstrates that MoS_2 based HS offers a promising way to improve future nanophotonic and optoelectronic devices, such as photodetectors, plasmonic field-effect transistors etc.

References

1. Nan, H., et al., Strong Photoluminescence Enhancement of Mos2 through Defect Engineering and Oxygen Bonding. *ACS Nano* **2014**, *8*, 5738-5745.
2. Wei, X.; Yu, Z.; Hu, F.; Cheng, Y.; Yu, L.; Wang, X.; Xiao, M.; Wang, J.; Wang, X.; Shi, Y., Mo-O Bond Doping and Related-Defect Assisted Enhancement of Photoluminescence in Monolayer Mos2. *AIP Advances* **2014**, *4*, 123004.
3. Mouri, S.; Miyauchi, Y.; Matsuda, K., Tunable Photoluminescence of Monolayer Mos2 Via Chemical Doping. *Nano Lett.* **2013**, *13*, 5944-5948.
4. Paul, K. K.; Sreekanth, N.; Biroju, R. K.; Narayanan, T. N.; Giri, P. K., Solar Light Driven Photoelectrocatalytic Hydrogen Evolution and Dye Degradation by Metal-Free Few-Layer Mos2

Nanoflower/Tio2(B) Nanobelts Heterostructure. *Solar Energy Materials and Solar Cells* **2018**, *185*, 364-374.

5. Paul, K. K.; Sreekanth, N.; Biroju, R. K.; Pattison, A. J.; Escalera-López, D.; Guha, A.; Narayanan, T. N.; Rees, N. V.; Theis, W.; Giri, P. K., Strongly Enhanced Visible Light Photoelectrocatalytic Hydrogen Evolution Reaction in an N-Doped Mos2 /Tio2(B) Heterojunction by Selective Decoration of Platinum Nanoparticles at the Mos2 Edge Sites. *Journal of Materials Chemistry A* **2018**, *6*, 22681-22696.

6. DiStefano, J. G.; Li, Y.; Jung, H. J.; Hao, S.; Murthy, A. A.; Zhang, X.; Wolverton, C.; Dravid, V. P., Nanoparticle@Mos2 Core–Shell Architecture: Role of the Core Material. *Chemistry of Materials* **2018**, *30*, 4675-4682.

7. Paul, K. K.; Jana, S.; Giri, P. K., Tunable and High Photoluminescence Quantum Yield from Self-Decorated Tio2 Quantum Dots on Fluorine Doped Mesoporous Tio2 Flowers by Rapid Thermal Annealing. *Particle & Particle Systems Characterization* **2018**, *35*, 1800198.

8. Paul, K. K.; Mawlong, L. P. L.; Giri, P. K., Trion-Inhibited Strong Excitonic Emission and Broadband Giant Photoresponsivity from Chemical Vapor-Deposited Monolayer Mos2 Grown in Situ on Tio2 Nanostructure. *ACS Applied Materials & Interfaces* **2018**, *10*, 42812-42825.

9. Baker, M. A.; Gilmore, R.; Lenardi, C.; Gissler, W., Xps Investigation of Preferential Sputtering of S from Mos2 and Determination of Mosx Stoichiometry from Mo and S Peak Positions. *Applied Surface Science* **1999**, *150*, 255-262.

10. Göpel, W.; Anderson, J. A.; Frankel, D.; Jaehnig, M.; Phillips, K.; Schäfer, J. A.; Rocker, G., Surface Defects of Tio2(110): A Combined Xps, Xaes and Els Study. *Surface Science* **1984**, *139*, 333-346.

11. Paul, K. K.; Giri, P. K., Role of Surface Plasmons and Hot Electrons on the Multi-Step Photocatalytic Decay by Defect Enriched Ag@Tio2 Nanorods under Visible Light. *The Journal of Physical Chemistry C* **2017**, *121*, 20016-20030.

12. Li, H.; Zhang, Q.; Yap, C. C. R.; Tay, B. K.; Edwin, T. H. T.; Olivier, A.; Baillargeat, D., From Bulk to Monolayer Mos2: Evolution of Raman Scattering. *Adv. Funct. Mater.* **2012**, *22*, 1385-1390.

13. Li, Y.; Wang, H.; Feng, Q.; Zhou, G.; Wang, Z.-S., Gold Nanoparticles Inlaid Tio2 Photoanodes: A Superior Candidate for High-Efficiency Dye-Sensitized Solar Cells. *Energy & Environmental Science* **2013**, *6*, 2156-2165.

14. Kim, M. S.; Roy, S.; Lee, J.; Kim, B. G.; Kim, H.; Park, J.-H.; Yun, S. J.; Han, G. H.; Leem, J.-Y.; Kim, J., Enhanced Light Emission from Monolayer Semiconductors by Forming Heterostructures with Zno Thin Films. *ACS Appl. Mater. Interfaces* **2016**, *8*, 28809-28815.

15. Mawlong, L. P. L.; Paul, K. K.; Giri, P. K., Direct Chemical Vapor Deposition Growth of Monolayer Mos2 on Tio2 Nanorods and Evidence for Doping-Induced Strong Photoluminescence Enhancement. *The Journal of Physical Chemistry C* **2018**, *122*, 15017-15025.

16. Wilcoxon, J. P.; Samara, G. A., Strong Quantum-Size Effects in a Layered Semiconductor: ${\Mathrm{Mos}}_{2}$ Nanoclusters. *Physical Review B* **1995**, *51*, 7299-7302.

17. Rajender, G.; Choudhury, B.; Giri, P. K., In Situ Decoration of Plasmonic Au Nanoparticles on Graphene Quantum Dots-Graphitic Carbon Nitride Hybrid and Evaluation of Its Visible Light Photocatalytic Performance. *Nanotechnology* **2017**, *28*, 395703.

18. Zeng, Y.; Li, X.; Chen, W.; Liao, J.; Lou, J.; Chen, Q., Highly Enhanced Photoluminescence of Monolayer Mos2 with Self-Assembled Au Nanoparticle Arrays. *Adv. Mater. Interf.* **2017**, *4*, 1700739.

19. Tongay, S., et al., Defects Activated Photoluminescence in Two-Dimensional Semiconductors: Interplay between Bound, Charged, and Free Excitons. *Sci. Rep.* **2013**, *3*, 2657.

20. Tanabe, K., Field Enhancement around Metal Nanoparticles and Nanoshells: A Systematic Investigation. *The Journal of Physical Chemistry C* **2008**, *112*, 15721-15728.

21. Jung, G.-H.; Yoo, S.; Park, Q. H., Measuring the Optical Permittivity of Two-Dimensional Materials without a Priori Knowledge of Electronic Transitions. In *Nanophotonics*, **2019**; 8, 263.

भारतीय प्रौद्योगिकी संस्थान गुवाहाटी
Indian Institute of Technology Guwahati

Chapter 5

Coupled Charge Transfer Dynamics and Photoluminescence Quenching in Monolayer MoS_2 Decorated with WS_2 Quantum Dots

In this chapter, we investigated the tunability of the photoluminescence (PL) and doping of the monolayer MoS_2 (1L-MoS_2) by decorating it with WS_2 quantum dots (WS_2 QD). The direct bandgap 1L-MoS_2 and WS_2 QDs are grown by chemical vapor deposition and liquid exfoliation methods, respectively. The PL intensity of bare 1L-MoS_2 is systematically quenched with its decoration with WS_2 QDs at different concentrations. A decrease in the work function of 1L-MoS_2 with the decoration of WS_2 QDs was established from the Kelvin probe force microscopy analysis. A detailed quantitative analysis using the four-energy level model involving coupled charge transfer was employed to explain the redshift and the systematic decrease in the intensity of the PL peak in 1L-MoS_2/WS_2 QD heterostructure. The modulation of the PL in the heterostructure is attributed to the increase in the formation of negative trions through the charge transfer from WS_2 QD to the 1L-MoS_2 and thus making the 1L-MoS_2 heavily n-type doped. This study establishes the contribution of defects in the coupled charge transfer dynamics in 1L-MoS_2, and it lays out a convenient strategy to manipulate the optical and electrical properties of 1L-MoS_2 for various optoelectronic applications.

5.1. Introduction

The monolayer transition metal dichalcogenides TMDs (e.g., MoS_2, WS_2, $MoSe_2$, WSe_2, etc.) have drawn great attention for their fascinating properties and diverse range of applications, such as transistors,[1-2] photodetectors,[2-4] light-emitting devices,[5] and sensors.[6] The strong Coulomb interaction between the charge carriers in the atomically thin two dimensional materials create stable excitonic states even at room temperature.[7-8] Among most investigated 2D TMDs, monolayer MoS_2 (1L-MoS_2) has attracted significant attention due to its abundance in nature, tunable optical band gap, high chemical stability and efficient carrier generation.[8-10] An effective and convenient method to tune the optical properties of MoS_2 is to control the charge density. To induce charge transfer to/from the 1L-MoS_2, numerous methods were used, such as chemical doping,[11-12] plasmonic hot-electron doping,[13] and electrical doping.[14-15] Construction of hybrid architectures with MoS_2 is favorable due to the excitonic nature of optical excitations in its

monolayer form. Interfacing 1L-MoS_2 with zero-dimensional semiconductor nanocrystal, also known as quantum dots (QDs) is one of the possible ways to control the optical properties of 1L-MoS_2. The QDs have remarkable properties such as strong absorption, size-dependent energy bandgap, and high-photoluminescence. In case of a hybrid 0D/2D structure, the absorptive properties of monolayer TMD are enhanced by the QD donors which improve the optoelectronic devices, producing more efficient photodetectors and solar cells. TMD QDs such as WS_2 QDs have gained wide interest due to their high solubility in both aqueous and non-aqueous solvents, good electrical conductivity and flexible to hybridize with other nanomaterials. Therefore, this material is highly promising for a wide range of applications. In a previous study, Li et al.[16] fabricated graphene QDs/1L-MoS_2 heterostructure (HS) and demonstrated charge transfer from graphene QDs to the 1L-MoS_2. This charge transfer at the interface between the QD and the 1L-MoS_2 induces competition between neutral exciton and charged exciton (trion) population resulting in the modulation in the photoluminescence (PL) of 1L-MoS_2. However, in these studies, the role of defects in PL quenching of the 1L-MoS_2 has not been addressed. To our knowledge, there is no report on the charge transfer from WS_2 QDs to 1L-MoS_2 and the resulting doping and PL quenching effect. It is interesting to study the role of defects in the charge transfer dynamics in the 1L-MoS_2 layers through PL spectroscopy and its implications for future applications. In this chapter, we show that by solving the carrier dynamics based on the coupled rate equations, we can have a better understanding of the contribution of the defects in the recombination dynamics of the 1L-MoS_2/WS_2 QD hybrid structure.

5.2. Experimental Details

5.2.1. Sample Preparation

5.2.1.1. Synthesis of WS_2 quantum dots

High purity WS_2 powder (Sigma Aldrich, 99%) was dispersed in 80 ml N-methyl-2-pyrrolidinone (NMP) (Alfa Aesar, HPLC grade, 95%) and sonicated using an ultrasonic homogenizer (Sonic Ruptor 250, Omni International) for 15 hours. Subsequently, the suspension was allowed to settle for 12 hours and was centrifuged for 45 minutes at 12000 rpm. The top 2/3rd of the solution (supernatant) contains the WS_2 quantum dots, while the bottom 1/3rd (centrifugate) comprises of the bigger WS_2 quantum dots and the nanosheets (See **Fig. 5.1**). The excess solvent from the

centrifugate was evaporated with constant stirring and the resultant residue was dispersed in Milli-Q water at various concentrations (4, 8, 12, 16, 20, 24, 28, 32, 36 mg/L) for further experiments.

5.2.1.2. Growth of monolayer MoS_2 by chemical vapor deposition (CVD) technique and formation of heterostructure with WS_2 quantum dots

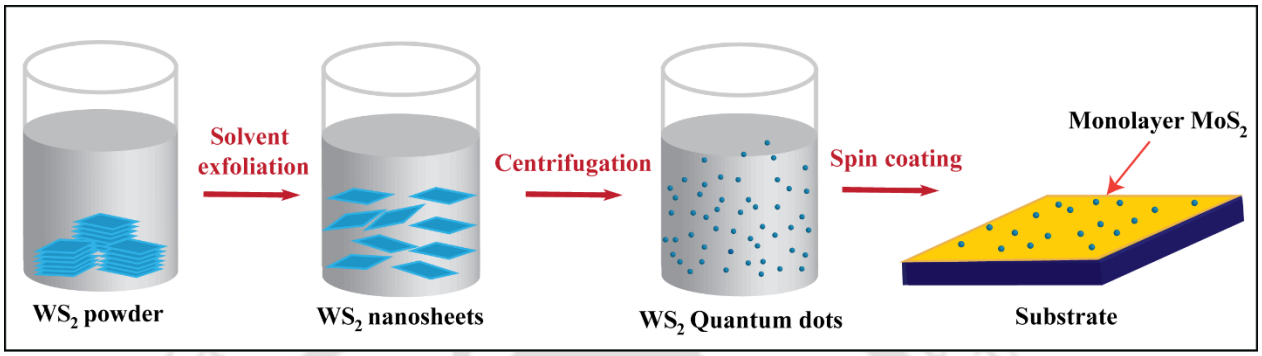

Fig. 5.1. Schematic illustration of the synthesis of WS_2 QDs and their decoration onto 1L-MoS_2.

1L-MoS_2 were grown by a typical CVD process using a two zone furnace. The precursors (MoO_3 and S) are placed inside a 2-inch quartz tube-based horizontal muffle furnace at the center of their respective zones. SiO_2 substrates were used for the growth of monolayer MoS_2. These substrates were then placed face down on top of the quartz mask with a circular opening, which were then put on top of the boat containing MoO_3 precursor. The temperature of the zone containing the substrate was ramped at a rate of 15 °C/min up to 700 °C and was maintained for 5 min, with an Ar flow rate of 10 sccm. Subsequently, the temperature of the other zone containing the sulfur precursor reaches 150 °C. The furnace was then allowed to cool down to room temperature. Further details of the experiment is described in **Chapter 2, Section 2.3.2.** The morphology, crystal structure and phase of the sample were characterized by FESEM, TEM, XRD, XPS and micro-Raman analyses. For the formation of the heterostructure, WS_2 QDs were spin-coated onto the 1L-MoS_2 and are dried before optical characterizations were carried out (See **Fig. 5.1**).

5.2.2. Characterization Techniques

The details of the FESEM, AFM, and Raman measurements were described in **Chapter 2, Section 2.1.3**. In order to carry out the surface potential (SP) analysis of the samples, the Kelvin probe force microscopy (KPFM) measurements were done. Conducting platinum (Pt)/iridium (Ir)-coated tips were used for KPFM studies, having the optimum frequency of operation ~72 kHz. To avoid the noise between the topographical and the surface potential measuring images, the measurements

were carried out in the dual-pass lift mode. The calculation of the work function for the sample (ϕ_s) was obtained from the AFM by using Pt/Ir tips in the KPFM mode. TEM imaging was used to examine the decoration of WS_2 QD on 1L-MoS_2. For this purpose, the CVD grown 1L-MoS_2 was transferred from the SiO_2 substrates to carbon-coated Cu-grids. To transfer the as-grown MoS_2 film, the sample was coated with polymethylmethacrylate (PMMA) by spin coating at 1500 rpm for 60 s, and then baked at 140 °C for 10 min. The PMMA-coated sample was then treated with 6 M NaOH solution for one hour to etch out the PMMA supported MoS_2 film, which was then repeatedly washed with DI water. Then, the film was fished out onto a Cu grid and allowed to dry at relatively low temperature (50 °C). The PMMA was removed from the MoS_2 film by the addition of acetone dropwise. WS_2 QDs of the concentration 4 mg/L was then drop cast on the sample for TEM imaging. X-ray photoelectron spectroscopy (XPS) has been carried out using a PHI X-tool automated photoelectron spectrometer (ULVAC-PHI, Japan) with an Al Kα X-ray beam (1486.6 eV) at a beam current of 20 mA. The C 1s spectrum at 284.8 eV was used as a standard value for the correction of the shift in the binding energy of various elements. A commercial spectrophotometer (PerkinElmer, Lambda 950) was used to study the UV−vis absorption spectra of the 1L-MoS_2/WS_2 QD HS as well as its individual counterparts. The details of the TEM measurements were discussed in **Chapter 3, Section 3.2.3**

5.3. Results and Discussion

5.3.1. Morphology Studies

Fig. 5.2(a) displays the optical image of monolayer MoS_2 film grown with triangular-shaped MoS_2 grains towards the edge of the sapphire substrate. These triangular shaped MoS_2 regions merge to form a large continuous monolayer film with millimeter-scale uniformity, as evident from **Fig. 5.2(a)**. The layer uniformity is evident from the small difference in contrast over the whole film. Details of the growth conditions for monolayer MoS_2 film over a large area have been discussed in **Chapter 2, Section 2.3.2.** **Fig. 5.2(b)** shows the AFM image of the triangular-shaped monolayer MoS_2. It reveals that the triangular-shaped MoS_2 have a tendency to interconnect with each other rather than overlap when they grow to form a continuous film as seen by the homogeneous color contrast, which further indicates a good uniformity. The AFM height profile taken along the black line in **Fig. 5.2(c)** indicates a thickness of ~ 0.7 nm, which corresponds to monolayer thickness. The AFM image of the 1L-MoS_2/WS_2 QD HS is shown in **Fig. 5.2(d)**. The

height profile of MoS_2 layer and the QDs decorated over it clearly revealed the growth of monolayer MoS_2 and monolayer WS_2 QDs, as shown in **Fig 5.2(e).**

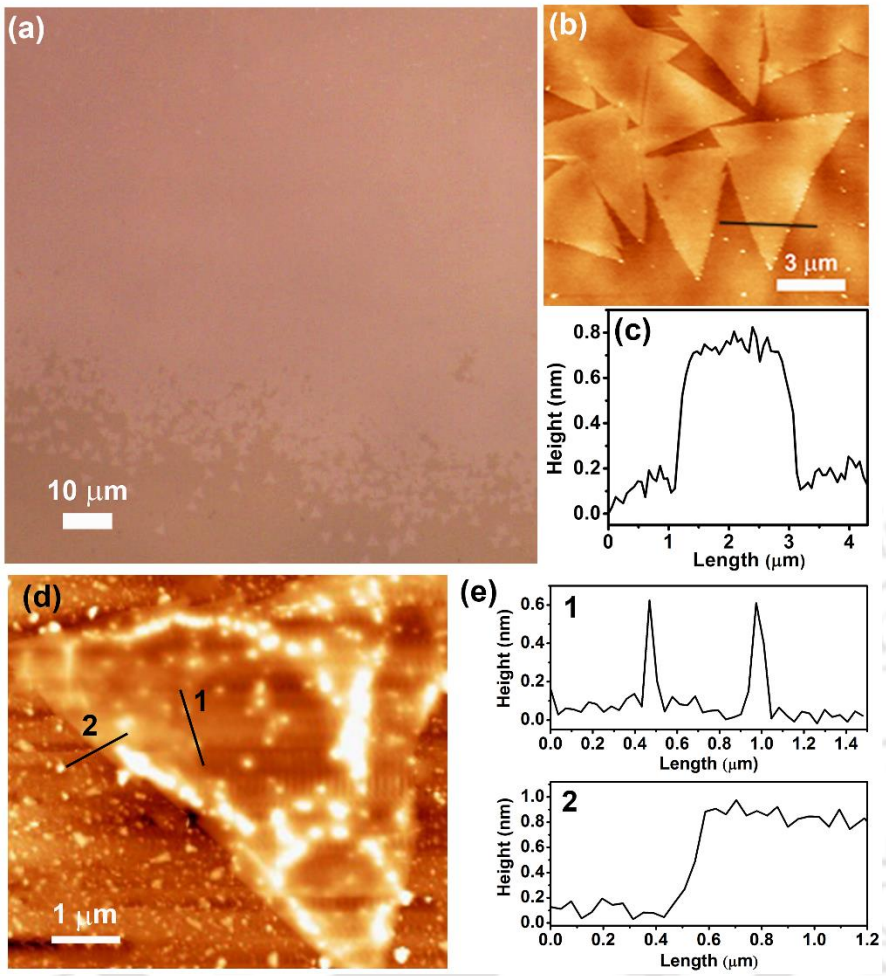

Fig. 5.2. (a) Optical microscope image of large area monolayer MoS_2 grown on sapphire substrate. (b) AFM image of triangular shaped monolayer MoS_2 on sapphire substrate, and (c) AFM height profile taken along the black line in (b) showing a step height of ~0.7 nm confirming the monolayer MoS_2 growth. (d) AFM image of triangular shaped monolayer MoS_2 decorated with WS_2 QDs on sapphire substrate, and (e) AFM height profile taken along the black lines (position 1 and 2) in (d) showing the height profile of WS_2 QDs and the monolayer MoS_2, respectively.

The typical morphological and structural properties of the as-prepared WS_2 QDs were studied using TEM. **Fig. 5.3(a)** shows the TEM image of the WS_2 QDs. The selected area electron diffraction (SAED) pattern (top right inset of **Fig. 5.3(a)**) shows the presence of diffused rings, which indicates the polycrystalline nature of the QD. The WS_2 QDs size ranges from 3-11 nm with an average diameter of ~ 4.5 nm, as shown in **Fig. 5.3(b)**. The high-resolution TEM (HRTEM) image of the WS_2 QD (**Fig. 5.3 (c)**) displays ordered lattice fringes. The inset in **Fig. 5.3(c)** shows the inverse fast Fourier transform (IFFT) image of the lattice fringes with an interplanar spacing

of 0.22 nm, which corresponds to the (103) plane of WS_2. To examine the coverage of the WS_2 QDs on the 1L-MoS_2, TEM imaging of the 1L-MoS_2/WS_2 QD HS was carried out. **Fig. 5.3(d)** shows a low magnification TEM image of the QD decorated on large area 1L-MoS_2 film. A higher magnification TEM image is depicted in **Fig. 5.3(e)**, where a uniform surface coverage of WS_2 QDs is clearly observed over the MoS_2 layer. The corresponding SAED pattern shows the polycrystallinity of the WS_2 QDs. In addition, hexagonally aligned diffraction spots are attributed to the (101) plane of MoS_2 (inset of **Fig. 5.3 (e)**). Thus, the as-grown 1L-MoS_2 is highly crystalline in nature and is uniformly

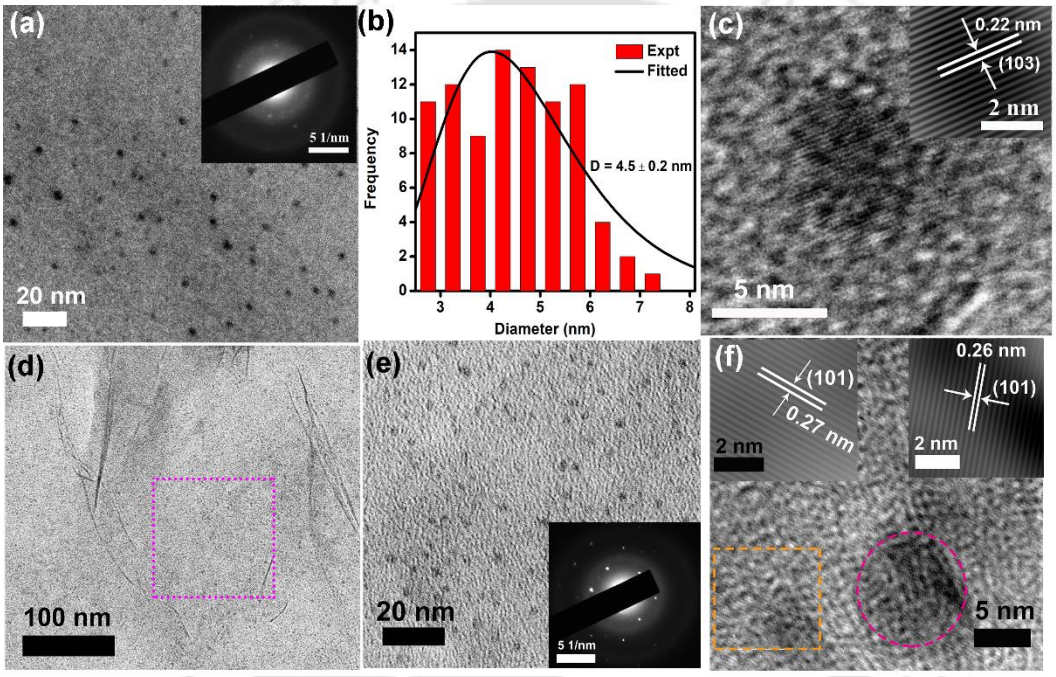

Fig. 5.3: (a) The TEM image of WS_2 QDs; the top right inset shows the corresponding (b) the size distribution of WS_2 QDs with an average size of 4.5 ± 0.2 nm; (c) HRTEM lattice image of a WS_2 QD; the inset shows the IFFT lattice image showing a d-spacing of 0.22 nm; (d,e) The TEM image of uniform decoration of WS_2 QDs on the 1L-MoS_2. The inset of 2(e) shows the SAED pattern with hexagonally aligned diffraction spots (1L-MoS_2) and diffused rings (WS_2 QDs). (f) HRTEM lattice fringe pattern of 1L-MoS_2/WS_2 QDs HS. The top-left inset is the IFFT of the region enclosed by the dotted square showing the planes corresponding to MoS_2. The top right inset is the IFFT of the area inside the dotted circle displaying the lattice fringe pattern of a WS_2 QD.

decorated with WS_2 QDs. The HRTEM image of the 1L-MoS_2/WS_2 QD HS is displayed in **Fig. 5.3(f)**, which shows distinct lattice planes. The top-left inset shows the IFFT of the atomic planes of the MoS_2 film. The lattice d-spacing is 0.27 nm that corresponds to (101) plane of MoS_2. Additional ordered domains are observed with a lattice spacing of 0.24 nm, which can be assigned to the (101) plane of WS_2 (top right inset of **Fig. 5.3(f)**).

5.3.2. Structural and Optical Analyses

5.3.2.1. XPS Analysis

The chemical composition of the 1L-MoS_2 and WS_2 QDs was confirmed from the XPS analysis. **Fig. 5.4** shows the XPS spectra of the core level Mo 3d, W 4f and S 2p bands for the 1L-MoS_2 and WS_2 QDs samples. **Fig. 5.4(a)** depicts the elemental composition of 1L-MoS_2 with the presence of the peaks of Mo and S. In **Fig. 5.4(b)**, several Mo $3d_{5/2}$ and $3d_{3/2}$ peaks fitted for Mo (3d) envelope, indicating that more than one Mo species were present. The first peak, centered at 226.4 eV, agrees well with that of the 2s binding energy of elemental S. The strongest Mo 3d doublet peaks for 1L-MoS_2 detected at 229.1 eV ($3d_{5/2}$) and 232.0 eV ($3d_{3/2}$) correspond to the +4 oxidation state of Mo, confirming the formation of MoS_2.[18] Additional Mo peaks were observed at 232.8 eV and 235.2 eV corresponding to the oxides of Mo metal (Mo^{6+}) probably due to the presence of traces of MoO_3 in the sample after CVD growth and post-synthesis exposure to air. **Fig. 5.4(c)** exhibits the S 2p XPS spectra of 1L-MoS_2 with peaks at ~161.8 eV (S $2p_{3/2}$) and ~162.9 eV (S $2p_{1/2}$) corresponding to the divalent sulfide ions (S^{2-}). Additionally, a peak at 162.1 eV (S $2p_{3/2}$) (with 8.1 % spectral weight) is present that could be due to the presence of surface defects introduced during the CVD growth. These defect sites are the S vacancies, as there are fewer S atoms around the Mo atoms at such sites.[19]

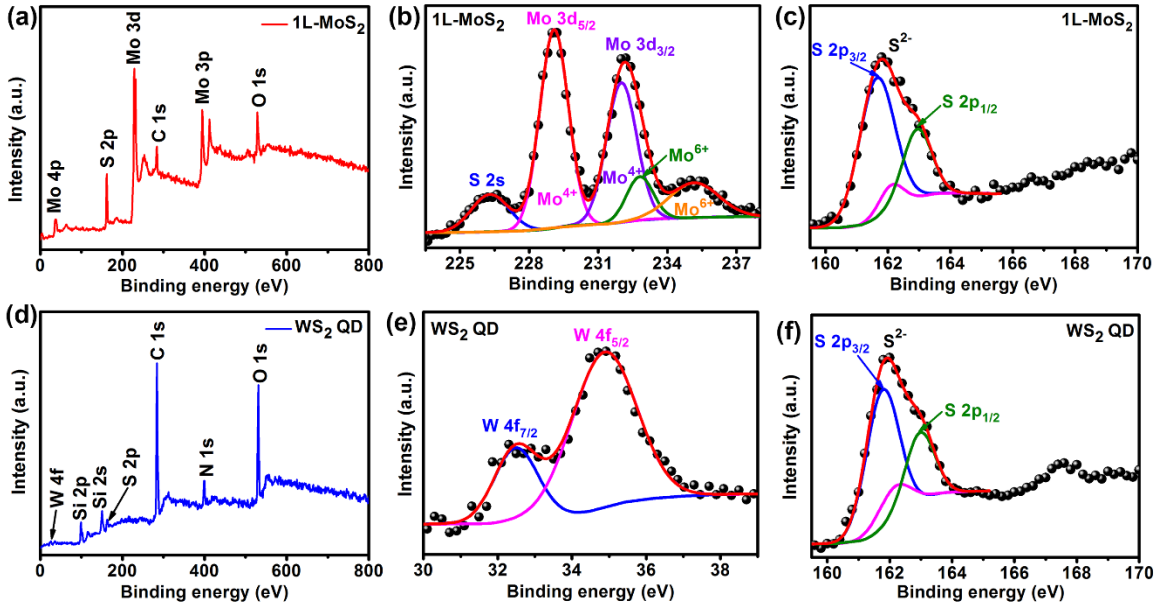

Fig. 5.4. (a) XPS survey spectrum of 1L-MoS_2. Core level XPS spectra of 1L-MoS_2 for (b) Mo 3d, (c) S 2p. (d) XPS survey spectrum of WS_2 QD. Core level XPS spectra of WS_2 QD for (e) W 4f and (f) S 2p, respectively. The symbols are experimental data and the solid curves are Gaussian fittings.

The survey scan XPS spectrum of WS_2 QDs shows the presence of W, S, C, N and O peaks (**Fig. 5.4(d)**). For the as-synthesized WS_2 QD, the peaks at 32.5 eV and 34.8 eV are identified to be from W $4f_{7/2}$ and W $4f_{5/2}$, respectively, corresponding to the 4+ oxidation state of W, as shown in **Fig. 5.4(c)**, which are consistent with those reported for 2H-WS_2.[20] **Fig. 5.4(d)** shows the S 2p XPS spectrum of the WS_2 QD with peaks at ~161.8 eV (S $2p_{3/2}$), and ~162.9 eV (S $2p_{1/2}$), which are similar to that of the 1L-MoS_2 sample. The existence of surface defects (S vacancies) in the WS_2 QD is shown by the presence of the peak at 162.1 eV (S $2p_{3/2}$) (with 13.5% spectral weight), which may have occurred during the synthesis by liquid exfoliation method. Additionally, there is a small peak at 167.5 eV corresponding to SO_2 which suggests the minor presence of oxidized sulfur edges.

5.3.2.2. Raman and XRD Analyses

Raman spectroscopy has been widely used for the determination of the number of layers,[21] the strain, the external field and doping effects[16, 21-22] in 2D TMDs. **Fig. 5.5(a)** shows the comparative Raman spectra for 1L-MoS_2 and 1L-MoS_2/WS_2 QD HS at room temperature. Two characteristic Raman modes E_{2g} and A_{1g} corresponding to the in-plane vibration of Mo and S atoms and out-of-plane vibration of S atoms, respectively, can be clearly seen.[21] The frequency difference (Δk) between E_{2g} and A_{1g} modes has been used to identify the number of layers in MoS_2.[21] For 1L-MoS_2 sample, the measured Δk is ~19.6 cm^{-1} confirming the monolayer growth,[21] which is consistent with the AFM result. WS_2 QDs also show the presence of two characteristic Raman modes E_{2g} and A_{1g} of WS_2, which confirms the crystallinity of the QDs.[23] A comparative Raman analysis of the WS_2 QDs and WS_2 nanosheets shows a red shift in the E_{2g} mode and a blue shift in the A1g mode in the QDs with respect to that of the nanosheets (see **Fig. 5.5(b)**). This shift in the Raman modes is attributed to the decrease in the number of layers of the WS_2 QD compared to the WS_2 nanosheets.[23] Interestingly, after the formation of the 1L-MoS_2/WS_2 QD HS, the position of the Raman modes of MoS_2, A_{1g} is red-shifted by 1.2 cm^{-1}, while that of E_{2g} is not influenced (See **Table 5.1**). This shift occurs due to the fact that the A_{1g} mode couples much more strongly with electrons than the E_{2g} mode.[22] The redshift of the A_{1g} mode indicates an effective n-type doping effect in the MoS_2 layer due to the strong electron-phonon coupling.[24] Crystallinity of the WS_2 QDs is further confirmed from the XRD analysis (see **Fig. 5.5(c)**) showing a strong peak at 14.3° corresponding to the (002) plane and multiple weak peaks corresponding to (004), (101), (103), (006) and (105) lattice planes of 2H-phase of crystalline WS_2 (JCPDS 08-0237).[25]

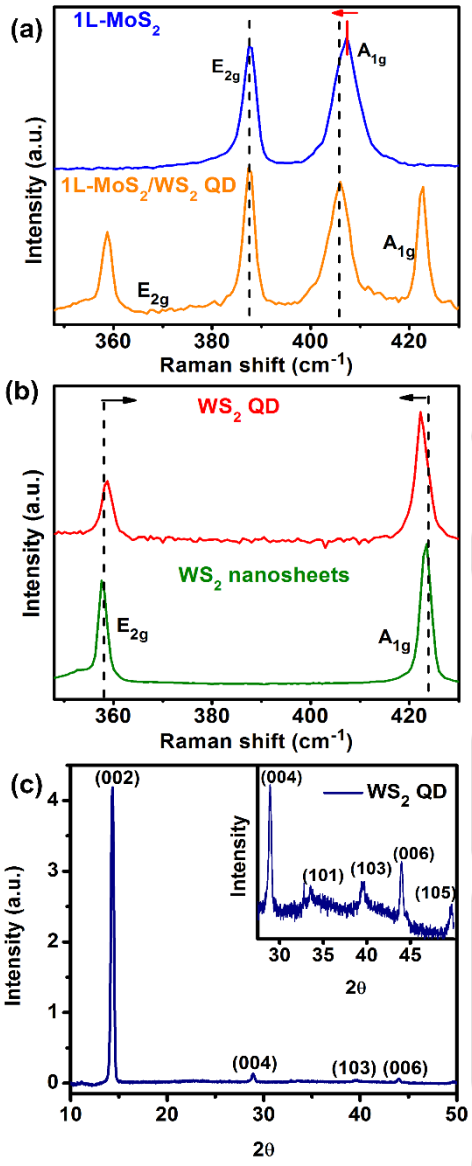

Fig. 5.5. (a) Comparison of the Raman spectra of 1L-MoS_2, WS_2 QD and 1L-MoS_2/WS_2 QD HS (with 24 mg/L concentration of WS_2 QD). The vertical dotted lines show no shift of the E_{2g} and a redshift of the A_{1g} Raman band of MoS_2 in the 1L-MoS_2/WS_2 QD HS. (b) Comparative Raman spectra of the WS_2 QD and WS_2 nanosheet depicting two Raman modes E_{2g} and A_{1g}, respectively. (c) XRD spectrum of WS_2 QD. The inset depicts a magnified view of the XRD pattern in the range 2θ=28° to 49°.

Table 5.1: *Summary of the Raman modes and their separation (Δ**k**) for 1L-MoS_2 and 1L-MoS_2/WS_2 QD HS.*

Sample	E_{2g} (cm^{-1})	A_{1g} (cm^{-1})	Δk (cm^{-1})
1L-MoS_2	387.6	407.2	19.6
1L-MoS_2 /WS_2 QD	387.6	406.0	18.4

5.3.2.3. UV-vis and Photoluminescence Study

Fig. 5.6(a) shows the UV-vis absorption spectra of the samples. The 1L-MoS_2 exhibits three excitonic absorption peaks A, B and C at 1.85, 2.00 and 2.74 eV, respectively. The excitonic A and B peaks originate from the transitions between the spin-orbit split valence band and the lowest conduction band at the K and K′ points of the Brillouin zone.[7] The C absorption peak is assigned to the direct transition from the deep valence band to the conduction band.[26] The absorption spectrum of WS_2 QDs (see **Fig. 5.6(a)**) shows low absorbance in the visible range and no distinct excitonic features in contrast to that of the monolayer WS_2 reported in the literature.[27] Since the QDs are mostly monolayer, the bandgap is expected to be direct type and the optical bandgap calculated from the Tauc plot is 3.45 eV as shown in **Fig. 5.6(b)**, which is much higher than the monolayer WS_2.[27]

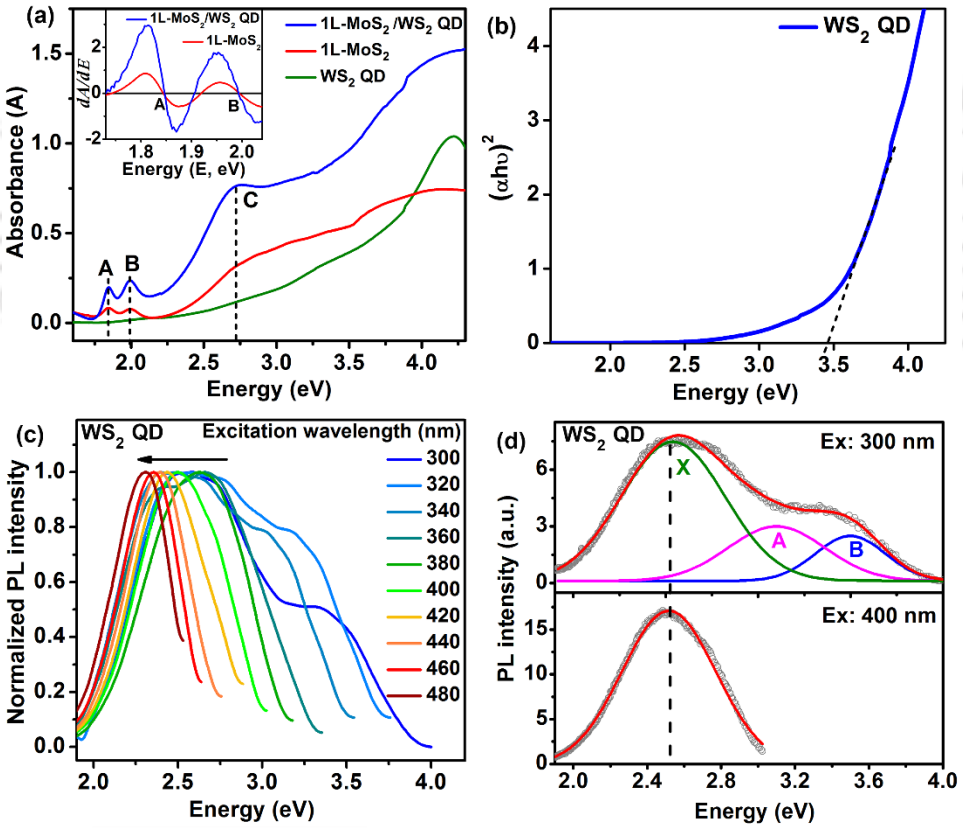

Fig. 5.6. (a) UV-visible absorption spectra of 1L-MoS_2, WS_2 QDs and 1L-MoS_2/WS_2 QD (with 24 mg/L concentration of WS_2 QD). A, B and C represent the characteristic excitonic absorption bands of the 1L-MoS_2. The inset shows the first derivative of the absorption spectra of 1L-MoS_2 and 1L-MoS_2/WS_2 QD. (b) Tauc plot for the WS_2 QDs indicating a bandgap of 3.45 eV. (c) Normalized PL emission spectra of WS_2 QDs at various excitation wavelengths (300–480 nm). (d) Gaussian fitting of the PL emission spectrum for the excitation of 300 nm and 400 nm. The constituent peaks are denoted as B, A, and X excitonic emissions.

In case of 1L-MoS_2/WS_2 QD HS, three absorption peaks (A, B, C) were observed, which are consistent with the spectrum of 1L-MoS_2. A marginal enhancement in the absorbance of 1L-MoS_2/WS_2 QD HS compared to that of individual absorbance of 1L-MoS_2 and WS_2 QDs is observed in the spectral range 2.48 to 4.59 eV, which may be due to the combined effect of the increase in the number of layers as well as the enhanced light-material interaction in the heterostructure.[28] To determine precisely the absorption peaks of spin-orbit split B and A excitons in the 1L-MoS_2 and 1L-MoS_2/WS_2 QDs, we have taken the first derivative of the absorption spectra (see the inset of **Fig. 5.6(a)**). The A and B excitonic peaks for 1L-MoS_2 are located at 1.844 eV and 1.990 eV, respectively. For 1L-MoS_2/WS_2 QD HS, there is only ~4 meV redshift in the A excitonic peak with respect to the 1L-MoS_2. This small redshift in the A peak may be due to the n-type doping of 1L-MoS_2 after the formation of the HS due to the charge transfer from the WS_2 QDs to the 1L-MoS_2. In contrast to our case of marginal shift, in case of a chemical doped system the shift in the excitonic peaks in the absorption spectra has been more prominent.[29]

The as-synthesized WS_2 QDs are highly fluorescent in nature with a quantum yield (QY) of ~15%. The PL emission spectra usually depend on the wavelength of excitation due to the contribution from multiple states and size distribution.[30] **Fig. 5.6(c)** displays the normalized PL emission spectra of the WS_2 QDs for various excitation wavelengths. As the excitation wavelength is increased gradually from 300 to 480 nm, the emission peak position systematically redshift from 2.52 eV to 2.31 eV. This excitation wavelength-dependent PL shift is poorly understood in the literature. The broadening in PL peak usually results from the polydispersity in the WS_2 QD size, which is attributed to the colloidal synthesis process.[31-32] To further explain the broad PL spectrum in WS_2 QDs under 300 nm excitation, we have deconvoluted the spectrum with three Gaussian peaks: the B exciton, the neutral A exciton, and the defect bound exciton X, as shown in **Fig. 5.6(d)**. The A and B-excitons centered at 3.1 eV and 3.5 eV arise from the giant spin-orbit splitting of the valence band in the K-K′ point.[20] The B and A excitons arise from the splitting of the valence band at the K point due to strong spin-orbit coupling in the W atom of WS_2.[7] The energy difference between these two peaks is found to be ~400 meV, which is similar to that of monolayer WS_2.[33] The contribution from the A and B exciton is gradually reduced with increasing excitation wavelength and hence the spectrum is narrower than that with low wavelength excitation. The X band in the fitting centered at 2.54 eV is associated with the surface defect bound exciton X, and at higher excitation wavelength (>380 nm), the PL emission arises only from the bound exciton

transition (**Fig. 5.6(d)**). Thus, a selective excitation of different states at different excitation wavelength is responsible for the red shift and narrowing of the PL peak at higher wavelength of excitation. This explains the wavelength-dependent shift in the PL emission peaks in WS_2 QDs. Note that the PL peak assignments are based on the measured bandgap and the relationship: $E_B=E_g-E_b+E_{SO}$,[34] where E_B is the B exciton peak position, E_b is the exciton binding energy (~0.3 eV for monolayer WS_2). E_{SO} is the energy difference arising due to splitting of the valence band due to strong spin-orbit coupling (~0.4 eV) in the W atom of WS_2.[33] Thus, based on the measured bandgap, E_B is expected to be ~3.5 eV. Likewise, the A exciton peak is expected at ~3.1 eV. The deconvoluted peaks positions in **Fig. 5.6(d)** closely match with the above. Note that the defect contribution (X-band) to the PL intensity is very significant in all the spectra.

Fig. 5.7(a) displays representative PL spectra of pristine 1L-MoS_2, WS_2 QD and 1L-MoS_2/WS_2 QD HS, measured with 488 nm laser excitation. The PL emission peak for the WS_2 QD is broad due to the size distribution of QDs and it is much weak compared that of the 1L-MoS_2. The PL peak position (~2.28 eV) is consistent with the result presented in **Fig. 5.6(c)**.[35] Interestingly, this peak is at a much higher energy than that of 1L-WS_2.[27] The broadening and blue shifting of the PL peak of the WS_2 QD originate from the quantum size effect as well as the surface defect states.[30] For 1L-MoS_2, we observe a PL peak at 1.86 eV with 488 nm excitation. However, after the formation of the 1L-MoS_2/WS_2 QD HS the PL peak position is redshifted by ~ 30 meV and the intensity is also partially quenched. Such a redshift and quenching of the PL is an indication of the possible charge transfer and n-type doping of 1L-MoS_2 due to the specific band alignment at the interface. This is consistent with the Raman analysis discussed earlier.

To further interpret the possible origin of the PL evolution, a deconvolution analysis was carried out on 1L-MoS_2 and 1L-MoS_2/WS_2 QD by fitting each spectrum with four Gaussian peaks: the neutral exciton (A^0), negative trion (A^-), B exciton, and the defect bound exciton (X). **Fig. 5.7(b)** shows the fitted PL spectra of the sample 1L-MoS_2 and 1L-MoS_2/WS_2 QD HS, respectively. The A^0 and B exciton peaks are associated with the direct bandgap transition at the K point in the Brillouin Zone, with energy split from the strong valence-band spin-orbit coupling.[8] It has been reported that the A^- trion peak arises from charged impurities in the 1L-MoS_2 grown by a CVD method on accounts of unintentional n-type doping,[36] and the X exciton peak is assigned to the radiative recombination of bound excitons from the defect trap states.[37] Note that in the fitting

process, we have fixed only the peak positions of the A^0 (1.88 eV), B (1.98 eV), A^- (1.83 eV) and the X (1.78 eV) bands and the rest are kept as free parameters.

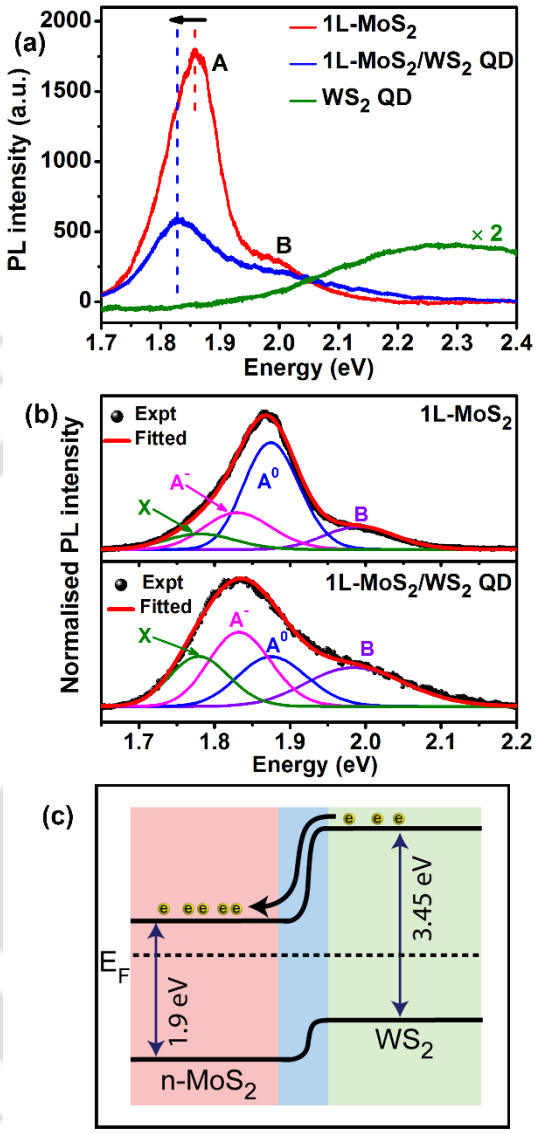

Fig. 5.7. (a) Comparative PL spectra of pristine 1L-MoS_2, WS_2 QDs and 1L-MoS_2/WS_2 QD HS (with 24 mg/L concentration of WS_2 QD) measured with 488 nm excitation using a micro-Raman system. (b) Gaussian deconvolution of PL spectra of pristine 1L-MoS_2 and 1L-MoS_2/WS_2 QD HS, respectively. (c) Energy band diagram of the 1L-MoS_2/WS_2 QD heterostructure under equilibrium.

With the decoration of the WS_2 QDs, the PL spectral weight of the A^0 exciton peak decreased from 53% to 20.6%, while that of the A^- trion peak increased from 23.2% to 37.2% (see **Fig. 5.7(b)** and **Table 5.2**). This increase in the spectral weight of the negative trion in 1L-MoS_2/WS_2 QD HS is due to an increase in the number of excess electrons in the 1L-MoS_2. This is an indication that electrons are transferred from the WS_2 QDs to the 1L-MoS_2. Upon illumination (at 488 nm) with

photon energy lesser than the bandgap (E_g) of the WS_2 QDs, only electrons in the defect states of the QDs absorb the photons and these electrons are excited to the conduction band. Some of these generated electrons are transferred to the 1L-MoS_2 resulting in n-type doping, as can be understood from the schematic of the band alignment of the 1L-MoS_2 and WS_2 QD depicted in **Fig. 5.7(c).** DFT calculations on the MoS_2/WS_2 HS from previous studies show charge transfer from 1L-WS_2 to 1L-MoS_2.[38] The spectral weight of the defect bound excitons X increases from 10.6% to 26.7% after the formation of HS. (see **Fig. 5.7(b)** and **Table 5.2**).

Table 5.2: *Summary of the Gaussian deconvoluted PL spectra showing various species for 1L-MoS_2 and 1L-MoS_2/WS_2 QD HS.*

	Relative weightage of PL peaks			
Sample	**B-exciton (B) (%)**	**A-exciton (A) (%)**	**Trion (A^-) (%)**	**Bound exciton (X) (%)**
1L-MoS_2	13.2	53.0	23.2	10.6
1L-MoS_2 /WS_2 QD	15.5	20.6	37.2	26.7

To provide a more direct evidence in support of the proposed charge transfer process, the change in the work function of 1L-MoS_2 before and after the decoration of WS_2 QD was estimated by KPFM (Kelvin probe force microscopy). **Fig. 5.8(a)** and **(c)** show the AFM topography of 1L-MoS_2 and 1L-MoS_2/WS_2 QD HS, while **Fig. 5.8(b)** and **(d)** show the surface potential image of 1L-MoS_2 and 1L-MoS_2/WS_2 QD HS, respectively. Before the measurement, the work function of the tip (Φ_t, in eV) was calibrated (~4.52 eV). The overall contact potential difference (V_{CPD}, in V) values of the measured samples were provided by the KPFM measurements. The measured V_{CPD} between the sample and the tip can be expressed as, $e \times V_{CPD} = \Phi_t - \Phi_s$, where e is the elementary charge and Φ_s is the work function of the sample. The contact potential difference for 1L-MoS_2 is ~85 mV, while that for 1L-MoS_2/WS_2 QD HS is ~120 mV. So, the work functions of 1L- MoS_2, $\Phi_{1L\text{-}MoS2}$ ~ 4.435 eV, which is similar to previously reported values[39] and $\Phi_{1L\text{-}MoS2/WS2}$ ~ 4.400 eV, respectively. Thus, there is a distinct decrease in the work function of the 1L-MoS_2/WS_2 QD HS by 35 meV compared to that of 1L-MoS_2. The reduction in the work function of the HS suggests the higher electron density in the 1L-MoS_2 due to the favorable band bending for the charge transfer from the WS_2 QDs to the 1L-MoS_2.

To further understand the change of the PL intensity of the 1L-MoS_2 with the addition of the WS_2 QDs (concentration 4 to 36 mg/L), PL intensity was measured for the HS system. **Fig. 5.9(a)** shows the variation of the PL spectra of the 1L-MoS_2 with different concentrations of WS_2 QDs. The PL intensity of the 1L-MoS_2 decreases systematically and PL peak broadens and red-shifts as the concentration of the WS_2 QDs is increased. The total PL intensity of the 1L-MoS_2 decreases dramatically after the formation of the 1L-MoS_2/WS_2 QD HS even at very low concentration (4 mg/L), as shown in **Fig. 5.9(b)**. Note that attachment of WS_2 QDs to 1L-MoS_2 surface is limited by the specific surface area of the 1L-MoS_2 and beyond a certain concentration, WS_2 QDs are not directly attached to the MoS_2 surface sites and hence further charge transfer is restricted at high concentration.

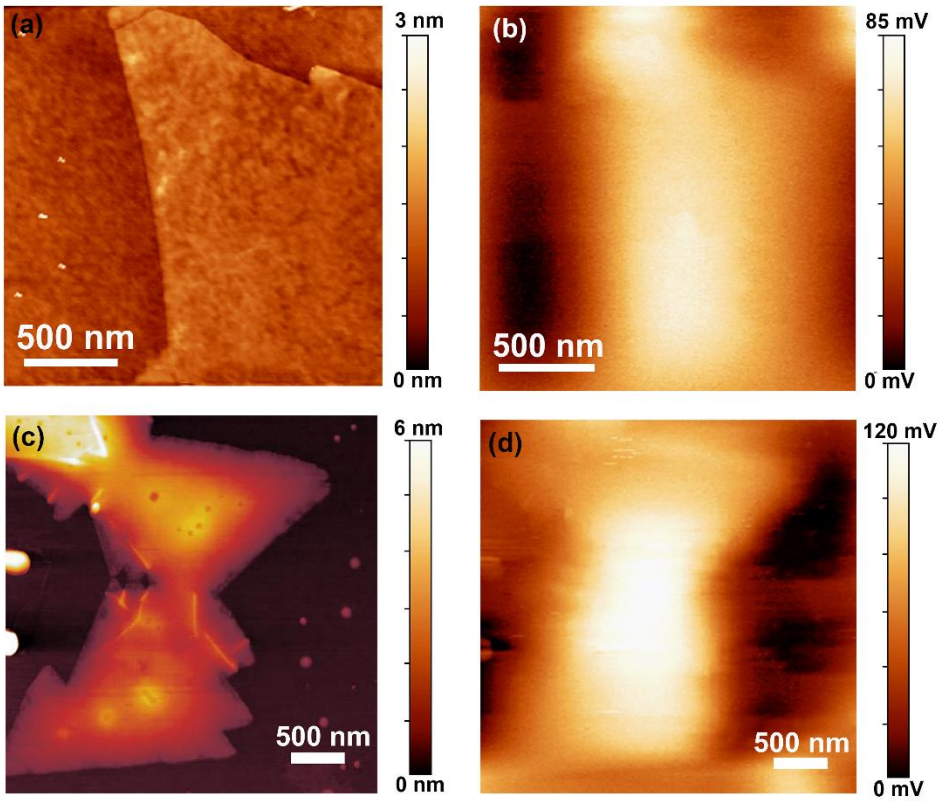

Fig. 5.8. (a, c) AFM surface topography images of 1L-MoS_2 and 1L-MoS_2/WS_2 QD, respectively. (b, d) The corresponding KPFM surface potential images.

To have a better understanding of the spectral changes in PL, we have considered the contribution of the neutral exciton, trion and defect bound exciton in the spectral deconvolution of PL peaks, as shown in **Fig. 5.9(c)**. It is evident that with increasing concentration of WS_2 QDs, charge carrier density increases in 1L-MoS_2. These doped electrons easily form trions and restrain the electron-

hole pair recombination and as a result, the PL intensity quenches systematically and the PL peak is redshifted. Therefore, the neutral excitons are gradually converted to trions resulting in the change of the spectral weight of the individual component. It is evident from the fitting shown in **Fig. 5.9(c)** that for low concentrations of the WS_2 QD (< 12 mg/L), the PL emission is dominated by the neutral exciton peak (A^0). At higher concentration of WS_2 QDs, the contribution of the trions becomes higher than the neutral exciton and hence induces quenching of the PL intensity and a redshift of the PL peak position.

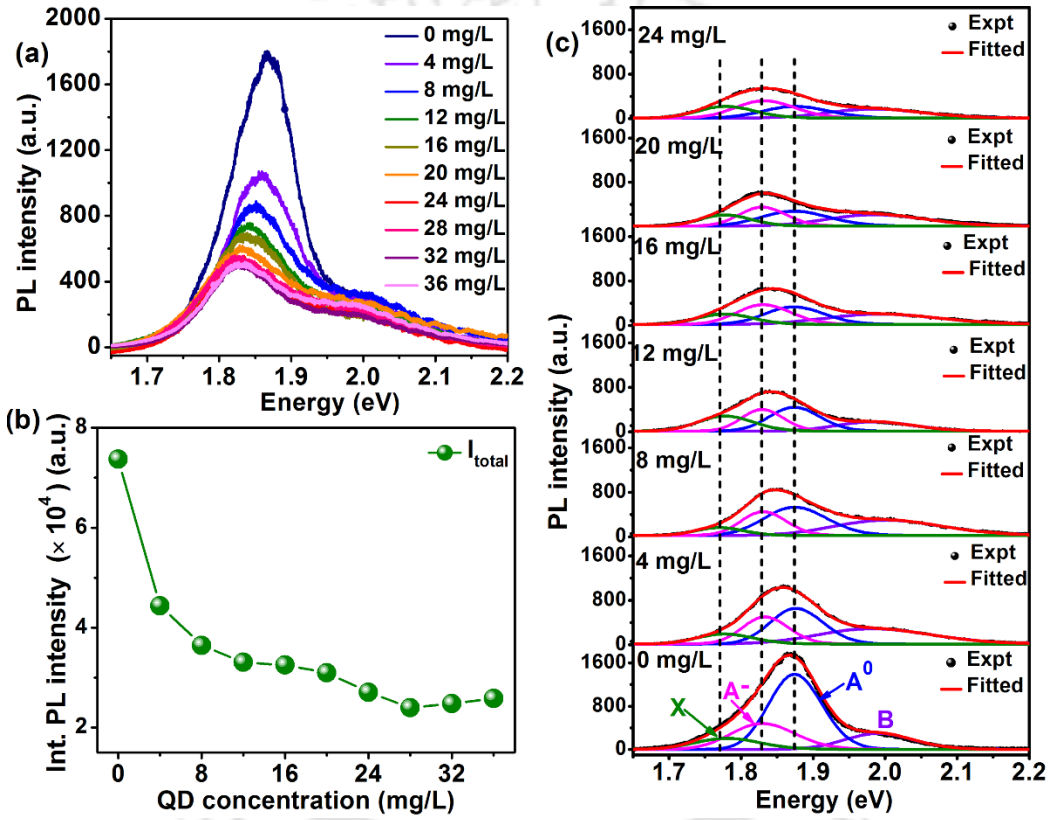

Fig. 5.9. (a) Variation of the PL spectra of the 1L-MoS_2 with different concentration of WS_2 QDs. (b) Total PL intensity of 1L-MoS_2 as a function of the concentration of WS_2 QDs. (c) Gaussian deconvolution of the PL spectra of 1L-MoS_2 measured at different concentration of the WS_2 QD. The PL spectra are deconvoluted with four peaks: B exciton (B), neutral exciton (A^0), trion (A^-), and the defect bound exciton (X).

Fig. 5.10(a) shows a plot of the integrated PL intensity of neutral excitons I_{A^0}, negative trions I_{A^-} and the bound excitons I_X as a function of the concentration of WS_2 QDs. We notice that the intensity of the neutral excitons I_{A^0} decreases gradually and then almost saturates at high concentration of the WS_2 QD (>24 mg/L). However, there is a very small change in the integrated intensity of the trions. This is because the trion emission saturates after a certain doping level due

to Pauli blocking effect.[15] Thus, the excess electrons that are transferred from the WS_2 QDs to the 1L-MoS_2 will further move to the defect trap states. It is interesting to note that despite the systematic decrease in the integrated PL intensity of A^0 and A^- peaks, the defect-related X peak intensity does not decrease with doping, which is essentially due to the charge transfer from the A- level to X level. In the absence of defect, one would expect an increase in trion population with increasing doping (electron) concentration, which is contrary to our experimental data. On the other hand, the total integrated PL intensity I_{Total} decreases in a similar way as that of I_{A^0}. **Fig. 5.10(b)** shows the change of the PL spectral weight of the neutral exciton (I_{A^0}/I_{Total}) with the increase in the concentration of the WS_2 QDs. For pristine 1L-MoS_2 the spectral weight is ~0.61, whereas with doping at higher concentration (>24 mg/L), the spectral weight decreases up to ~0.29. This is an indication of the transition from neutral exciton to trion with the increase in the doping.

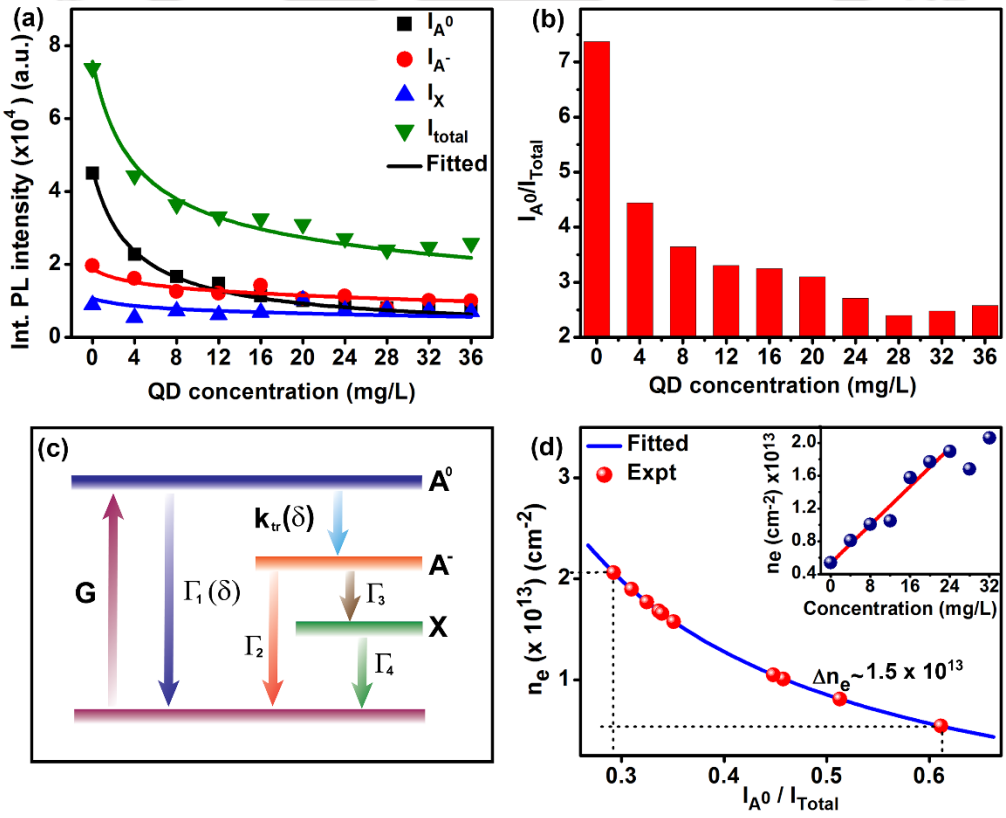

Fig. 5.10. (a) Integrated PL intensity of neutral exciton (I_{A^0}), trion (I_{A^-}), defect bound exciton (I_X) and the sum (I_{Total}) of I_{A^0}, I_{A^-} and I_X as a function of the concentration of WS_2 QD. Symbols are the experimental data, while the solid lines are fitted data based on analytical solutions of rate equations. (b) The neutral exciton spectral weight (I_{A^0}/I_{Total}) as a function of the concentration of WS_2 QD. (c) Schematic representation of electronic transitions through a four-level energy diagram involving the neutral exciton (I_{A^0}), trion (I_{A^-}), defect bound exciton (I_X) and the ground state. Other symbols are described in the text. (d) Calculation of electron density (n_e) based on the law of mass action; inset shows n_e as a function of the concentration of WS_2 QDs.

For a quantitative understanding of the relative change in the PL intensity of the neutral exciton I_{A^0}, trion I_{A^-} and defect bound exciton I_X, we discuss the exciton and trion relaxation dynamics with rate equations based on a four-energy level model, as shown in **Fig. 5.10(c).**[40] Here, G represents the generation rate of excitons, Γ_1 and Γ_2 represent the decay rates of the exciton and trions, respectively. $k_{tr}(\delta)$ is the formation rate of trion from the exciton, which is dependent on the doping concentration (δ) of the WS_2 QDs. To better model our experimental observation, we have assumed Γ_1 to be dependent of δ and it is taken as proportional to doping concentration δ, without which the trion population would not decay with increasing δ, which will be evident from the solution of the rate equations discussed below. In case of high doping density, carrier-density-dependent recombination dynamics of excitons is rational and it has been reported for InGaN/GaN quantum wells.[41] Thus, the dependence of Γ_1 on doping density δ is reasonable in the present case. The trions also decay through the defect trapping state at the rate Γ_3. Lastly, Γ_4 represents the decay rate of the defect bound excitons. Thus, based on the evolution of the three peaks with different doping concentrations, the electronic transitions are shown in **Fig. 5.10(c)**. The corresponding rate equations for the population of neutral excitons N_{A^0}, trions N_{A^-} and the defect bound excitons N_X can be expressed as:

$$\frac{dN_{A^0}}{dt} = G - [\Gamma_1(\delta) + k_{tr}(\delta)]N_{A^0} \quad (1)$$

$$\frac{dN_{A^-}}{dt} = k_{tr}(\delta)N_{A^0} - (\Gamma_2+\Gamma_3)N_{A^-} \quad (2)$$

$$\frac{dN_X}{dt} = \Gamma_3 N_{A^-} - \Gamma_4 N_X \quad (3)$$

$$k_{tr}(\delta) = k_{tr}(0)\left(1 - s.\frac{1}{\alpha\delta+1}\right) \quad (4)$$

$$\Gamma_1(\delta) = \Gamma_1(0)(1+\beta\delta) \quad (5)$$

where G is the generation rate of the A exciton, δ is the concentration of WS_2 QDs solution. The parameter α in eq. (4) represents the WS_2 QD adsorption probability and β in eq. (5) is a proportionality constant. Considering that the rate of adsorption of WS_2 QDs obeys the Langmuir's law, the formation rate of trions with doping concentrations can be described as $k_{tr}(\delta)$ given in eqn. (4), and s (~85% for our best-fitted data) reflects the ability of charge transfer from WS_2 QD to 1L-MoS_2. Doping concentration δ is increased in steps for 4 mg/L in our experiment. Γ_1 and Γ_2

are the decay rate of neutral exciton and trion, respectively. The time dependent population of excitons, trions and defect charges can be analytically solved as:

$$N_{A^0}(\delta,t) = \frac{1}{\Gamma_1(\delta)+k_{tr}(\delta)}\left(G - e^{-(\Gamma_1+k_{tr}(\delta))t}\right) \quad (6)$$

$$N_{A^-}(\delta,t) = \frac{k_{tr}(\delta)}{(\Gamma_2+\Gamma_3)}\frac{G}{(\Gamma_1(\delta)+k_{tr}(\delta))}\left(1 - e^{-(\Gamma_2+\Gamma_3)t}\right) - \frac{k_{tr}(\delta)}{(\Gamma_2+\Gamma_3-(\Gamma_1(\delta)+k_{tr}(\delta))(\Gamma_1(\delta)+k_{tr}(\delta))}\left[e^{-(\Gamma_1(\delta)+k_{tr}(\delta))t} - e^{-(\Gamma_2+\Gamma_3)t}\right] \quad (7)$$

$$N_X(\delta,t) = \frac{\Gamma_3}{\Gamma_4}\frac{k_{tr}(\delta)}{(\Gamma_2+\Gamma_3)}\frac{G}{(\Gamma_1(\delta)+k_{tr}(\delta))}\left(1 - e^{-\Gamma_4 t}\right) - \frac{\Gamma_3 k_{tr}(\delta)}{(\Gamma_4-(\Gamma_2+\Gamma_3))}\frac{G}{(\Gamma_2+\Gamma_3)(\Gamma_1(\delta)+k_{tr}(\delta))}\left[e^{-(\Gamma_2+\Gamma_3)t} - e^{-\Gamma_4 t}\right] - \frac{\Gamma_3 k_{tr}(\delta)}{(\Gamma_2+\Gamma_3-(\Gamma_1(\delta)+k_{tr}(\delta)))(\Gamma_1(\delta)+k_{tr}(\delta))}\left[\frac{1}{(\Gamma_1(\delta)+k_{tr}(\delta))}\left(e^{-\Gamma_4 t} - e^{-(\Gamma_4+\Gamma_1(\delta)+k_{tr}(\delta))t}\right) - \frac{1}{(\Gamma_2+\Gamma_3)}\left(e^{-\Gamma_4 t} - e^{-(\Gamma_2+\Gamma_3+\Gamma_4)t}\right)\right. \quad (8)$$

Under steady state condition, the above equations reduces to

$$N_{A^0}(\delta) = \frac{G}{\Gamma_1(\delta)+k_{tr}(\delta)} \quad (9)$$

$$N_{A^-}(\delta) = \frac{k_{tr}(\delta)}{(\Gamma_2+\Gamma_3)}\frac{G}{(\Gamma_1(\delta)+k_{tr}(\delta))} = \frac{k_{tr}(n)}{(\Gamma_2+\Gamma_3)}\,N_{A^0}(\delta) \quad (10)$$

$$N_X(\delta) = \frac{\Gamma_3}{\Gamma_4}\frac{k_{tr}(\delta)}{(\Gamma_2+\Gamma_3)}\frac{G}{(\Gamma_1(\delta)+k_{tr}(\delta))} = \frac{\Gamma_3}{\Gamma_4}\,N_{A^-}(\delta) \quad (11)$$

$$\frac{N_X}{N_{A^0}} = \frac{N_X}{N_{A^-}} \times \frac{N_{A^-}}{N_{A^0}} \quad (12)$$

The steady-state PL intensities of neutral exciton (I_{A^0}), trion (I_{A^-}) and defect bound exciton (I_X) can be represented as follows:

$$I_{A^0}(\delta) = \frac{AG\gamma_{ex}}{\Gamma_1(\delta)+k_{tr}(\delta)} \quad (13)$$

$$I_{A^-}(\delta) = \frac{k_{tr}(\delta)}{(\Gamma_2+\Gamma_3)}\frac{AG\gamma_{tr}}{(\Gamma_1(\delta)+k_{tr}(\delta))} \quad (14)$$

$$I_X(\delta) = \frac{\Gamma_3}{\Gamma_4}\frac{k_{tr}(\delta)}{(\Gamma_2+\Gamma_3)}\frac{AG\gamma_X}{(\Gamma_1(\delta)+k_{tr}(\delta))}, \quad (15)$$

where A is the collection efficiency of luminescence, γ_{ex}, γ_{tr} and γ_X are the radiative decay rates of neutral exciton, trion and defect bound exciton, respectively. The calculated/fitted PL intensities

I_{A^0}, I_{A^-} and I_X in equations (13), (14) and (15), are in excellent agreement with the experimental results, as shown in **Fig. 5.10(a)**. The parameters used in this analysis are $\Gamma_1(0)$ =0.002 ps^{-1}, Γ_2 = 0.02 ps^{-1}, Γ_3=0.05 ps^{-1}, and $k_{tr}(0)$ = 0.5 ps^{-1} , which are based on previously reported data.[15, 42] We have assumed an intermediate decay rate from the defect trap state, Γ_4 = 0.01 ps^{-1} for a good fit to the carrier recombination dynamics. The fitting parameters of $AG\gamma_{tr}/AG\gamma_{ex}$ and $AG\gamma_X/AG\gamma_{ex}$ to match the experimental data are 0.38 and 0.01, respectively, which implies that $\gamma_{tr} < \gamma_{ex}$ and $\gamma_X << \gamma_{ex}$, consistent with their relative PL intensities observed experimentally. Note that our value of γ_{tr}/γ_{ex} is nearly double of the reported value (γ_{tr}/γ_{ex} = 0.15),[12] due to the specific band alignment for favorable charge transfer and formation of trions. Due to the higher bandgap of WS_2 QDs than that of monolayer WS_2, the band bending is higher in our case resulting in more efficient charge transfer. Our results further imply that the defect (X) contribution to the PL evolution is smaller than the trion (A^-) contribution. However, it is significant enough and necessary to consider it in the rate equation to match with the experimental data.

Assuming the validity of the law of mass action here, the relationship between the population of the neutral exciton (N_A^0), trions (N_A^-) and the charge density n_e in the 1L-MoS_2 is expressed as

$$\frac{N_{A^0} n_e}{N_{A^-}} = \left(\frac{16\pi m_{A^0}\, m_e}{h^2 m_{A^-}}\right) k_B T \exp\left(-\frac{E_b}{k_B T}\right) \qquad (16)$$

where h is the Planck's constant, k_B is the Boltzmann constant, T is the temperature and E_b is the trion binding energy. The effective masses of the electron, hole, and trion are m_e, m_h and m_A^-, respectively. m_e and m_h are 0.35 m_0 and 0.45 m_0, where m_0 is a free electron mass.[15] Therefore, the effective mass of a neutral exciton (m_{A^0}) and a trion (m_{A^-}) can be calculated as as m_{A^0} = m_e + m_h = 0.8 m_0, m_{A^-} = 2m_e + m_h = 1.15 m_0, respectively. Therefore, the calculated the PL spectral weight of the exciton can be expressed as

$$\frac{I_{A^0}}{I_{total}} = \frac{1}{1+\frac{\gamma_{tr} N_{A^-}}{\gamma_{ex} N_{A^0}}+\frac{\gamma_X N_X}{\gamma_{ex} N_{A^0}}} \approx \frac{1}{1+7.4\times10^{-14} n_e+4.4\times10^{-14} n_e} \approx \frac{1}{1+11.8\times10^{-14} n_e} \qquad (17)$$

where $I_{total} = I_{A^0} + I_{A^-} + I_X$, and the E_b and T are taken as 25 meV and 300 K, respectively. The γ_{tr}/γ_{ex} and γ_X/γ_{ex} values as obtained from the fitting are substituted here. Thus, the charge density n_e is calculated from the exciton spectral weight using equation (17) and is shown in **Fig. 5.10(d).** For pristine 1L-MoS_2, the charge density is ~ 5.5 × 10^{12} cm^{-2} owing to its unintentional n-doping attributes.[43] After WS_2 QD doping, in the saturation region, the calculated electron density of the

1L-MoS_2/WS_2 QD HS increases to 20.5×10^{12} cm^{-2}. It is important to note that the difference in the electron density before and after the formation of the HS, $\Delta n_e \sim 1.5 \times 10^{13}$ cm^{-2}, which is significant. This change in the electron density signifies the approximate density of doped electrons in 1L-MoS_2. The inset in **Fig. 5.10(d)** shows the gradual increase in the charge density n_e in the 1L-MoS_2 with the increase in the WS_2 QD concentration. Thus, these results demonstrate effective control of doping/electron density in 1L-MoS_2 about one order of magnitude by the decoration of WS_2 QDs. We believe that the electron density in the 2D materials can be effectively tuned by decorating with QDs of other 2D materials with high bandgap and thus, enable suitable control of the electrical and optical properties of the 2D materials, which is very significant for the ensuing applications.

5.4. Conclusion

In conclusion, we have demonstrated the tunability in the light emission of the 1L-MoS_2 by doping it with the WS_2 QD. KPFM analysis revealed a decrease in the work function of 1L-MoS_2 with the decoration of WS_2 QDs. Systematic quenching of the PL intensity of 1L-MoS_2 with the decoration of WS_2 QDs was explained on the basis of charge transfer from WS_2 QDs to 1L-MoS_2. A detailed analysis using coupled charge transfer among four-energy level model was employed to explain the redshift and the decrease in the PL intensity of the 1L-MoS_2 after decoration with the WS_2 QDs. An analytical solution to the coupled rate equations for change in the population of different excitonic emissions including bound excitonic transition was successfully employed to quantitatively understand the quenching process. The contribution of defects in the charge transfer induced quenching of PL and the carrier-density-dependent recombination dynamics of excitons were established through the quantitative analysis of the spectral evolution. Charge transfer induced increase in electron density in 1L-MoS_2 leads to the transition of the neutral excitons to trions. The doped electron density up to $\Delta n_e \sim 1.5 \times 10^{13}$ cm^{-2} indicates high n-type doping in the 1L-MoS_2 by a simple approach. Our results suggest an effective way to manipulate the electron density through the heterostructure approach, which is advantageous to tune the optical and electrical properties of monolayer TMDs for optoelectronic applications.

References

1. Radisavljevic, B.; Radenovic, A.; Brivio, J.; Giacometti, V.; Kis, A., Single-Layer MoS_2 Transistors. *Nat. Nanotechnol.* **2011**, *6*, 147.
2. Lee, H. S.; Min, S.-W.; Chang, Y.-G.; Park, M. K.; Nam, T.; Kim, H.; Kim, J. H.; Ryu, S.; Im, S., MoS_2 Nanosheet Phototransistors with Thickness-Modulated Optical Energy Gap. *Nano Lett.* **2012**, *12*, 3695-3700.
3. Yu, X.; Dong, Z.; Liu, Y.; Liu, T.; Tao, J.; Zeng, Y.; Yang, J. K. W.; Wang, Q. J., A High Performance, Visible to Mid-Infrared Photodetector Based on Graphene Nanoribbons Passivated with HfO_2. *Nanoscale* **2016**, *8*, 327-332.
4. Paul, K. K.; Mawlong, L. P. L.; Giri, P. K., Trion-Inhibited Strong Excitonic Emission and Broadband Giant Photoresponsivity from Chemical Vapor-Deposited Monolayer MoS_2 Grown in Situ on TiO_2 Nanostructure. *ACS Applied Materials & Interfaces* **2018**, *10*, 42812-42825.
5. Ghorai, A.; Bayan, S.; Gogurla, N.; Midya, A.; Ray, S. K., Highly Luminescent WS_2 Quantum Dots/ZnO Heterojunctions for Light Emitting Devices. *ACS Applied Materials & Interfaces* **2017**, *9*, 558-565.
6. Koo, W.-T.; Cha, J.-H.; Jung, J.-W.; Choi, S.-J.; Jang, J.-S.; Kim, D.-H.; Kim, I.-D., Few-Layered WS_2 Nanoplates Confined in Co, N-Doped Hollow Carbon Nanocages: Abundant WS_2 Edges for Highly Sensitive Gas Sensors. *Advanced Functional Materials* **2018**, *28*, 1802575.
7. Mak, K. F.; Lee, C.; Hone, J.; Shan, J.; Heinz, T. F., Atomically Thin MoS_2: A New Direct-Gap Semiconductor. *Phys. Rev. Lett.* **2010**, *105*, 136805.
8. Splendiani, A.; Sun, L.; Zhang, Y.; Li, T.; Kim, J.; Chim, C.-Y.; Galli, G.; Wang, F., Emerging Photoluminescence in Monolayer Mos2. *Nano Lett.* **2010**, *10*, 1271-1275.
9. Li, H.; Wu, J.; Yin, Z.; Zhang, H., Preparation and Applications of Mechanically Exfoliated Single-Layer and Multilayer MoS_2 and WSe_2 Nanosheets. *Accounts of Chemical Research* **2014**, *47*, 1067-1075.
10. Lopez-Sanchez, O.; Lembke, D.; Kayci, M.; Radenovic, A.; Kis, A., Ultrasensitive Photodetectors Based on Monolayer Mos2. *Nature Nanotechnology* **2013**, *8*, 497.
11. Tao, Y.; Yu, X.; Li, J.; Liang, H.; Zhang, Y.; Huang, W.; Wang, Q. J., Bright Monolayer Tungsten Disulfide Via Exciton and Trion Chemical Modulations. *Nanoscale* **2018**, *10*, 6294-6299.
12. Mouri, S.; Miyauchi, Y.; Matsuda, K., Tunable Photoluminescence of Monolayer MoS_2 Via Chemical Doping. *Nano Lett.* **2013**, *13*, 5944-5948.
13. Kang, Y., et al., Plasmonic Hot Electron Induced Structural Phase Transition in a MoS_2 Monolayer. *Advanced Materials* **2014**, *26*, 6467-6471.
14. Ross, J. S., et al., Electrical Control of Neutral and Charged Excitons in a Monolayer Semiconductor. *Nat. Commun.* **2013**, *4*, 1474.
15. Mak, K. F.; He, K.; Lee, C.; Lee, G. H.; Hone, J.; Heinz, T. F.; Shan, J., Tightly Bound Trions in Monolayer MoS_2. *Nat. Mater.* **2012**, *12*, 207.
16. Li, Z.; Ye, R.; Feng, R.; Kang, Y.; Zhu, X.; Tour, J. M.; Fang, Z., Graphene Quantum Dots Doping of Mos2 Monolayers. *Advanced Materials* **2015**, *27*, 5235-5240.
17. Mawlong, L. P. L.; Paul, K. K.; Giri, P. K., Direct Chemical Vapor Deposition Growth of Monolayer Mos2 on Tio2 Nanorods and Evidence for Doping-Induced Strong Photoluminescence Enhancement. *The Journal of Physical Chemistry C* **2018**, *122*, 15017-15025.
18. Baker, M. A.; Gilmore, R.; Lenardi, C.; Gissler, W., Xps Investigation of Preferential Sputtering of S from MoS_2 and Determination of Mosx Stoichiometry from Mo and S Peak Positions. *Applied Surface Science* **1999**, *150*, 255-262.

19. Kondekar, N. P.; Boebinger, M. G.; Woods, E. V.; McDowell, M. T., In Situ Xps Investigation of Transformations at Crystallographically Oriented MoS_2 Interfaces. *ACS Applied Materials & Interfaces* **2017**, *9*, 32394-32404.
20. Lin, L.; Xu, Y.; Zhang, S.; Ross, I. M.; Ong, A. C. M.; Allwood, D. A., Fabrication of Luminescent Monolayered Tungsten Dichalcogenides Quantum Dots with Giant Spin-Valley Coupling. *ACS Nano* **2013**, *7*, 8214-8223.
21. Li, H.; Zhang, Q.; Yap, C. C. R.; Tay, B. K.; Edwin, T. H. T.; Olivier, A.; Baillargeat, D., From Bulk to Monolayer MoS_2: Evolution of Raman Scattering. *Adv. Funct. Mater.* **2012**, *22*, 1385-1390.
22. Chakraborty, B.; Bera, A.; Muthu, D. V. S.; Bhowmick, S.; Waghmare, U. V.; Sood, A. K., Symmetry-Dependent Phonon Renormalization in Monolayer MoS_2 Transistor. *Phys. Rev. B* **2012**, *85*, 161403.
23. Berkdemir, A., et al., Identification of Individual and Few Layers of WS_2 Using Raman Spectroscopy. *Scientific Reports* **2013**, *3*, 1755.
24. Roy, S.; Neupane, G. P.; Dhakal, K. P.; Lee, J.; Yun, S. J.; Han, G. H.; Kim, J., Observation of Charge Transfer in Heterostructures Composed of $MoSe_2$ Quantum Dots and a Monolayer of MoS_2 or WSe_2. *The Journal of Physical Chemistry C* **2017**, *121*, 1997-2004.
25. Yin, W.; Bai, X.; Chen, P.; Zhang, X.; Su, L.; Ji, C.; Gao, H.; Song, H.; Yu, W. W., Rational Control of Size and Photoluminescence of WS_2 Quantum Dots for White Light-Emitting Diodes. *ACS Applied Materials & Interfaces* **2018**, *10*, 43824-43830.
26. Wilcoxon, J. P.; Samara, G. A., Strong Quantum-Size Effects in a Layered Semiconductor: MoS_2 Nanoclusters. *Physical Review B* **1995**, *51*, 7299-7302.
27. Gutiérrez, H. R.; Perea-López, N.; Elías, A. L.; Berkdemir, A.; Wang, B.; Lv, R.; López-Urías, F.; Crespi, V. H.; Terrones, H.; Terrones, M., Extraordinary Room-Temperature Photoluminescence in Triangular WS_2 Monolayers. *Nano Letters* **2013**, *13*, 3447-3454.
28. Wang, W.; Li, K.; Wang, Y.; Jiang, W.; Liu, X.; Qi, H., Investigation of the Band Alignment at MoS_2/$PtSe_2$ Heterojunctions. *Applied Physics Letters* **2019**, *114*, 201601.
29. Dhakal, K. P.; Duong, D. L.; Lee, J.; Nam, H.; Kim, M.; Kan, M.; Lee, Y. H.; Kim, J., Confocal Absorption Spectral Imaging of Mos2: Optical Transitions Depending on the Atomic Thickness of Intrinsic and Chemically Doped MoS_2. *Nanoscale* **2014**, *6*, 13028-13035.
30. Xu, S.; Li, D.; Wu, P., One-Pot, Facile, and Versatile Synthesis of Monolayer MoS_2/WS_2 Quantum Dots as Bioimaging Probes and Efficient Electrocatalysts for Hydrogen Evolution Reaction. *Advanced Functional Materials* **2015**, *25*, 1127-1136.
31. Lin, H.; Wang, C.; Wu, J.; Xu, Z.; Huang, Y.; Zhang, C., Colloidal Synthesis of MoS_2 Quantum Dots: Size-Dependent Tunable Photoluminescence and Bioimaging. *New Journal of Chemistry* **2015**, *39*, 8492-8497.
32. Wang, N.; Wei, F.; Qi, Y.; Li, H.; Lu, X.; Zhao, G.; Xu, Q., Synthesis of Strongly Fluorescent Molybdenum Disulfide Nanosheets for Cell-Targeted Labeling. *ACS Applied Materials & Interfaces* **2014**, *6*, 19888-19894.
33. Chernikov, A.; Berkelbach, T. C.; Hill, H. M.; Rigosi, A.; Li, Y.; Aslan, O. B.; Reichman, D. R.; Hybertsen, M. S.; Heinz, T. F., Exciton Binding Energy and Nonhydrogenic Rydberg Series in Monolayer WS_2. *Physical Review Letters* **2014**, *113*, 076802.
34. Li, Z.-W.; Hu, Y.-H.; Li, Y.; Fang, Z.-Y., Light–Matter Interaction of 2d Materials: Physics and Device Applications. *Chinese Physics B* **2017**, *26*, 036802.
35. Wei, G.; Czaplewski, D. A.; Lenferink, E. J.; Stanev, T. K.; Jung, I. W.; Stern, N. P., Size-Tunable Lateral Confinement in Monolayer Semiconductors. *Scientific Reports* **2017**, *7*, 3324.
36. Nan, H., et al., Strong Photoluminescence Enhancement of Mos2 through Defect Engineering and Oxygen Bonding. *ACS Nano* **2014**, *8*, 5738-5745.
37. Tongay, S., et al., Defects Activated Photoluminescence in Two-Dimensional Semiconductors: Interplay between Bound, Charged, and Free Excitons. *Sci. Rep.* **2013**, *3*, 2657.

38. Wang, F.; Wang, J.; Guo, S.; Zhang, J.; Hu, Z.; Chu, J., Tuning Coupling Behavior of Stacked Heterostructures Based on MoS_2, WS_2, and WSe_2. *Scientific Reports* **2017**, *7*, 44712.
39. Wu, H.; Si, H.; Zhang, Z.; Kang, Z.; Wu, P.; Zhou, L.; Zhang, S.; Zhang, Z.; Liao, Q.; Zhang, Y., All-Inorganic Perovskite Quantum Dot-Monolayer MoS_2 Mixed-Dimensional Van Der Waals Heterostructure for Ultrasensitive Photodetector. *Advanced Science* **2018**, *5*, 1801219.
40. Gao, F.; Gong, Y.; Titze, M.; Almeida, R.; Ajayan, P. M.; Li, H., Valley Trion Dynamics in Monolayer $MoSe_2$. *Physical Review B* **2016**, *94*, 245413.
41. Liu, W.; Butté, R.; Dussaigne, A.; Grandjean, N.; Deveaud, B.; Jacopin, G., Carrier-Density-Dependent Recombination Dynamics of Excitons and Electron-Hole Plasma in M-Plane InGaN/GaN Quantum Wells. *Physical Review B* **2016**, *94*, 195411.
42. Wang, H.; Zhang, C.; Rana, F., Ultrafast Dynamics of Defect-Assisted Electron–Hole Recombination in Monolayer MoS_2. *Nano Letters* **2015**, *15*, 339-345.
43. Suh, J., et al., Doping against the Native Propensity of MoS_2: Degenerate Hole Doping by Cation Substitution. *Nano Letters* **2014**, *14*, 6976-6982.

Chapter 6

A High-Performance Hybrid 2D/0D Photodetector based on 1L-MoS_2/WS_2 Quantum Dot Heterostructure

In this chapter, we present the CVD growth of monolayer MoS_2 decorated with WS_2 QDs for optoelectronic applications. In this work, we incorporate WS_2 QDs with direct CVD grown monolayer MoS_2 on Si/SiO_2 substrate and fabricate a vertical heterojunction photodetector (PD). The 1L-MoS_2/WS_2 QD heterojunction PD can operate at a very low bias (0.1 V) and with fast photo-response speed exhibiting photocurrent growth and decay times of 18.5 µs and 95.4 µs, respectively. The photoresponsivity and detectivity of 1L-MoS_2/WS_2 QD hybrid photodetector are 2.17 A/W and 1.18×10^{12} Jones under 405 nm illumination, respectively, which are much superior to that of pristine MoS_2 photodetector. The enhanced performance of the heterojunction PD is attributed to the fast transfer of photogenerated electrons from WS_2 QDs to monolayer MoS_2 and n-type doping of MoS_2 layer due to the appropriate band bending at the interface. We evaluate various device parameters to demonstrate the superiority of the p-n heterojunction photodetector operated under a low bias. This work offers a detailed insight to understand and fabricate the next generation multifunctional optoelectronic devices based on the 1L-MoS_2 and WS_2 heterojunction.

6.1. Introduction

Since the discovery of graphene, two-dimensional materials have received remarkable attention in the optoelectronics industry due to their fascinating properties such as light-matter interaction and substantial band gaps.[1-3] In the previous chapter, we have demonstrated the tunability of photoluminescence (PL) emission from monolayer MoS_2 (1L- MoS_2) by decorating with WS_2 quantum dots (WS_2 QDs). The system collectively exhibited an orderly quenching of the PL of 1L-MoS_2, which was explained on the basis of charge transfer from WS_2 QDs to 1L-MoS_2. We presented a detailed analysis of the coupled charge transfer using a four-energy level model. The decrease in the PL intensity accompanied by the redshift was explained on the basis of the contribution of trions as well as defects and carrier density-dependent recombination dynamics, which led to an effective high n-type doping effect in the 1L-MoS_2. This manipulation of charge density in the 1L-MoS_2 paves the way for interesting optoelectronic applications. According to previous literature, MoS_2-based photodetectors still suffer from drawbacks owing to factors, such

as traditional monolayer of 2D materials, exhibits poor optical absorption,[4-5], and low interlayer transport speed.[6] In the case of multilayer MoS_2 photodetectors, the optical absorption is improved, thus, enhancing the overall responsivity of the detector. However, there is a major drawback in the performance of the device as the interlayer mobility is compromised.[5, 7] There have been reports on the hybridization of the 2D materials to improve upon the carrier mobility and overall quantum efficiency of the photodetectors.[3-4, 8-9] In the present chapter, we report the fabrication of a novel MoS_2-WS_2 based photodetector with the ultrafast response and high photoconductive gain. The WS_2 QD decorated on CVD grown 1L-MoS_2 forms an effective type II heterojunction. The response rise/fall times of the heterojunction were measured to be 18.5/95.4 µs, which is an order faster than pristine 1L-MoS_2 photodetector. Our results show that the heterojunction photodetector exhibits a broad spectral response with a peak photoresponsivity of 2.17 A/W and peak detectivity of 1.18×10^{12} Jones at 405 nm.

6.2. Experimental Details

6.2.1. Sample Preparation

6.2.1.1. Synthesis of WS_2 quantum dots

WS_2 quantum dots were synthesized by liquid exfoliation method using high purity WS_2 powder (Sigma Aldrich, 99%) dispersed in N-methyl-2-pyrrolidinone (NMP) (Alpha Aesar, HPLC grade, 95%) and sonicated for 15 hours. The solution was allowed to settle down and was centrifuge for 45 minutes. The WS_2 quantum dots are present on the top 2/3rd of the solution, while the bottom 1/3rd consists of the larger WS_2 quantum dots and the nanosheets. Further details are described in **Chapter 5, Section 5.2.1.1.** To confirm the crystallinity of the WS_2 QDs, micro-Raman analysis was performed.

6.2.1.2. Growth of monolayer MoS_2

1L-MoS_2 were directly grown on the SiO_2 substrate by the CVD process using a two zone furnace. High-purity MoO_3 (99.5%, Sigma-Aldrich) and sulfur powder (99.95%, Sigma-Aldrich) were used as precursors and placed inside a 2-inch quartz tube-based horizontal muffle furnace at the center of their respective zones, for the monolayer growth of MoS_2. The substrates were then placed face down on top of the quartz mask with a circular opening, which were then put on top of the boat containing MoO_3 precursor. The temperature of the zone containing the substrate was ramped at a rate of 15 °C/min up to 700 °C and was maintained for 5 min, with an Ar flow rate of 10 sccm.

Subsequently, the temperature of the other zone containing the sulfur precursor reaches 150 °C. The furnace was then allowed to cool down to room. It resulted in the large area growth of monolayer MoS_2. Further details of the growth is described in **Chapter 2, Section 2.3.2.**

6.2.1.3. Fabrication of 1L-MoS_2/WS_2 QD heterojunction photodetector

To fabricate the 1L-MoS_2/WS_2 QD heterojunction, WS_2 QDs were spin-coated onto the 1L-MoS_2 grown on Si/SiO_2 and are dried, as described in **Chapter 5, Section 5.2.1.2**. Next, a 100 nm thick Au layer was deposited through a shadow mask placed on top of the sample by a thermal evaporation method (base pressure of ~1×10^{-6} torr). Note that the shadow mask was properly fixed on the sample and examined using an optical microscope to ensure that one opening for electrode deposition was on the top WS_2 QD layer and the other opening is on the pristine 1L-MoS_2 film. For the fabrication of pristine 1L-MoS_2 photodetector, the two Au electrodes were directly deposited on the 1L-MoS_2 film. The electrodes were connected to the microprobe station for measurements.

6.2.2. Characterization Techniques

The details of AFM, Raman, FESEM, and PL measurements were discussed in **Chapter 2, Section 2.1.3**. The details of FETEM, UV-Visible absorption, and XRD measurement were discussed in **Chapter 3, Section 3.2.3**. The XPS measurements were carried out with an automated photoelectron spectrometer (PHI X-tool, ULVAC-PHI Inc.) using Al Kα X-ray beam (1486.6 eV) with a beam current of 5 mA. Temporal response of photocurrent and I-V measurement of the photodetector were measured using a microprobe station (ECOPIA EPS−500) connected to a source measure unit (Keithely 2400, USA) and a 405 nm laser with TTL modulation. A 250 W Xenon lamp (Newport, USA) with a manual monochromator (Oriel Instruments, USA) and the source meter (Keithely 2400, USA) were used to measure the spectral photoresponsivity of the photodetector.

6.3. Results and Discussion

6.3.1. Morphological Studies

6.3.1.1. TEM and AFM Analyses

Fig. 6.1(a) depicts the optical microscope image of large area continuous monolayer MoS_2 film grown on SiO_2/Si substrate. The as-grown MoS_2 thin film shows uniformity and continuity along with triangular-shaped MoS_2 flakes towards the edge of the substrate. It appears that during the

growth, these MoS_2 flakes tend to merge together to form a large continuous monolayer film across a few millimeter square area.

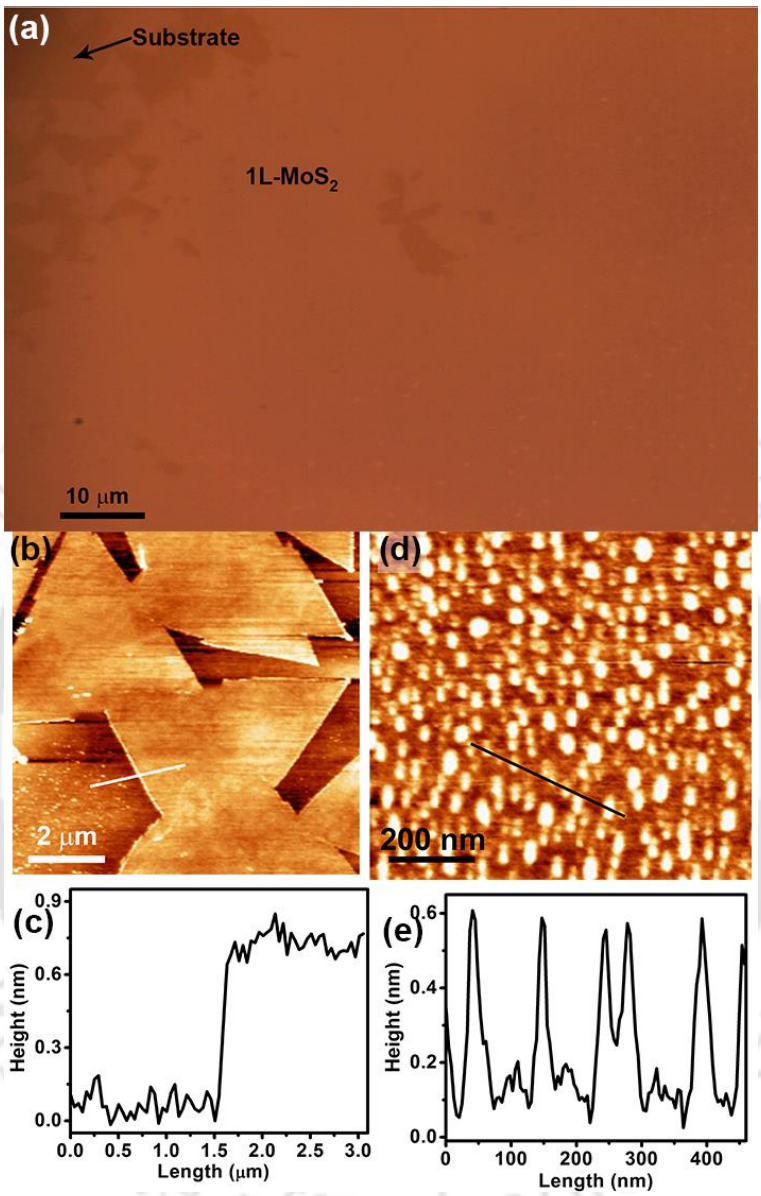

Fig. 6.1. (a) Optical microscope image of large-area monolayer MoS_2 grown by the CVD technique. (b) AFM image of monolayer MoS_2 on Si/SiO_2 substrate, and (c) AFM height profile of monolayer MoS_2. (d) AFM image and (e) AFM height profile of the WS_2 quantum dots.

The surface morphology of the film is further characterized by AFM analysis. The result of a typical AFM measurement is presented in **Fig. 6.1(b)**, which shows a few triangular domains interconnected with each other. The homogeneous color contrast indicates a good uniformity of the as-grown sample. **Fig. 6.1(c)** shows the height profile along the white line drawn at the edge in **Fig. 6.1(b)** revealing a film thickness of ~0.7 nm, which agrees well with the monolayer MoS_2.

The layer thickness and film uniformity are further confirmed by Raman spectroscopy analysis. **Fig. 6.1(d)** displays the AFM image of uniformly distributed spherical WS_2 QDs. The height profile of the quantum dots indicates a thickness of ~0.6 nm (as shown in **Fig. 6.1(e)**), which corresponds to the monolayer thickness of the WS_2 QDs.

To further characterize the morphology of the as-prepared WS_2 QDs, FETEM measurement was carried out. The FETEM image of prepared WS_2 QDs is shown in **Fig. 6.2(a).** It is observed that the as-prepared QDs have sizes in the range 2-6 nm, with an average diameter of 3.3 nm (see the inset of **Fig. 6.2(a)**). The high-resolution TEM (HRTEM) image suggests that the QDs are highly crystalline with highly ordered fringes, as shown in **Fig. 6.2(b).** The inset of **Fig. 6.2(b)** displays the inverse fast Fourier transform (IFFT) of the lattice fringes showing a d-spacing of 0.23 nm, which corresponds to the (103) plane of WS_2.

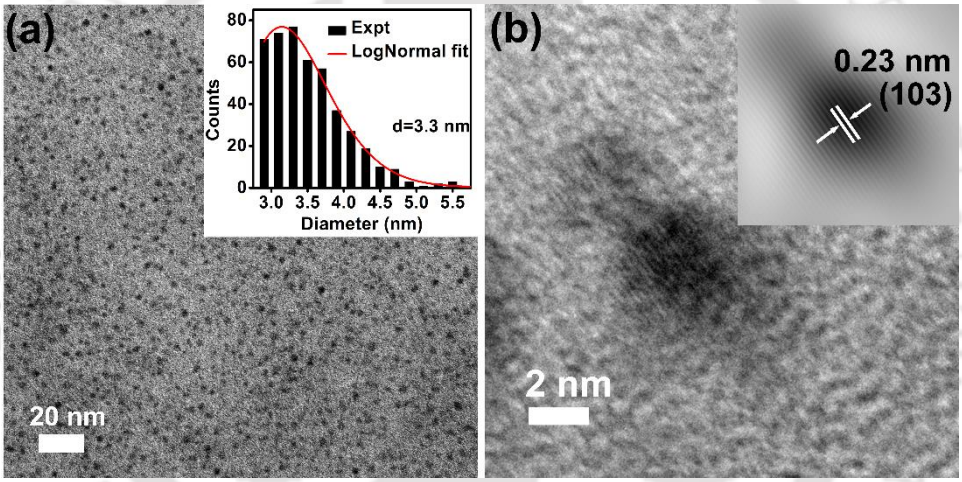

Fig. 6.2: (a) The TEM image of WS_2 QDs; the shows the size distribution of the QDs showing an average diameter (d) of 3.3 nm; (b) HRTEM lattice image of a WS_2 QD; the inset shows the IFFT lattice image showing a d-spacing of 0.23 nm

6.3.2. Structural Analysis

6.3.2.1. XPS Analysis

To investigate the surface chemical composition of the as-grown samples, the X-ray photoelectron spectroscopy (XPS) was carried out. **Fig. 6.3(a)** shows the survey scan XPS spectra of pristine 1L-MoS_2, WS_2 QD and 1L-MoS_2/WS_2 QD. Here, the presence of Mo 3d, Mo 3p, W 4f, and S 2p are observed in 1L-MoS_2/WS_2 QD HS sample confirming the presence of the elements of MoS_2 and WS_2 QD in the HS. **Fig. 6.3 (b,c)** shows the comparative Mo 3d and S 2p core-level XPS spectra, for 1L-MoS_2 and 1L-MoS_2/WS_2 QD samples, respectively.

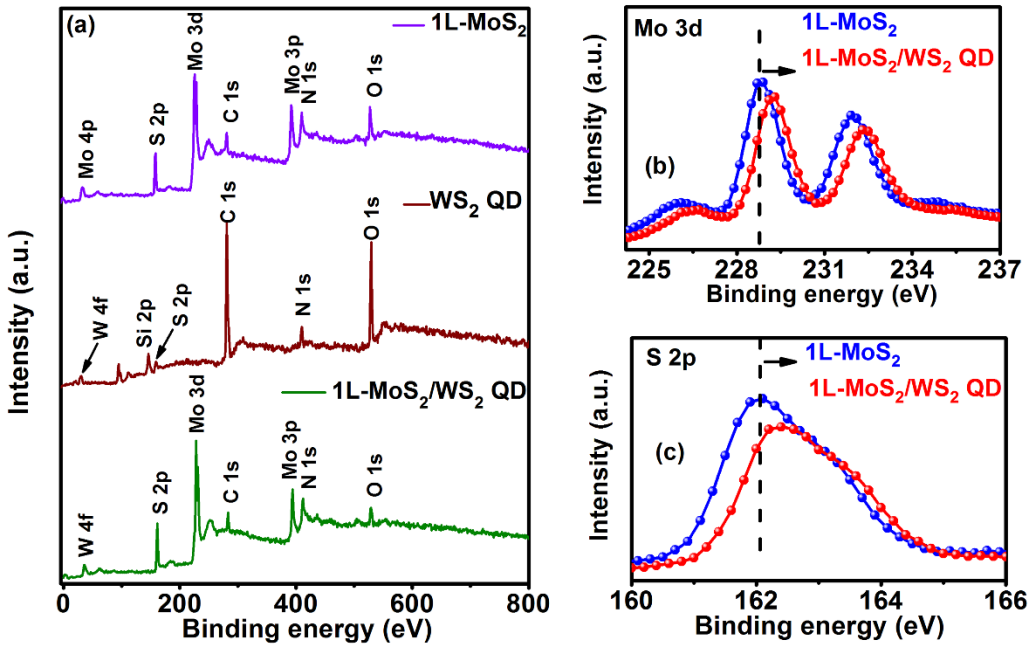

Fig. 6.3: (a) XPS survey spectra of 1L-MoS_2, WS_2 QD and 1L-MoS_2/WS_2 QD HS. (b, c) Core-level XPS spectra of 1L-MoS_2 and 1L-MoS_2/WS_2 QD HS for Mo 3d and S 2p, respectively. The vertical dotted line with arrow indicates the shift in the binding energy in each case.

Fig. 6.3(b) displays two distinct peaks characteristic of Mo $3d_{5/2}$ and Mo $3d_{3/2}$ at 228.8 eV and 231.9 eV for 1L-MoS_2, indicating the presence of Mo^{4+} oxidation states in the sample. The S 2p spectrum for 1L-MoS_2 shows two peaks attributed to S $2p_{3/2}$ at 162.1 eV and S $2p_{1/2}$ at 163.2 eV, respectively, which are attributed to the 2^- oxidation state of sulfur as shown in **Fig. 6.3(c)**. We observed that in the case of the 1L-MoS_2/WS_2 QD HS, both the Mo 3d and S 2p peaks are red-shifted by~0.4 eV, toward higher binding energy. This shift in the peak positions is due to the movement of the Fermi level toward the conduction band, indicating the charge transfer from WS_2 QDs to 1L-MoS_2.[10]

6.3.2.2. Raman and XRD Analyses

Raman spectroscopy is an indispensable tool to determine the atomic layer number in 2D materials. Micro-Raman measurements were performed on the as-grown 1L-MoS_2, and 1L-MoS_2/WS_2 QD HS recorded using 514 nm Ar laser. **Fig. 6.4(a)** shows the comparative Raman spectra for the samples. The Raman spectrum of 1L-MoS_2 shows the presence of two characteristic Raman peaks, the E_{2g} (in-plane) and A_{1g} (out of plane) vibrational mode, which confirms the MoS_2 growth. The frequency difference Δk between these two peaks is ~ 20.6 cm^{-1}, which suggests that the MoS_2 is of monolayer thickness.[11] The Raman spectrum of 1L-MoS_2/WS_2 QD HS exhibits two

additional peaks at 359.5 and 423.8 cm^{-1}, which can be attributed to the E_{2g} and A_{1g} modes of WS_2 QD, and this confirms the co-existence both the phases in the HS. Interestingly, the peak position of A_{1g} mode of MoS_2 in the 1L-MoS_2/WS_2 QD HS is red-shifted by 1.2 cm^{-1}, while there is no measurable shift in the E_{2g} mode. This red shift of the A_{1g} peak is attributed to the increase of electron concentration in MoS_2 and has been reported as evidence of n-type doping of monolayer MoS_2 by other dopants.[12] Therefore, the MoS_2 is n-type doped due to the formation of the heterostructure.

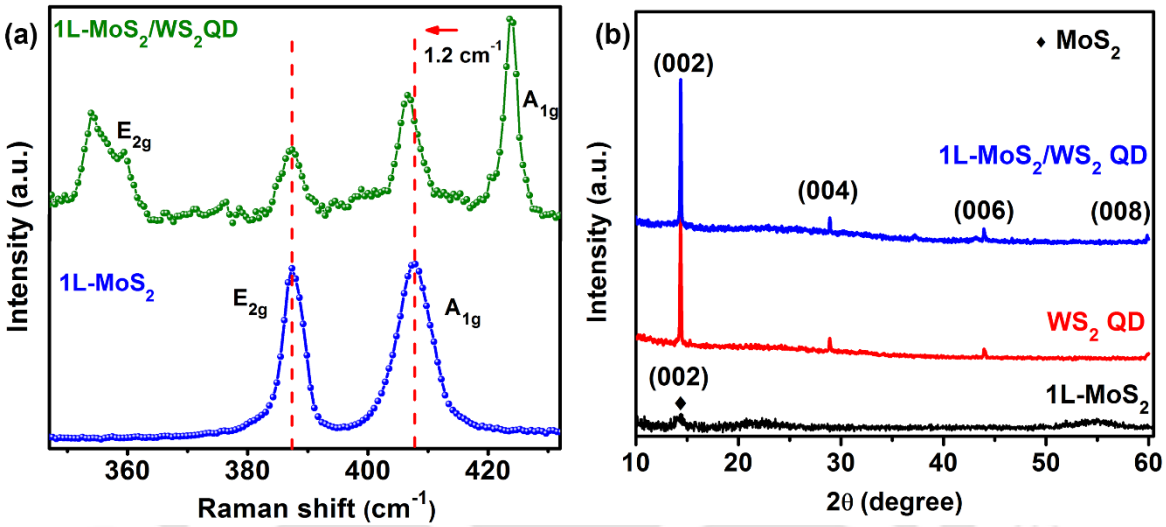

Fig. 6.4: (a) Comparison of the Raman spectra of pristine 1L-MoS_2, and 1L-MoS_2@WS_2 QD HS. (b) XRD patterns of 1L-MoS_2, WS_2 QD, and 1L-MoS_2/WS_2 QD HS. The curves are vertically shifted for clarity of presentation.

The crystalline structure and phase composition of the as-grown samples were confirmed from the X-ray diffraction analysis. **Fig. 6.4(b)** shows the XRD patterns of 1L-MoS_2, WS_2 QD, and 1L-MoS_2/WS_2 QD HS. The diffraction pattern of the thin, pristine 1L-MoS_2 shows only one small peak (labeled with "♦" symbol) at $2\theta \approx 14.3°$, which can be attributed to the (002) plane of MoS_2. It is observed that the reflection peak can be perfectly indexed to the hexagonal MoS_2 with a= b = 3.16 Å and c = 12.30 Å, which is consistent with the standard JCPDS card no. 37-1492. The XRD pattern of the WS_2 QD displays diffraction peaks at $2\theta \approx 14.3°$, 28.9°, 43.9°, and 59.9° assigned to (002), (004), (006) and (008) planes of hexagonal WS_2 (JCPDS #84-1398), respectively. The peaks of both MoS_2 and WS_2 were present in the XRD pattern of the 1L-MoS_2/WS_2 QD HS. However, it was difficult to distinguish the characteristic peak of MoS_2 (002) from that of WS_2 due to their similar 2θ values (~14.3°).

6.3.3. Optical Analysis

6.3.3.1. UV-Vis Absorption and Photoluminescence Study

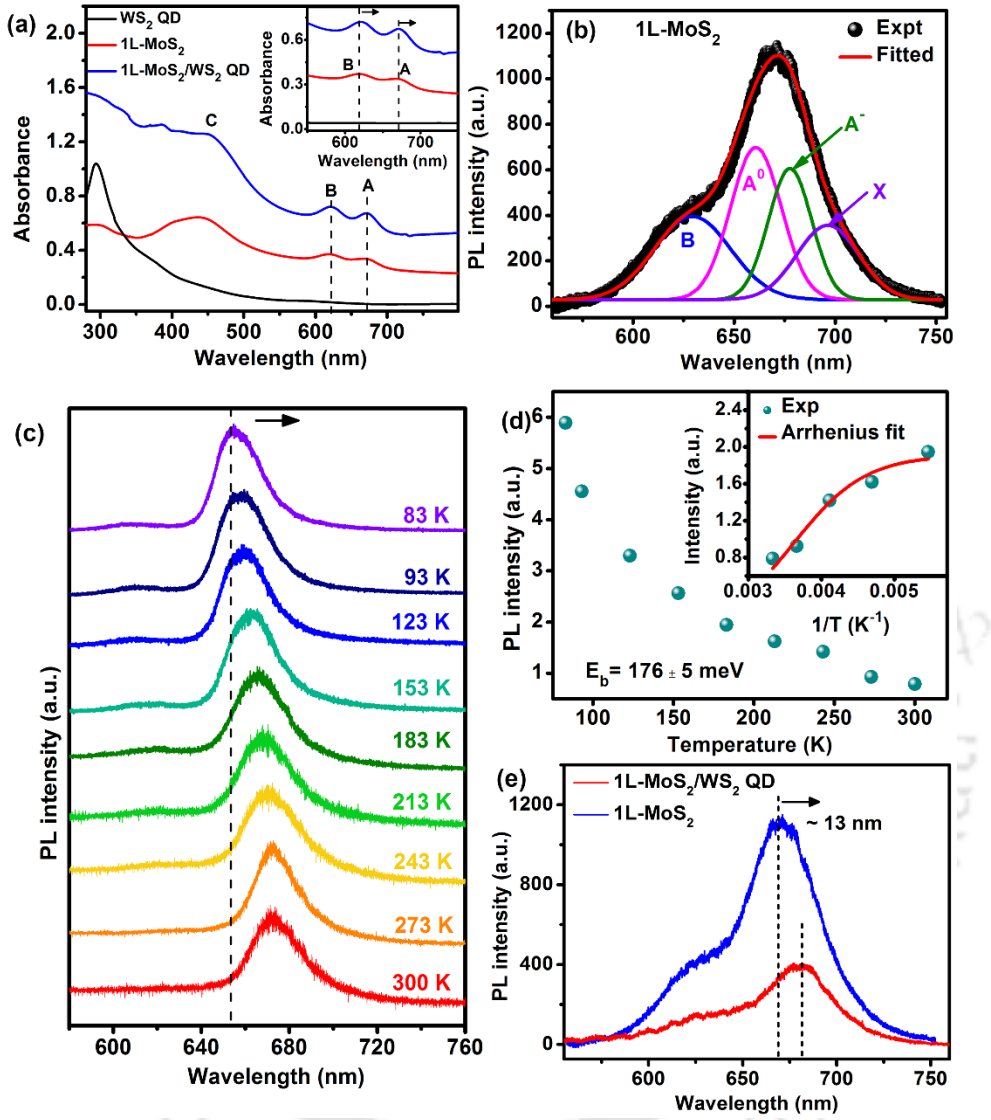

Fig. 6.5 (a) UV-visible absorption spectra of 1L-MoS_2, WS_2 QDs, and 1L-MoS_2/WS_2 QD. Inset shows the magnified view. A, B, and C represent the characteristic excitonic absorption bands of the 1L-MoS_2; (b) PL spectra of pristine 1L-MoS_2 at room temperature. (c) Low-temperature PL spectra for pristine 1L-MoS_2 taken from 83 to 300 K at a regular interval. (d) A plot of PL intensity (A exciton) as a function of temperature for the 1L-MoS_2. Inset shows the Arrhenius plot for the region 285-330 K. The experimental data have been fitted with the Arrhenius equation to extract the exciton binding energy (E_b). (e) Comparative PL spectra of 1L-MoS_2 and 1L-MoS_2/WS_2 QD HS. The vertical dashed lines and the arrow indicate the redshift of the PL peak in the HS sample.

Fig. 6.5(a) displays a comparison of the UV-visible absorption spectra of 1L-MoS_2, WS_2 QD, and 1L-MoS_2/WS_2 QD HS. The absorption spectrum of 1L-MoS_2 shows three characteristic absorption peaks A, B, and C at 667.7 nm, 618.5 nm, and 436.4 nm, respectively. The A and B excitonic peaks correspond to the direct excitonic transitions of the MoS_2 originated from the energy split

of valence-band and spin-orbital coupling.[13] The C excitonic peak is attributed to the direct transition from the deep valence band to the conduction band.[14] On the other hand, WS_2 QD displays an absorption peak in the near-UV region ($\lambda < 300$ nm), which is assigned to the excitonic features of WS_2 quantum dots.[15] In the 1L-MoS_2/WS_2 HS, all the three absorption peaks (A, B, and C) of 1L-MoS_2 are observed. In addition, as compared to the pristine 1L-MoS_2 and WS_2 QD, the 1L-MoS_2/WS_2 HS exhibits enhanced absorption, which may be ascribed to the increase in the number of layers in the HS.[16] The inset shows the magnified view of the spectra in the selected region of 550-750 nm, evidently revealing a red-shift of A and B peaks by ~ 3.7 nm and ~ 2.5 nm for the 1L-MoS_2/WS_2 QD HS as compared to that of bare 1L-MoS_2. This shift in the peaks in the HS sample may be due to the charge transfer from the WS_2 QD to the 1L-MoS_2, which leads to the effective n-type doping of the 1L- MoS_2 film due to the HS formation.[17] This n-type doping of the 1L-MoS_2/WS_2 QD HS is consistent with the Raman spectral shift shown in **Fig. 6.4(a)**. **Fig. 6.5(b)** displays the PL spectrum of pristine 1L-MoS_2, measured at room temperature. The spectrum is featured by a broad peak appearing at 670 nm. We examine the evolution of the PL spectrum of 1L-MoS_2 in more detail by fitting it with four Gaussian peaks: the neutral exciton (A^0), B exciton, trion (A^-), and the bound exciton (X), respectively. The A^0 and B exciton peaks are associated with direct optical transitions from the highest valence-band spin-orbit to the lowest conduction band at the K point in the Brillouin Zone.[18] The A^- exciton peak (trion) is a negatively charged exciton. When excess electrons are introduced, these electrons bind with photoexcited electron-hole pairs resulting in the formation of trions, which causes a reduction of exciton absorption and PL intensity. The spectral weight of the neutral exciton is then transferred to the trion. Thus, the doping level of the CVD grown MoS_2 often govern the spectral weight of trion emission peak. The presence of peak X is ascribed to the radiative recombination of bound excitons.[19] To further investigate the excitonic properties of the CVD grown 1L-MoS_2, temperature dependent PL measurement was carried out in the range of 83-300 K, as shown in **Fig. 6.5(c)**. As the temperature increases from 83 to 300 K, the intensity of PL peak decrease systematically (see **Fig. 6.5(c)**). This decrease in PL peak intensity of 1L-MoS_2 with increasing temperature is mainly due to the higher rate of the non-radiative recombination process with an increase in the thermal energy, as explained earlier.[20] A redshift in the PL peak position is also observed with the increase in the temperature. This shift is attributed to the decrease in the bandgap with the increase in the temperature.[21] From the low-temperature PL analysis, we can estimate the exciton binding energy

(E_b) of the CVD grown pristine 1L-MoS_2 and can be expressed in terms of the Arrhenius equation as follows:

$$I(T) = \frac{I_0}{1+Ce^{\left(-\frac{E_b}{k_B T}\right)}} \quad (1)$$

Here I(T) and I_0 are the PL peak intensities of the A exciton at temperature T and 0 K, respectively, and C is a constant, E_b is the exciton binding energy and k_B is the Boltzmann constant. We considered the temperature range of 183-300 K to extract the exciton binding energy of ~176 meV from the Arrhenius plot, as shown in the inset of Fig. 4(f), which is comparable to the reported value for monolayer MoS_2.[22] **Fig. 6.5(e)** displays the comparative PL spectra of 1L-MoS_2 and 1L-MoS_2/WS_2 QD. The PL intensity of 1L-MoS_2/WS_2 QD was observed to be partly quenched when compared with the pristine 1L-MoS_2. Also, the PL peak position was considerably redshifted by 13 nm in the 1L-MoS_2/WS_2 QD HS as compared to that of 1L-MoS_2. This redshift in the PL peak position and partial quenching of the PL intensity in the 1L-MoS_2/WS_2 QD HS can be attributed to the increase in the trion (A^-) population due to the presence of excess electrons after the formation of the HS. This is a result of the charge transfer from the WS_2 QDs to the 1L-MoS_2 leading to the n-doping effect of the HS. A thorough understanding of the PL behavior of the HS was presented in the previous chapter.

6.3.4. Performance study of 1L-MoS_2/WS_2 QD heterojunction photodetector

In this section, we discuss about the 1L-MoS_2/WS_2 QD heterojunction as an efficient photodetector over a wide spectral range. **Fig. 6.6(a)** shows the schematic representation of the device configuration of the 1L-MoS_2/WS_2 QD heterojunction photodetector. We studied the comparative performance of pristine 1L-MoS_2 and 1L-MoS_2/WS_2 QD as photodetectors. **Fig. 6.6(b,c)** depicts the current-voltage (I–V) characteristics of pristine 1L-MoS_2 and 1L-MoS_2/WS_2 QD in the dark and under the illumination with 405 nm laser with an illumination power density of 2.35 mW/cm^2. The I-V characteristics curve for the 1L-MoS_2 shown in **Fig. 6.6(b)** is nearly symmetric both in the dark and light conditions, indicating the formation of back- to-back Schottky diode contact. On the other hand, for the 1L-MoS_2/WS_2 QD, the I-V characteristic curve exhibits asymmetric diode like rectifying behavior, as shown in **Fig. 6.6(c)**. This indicates the formation of type-II heterojunction between 1L-MoS_2 and WS_2 QD.

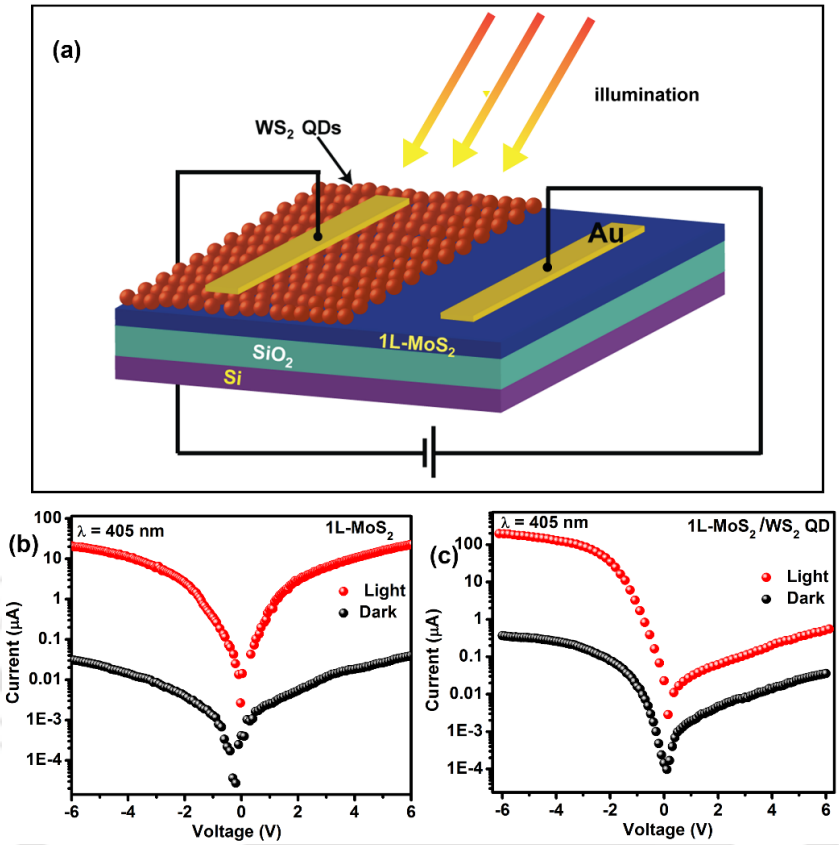

Fig. 6.6: Schematic illustration of 1-LMoS$_2$/WS$_2$ QD heterojunction vertical type photodetector under reverse bias. I–V characteristics of (b) 1L-MoS$_2$ and (c) 1-LMoS$_2$/WS$_2$ QD heterojunction photodetector in the dark and under the illumination of intensity 2.35 mW/cm^2 of wavelength 405 nm.

To analyze the dependence of the photocurrent on the incident light power, we measure the photocurrent of the HS photodetector with different power densities, as shown in **Fig. 6.7(a)**. It is clear that with the increase in the irradiation power, there is a systematic increase in the photocurrent. This dependence of the photocurrent on the incident power can be fitted well by the power law:

$$I_{ph} = AP^{\theta} \qquad (2)$$

where I_{ph} is the photocurrent, P is the incident light power density, A is a constant, and θ is an exponent that determines the response of the photocurrent to light intensity. By fitting the data using the power law, the θ value is found to be 0.78. The obtained exponent value of <1 is due to the loss of carriers due to the trapping as well as recombination of photogenerated charge carriers due to the presence of some trap states at the interface between 1-LMoS$_2$ and WS$_2$ QDs.[23] **Fig. 6.7(b)** shows the typical temporal response of the photocurrent under illumination under different

bias voltages. We observed that over a long operational period, the photoresponse of the device is quite stable and reproducible. In the region of higher bias voltages, a linear increase in the photocurrent with an increase in the bias voltage was observed, which is due to the efficient separation and transport of photocarriers and the suppression of the recombination loss. On the other hand, there is a rapid increase in the photocurrent at lower bias voltages region (0.1 to 1.5 V), as shown in the inset of **Fig. 6.7(b)**. Furthermore, we measure and compare the optoelectronic figures of merit of the bare 1L-MoS_2 photodetector and the 1L-MoS_2/WS_2 QD HS photodetector to evaluate their photodetection performance. The photoresponsivity (R) and the detectivity (D*) are critical parameters to determine the sensitivity for an optoelectronic device. **Fig. 6.7(c)** shows a comparison of spectral responsivity of the pristine and HS photodetectors in the spectral range of 300-800 nm at 5V bias. Spectral responsivity (R(λ)) of a photodetector is defined by the following equation:[24]

$$R(\lambda) = \frac{I_{ph}(\lambda)}{P_{in}A} \quad (3)$$

where, $I_{ph}(\lambda)$ is the photocurrent at a particular wavelength λ, P_{in} is the incident optical power density at λ, and A is the effective device surface area (A ~ 0.01 cm^2). Pristine 1L-MoS_2 shows a broadband response with a peak responsivity ~1.08 A/W at a wavelength of 658 nm, while the hybrid photodetector exhibits a relatively higher responsivity with the highest responsivity ~2.17 A/W at ~600 nm, which is more than two times of the pristine 1L-MoS_2 photodetector. Thus, the hybrid photodetector shows superior performance than the pristine 1L-MoS_2 photodetector due to the efficient charge transfer between MoS_2 and WS_2 QDs.

The detectivity (D^*) of a photodetector can be expressed as:

$$D^*(\lambda) = R(\lambda)\left(\frac{A}{2QI_D}\right)^{1/2} \quad (4)$$

where I_D is the dark current, and Q is the electronic charge (1.6×10^{-19} C). The D* value of pristine 1L-MoS_2 photodetector is found to be ~5.95×10^{11} Jones, while that of the 1L-MoS_2/WS_2 QD HS is 1.18×10^{12} Jones under the same condition, as shown in **Fig 6.7(d)**. Thus, the D* of the HS photodetector is two times that of the pristine MoS_2 photodetector.

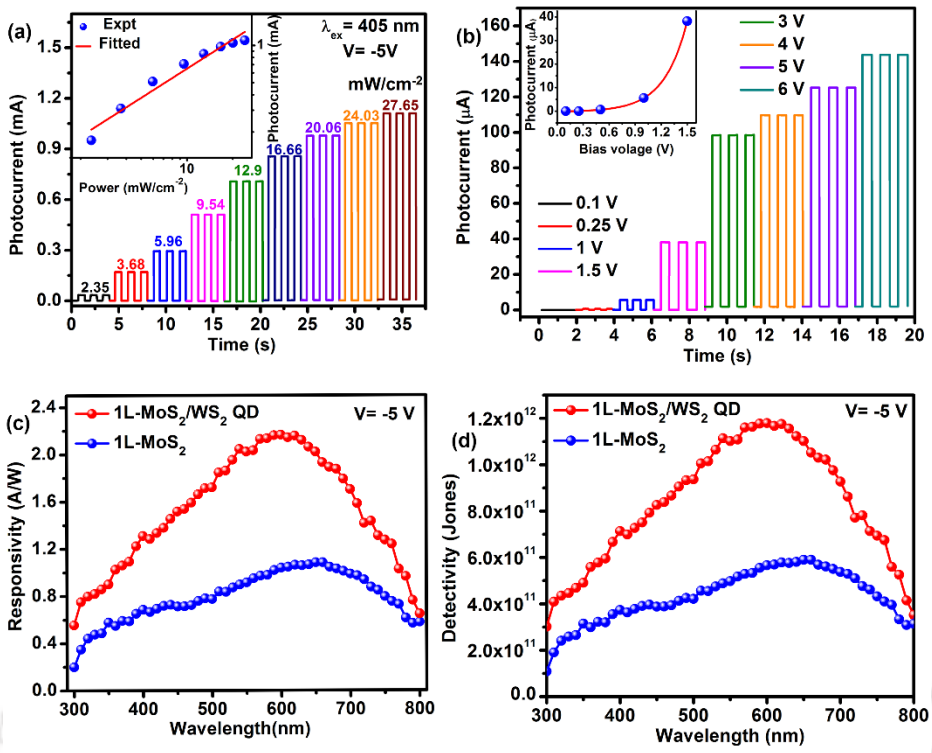

Fig. 6.7: (a) Power dependent photocurrent response of 1-LMoS_2/WS_2 QD with 405 nm pulsed laser excitation at 5V (reverse bias) applied bias. Inset shows the variation photocurrent of the 1-LMoS_2/WS_2 QD photodetector as a function of illumination intensity with the corresponding fitting. (b) Time-dependent photocurrent response of 1-LMoS_2/WS_2 QD under 405 nm light illumination (2.35 mW/cm^2) recorded at different bias voltages. The inset shows the photocurrent vs. bias voltage for a fixed intensity of illumination. The comparison of (c) responsivity and (d) detectivity of 1L-MoS_2 and 1L-MoS_2/WS_2 QD with -5 V applied bias.

Next, we investigated the temporal response of the photodetectors using a pulsed laser source. **Fig. 6.8(a)** and **(b)** displays the time-dependent photoresponse curves of pristine 1L-MoS_2 and 1L-MoS_2/WS_2 QD HS measured at a reverse bias of 5 V and 405 nm pulsed laser excitation with an power density of 2.35 mWcm^{-2}. To estimate the characteristic rise/fall time of the photodetector, the experimental data are fitted by a single exponential function as

$$I(t) = I_0 + A\exp(-t/\tau), \quad (5)$$

where τ is the time constant, and I_0 and A are constants. The value of the time constants of photocurrent rise and fall for pristine 1L-MoS_2 photodetector are found to be 49 μs and 638 μs, as shown in **Fig. 6.8 (a)**. In contrast, the rise and fall time of the hybrid photodetector is reduced to 18.5 μs and 95.4 μs (see **Fig. 6.8(b)**), which further demonstrates that the hybrid photodetector is significantly faster in response than the pristine 1L-MoS_2 photodetector. The improved response of 1L-MoS_2/WS_2 QD photodetector is attributed to the efficient transfer of charges between MoS_2

and WS_2 QDs due to the appropriate band alignment at the heterojunction, as explained earlier in Chapter 5 (**Section 5.3.2.2).** Furthermore, the defect states in MoS_2 are provided with electrons from the WS_2 QDs, which can significantly decrease the number of trapped electrons.[25] We summarize the key figure of merit of the HS photodetector in **Table 6.1,** to demonstrate the improvement achieved by the hybrid 1L-MoS_2/WS_2 QD photodetector in comparison with other 0D-2D heterojunction photodetectors.

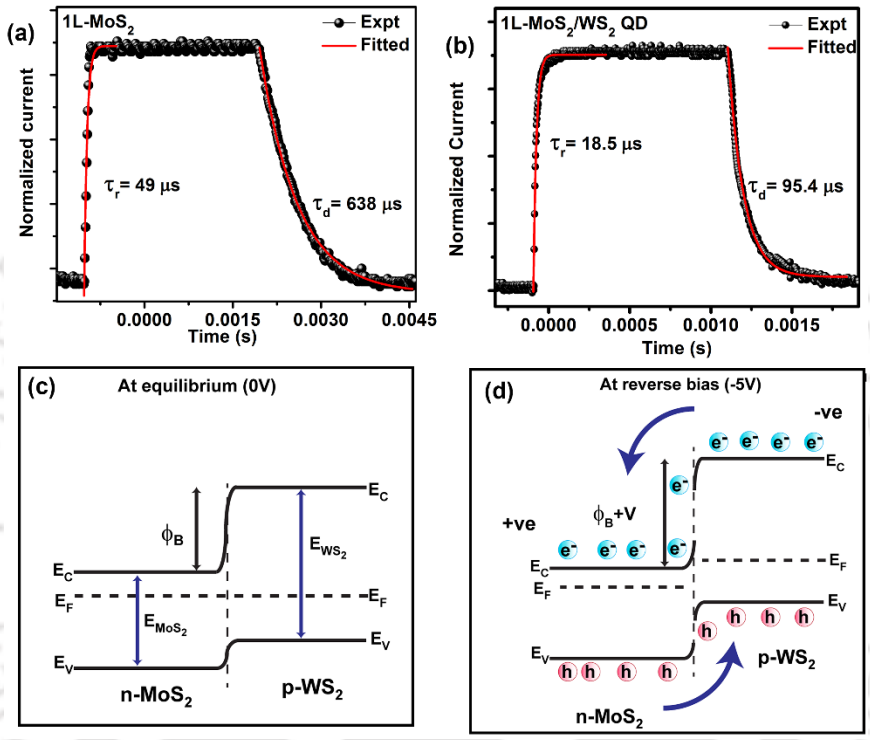

Fig. 6.8: Time-dependent photoresponse of (a) 1-LMoS_2 and (b) 1-LMoS_2/WS_2 QD under 405 nm light illumination recorded at different bias voltages. Schematic of the band diagram of 1L-MoS_2/WS_2 QD heterojunction at (c) equilibrium (zero bias), and (d) reverse bias condition.

To visualize the mechanism of improved photoresponse of the HS photodetector, a schematic band diagram of the 1L-MoS_2/WS_2 QD heterojunction is illustrated in **Fig. 6.8(c,d)**. Note that the measured work function of the 1L-MoS_2 is 4.435 eV, which is higher than that of 1L-MoS_2/WS_2 QD heterojunction, as discussed in the previous chapter (**Section 5.3.2.2)**. This suggests a favorable band bending in the HS for the charge transfer from WS_2 QDs to 1L-MoS_2. When WS_2 QDs and 1L-MoS_2 are in contact, potential barrier Φ_B is developed at the interface of p-type WS_2 QDs and n-type 1L-MoS_2, and the Fermi levels are aligned at the same energy value (equilibrium), as shown in **Fig 6.8 (c).** This leads to the type II band alignment between WS_2 QDs and 1L-MoS_2. Under illumination, the incident light is absorbed by the 1L-MoS_2/WS_2 QD heterojunction, and

the photocarriers are separated at the p–n interface between WS_2 QDs and 1L-MoS_2. **Fig. 6.8(d)** shows the energy band diagram of the 1L-MoS_2/WS_2 QD heterojunction at a reverse bias, under illumination. Under this condition, the potential difference increases to (Φ_B +V) due to the shift of the Fermi level, which further leads to the expansion of the barrier potential across the depletion region as well as enhanced electric field, as shown in **Fig. 6.8(d).** Subsequently, the photo-generated electrons and holes flow towards the opposite electrodes, leading to the high photocurrent in the 1L-MoS_2/WS_2 QD photodetector. The fast response of the heterojunction is attributed to the high carrier mobility of MoS_2 and the fast charge separation at the heterojunction.

Table 6.1: *Comparison of the performance of the 1L-MoS_2/WS_2 QD photodetector with commercial photodetector and other reported MoS_2 and MoS_2 based photodetectors.*

Device structure	Responsivity (A/W)	Detectivity (Jones)	Rise time	Fall time	Ref.
MoS_2/PbSe QD	1.9×10^{-6}	-	250 s	430 s	[24]
Si/MoS_2	7.2	~7.5×10^{9}	-	-	[26]
Commercial PD (Advanced Photonix, 008-2151-112)	0.18	-	~1ns	-	-
Few layer MoS_2 Schottky	0.57	~10^{10}	70 µs	110 µs	[27]
1L-MoS_2/WS_2 QD	2.17	1.18×10^{12}	18.5 µs	95.4 µs	This work

6.4. Conclusion

In summary, a high-performance heterojunction photodetector was fabricated by combining the CVD grown n-type 1L-MoS_2 with p-type WS_2 QDs synthesized by liquid exfoliation method, for the first time. Raman and PL measurements indicated charge transfer across the 1L-MoS_2/WS_2 QDs heterojunction. The hybrid 1L-MoS_2/WS_2 QD photodetector shows much improved performance compared to the pristine MoS_2 counterpart. The device exhibits high responsivity of ~2.17 A/W at 600 nm, detectivity of 1.18×10^{12} Jones, which is two times of the pristine 1L-MoS_2. The response rise and fall time of the hybrid photodetector are reduced to 18.5 µs and 95.4 µs from 49 µs and 638 µs of the pristine 1L-MoS_2 photodetector. The mechanism behind the improved photodetection was explained on the basis of efficient charge transfer at the interface and reduced

trapaping of carriers at the interface. Employing atomically thin 2D heterostructures of different material platforms may pave the way for a promising route for future novel high-performance optoelectronic devices.

References

1. Novoselov, K. S.; Geim, A. K.; Morozov, S. V.; Jiang, D.; Zhang, Y.; Dubonos, S. V.; Grigorieva, I. V.; Firsov, A. A., Electric Field Effect in Atomically Thin Carbon Films. *Science* **2004**, *306*, 666.
2. Borzda, T., et al., Charge Photogeneration in Few-Layer Mos2. *Advanced Functional Materials* **2015**, *25*, 3351-3358.
3. Liu, B., et al., High Performance Photodetector Based on Graphene/Mos2/Graphene Lateral Heterostrurcture with Schottky Junctions. *Journal of Alloys and Compounds* **2019**, *779*, 140-146.
4. Qiao, S.; Cong, R.; Liu, J.; Liang, B.; Fu, G.; Yu, W.; Ren, K.; Wang, S.; Pan, C., A Vertically Layered Mos2/Si Heterojunction for an Ultrahigh and Ultrafast Photoresponse Photodetector. *Journal of Materials Chemistry C* **2018**, *6*, 3233-3239.
5. Choi, W., et al., High-Detectivity Multilayer Mos2 Phototransistors with Spectral Response from Ultraviolet to Infrared. *Advanced Materials* **2012**, *24*, 5832-5836.
6. Das, S.; Chen, H.-Y.; Penumatcha, A. V.; Appenzeller, J., High Performance Multilayer Mos2 Transistors with Scandium Contacts. *Nano Letters* **2013**, *13*, 100-105.
7. Zhang, Y.; Yu, Y.; Mi, L.; Wang, H.; Zhu, Z.; Wu, Q.; Zhang, Y.; Jiang, Y., In Situ Fabrication of Vertical Multilayered Mos2/Si Homotype Heterojunction for High-Speed Visible–near-Infrared Photodetectors. *Small* **2016**, *12*, 1062-1071.
8. Konstantatos, G.; Badioli, M.; Gaudreau, L.; Osmond, J.; Bernechea, M.; de Arquer, F. P. G.; Gatti, F.; Koppens, F. H. L., Hybrid Graphene–Quantum Dot Phototransistors with Ultrahigh Gain. *Nature Nanotechnology* **2012**, *7*, 363-368.
9. Xu, H.; Wu, J.; Feng, Q.; Mao, N.; Wang, C.; Zhang, J., High Responsivity and Gate Tunable Graphene-Mos2 Hybrid Phototransistor. *Small* **2014**, *10*, 2300-2306.
10. Kaushik, N.; Karmakar, D.; Nipane, A.; Karande, S.; Lodha, S., Interfacial N-Doping Using an Ultrathin Tio2 Layer for Contact Resistance Reduction in Mos2. *ACS Applied Materials & Interfaces* **2016**, *8*, 256-263.
11. Li, H.; Zhang, Q.; Yap, C. C. R.; Tay, B. K.; Edwin, T. H. T.; Olivier, A.; Baillargeat, D., From Bulk to Monolayer Mos2: Evolution of Raman Scattering. *Adv. Funct. Mater.* **2012**, *22*, 1385-1390.
12. Chakraborty, B.; Bera, A.; Muthu, D. V. S.; Bhowmick, S.; Waghmare, U. V.; Sood, A. K., Symmetry-Dependent Phonon Renormalization in Monolayer Mos${}_{2}$ Transistor. *Phys. Rev. B* **2012**, *85*, 161403.
13. Mak, K. F.; Lee, C.; Hone, J.; Shan, J.; Heinz, T. F., Atomically Thin ${\Mathrm{Mos}}_{2}$: A New Direct-Gap Semiconductor. *Phys. Rev. Lett.* **2010**, *105*, 136805.
14. Wilcoxon, J. P.; Samara, G. A., Strong Quantum-Size Effects in a Layered Semiconductor: ${\Mathrm{Mos}}_{2}$ Nanoclusters. *Physical Review B* **1995**, *51*, 7299-7302.
15. Gutiérrez, H. R.; Perea-López, N.; Elías, A. L.; Berkdemir, A.; Wang, B.; Lv, R.; López-Urías, F.; Crespi, V. H.; Terrones, H.; Terrones, M., Extraordinary Room-Temperature Photoluminescence in Triangular Ws2 Monolayers. *Nano Letters* **2013**, *13*, 3447-3454.
16. Wang, W.; Li, K.; Wang, Y.; Jiang, W.; Liu, X.; Qi, H., Investigation of the Band Alignment at Mos2/Ptse2 Heterojunctions. *Applied Physics Letters* **2019**, *114*, 201601.
17. Dhakal, K. P.; Duong, D. L.; Lee, J.; Nam, H.; Kim, M.; Kan, M.; Lee, Y. H.; Kim, J., Confocal Absorption Spectral Imaging of Mos2: Optical Transitions Depending on the Atomic Thickness of Intrinsic and Chemically Doped Mos2. *Nanoscale* **2014**, *6*, 13028-13035.

18. Splendiani, A.; Sun, L.; Zhang, Y.; Li, T.; Kim, J.; Chim, C.-Y.; Galli, G.; Wang, F., Emerging Photoluminescence in Monolayer Mos2. *Nano Lett.* **2010**, *10*, 1271-1275.
19. Tongay, S., et al., Defects Activated Photoluminescence in Two-Dimensional Semiconductors: Interplay between Bound, Charged, and Free Excitons. *Sci. Rep.* **2013**, *3*, 2657.
20. Mawlong, L. P. L.; Paul, K. K.; Giri, P. K., Direct Chemical Vapor Deposition Growth of Monolayer Mos2 on Tio2 Nanorods and Evidence for Doping-Induced Strong Photoluminescence Enhancement. *The Journal of Physical Chemistry C* **2018**, *122*, 15017-15025.
21. Korn, T.; Heydrich, S.; Hirmer, M.; Schmutzler, J.; Schüller, C., Low-Temperature Photocarrier Dynamics in Monolayer Mos2. *Applied Physics Letters* **2011**, *99*, 102109.
22. Thilagam, A., Dielectric Constant of Monolayer Transition Metal Dichalcogenides across Excitonic Resonances. *arXiv preprint arXiv:1810.12551* **2018**.
23. Cunningham, G.; Khan, U.; Backes, C.; Hanlon, D.; McCloskey, D.; Donegan, J. F.; Coleman, J. N., Photoconductivity of Solution-Processed Mos2 Films. *Journal of Materials Chemistry C* **2013**, *1*, 6899-6904.
24. Schornbaum, J.; Winter, B.; Schießl, S. P.; Gannott, F.; Katsukis, G.; Guldi, D. M.; Spiecker, E.; Zaumseil, J., Epitaxial Growth of Pbse Quantum Dots on Mos2 Nanosheets and Their near-Infrared Photoresponse. *Advanced Functional Materials* **2014**, *24*, 5798-5806.
25. Liu, H.; Gao, F.; Hu, Y.; Zhang, J.; Wang, L.; Feng, W.; Hou, J.; Hu, P., Enhanced Photoresponse of Monolayer Mos 2 through Hybridization with Carbon Quantum Dots as Efficient Photosensitizer. *2D Materials* **2019**, *6*, 035025.
26. Li, Y.; Xu, C.-Y.; Wang, J.-Y.; Zhen, L., Photodiode-Like Behavior and Excellent Photoresponse of Vertical Si/Monolayer Mos2 Heterostructures. *Scientific Reports* **2014**, *4*, 7186.
27. Tsai, D.-S.; Liu, K.-K.; Lien, D.-H.; Tsai, M.-L.; Kang, C.-F.; Lin, C.-A.; Li, L.-J.; He, J.-H., Few-Layer Mos2 with High Broadband Photogain and Fast Optical Switching for Use in Harsh Environments. *ACS Nano* **2013**, *7*, 3905-3911.

भारतीय प्रौद्योगिकी संस्थान गुवाहाटी
Indian Institute of Technology Guwahati

Chapter 7

Summary and Outlook

This chapter presents a summary of the contributions of the thesis and highlights the new findings on the synthesis of monolayer MoS_2 and its heterostructures with TiO_2 nanostructures, plasmonic nanoparticles (NPs), and WS_2 quantum dots, and their applications in light emission and broadband photodetection. Outlook and scope for future work are also presented at the end.

7.1. Summary and Highlights of the Thesis Contribution

In this dissertation, we have presented the controlled growth of monolayer MoS_2 by chemical vapor deposition (CVD) method. We have controlled various growth parameters such as the carrier gas, growth temperature, precursors, and substrates to obtain high-quality monolayer MoS_2 over large area on SiO_2 and sapphire substrates (Chapter 2). Next, we have demonstrated a simple one-step direct synthesis process of 1L-MoS2 film by CVD method over the hydrothermally prepared TiO_2 nanorods (NRs) and investigated the mechanism of strong enhancement of the photoluminescence (PL) intensity of the 1L-MoS_2 due to the formation of the heterostructure (HS) with TiO_2 NRs (Chapter 3). Further, we have demonstrated a dramatically enhanced PL emission from the large area monolayer MoS_2 grown over an array of Au nanoparticles (NPs) coated over hierarchical TiO_2 nanostructure forming a core-shell TiO_2/Au/MoS_2 hybrid structure, where the PL intensity is enhanced by about three orders of magnitude, highest among the reported values (Chapter 4). Next, we investigated the tunability of the PL and doping of monolayer MoS_2 by decorating it with WS_2 quantum dots (WS_2 QD). A detailed quantitative analysis using the four-energy level model involving coupled charge transfer dynamics was employed to explain the behavior of the PL in 1L-MoS_2/WS_2 QD HS as a function of the concentration of WS_2 QDs (Chapter 5). Finally, we have fabricated a vertical heterojunction photodetector (PD) by incorporating WS_2 QDs over a CVD grown monolayer MoS_2 on SiO_2 substrate. The 1L-MoS_2/WS_2 QD p-n heterojunction acts as an efficient, high-performance broadband photodetector, reported for the first time (Chapter 6).

The major contributions of the present thesis work are summarized below.

A. Controlled Growth of Monolayer MoS_2 by Chemical Vapor Deposition Method

First, we demonstrated the growth of luminescent monolayer and bilayer MoS_2 dots with controlled size and shape on SiO_2 substrate by a low temperature (510-560˚C) CVD technique. The Raman spectra of the samples at room indicated the growth of the crystalline MoS_2 dots array. Position dependent Raman profiles indicated some kind of non-uniformity in the layer thickness across the dots. Next, we demonstrated that the growth parameters such as the carrier gas, growth temperature, precursors, and substrates play an important role in the growth of high-quality monolayer MoS_2. By tuning these growth parameters, the growth of purely monolayer triangular MoS_2 was achieved. The size of these triangular monolayer MoS_2 could be varied from 1 to 6 μm and are found to be highly crystalline. Finally, we have grown large area continuous monolayer MoS_2, covering a few mm^2 on various substrates by CVD technique. This is achieved by controlling the vapor pressure locally with the use of a specially designed quartz mask between the MoO_3 source and the substrate. We have systematically studied the Raman and PL properties of the as-grown MoS_2 on the different substrates. The substrates have significant effect on the PL peak intensity and emission wavelengths.

B. Direct CVD Growth of Monolayer MoS_2 on TiO_2 Nanorods and Evidence for Doping Induced Strong Photoluminescence Enhancement

We have demonstrated the growth of monolayer MoS_2 shell by a direct CVD process on the hydrothermally grown vertical TiO_2 NRs, forming a MoS_2@TiO_2 core-shell heterostructure (HS). The HS sample exhibited a strong enhancement in PL intensity (by nearly two orders of magnitude) at room temperature as compared to the bare 1L-MoS2 grown on SiO_2 substrate. The observed strong PL enhancement is explained on the basis of oxygen bonding induced p-type doping in intrinsically n-type MoS_2 lattice, which suppresses the trion formation/ emission and increases in neutral exciton emissions. Low-temperature PL measurement on the HS sample indicates the suppression of nonradiative recombination of excitons at the MoS_2, which eventually boosts the PL emission at room temperature. Finally, oxygen plasma irradiation was performed on pristine MoS_2 and MoS_2@TiO_2 HS samples to verify the p-doping through the oxygen bonding at the defect sites in MoS_2, resulting in the enhancement of PL. Our results provide a new and easy way to fabricate MoS_2 based heterostructure and tune the optical properties of MoS_2 to realize its

practical applications in optoelectronic or nanophotonic devices. *This work has been published in "J. Phys. Chem. C 121, 15017-15025 (2018)".*

C. Exciton-Plasmon Coupling and Giant Photoluminescence Enhancement in Hierarchical designed TiO_2/Au/MoS_2 Ternary Core-Shell Heterostructure

We have developed a simple and powerful strategy to achieve a dramatically high PL enhancement in 1L-MoS_2 using plasmonic substrate consisting of Au/Ag NPs grown on TiO_2 NSs. An array of Au NPs was grown on the hydrothermally grown hierarchical TiO_2 NSs followed by a direct CVD growth of monolayer MoS_2 shell, for the first time, forming a TiO_2/Au/MoS_2 ternary core-shell HS. This ternary core-shell structure allows a stronger interaction between the incident light and 1L-MoS_2, leading to a ~463-fold enhancement in PL intensity compared to the pristine 1L-MoS_2 at room temperature. We consider two major mechanisms for the enhancement of PL intensity in 1L-MoS_2 in the ternary heterostructure: (a) the excess electrons responsible for trion formation are transferred from the MoS_2 to TiO_2 at the interface of MoS_2/TiO_2, leading to the effective p-type doping of 1L-MoS_2, which inhibits the trion emission and enhances the neutral exciton emission significantly. (b) The exciton-plasmon coupling between the excitons of the 1L-MoS_2 and surface plasmons of the Au NPs at the MoS_2/Au interface is believed to enhance the PL emission enormously, as shown from the theoretical estimate of the field enhancement factor that matches closely with the PL enhancement factor. The present study demonstrates that MoS_2 based heterostructures offer a promising way to improve the performance of future nanophotonic and optoelectronic devices.

D. Coupled Charge Transfer Dynamics and Photoluminescence Quenching in Monolayer MoS_2 Decorated with WS_2 Quantum Dots

We have demonstrated the tunability in the light emission of the CVD grown 1L-MoS_2 by doping it with a 2D semiconducting WS_2 QD. A systematic quenching of the PL intensity of 1L-MoS_2 with the decoration of WS_2 QDs was observed. The relative changes in the constitient emission peaks was quantitatively analysied and explained on the basis of charge transfer from WS_2 QDs to 1L-MoS_2. The KPFM analysis revealed a decrease in the work function of 1L-MoS_2 with the decoration of WS_2 QDs providing a direct evidence for the charge transfer. A detailed analysis

using coupled charge transfer among four-energy level model was employed to explain the redshift and the decrease in the PL intensity of the 1L-MoS_2 as a function of the concentration of the WS_2 QDs. An analytical solution to the coupled rate equations for change in the population of different excitonic emissions, including bound excitonic transition, was successfully employed to quantitatively understand the quenching process. The contribution of defects in the charge transfer induced quenching of PL and the carrier-density-dependent recombination dynamics of excitons were established through the quantitative analysis of the spectral evolution. Charge transfer induced increase in electron density in 1L-MoS_2 leads to the transformation of the neutral excitons to trions. The doped electron density up to $\Delta n_e \sim 1.5 \times 10^{13}$ cm^{-2} indicates high n-type doping in the 1L-MoS_2. Our results suggest an effective and simple approach to manipulate the electron density through the doping technique, which is advantageous to tune the optical and electrical properties of monolayer TMDs for various optoelectronic applications. *This work has been published in "Scientific Report 9, 1-14 (2019)".*

E. A High-Performance Hybrid 2D/0D Photodetector based on 1L-MoS_2/WS_2 Quantum Dot Heterostructure

We have demonstrated a high-performance heterojunction photodetector by combining an n-type CVD grown 1L-MoS_2 with p-type WS_2 QDs synthesized by liquid exfoliation method, for the first time. The successful formation of the 1L-MoS_2/WS_2 QDs heterojunction was confirmed from Raman and PL measurements. The I–V characteristics of the hybrid photodetector confirms the formation of rectifying p-n junction at the interface between the p-type WS2 QDs and n-type 1L-MoS_2. The hybrid 1L-MoS_2/WS_2 QD photodetector shows a higher photodetection performance compared to the pristine MoS_2 counterpart. The device exhibits high responsivity of ~2.17 A/W at 600 nm, detectivity of 1.18×10^{12} Jones, which is higher than pristine 1L-MoS_2. The response rise and fall time of the hybrid photodetector are reduced to 18.5 µs and 95.4 µs, respectively, from 49 µs and 638 µs of the pristine 1L-MoS_2 photodetector. Employing atomically thin 2D heterostructures of different material platforms may pave the way for a promising route for future novel high-performance optoelectronic devices.

7.2. Scope of Future Work

In the present thesis, we have demonstrated the controlled growth of device quality large-area monolayer MoS_2 by CVD technique and the fabrication of MoS_2 based heterostructures with TiO_2

NRs, TiO_2 NSs, metal NPs (Au and Ag), and WS_2 QDs for the light emission and broadband photodetection applications. There is a vast scope to extend the present work for a broad range of applications, as described below:

1. Monolayer MoS_2 can be combined to form heterostructures with several other 2D materials, e.g, $MoSe_2$, WSe_2, h-BN, Bi_2O_2Se, MXenes, etc. to enable a wide range of device applications.

2. Low temperatures CVD growth of 1L-MoS_2 and its heterostructure for the fabrication of flexible devices.

3. Direct CVD growth of other compatible 2D transition metal dichalcogenide (TMDs) layers for multi-junction formation and studies on its fundamental aspects as well as optoelectronic applications.

4. The hybrid structure of monolayer MoS_2 with TiO_2 displays an excellent absorption in the UV-visible region and thus can serve as a promising system for photoelectrochemical hydrogen production and photodetection.

5. Further investigation of the carrier trapping and charge transfer dynamics in MoS_2 based heterostructure for future improvement in the optical and electrical properties, which will be useful for various optoelectronic applications.

6. TiO_2/Au/MoS_2 ternary heterostructure exhibited a giant enhancement of the PL intensity compared to MoS_2. Thus, further investigation of similar ternary systems with different plasmonic nanoparticles can be promising for next-generation photonic devices.